R-06-08

Reliability of nondestructive testing (NDT) of the copper canister seal weld

Ch Müller, M Elagin, M Scharmach, C Bellon,
G-R Jaenisch, S Bär, B Redmer, J Goebbels,
U Ewert, U Zscherpel, R Boehm, G Brekow,
A Erhard, T Heckel, U Tessaro, D Tscharntke
BAM – Federal Institute for Materials Research
and Testing, Berlin

U Ronneteg
Bodycote Materials Testing, Linköping

April 2006

Svensk Kärnbränslehantering AB
Swedish Nuclear Fuel
and Waste Management Co
Box 5864
SE-102 40 Stockholm Sweden
Tel 08-459 84 00
+46 8 459 84 00
Fax 08-661 57 19
+46 8 661 57 19

ISSN 1402-3091
SKB Rapport R-06-08

Reliability of nondestructive testing (NDT) of the copper canister seal weld

Ch Müller, M Elagin, M Scharmach, C Bellon,
G-R Jaenisch, S Bär, B Redmer, J Goebbels,
U Ewert, U Zscherpel, R Boehm, G Brekow,
A Erhard, T Heckel, U Tessaro, D Tscharntke
BAM – Federal Institute for Materials Research
and Testing, Berlin

U Ronneteg
Bodycote Materials Testing, Linköping

April 2006

Abstract

This report “NDT reliability” describes methodology and results of the reliability investigations performed by BAM for the non-destructive testing (NDT) methods developed at the SKB Canister Laboratory for the future canister manufacturing. On the one hand it creates a link from the assessment of the reliability and inspection performance to the full risk assessment process of the canister or deposit project. On the other hand it gives the confirmation of the basic quality of the NDT methods to verify they are suited to indicate the weld quality.

Additional reference X-ray examination using high sensitive technique and cross sectioning has been done to give a deeper confirmation of the weld quality down to a micro-structure level. The assessment of physical parameters and their evaluation according to EN standards of the applied NDT techniques was also a part of the project. Of special importance was the insight about local signal to noise ratios with consequence for the POD (probability of detection) settings. The probability of detection curves are in principle determined according to the MIL 1823 Reliability Guideline which was developed for the determination of integrity of gas turbine engines for the US military. Extensions for the more complex discontinuity situations in the copper friction stir and electron beam welds were necessary which are for both the welding and the NDT technique a challenge.

As the key parameter for the flaw detectability the $a_{90/95}$ magnitudes are determined, i.e. the size a of the flaw for which the lower 95% confidence bound crosses the 90% POD level. This means it is guaranteed that flaws with a size of $a_{90/95}$ will be detected with 90% probability where only 5% might fall outside this confidence limit in case the experiment is repeated. Modelling calculations for both radiographic and ultrasonic technique are used to assist for a serious physical argumentation accompanying the empirical POD curves.

Contents

1 Introduction

1.1 The KBS-3 concept for the Swedish nuclear waste

SKB plan to deposit the spent nuclear fuel according to the KBS-3-method, developed during the last 20 years. The main features of KBS-3 are that the spent fuel shall be encapsulated into copper canisters and placed in the bedrock at 400–700 m depth. SKB's efforts are based on a stepwise implementation of deep geological disposal of spent nuclear fuel including concurrent activities in the areas of deep repository- and encapsulation technology. Major milestones in the program are application for construction and building of an encapsulation plant at 2006 and a deep repository at 2008. According to the program initial operation of the system will start at 2017.

The Swedish system for the spent nuclear fuel includes several sub-systems. Today SKB has a central interim storage for spent nuclear fuel (Clab) in Oskarshamn, a final disposal for radioactive operational waste (SFR) in Forsmark and a transportation system. To be able to deposit the fuel according to KBS-3 concept, SKB needs to build a final repository, develop a production system for canisters and build a plant for encapsulation of the spent fuel.

The deposit according to the KBS-3-method is designed to isolate the spent fuel for at least 100,000 years. Several barriers accomplish the safety; the fuel itself within the cladding tube, the copper canister that have the mechanical and chemical resistance, a protecting buffer of bentonite clay and finally the crystalline rock of 400–700 m depth, see Figure 1-1.

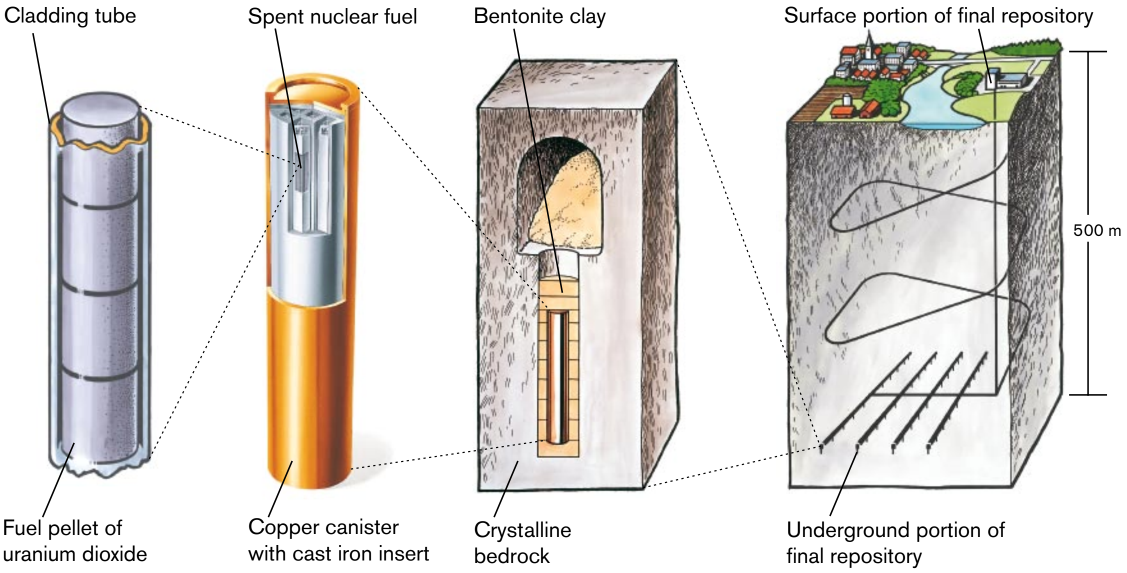

Figure 1-1. *The KBS-3 method for deposit of the spent nuclear fuel.*

1.2 Background of reliability studies

The “Non Destructive Testing (NDT) Reliability Project” is a subpart of the total risk assessment for the final repository. It covers the integrity of the sealing welds of the copper canisters due to discontinuities possibly occurring during the sealing process. It analyses the non-destructive testing (NDT) techniques applied at the SKB Canister Laboratory (CL) in Oskarshamn concerning the question: “Which is the size of the discontinuity which will be detected for sure or which is the size of the discontinuity which might be overseen?” and delivers this magnitudes together with the underlying parameters (of the welding process, of the NDT set up, of selection of discontinuity features and of levels of confidence) to the further risk evaluation. On the other hand it investigates the basic reliability of the NDT methods to make sure they are sensitive enough to accompany the development of the welding procedure as analysis method for any possible occurring discontinuities. So the first task for the risk assessment is oriented to the higher end of possible discontinuity sizes and the second part of basic reliability is oriented to mid part and lower end of possible discontinuity sizes.

For the reliability analysis the basic guidelines of the American Military Standard MIL 1823 were applied with further development and adaptation to the more complex testing task compared to the “one dimensional task” to detect cracks with eddy current in gas turbine engines. To be able to understand and optimize the state of the art performance of the NDT methods BAM is performing – especially for the X-ray equipment – detailed parameter measurements according to the present European standards. Because of the complexity and the uniqueness of the testing task and equipment both the parameter analysis of the experiments and the reliability investigations are assisted by modelling calculations.

The welding experiments and NDT-experiments are carried out at the CL. SKB has built the CL to demonstrate and develop the encapsulation technique in full scale. The critical part of the encapsulation of spent fuel is the sealing of the canister, which is done by welding the copper lid to the cylindrical part of the canister. Two welding techniques have been developed in parallel, Electron Beam Welding (EBW) and Friction Stir Welding (FSW).

To learn about possible discontinuities the NDT indications have been compared with results from other inspection methods. To indicate and characterize the true discontinuities in the weld specialized 3D computerized tomographic (CT) methods of BAM were applied. The analysis were done on almost full-scale objects by high energy computerized tomography (HECT) and on a smaller level towards micro-structure analysis using a CT unit with small spot size (micro-CT) with highest possible X-ray energy (unique in Europe). The CT techniques provides close to true indications of macroscopic volumetric discontinuities complementary to destructive cross sectioning. An important advantage is the provided structural information about the discontinuity plus the confirmation of all smallest possible discontinuity configurations in a volume instead of tedious micro metallographic methods. The complete CAD reconstruction of the CT results provided the advantage to look for all discontinuity features while the parts were still existent.

The CT reference methods where completed by some reference ultrasonic (UT) scans at BAM for the non volumetric discontinuities of electron beam welds (EBW). Due to the very special discontinuity configuration with compressed discontinuities – actually at the limit of NDT capabilities – in FSW the reference for the already highly specialized SKB phased array technique could only be careful destructive sectioning. This procedure was not carried out to full extent for EBW because in early 2005 the focus was put on FSW.

1.3 Structure of the report

The report is organized as follows: The chapter “Strategy” describes the underlying “Probability of Detection Philosophy” for the reliability assessment and its connection to the risk assessment. In Chapter 3 the subject of investigation – the copper canister –is described including the EBW and FSW processes as well as the occurring discontinuities where this project phase is focused on. Chapter 4 describes the NDT techniques applied at SKB. In Chapter 5, the reference methods i.e. the destructive testing at SKB and the above mentioned specialized high energy macro- and micro 3D CT methods are outlined. Chapter 6 provides the basic principles of the BAM-X-ray and ultrasonic modelling tools. In Chapter 7 a summary is given about the BAM experiments for the assessment of the SKB system for digital radiography and the concluding evaluation against CEN standards. Chapter 8 deals with the main part of the reliability assessment by POD where the modelled POD’s provides additional input for the understanding for the POD-curves calculated from experimental data. The assessment of the capability of detection is accompanied by the assessment of the sizing capability. Finally, the chapter “Results” provides a summary about the detectable discontinuity sizes, uncertainty in sizing and the completion of NDT examination by reference radiography.

2 Strategy

2.1 Subject

A subpart of the final risk assessment of the deep repository construction is to determine the risk of premature canister leak caused by discontinuities in the sealing weld. The discontinuities occurring during the production welding process create a diminishing of the wall thickness, which could affect the long-term integrity of the canister. The consequence for the applied NDT methods is to detect all discontinuities, which would reduce the wall thickness with a validated high reliability. This study has been based on a conservative assumption that the minimum copper wall thickness has to be 15 mm to guarantee the long-term integrity of the canister. Ongoing studies indicate however that the corrosion integrity requirement could be considerably lower.

The POD's considered in this report reveal the basic, or intrinsic capability of the NDT methods and do not yet take into account the final industrial application factors and the human factor as shown in the "Reliability Formula" in Figure 2-4 which will be applied to the canister welds on a later stage of the project. This one reason we held on the very conservative integrity requirement throughout the project.

2.1.1 Inspection techniques

The NDT systems to be analyzed were the X-ray system and the ultrasonic system at CL. The result of using the two inspection systems in combination was also analyzed.

The inspection tasks to study are inspection of sealing welds produced using EBW and FSW.

The X-ray inspection system at CL consists of a 9 MeV Varian accelerator with a 16 bits AD and viewing system provided by Bio-Imagine Research, Lincolnshire, USA. The ultrasonic system is a phased array 10 bit system. The inspection of the welds is carried out using an 80 element array working at a centre frequency of 2.7 MHz for EBW and 5 MHz for FSW. The NDT inspection systems at CL are described in detail in Chapter 4.

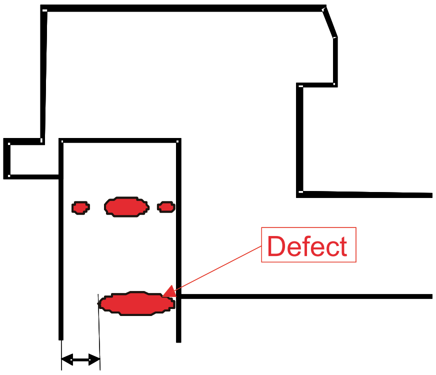

Remaining wall-thickness must be at least 15 mm

Figure 2-1. *The weld with possible discontinuity configurations.*

From the physical point of view the two methods are complements to each other. In radiography the signal for discontinuity detection is essentially the X-ray intensity difference in direction of the radiated direction of the discontinuity. The ultrasonic echo intensity is mainly proportional to the area perpendicular to the ultrasonic beam. Due to these facts the radiographic method is better suited for volumetric discontinuities and the ultrasonic method for area like discontinuities. However the modern phased array techniques applied in the project are capable to, in some extent, overcome these limitations by the additional degree of freedom in beam angle steering by electronic means.

2.1.2 Strategy for the determination of NDT reliability

The NDT Reliability is the degree to which the NDT system is capable to reach the intended aim in discontinuity detection and characterization and considering false calls (Second European-American Workshop on NDT Reliability 1999). The intended aim of the reliability study of the NDT of lid welds of copper canisters is:

- To be able to, in quantitative terms, express the risk for failing to detect canisters containing discontinuities in the sealing weld that exceeds the acceptance criteria.
- Being able to define the measurement accuracy of the inspection in terms of discontinuity size and location.

The work is aimed to result in a general methodology that can be applied for other inspection tasks for the canister.

2.1.3 Strategies in measuring reliability of NDT

Three different ways to investigate the reliability of NDT signals will be described which are to a more or less greater extent applied during the project. The first way of investigation, the performance demonstration, is preferred e.g. in the US American nuclear power industry qualitatively and quantitatively in the aerospace industry. This is an integral consideration of the non-destructive test as a system where the whole NDT system is packed in a black box and only the input in terms of the real existing flaws in the component is considered. This is compared to the output in terms of the indications of the human inspector or of the automated system.

The second – the European tradition – relies on a standardized description of physical/technical parameters of the NDT system, which are preconditions for successful system performance. As example for such a standardized set of performance parameters the X-ray system of SKB is characterized completely against the existing European standards. The third approach – the modular conception – is a marriage of both: The signal chain is cut into main modules. Each module is assessed in a most appropriate individual way e.g. via modelling calculations. The single results are joint together according to the reliability theory of systems or in simpler cases by technical justification or physical reasoning.

The NDT system consists of the procedures, equipment and personnel that are used in performing NDT inspection. According to this definition we consider in the situation in Figure 2-2, where we have on the left hand side the “truth” of the component, which is in our case a weld with discontinuities and on the right hand side the corresponding inspection protocol with discontinuity indications. This means that we have a 100% reliability when we would have a 1:1 correspondence between both sides. Since this is in almost all practical examples not the case we have to set up tools to measure and maintain reliability.

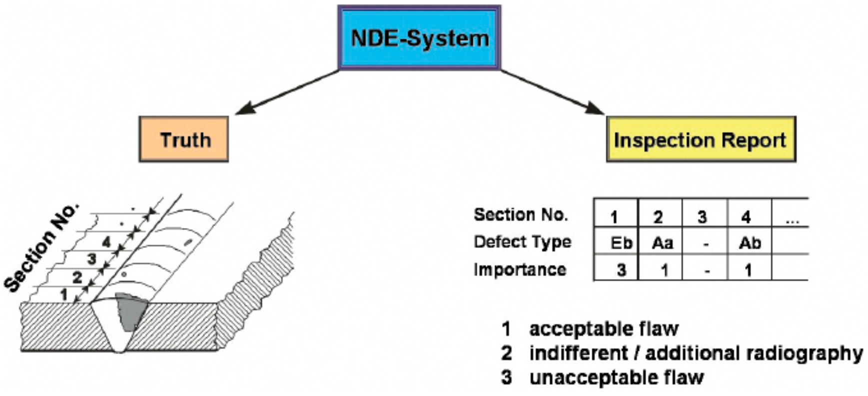

Section No.	1	2	3	4	...
Defect Type	Eb	Aa	-	Ab	
Importance	3	1	-	1	

1 acceptable flaw
2 indifferent / additional radiography
3 unacceptable flaw

Figure 2-2. *Aim of NDE – Describe the real status.*

In Figure 2-3 we take a closer look to an NDT signal transfer chain: The signal starts in terms of an energy beam or wave from a source and interacts with matter in terms of *a* component and its possible discontinuities creating an output signal which is driven by the physics of the method. This output signal is now further influenced by the physical and technical properties of the more or less complex receiver and converter in our case the imaging item for X-rays and the digitization and processing unit.

Now we consider how to measure and ensure the reliability. We start with the European approach: This approach is by far the most widely used, and is in use in most, or perhaps all, industries. One or more reference objects (such as EN 462 image quality indicators for radiography, or ASTM E 127 reference blocks for ultrasonic inspection) are used, in combination with written procedures controlling details of the inspection method, to reach and demonstrate consistency. The intent is to achieve essentially the same inspection conditions, independent of where, when, or by whom an inspection is conducted.

This type of European approach is often used to provide process control information of a qualitative nature: loss of control at some earlier manufacturing stage is indicated by the unexpected occurrence of numerous or large indications, for example. Capability for detection of “real” (naturally-occurring) discontinuities is not given for all applications, but is sometimes inferred from the size of the simulated discontinuities in the reference objects, or from the size of discontinuities that have been detected in past inspections using the same conditions. This inferential process can often lead to false conclusions about the detectability of real discontinuities.

The first step of a performance demonstration is also to define the essential technical parameters of the system. The receiver operating characteristic (ROC) and POD methods are appropriate tools to provide a clear measure of integral performance of the system. It has though to be paid by high effort in test series with realistic test samples and should be completed by a series of affordable “computer experiments” using theoretical modelling techniques. With POD the user can learn about the detection capability whereas the ROC gives more information about the system’s capability to distinguish between signal and noise. The modular approaches open the door to a promising technique – more efficient and with the capability also to optimize the system.

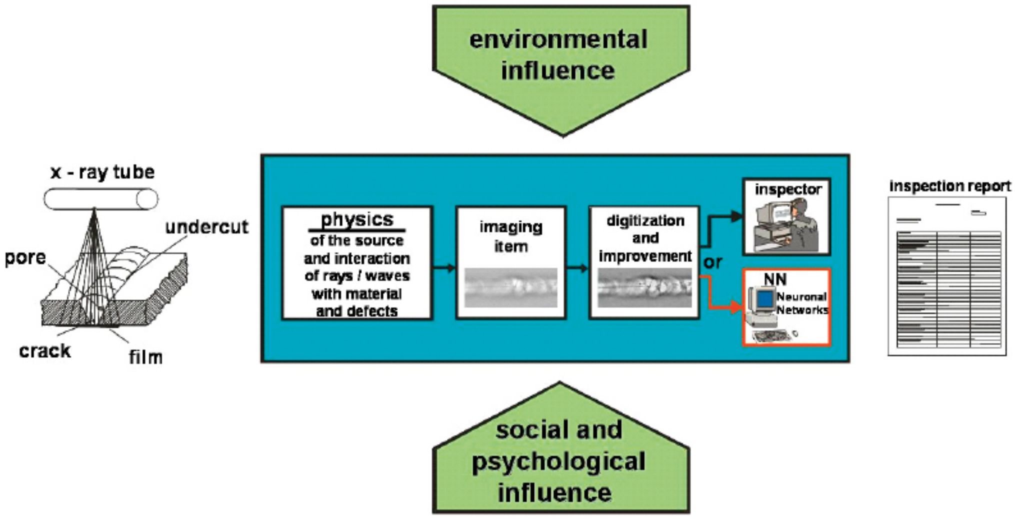

Figure 2-3. *The signal transfer chain of a radiographic system.*

2.1.4 Selection of reliability data evaluation methods to be applied

Since the main goal is a high precision assessment of the flaw size that might be overseen by NDT the quantitative POD (Probability of Detection) method according to MIL-STD 1823 /1/ was selected for this assessment. The (1-POD) curve will provide the probability of missing a discontinuity as function of discontinuity size which can be used as input for probabilistic risk assessment of failing with the assumption of a certain flaw growth behaviour under a certain load.

The conventional procedure provides a mean POD curve as function of discontinuity size with a corresponding 95% confidence limit curve due to the scatter in the experimental values. The discontinuity size "*a*" which is counted as practically sure detectable is when the 95% confidence limit curve reaches the 90% POD level. For all applied methods it has to be shown that this size a or better its projection/component in radial dimension is smaller than the allowed discontinuity size (35 mm). The POD level gives a quality feature about the NDT method showing which discontinuity sizes are detected for sure.

2.1.5 Signal POD, hit miss, ROC and plan of experiments

Both SKB-NDT-Methods are 100% digitized and fully mechanized methods so that a full signal analysis is possible according to the "$\hat{a}$ versus a" method. The method analyzes the full potential power of the NDT method to detect a signal $\hat{a}$ from a noisy background caused originally by a physical discontinuity dimension of size "a" in the object under test. The shape of the final POD curve depends on the selection of the threshold from which on a signal is counted as a real signal from a discontinuity in contrast to a noise signal. The method is described in more detail in Chapter 8.

Considering the reliability formula in Figure 2-4 this context the current investigation covers mainly the assessment of the intrinsic capability and controlled application factors. The investigation of influences from industrial application factors and from human factors has to be planned for further project stages. When human beings carry out the signal detection a so called "hit miss" POD has to be determined where the Human Factor is also assessed via a statistically reliable experiment using a number of different human interpreters. These results will then further be analyzed via the ROC method as described above to allow to select the optimum operation point also with respect to the economy of false calls.

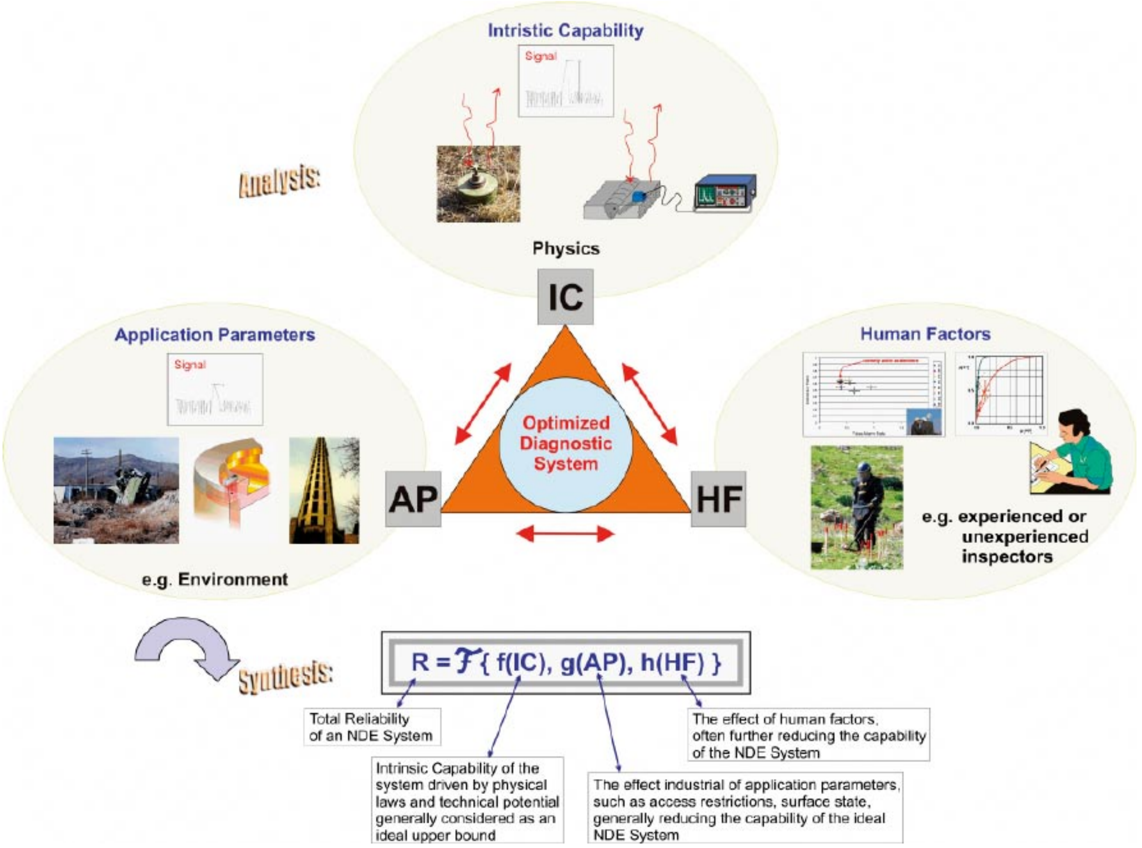

Figure 2-4. *Identifying the main influencing factors by the reliability formula.*

As mentioned before the current report is focused on the intrinsic capability of the ultrasonic technique and the radiographic technique to detect all possible and relevant discontinuities in EBW- and FSW-welds. More extensive work in characterization of discontinuities has been done for FSW as the method which was selected as the main welding technique in April 2005. The FSW welding technique and the formation of discontinuities is a "new land" for NDT techniques as well as their reliability assessment. So while demonstrating the techniques are basically capable of meeting the safety requirements they are still under further development including the multidimensional/multi-parameter POD approach.

For the safety relevant reliability assessment of the intrinsic capability and part of application factors of NDT-reliability the signal-POD (or $\hat{a}$ versus a) method according to MIL 1823 is already well suited to determine the remaining probability of the applied NDT method to oversee a discontinuity of a certain size. The originally 1-dimensional conception can be used in defining "effective" 1D parameters. A comprehensive treatment of the problem, especially in separating all the physically actually influencing factors from the factor of interest, the radial dimension of the discontinuities, the full 2D approach needs to be applied in further project stages. To cover possible gaps in the empirical evaluation schemes high qualified modelling techniques are applied to complete the physical reasoning of the results and to provide a broader parameter range then possible from the real experiments.

The common approach is to determine the real discontinuity sizes via destructive tests. In the original approaches in the gas turbine industry the discontinuities were even surface cracks to be easily measurable via optical surface methods. In our approach a high value was assigned to the possibility to have still access to the complete discontinuities in the welds even in sections. When they are once destroyed no more reconstruction of the full

3D situation is possible since during destructive tests parts of information get lost. For this reason a full 3D high energy CT /2/ is used as reference methods to characterize all volumetric discontinuities down to 1 mm diameter. The final validation was done for all discontinuities of FSW via destructive tests and metallographic inspection.

3 The copper canister

In the final repository the copper canister shall isolate the nuclear fuel from the outer surroundings. The reference design of the copper canister consists of an outer corrosion shield of copper and a cast iron insert that shall held the mechanical strength, see Figure 3-1. The copper shield consists of a composition of an extruded tube where a base as well as a lid is welded together. The complete canister that has a copper shield of 5 cm thickness is almost five metres long and has a diameter of about 1 m. The weight is about 25 tons loaded with fuel.

3.1 Welding processes

For sealing the canister in the encapsulation plant, SKB developed welding processes, i.e. weld the copper lid onto the tube. The processes that are developed at the Canister Laboratory are friction stir welding (FSW) and electron beam welding (EBW).

50 mm koppar

Beräknad vikt (kg):

Kopparkapsel	7 400
Insats	13 600
Bränsleelement (BWR)	3 600
Totalt	24 600

Figure 3-1. *The copper canister with a cast iron insert.*

3.1.1 Electron beam welding (EBW)

EBW is a high power beam welding process, which melts the parent material by using a focused beam of electrons. The electrons are produced by an electron gun to form a narrow, deep weld. The mechanism which allows an electron beam to penetrate deep sections of metal can be described as follows; the high power density of the beam impinging on the work surface and forms a molten pool which is rapidly heated above the boiling point of the metal. The pressure of escaping metal vapour maintained by the beam then allows the molten surface to tunnel through the material until the beam fully penetrates. The result is a metal vapour filled column termed a “keyhole” surrounded by molten metal. Welding is then achieved by relative motion between the joint and the beam so that the keyhole passes along the joint. This causes molten metal from the fused joint surfaces to flow around the weld cavity and re-solidify shortly after passing the beam.

The depth of penetration for any given material is primarily determined by the beam power and the weld speed. Penetration takes only about 1 second for 50 mm thick material, so that a steady state welding condition is rapidly established.

The main components of an electron beam welding plant are the gun, the gun column, the acceleration voltage and beam current systems, the weld chamber with vacuum pumps and turntable. TWI has developed the welding system at SKB (Figure 3-2) which has the gun leaded through the chamber wall in a fixed horizontal position with only the bottom of the gun column inside the chamber. The canister with the lid is lifted into the welding position through an opening at the bottom of the chamber with a combined lifting and rotating device called “Jacking frame”. The entire gun, gun column and weld chamber is held under vacuum during welding. Deflection coils situated at the bottom of the gun column allow the beam to be deflected for surface treatment of the weld bead.

3.1.2 Friction stir welding (FSW)

FSW was invented at The Welding Institute (TWI) in 1991 and is a solid-state thermo-mechanical joining process, which is a combination of extruding and forging. A cylindrical, shouldered tool with a profiled probe (pin) is rotated and slowly plunged into the material (Figure 3-3). For thick sections, a pilot hole has to be drilled to make the plunge sequence possible without probe fracture. Frictional heat is generated between the wear-resistant tool shoulder and the material, causing the material to soften without reaching the melting point, and allowing the tool to traverse the joint line.

One reason for the rapid success of FSW is the ease of process control due to the relatively few input parameters. The tool is rotated at a specified rotation rate and the tool is traversed along the joint line at a specified traverse rate. The tool is usually also tilted relative to the work piece so that the leading edge is above the surface. In order to create piece penetration the tool shoulder is controlled by applying a specified downward force or by specifying the position of the shoulder relative to the work piece. In addition to the input values, the tool temperature and the spindle motor torque are measured which provides an indication of the state of the process and the amount of frictional heat generated.

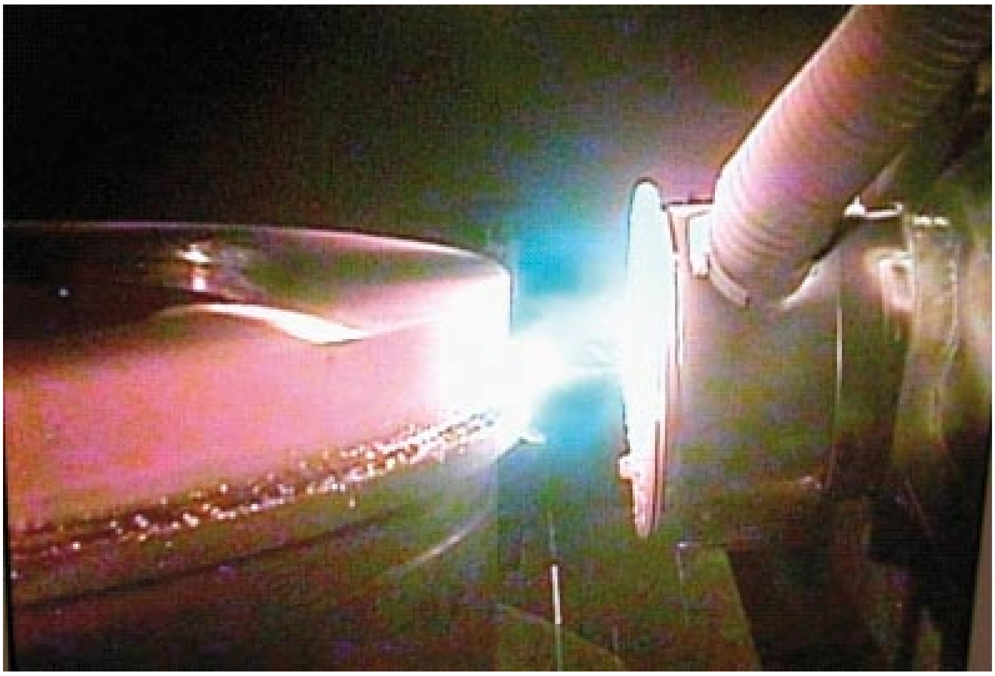

Figure 3-2. Electron beam welding at SKB.

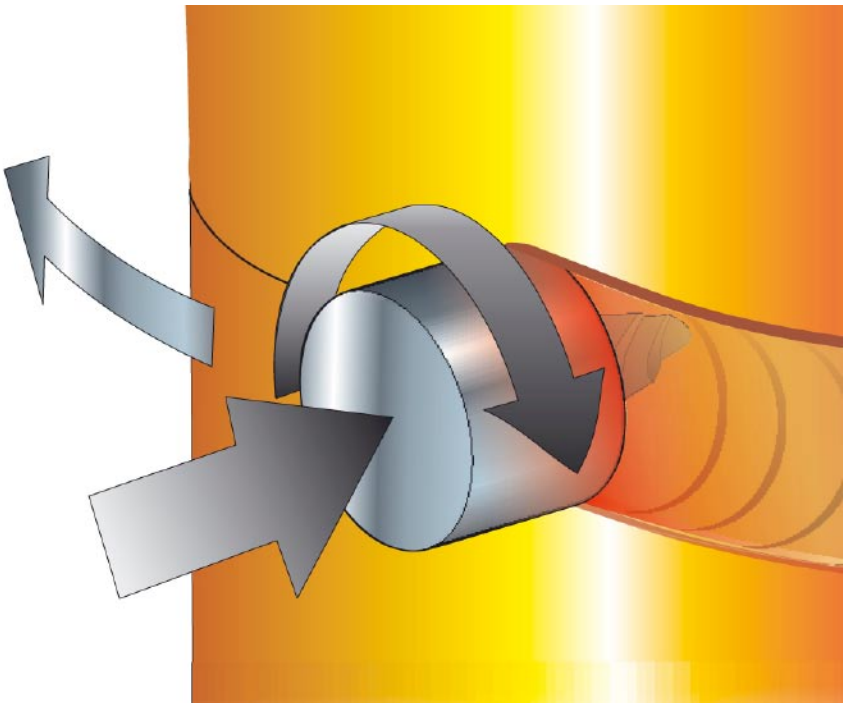

Figure 3-3. Friction stir welding process.

3.2 Geometry

To be able to optimize the welding processes different lid and joint design were used for the two techniques.

3.2.1 Electron beam welding (EBW)

The EBW process is a melting process. Therefore a fronting bar is implemented to prevent the weld melt to pour out. The fronting bar is machined after welding to get a smooth surface for the NDT. The geometry of the lid weld is shown in Figure 3-4.

3.2.2 Friction stir welding (FSW)

As the FSW process starts and stops above the joint line, the lid has extra material on the top. This material is machined after welding to get a smooth surface for the NDT. The geometry of the lid weld is shown in Figure 3-5.

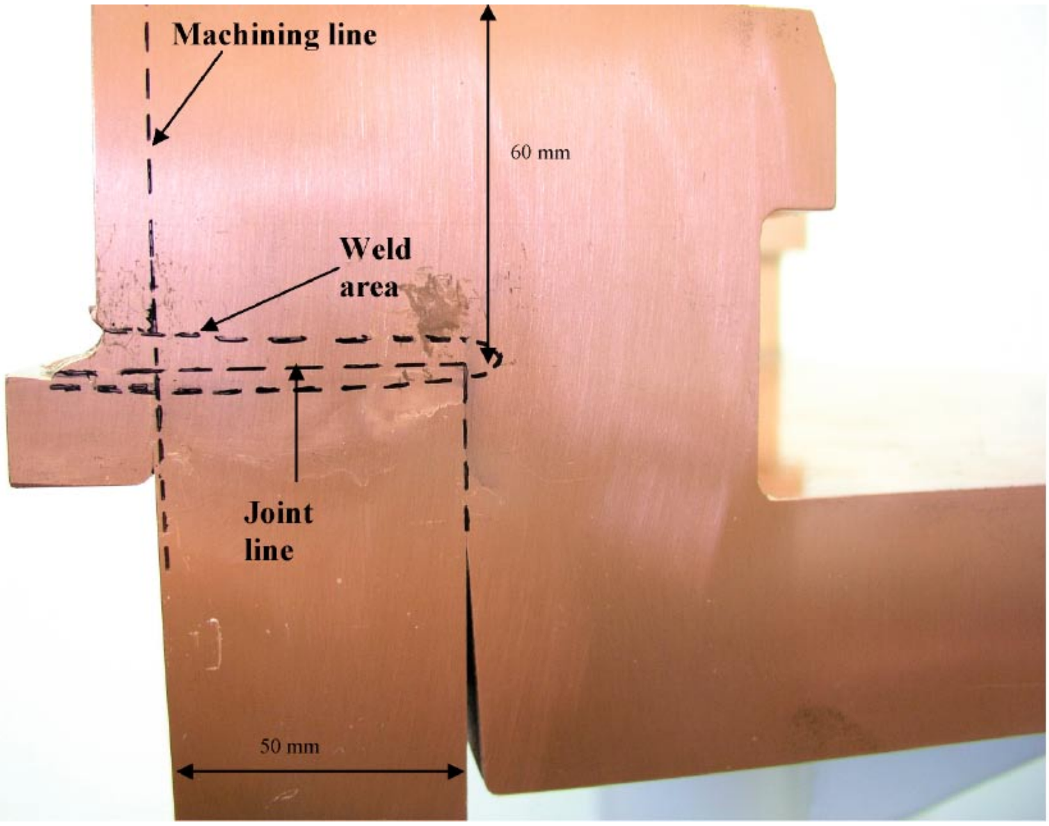

Figure 3-4. *Joint design, electron beam welding.*

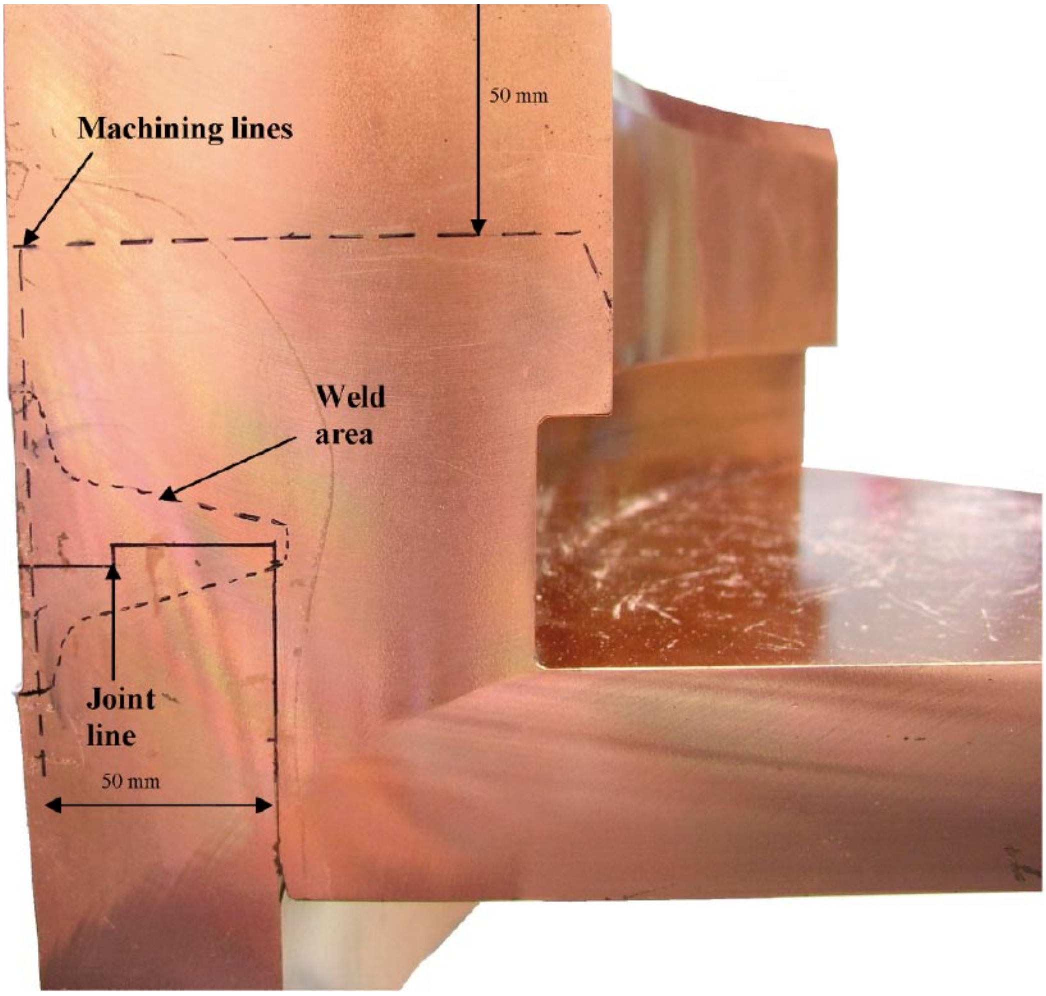

Figure 3-5. *Joint design, friction stir welding.*

3.3 Discontinuities found in the project

This part describes the critical discontinuities for the two welding processes for the canister.

3.3.1 Electron beam welding (EBW)

During the welding trials with EBW at the Canister Laboratory mainly two types of discontinuities have been found using relevant process parameter settings. These two types can be called wormholes and root porosity. The wormholes can be located anywhere in the upper part of the weld and are mainly volumetric (see Figure 3-6a) while the root porosity is located in the weld root and can either be volumetric or non-volumetric, see Figure 3-6b.

3.3.2 Friction stir welding (FSW)

During the welding trials with FSW at the Canister Laboratory two types of discontinuities have been found using relevant process parameter settings. These two types can be called wormholes and joint line hooking (JLH), see Figure 3-7. The wormholes are located in the outer part of the weld and are more or less volumetric (see Figure 3-8a) while the JLH is located in the weld root and are non-volumetric, see Figure 3-8b.

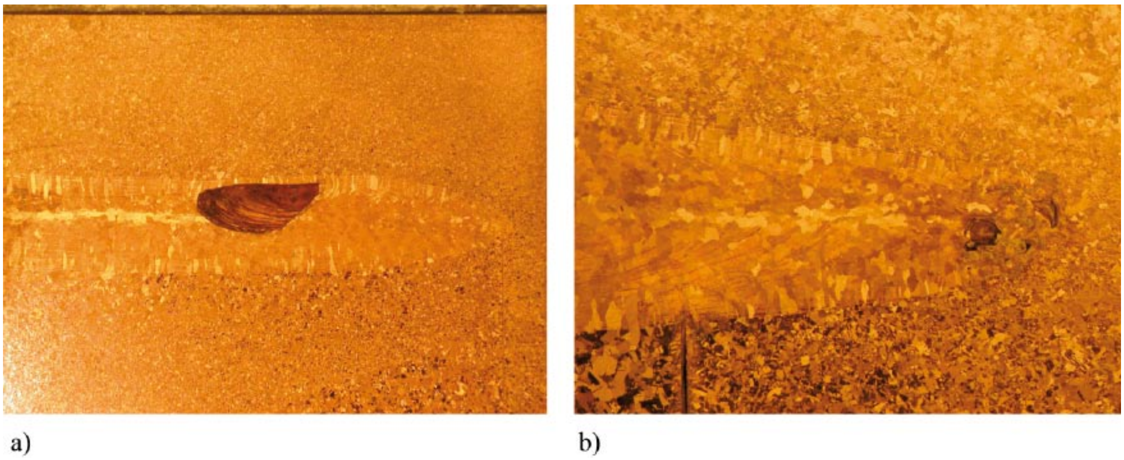

a) b)

Figure 3-6. Macro section of wormholes.

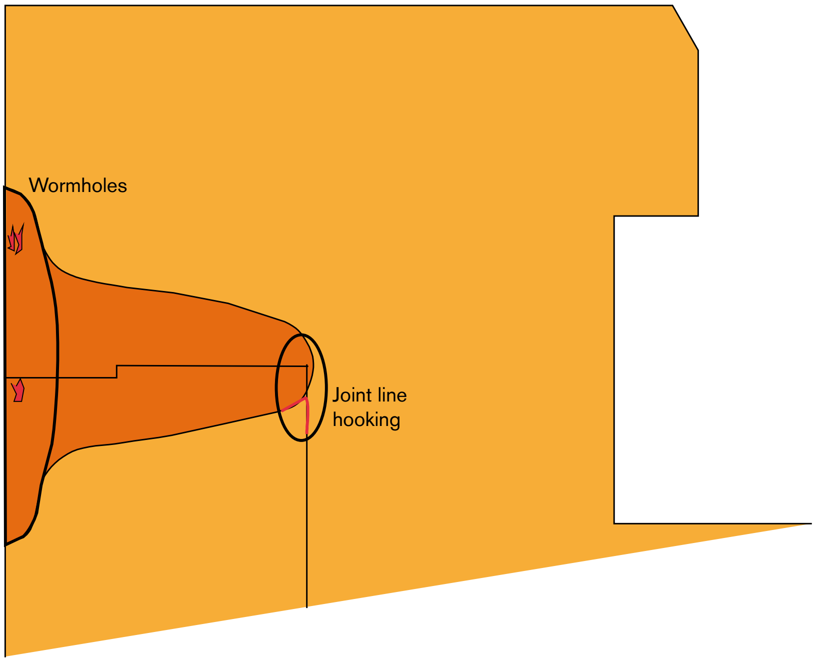

Figure 3-7. *Location of discontinuities in FSW.*

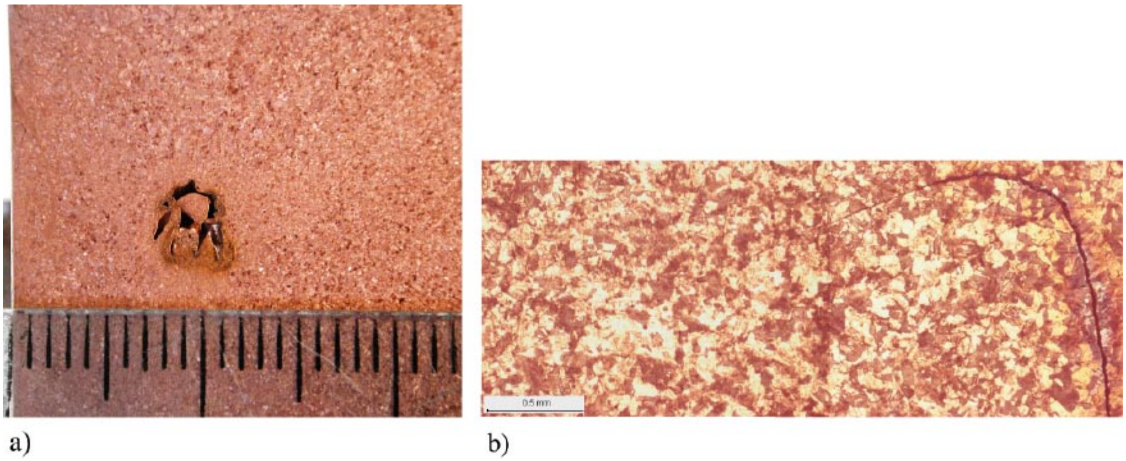

a) b)

Figure 3-8. *Macro section a) of wormholes and b) of joint line hooking.*

4 Evaluated inspection methods

In this reliability study NDT-methods for digital radiography and phased array ultrasound have been evaluated.

4.1 Digital radiography for EBW and FSW

The system for digital radiography is supplied by BIR (Bio-Imagine Research Inc.), see Figure 4-1. The main components are:

- 9 MV linear accelerator from Varian.
- Manipulator for positioning of accelerator and detector.
- Detector system consisting of a vertical line-camera.
- Computer system for setting up the inspection and evaluation of results.

The inspection procedure that has been used in this study is the same for both FSW as for EBW.

The main principle is that the canister rotates, while the accelerator generates X-rays through the weld with an angle of incident of 35°, see Figure 4-2. The line camera collects the transmitted X-rays and an X-ray image with 0.4 mm resolution is generated, see Figure 4-3.

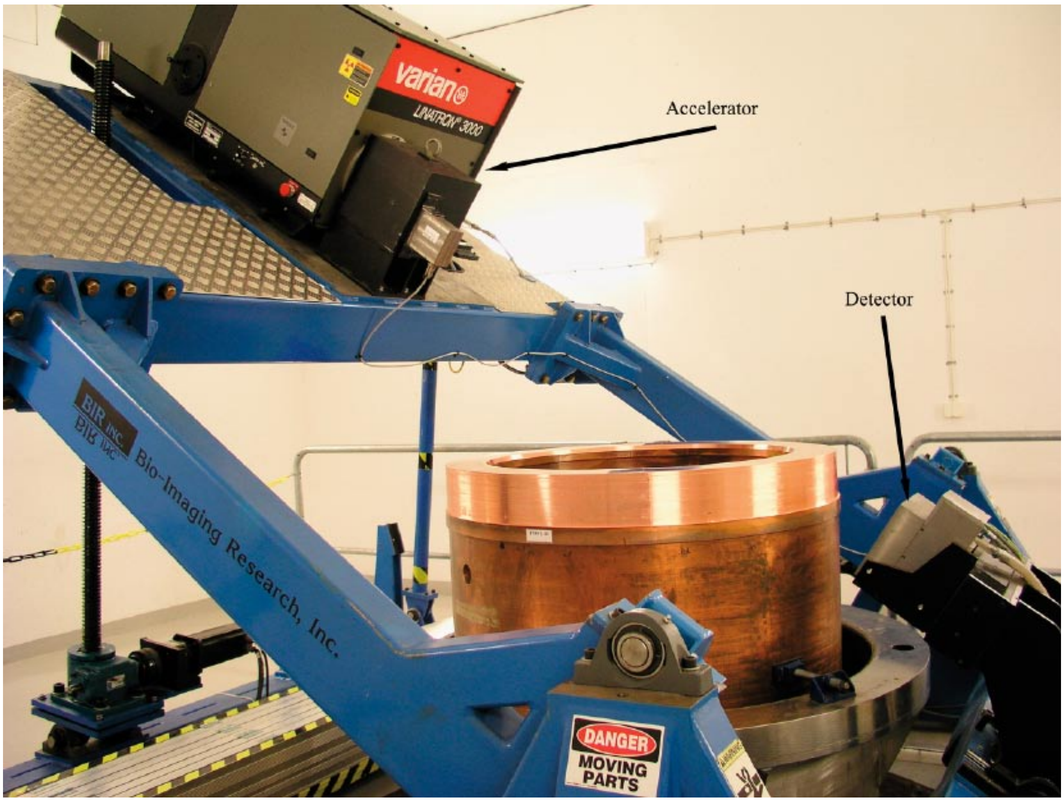

Figure 4-1. *X-ray system used for inspection of the seal weld at the Canister Laboratory.*

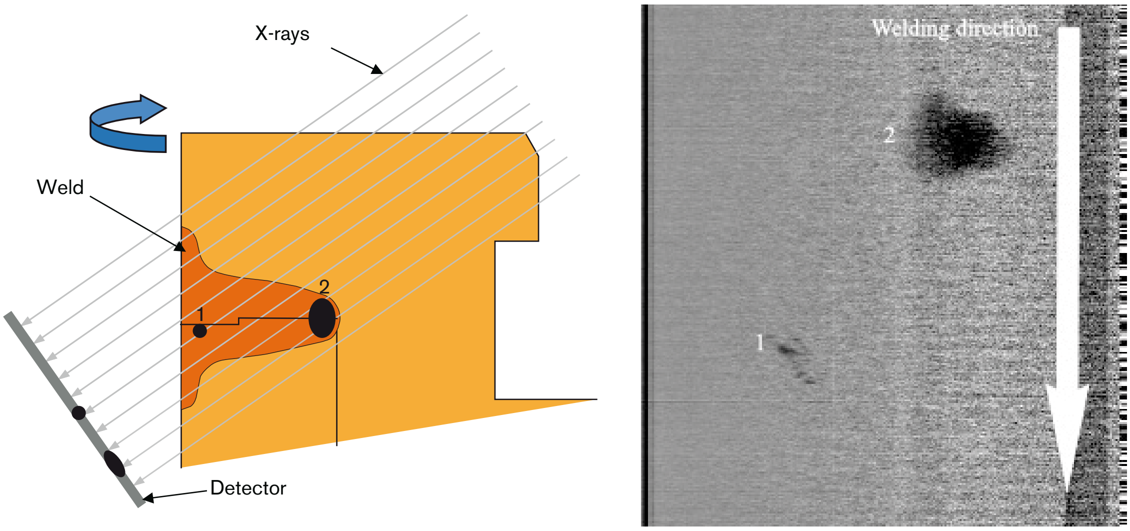

a) Sketch of radiographic inspection

b) X-ray image

Figure 4-2. *X-ray image of FSW.*

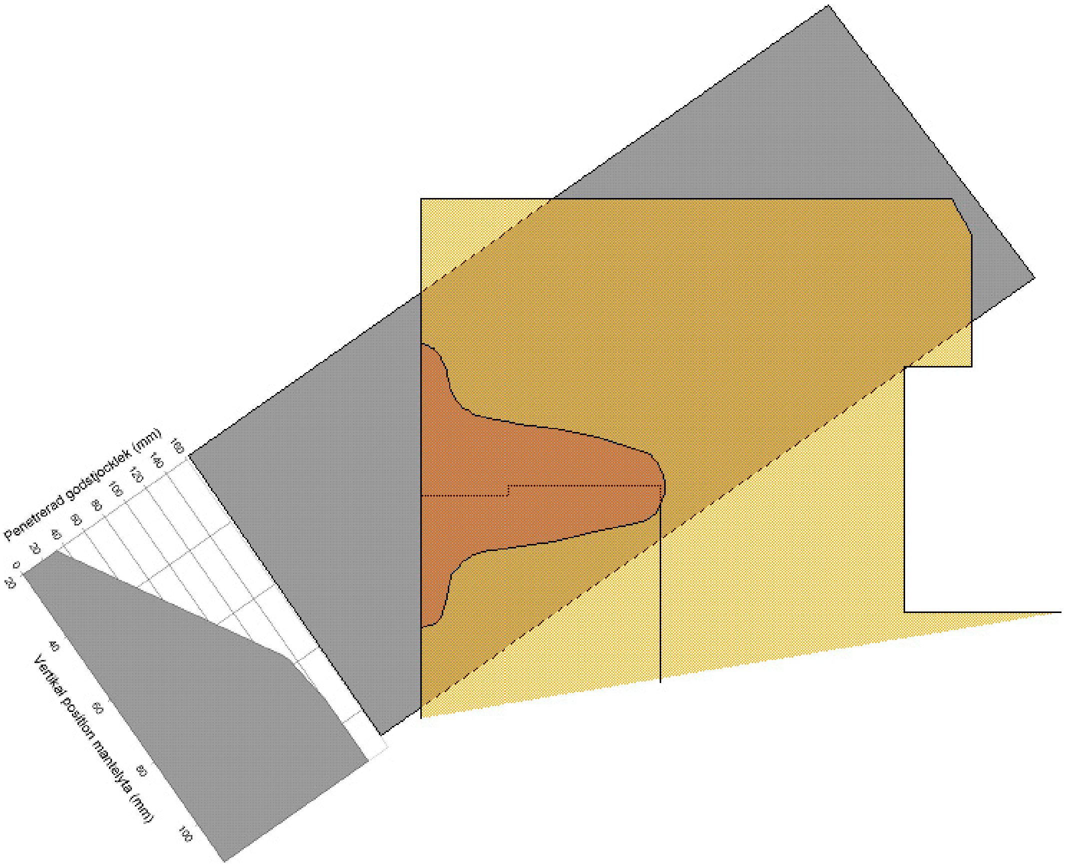

Figure 4-3. *Thickness variations in the X-ray inspection of the FSW.*

A collimator placed at the front of the accelerator focus the beam and the detector is placed into a housing of tungsten to reduce the scatter. The X-rays passes through the 70 mm housing in a 0.4 mm wide vertical slit.

As the penetrated thickness varies (see Figure 4-3) in the X-ray inspection of the weld, a thickness correction is made to calibrate the system. The correction is made by a mean value calibration from 500 samples around the weld circumference.

4.2 Phased array ultrasound

The system for phased array ultrasound is supplied by Technology Design Ltd., see Figure 4-4. The main components are:

- Phased array system TD Focus-scan MKI.
- Linear array transducers of 32–128 elements with centre frequencies of 2.7–10 MHz.
- Manipulator for positioning of array transducers.
- Software (TD-Scan) for setting up the inspection and evaluation of results.

4.2.1 Electron beam welding (EBW)

The main principle is that the canister rotates, while the array-transducer electronically sweeps the ultrasound in the radial direction of the canister. The transducer for inspection of FSW is a planar array with 80 elements and a centre frequency of 2.7 MHz. The inspection is made from the top of the canister lid (see Figure 4-5) with a thin water path which obtains acoustic contact.

The weld is inspected with a configuration that includes three sequences, one where the sound is steered towards the outer surface with angles in the region of –16° to 0° to cover the outer part of the weld. The second sequence use normal incident waves and electronic scanning along the whole array transducer. Finally, the third sequence steer's the beam towards the centre of the canister in angles of 0–16° to make sure that the whole weld depth is covered. Focus depth is set to 60 mm.

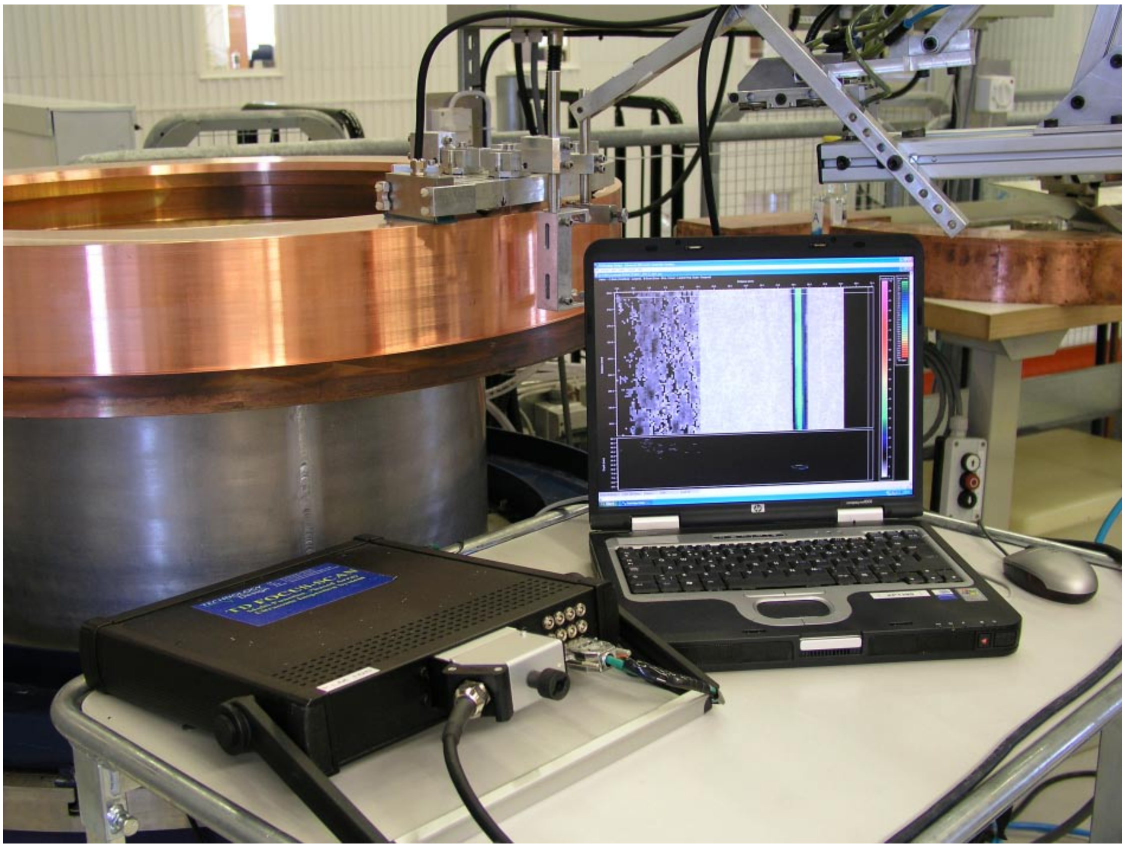

Figure 4-4. *Phased array system used for inspection of the seal weld at the Canister Laboratory.*

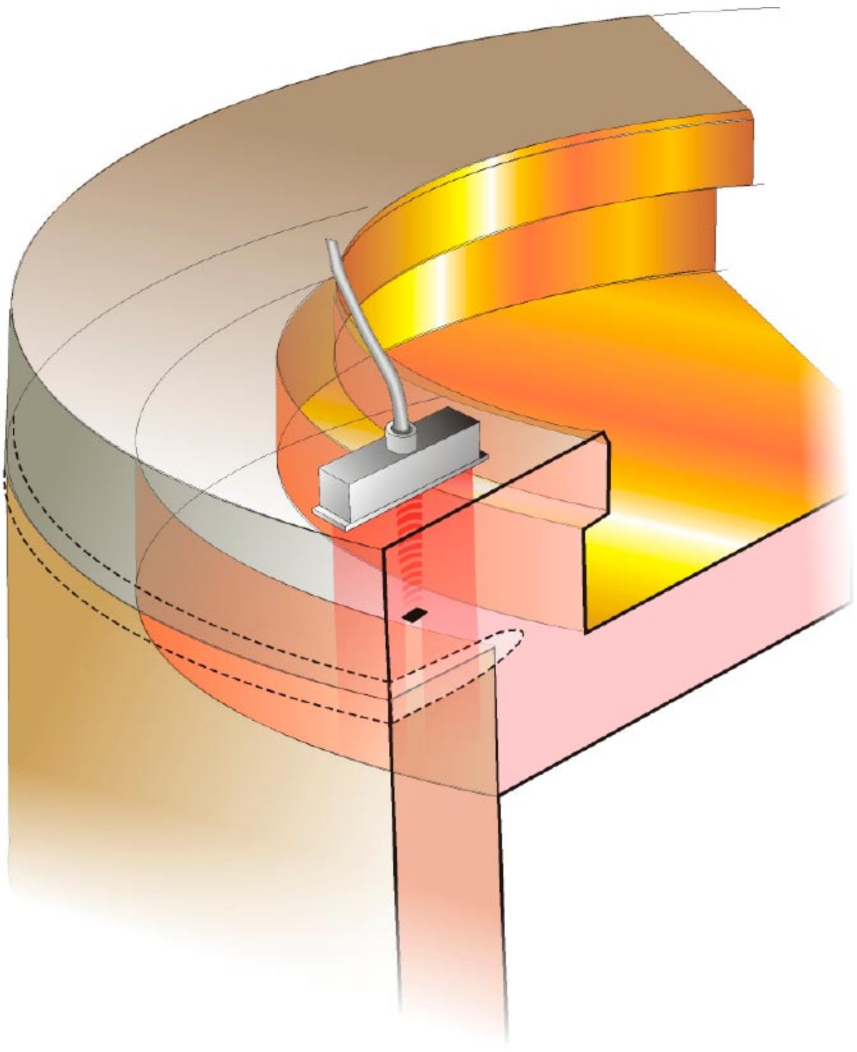

Figure 4-5. Sketch of phased array ultrasonic inspection of EBW.

The results are presented as a-, b- and c-scans (see Figure 4-6) and the evaluation of the indications have been made, using the 6 dB drop from the maximum signal /3/.

4.2.2 Friction stir welding (FSW)

The main principle of the inspection of FSW is the same as for EBW. The main difference is that the array has a centre frequency of 5 MHz for FSW. The inspection is also made from the top of the canister lid (see Figure 4-7) with a thin water path obtains acoustic contact. For the weld inspection two configurations have been used that both uses 32 elements in the focusing apertures.

1. The first configuration is including two sequences, one where the sound is steered towards the outer surface with angles in the region of 0–30° to cover the outer part of the weld. The second sequence use normal incident waves and electronic scanning along the whole array transducer. Focus depth is set to 50 and 60 mm with dynamic depth focusing on the receiver side.
2. The purpose of the second configuration is mainly to characterize the joint line hooking type of discontinuity. This inspection use 5 fixed angles, 0, ± 10 and ± 20°. The focus is set to 60 mm with dynamic depth focusing on the receiver side.

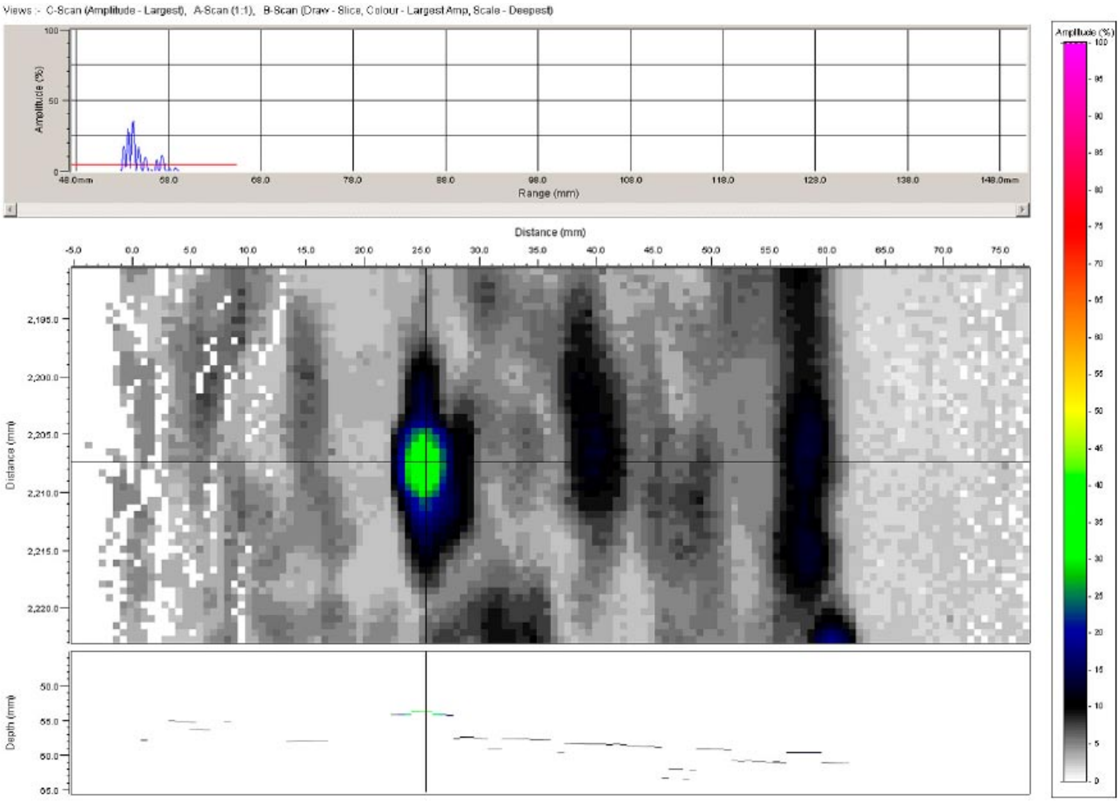

Figure 4-6. *Phased array ultrasonic inspection of EBW, a-scan at top, c-scan in the middle and b-scan at bottom.*

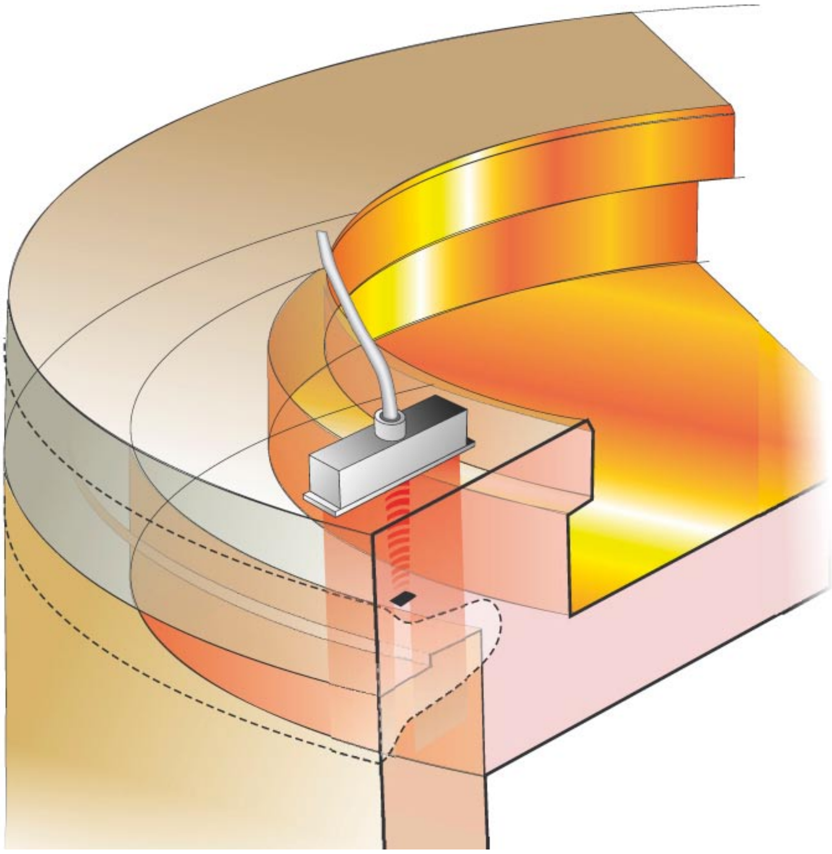

Figure 4-7. *Sketch of phased array ultrasonic inspection of FSW.*

The results are presented as a-, b- and c-scans (see Figure 4-8) and evaluation of the indications have been made, using the 6 dB drop from the maximum signal /3/.

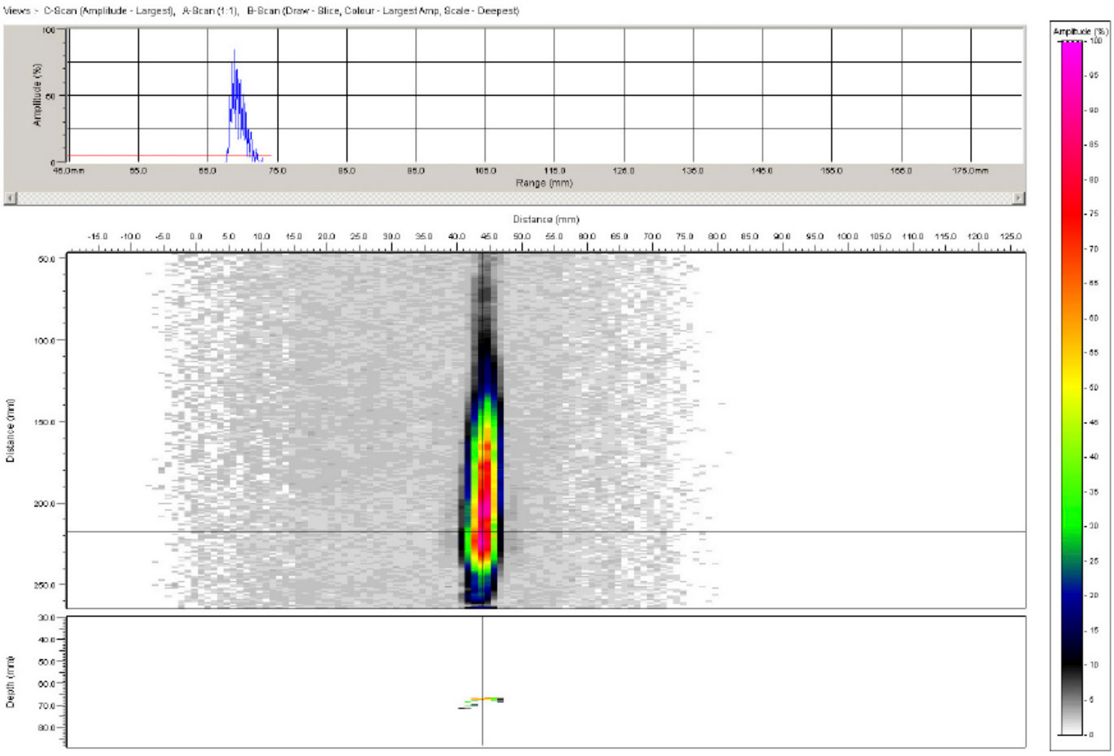

Figure 4-8. *Phased array ultrasonic inspection of FSW, a-scan at top, c-scan in the middle and b-scan at bottom.*

5 Reference methods

5.1 Destructive testing

To verify the real size of the indicated discontinuities have destructive tests been performed at SKB. As the characteristics of the different types of discontinuities varying, have different techniques for determine the sizes been used.

For the joint line hooking type have following methodology been used:

- From the weld surface have cores with 40 mm diameter been drilled at positions where NDT have indicated presence of discontinuities.
- The cores have been split into two halves, see Figure 5-1.
- One of the halves have then been polished and etched.
- Finally have the discontinuities been characterized with a microscope, see Figure 5-2.

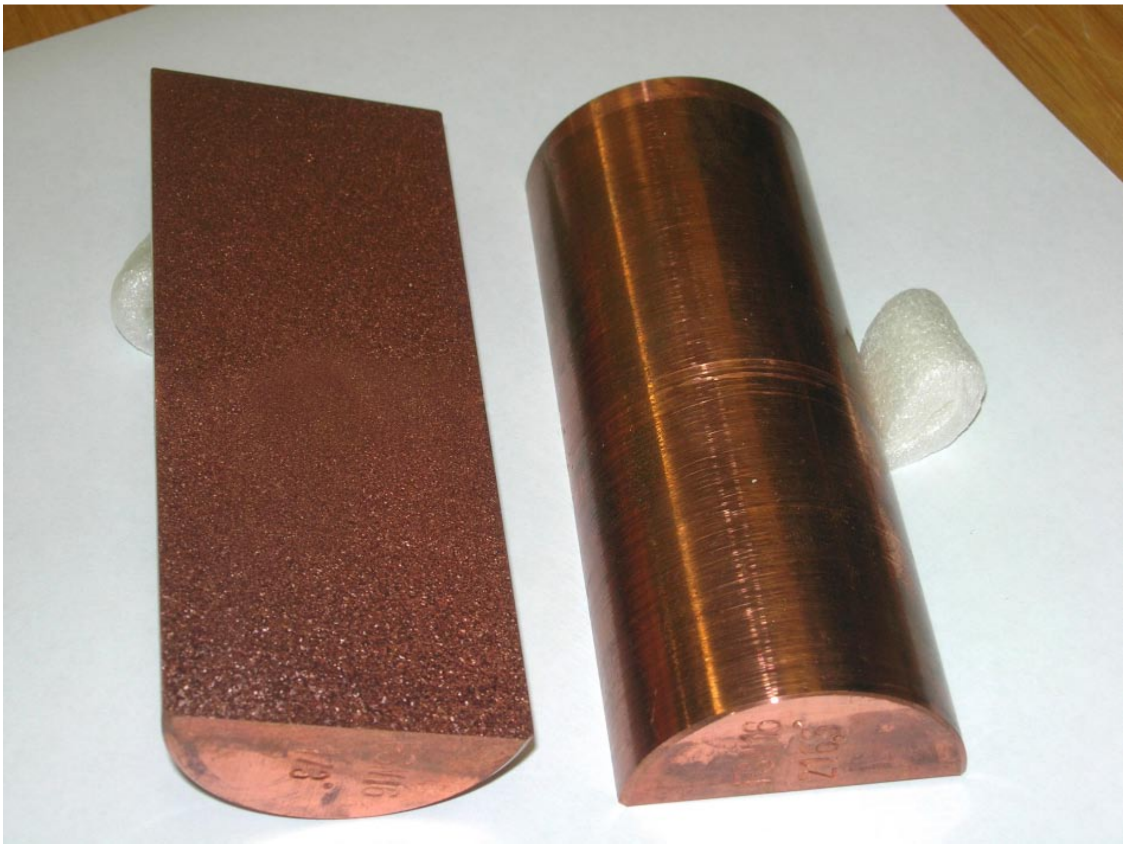

Figure 5-1. *Core for destructive evaluation of joint line hooking.*

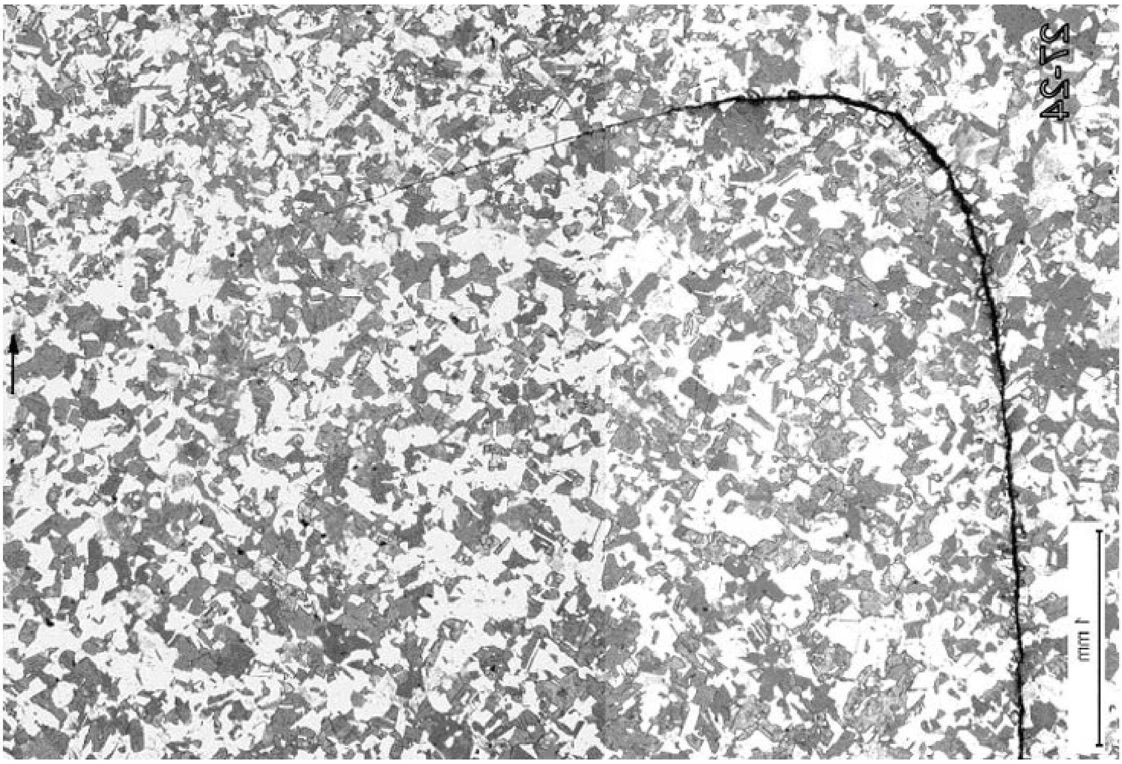

Figure 5-2. Macrograph of the joint line hooking in weld FSW27.

To determine the sizes of the wormholes have following methodology been used:

- From the weld segments (FSW5) have areas where discontinuities indicated by NDT been marked. In this areas have cubes of the size of 50 mm been machined, see Figure 5-3.
- The cubes have been X-rayed in three directions at the Canister Laboratory to locate the discontinuities.
- Four of these cubes have finally been machined step by step with increment of 0.1 mm and for each slice have the discontinuities been documented by digital camera.
- Finally the discontinuities on the digital photos (Figure 5-4) have been grouped into clusters and the sizes have been determined.

5.2 Computed tomography and discontinuity extraction

High energy computerized tomography was used as preliminary reference method to describe the presence, the size and also the full shape of volumetric discontinuities in terms of CAD images. In that way a ”true” defect description was available while the part was still available for further measurements. In case of FSW the reference measurements were completed by full destructive testing and CAD reconstruction of cross sections afterwards. It revealed a “HECT”-sizing error by about 0.4 which is described in the section “Critical discussion of experimental values of radiographic penetrated length using destructive results” included in Chapter 8. In that way all the so called preliminary results gave a very conservative $a_{90/95}$ assessment.

Figure 5-3. *Copper cubes for destructive evaluation of wormholes.*

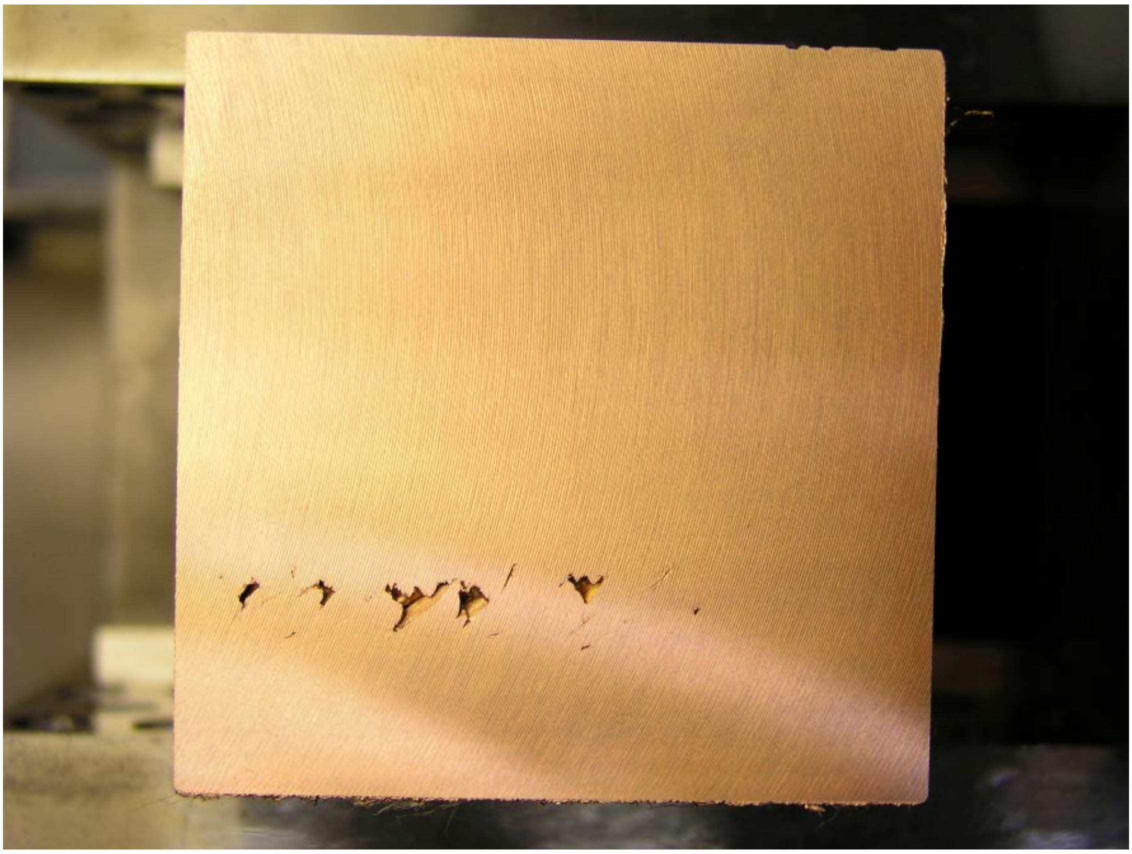

Figure 5-4. *Photograph at 6.2 mm depth of wormholes in weld FSW5.*

5.2.1 High energy computerized tomography (HECT)

The multi-purpose CT system developed at BAM /4/ works with different combinations of radiation sources and detector systems. For high attenuation materials like Copper an electron linear accelerator (LINAC) is used as X-ray source (Energy: 10.5 MeV; Dose 15 Gy/min) together with an amorphous Silicon flat panel detector with 256×256 pixel. The pixel size is $0.8 \times 0.8\ \text{mm}^2$. Figure 5-5 shows an overview of the multi-purpose CT system with the LINAC at right and the flat panel detector at left.

Figure 5-5. *Multi-purpose-Tomograph of BAM with the LINAC X-ray source at right and the flat panel detector at left.*

Figure 5-6 shows the flat panel detector en detail together with a Cu sample on the scanner table.

Due to the magnification, that means the ratio of distance source-detector to distance source-centre-of rotation of the scanner table, the pixel size in the object plane is 0.65×0.65 mm^2. That means that a cylindrical sample volume with a height of about 140 mm can be measured in one cycle. Therefore the Cu samples with a height up to about 30 cm are measured in three different heights and the overlapping volume image data sets are merged to a geometrical correct overall data set.

Each of the three partial volumes of the sample was measured with 720 projections over 360°, the integration time per projection was 0.8 sec. Due to the angular over-sampling the data could be reconstructed in an image matrix of 511×511×255 voxel with an voxel size of (0.325 mm)^3.

The result of the measurement is the material dependent linear attenuation coefficient μ, averaged over one voxel, the unit is cm^{-1}. For an image representation these values are normalised to 8 Bit:

- grey level 0 ↔ $\mu = 0.0$ cm^{-1}
- grey level 250 ↔ $\mu = 1.7$ cm^{-1}

assuming the attenuation value for air is $\mu = 0.0$ cm^{-1}, which is valid for the used high X-ray energies.

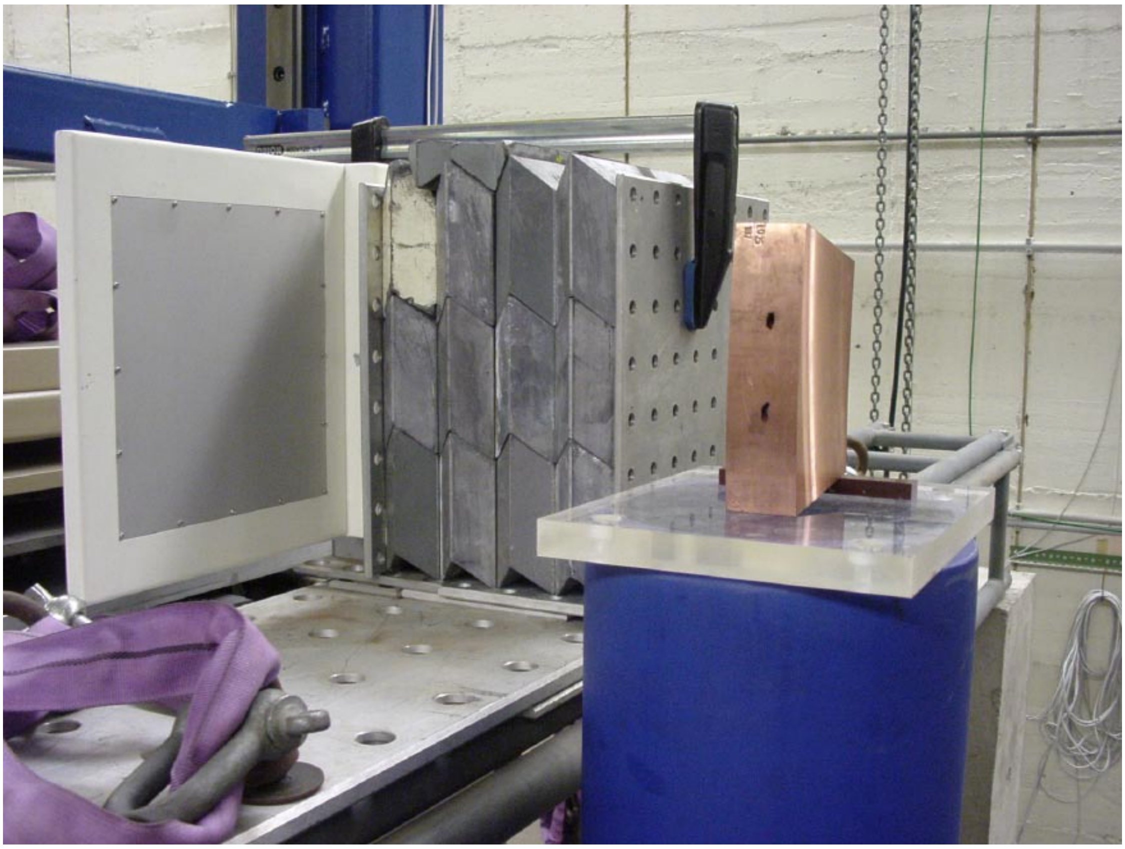

Figure 5-6. *Display detail of flat panel detector and Cu sample on the scanner table. The electronic part of the detector was shielded against X-ray radiation with 20 cm of lead.*

There are mainly two sources of artefacts:

- the energy spectrum of the X-ray source, resulting in beam hardening artefacts,
- inherent properties of flat panel detectors.

To eliminate beam-hardening artefacts the energy spectrum of the LINAC is filtered by 90 mm Fe. The fact that flat-panel detectors are not collimated leads to some artefacts, especially that edges are smoothed. Therefore a pre-processing step of the raw data was performed, a high-pass convolution filter.

The back-projection of the raw or pre-processed data is done by the well-known Feldkamp algorithm. Figure 5-7 shows a vertical slice from the image data set of the reconstructed raw data after pre-processing.

For the further processing the voxel based data format are converted to the ‘stl’-data format using a threshold operation. Due to the detector limitations smaller flaws are handled separately using Region-of-Interest operations. Simplified this means that for small flaws object depending thresholds are used. The different steps of image processing tools hereby are:

- Segmentation of the envelope of the sample, setting of a threshold and conversion to the stl-format.
- Segmentation of single flaws, setting of a threshold and conversion to stl-format.
- Merging of the different stl-data sets of the envelope and the isolated flaws.

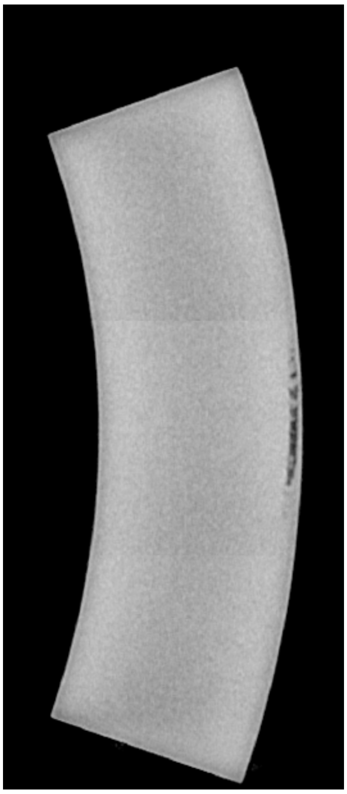

Figure 5-7. *Vertical slice from the 3D image data set after pre-processing of the raw data with an high-pass convolution filter.*

5.2.2 Discontinuity extraction

The discontinuity extraction procedure is presented in the flow chart of Figure 5-11. On the basis of a CT data set the radial lengths were determined for the voluminous discontinuities. The discontinuity extraction was carried out with the function "Discontinuity Analysis" implemented in the software package "VGStudio MAX" by Volume Graphics /5/.

The discontinuity extraction procedure contains two steps: (1) calibration and (2) discontinuity analysis. The calibration process is designed for 3D data sets including two different materials. One range of values represents the background (e.g. air, noise) and the other the scanned material under consideration. The calibration process adjusts the maximum discontinuity gray-value of the discontinuity analysis to distinguish between background and material.

A discontinuity is an area of voxels with (1) gray values lower than a predefined maximum gray value, (2) completely surrounded by material and (3) within a user defined range in size. Material means structures with gray values above the predefined maximum gray value.

The discontinuity analysis tool is designed to process 3D data sets for internal discontinuities. After the calibration process the tool detects discontinuities and provides analysis results with information on each discontinuity. The results of the discontinuity extraction procedure are presented in the Figure 5-8. The SX dimension of the bounding box of reported discontinuities (see Figure 5-8) was used as first assumption of the radial discontinuity length needed for POD calculation.

For further processing the extracted discontinuities are converted to 3D boundary representations in STL data format using a threshold operator. The BAM RT simulation tool XRay was used to extract the radial length from the STL data. The virtual representation of a lid weld segment with extracted discontinuity geometries is shown in Figure 5-9. Figure 5-10 shows the result of the radial projection within the XRay simulation tool as a gray value coded thickness map. The radial length of a discontinuity is measured as maximum gray value of its indication.

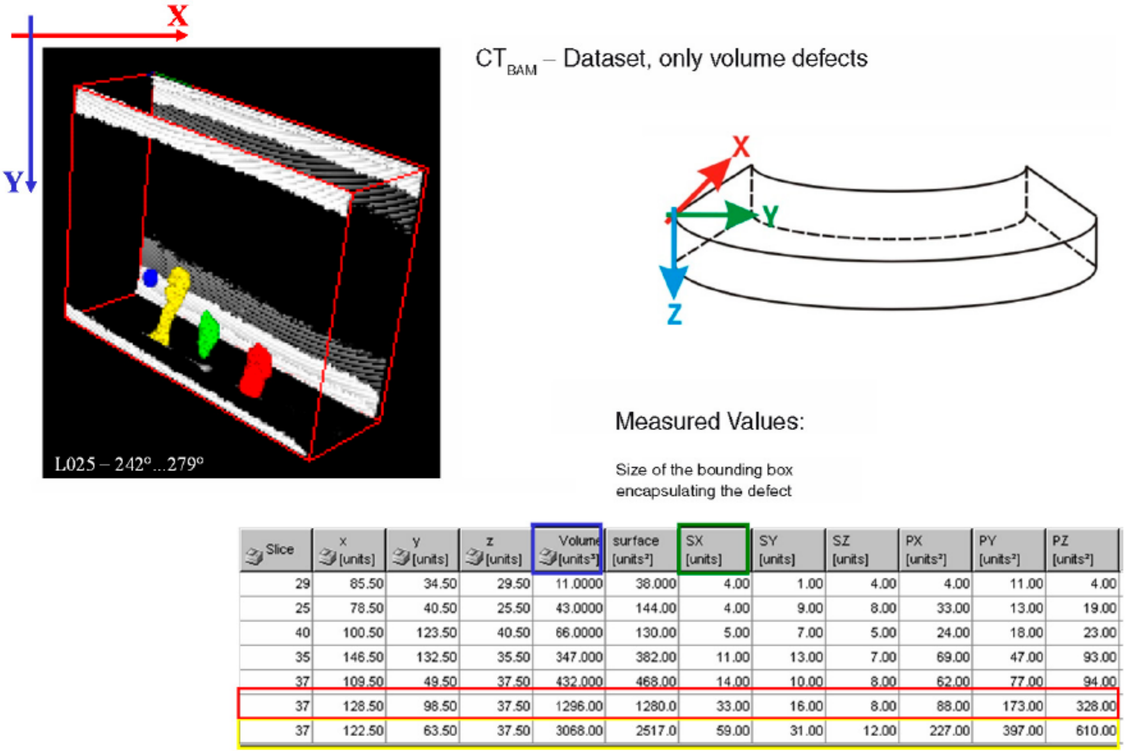

Measured Values:

Size of the bounding box encapsulating the defect

Slice	x [units]	y [units]	z [units]	Volume [units^3]	surface [units^2]	SX [units]	SY [units]	SZ [units]	PX [units^2]	PY [units^2]	PZ [units^2]
29	85.50	34.50	29.50	11.0000	38.000	4.00	1.00	4.00	4.00	11.00	4.00
25	78.50	40.50	25.50	43.0000	144.00	4.00	9.00	8.00	33.00	13.00	19.00
40	100.50	123.50	40.50	66.0000	130.00	5.00	7.00	5.00	24.00	18.00	23.00
35	146.50	132.50	35.50	347.000	382.00	11.00	13.00	7.00	69.00	47.00	93.00
37	109.50	49.50	37.50	432.000	468.00	14.00	10.00	8.00	62.00	77.00	94.00
37	128.50	98.50	37.50	1296.00	1280.0	33.00	16.00	8.00	88.00	173.00	328.00
37	122.50	63.50	37.50	3068.00	2517.0	59.00	31.00	12.00	227.00	397.00	610.00

Figure 5-8. *Determination of the radial size at CT (BAM)-data (Volume Studio MAX by Volume Graphics).*

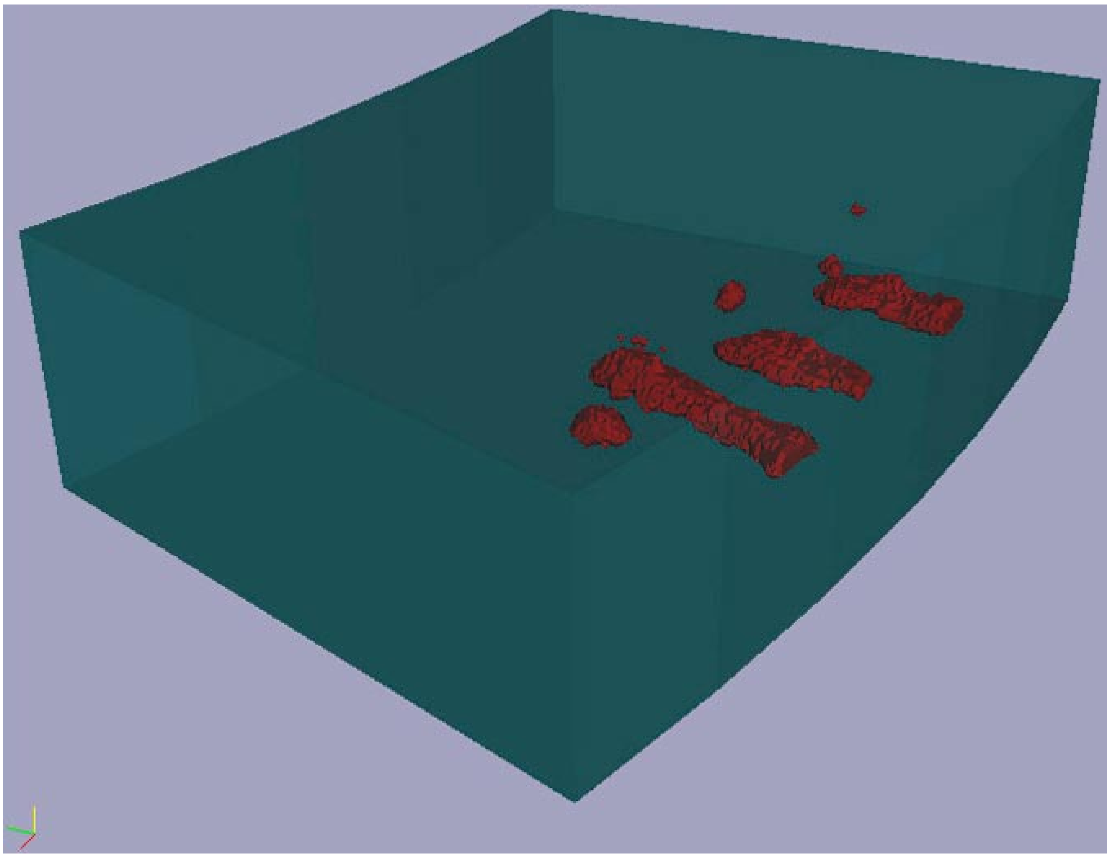

Figure 5-9. *Virtual representation of a lid weld segment with extracted flaw geometries.*

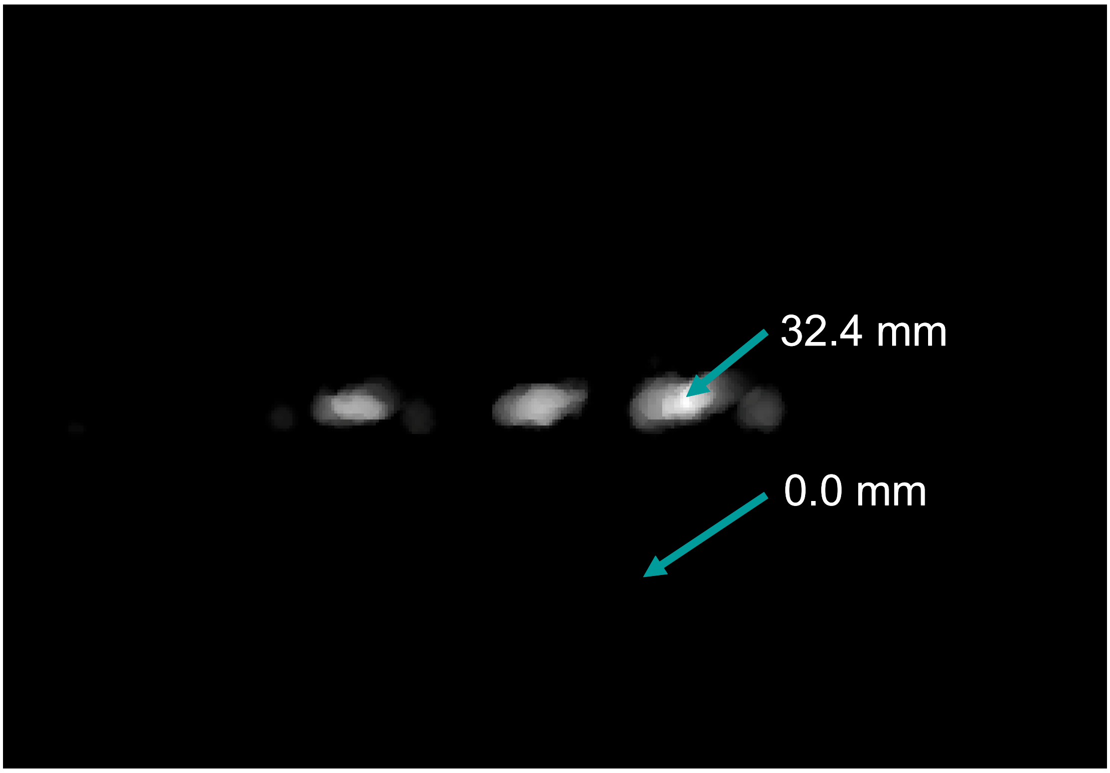

Figure 5-10. *Gray value coded thickness map (radial flaw dimension) of extracted flaw geometries generated by the XRay simulation tool while radial (in terms of the canister) projection. Range: 0.0 mm (black) to 32.4 mm (maximum radial flaw extent; white).*

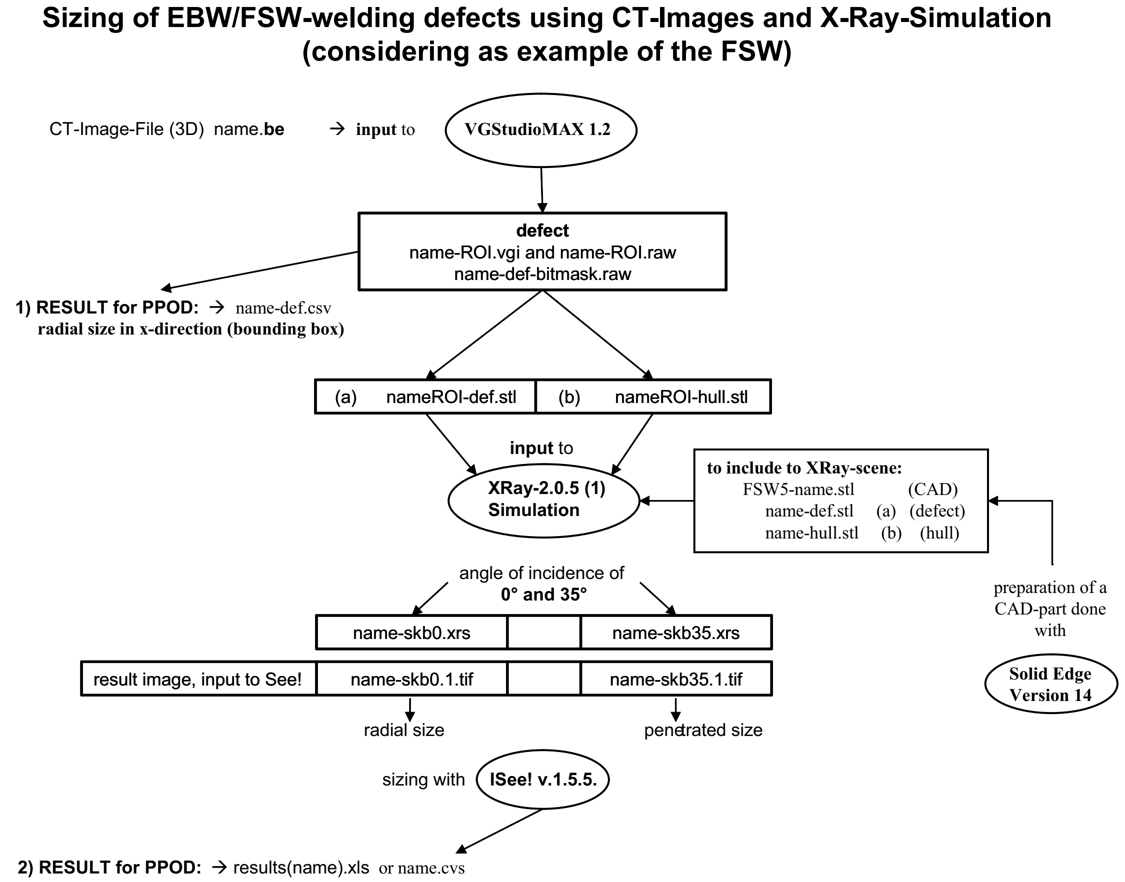

Figure 5-11. Flow chart of the sizing and STL-extraction procedure of the EBW- and FSW-measurement.

5.3 Micro-focus computed tomography

Computerized X-ray tomography measures the linear attenuation coefficient of the examined material in each point of the region of interest. The coefficient is dependant on the incident X-ray energy and on the atomic number of the material. In most cases it can be regarded as linear correlating to the specific density. In conventional (medical) systems tomograms are measured slice by slice, in more modern types the object to be measured is moved constantly allowing the slices to generate a continuous volume. In the case of 3D CT the detector no longer consists of a row of detectors but of a square field with an array of detector elements. The detector measures a conventional radiological image. In turning the object in front of the detector a complete data set is collected by one turn. Resolutions in the micro meter range are achieved either by a high resolving detector and a parallel beam source, or, as in this case, by an X-ray beam spot in the micro-meter range, a coarse but efficient detector and a magnification set up. /6/ Moreover for examinations of highly absorbing materials (metals), the choice of the highest possible X-ray energy is appropriate. Artefacts from beam hardening and exponential edge gradient effects are reduced.

In 2003 a 320 kV micro focus X-tray tube was built into the µCT system /7/. The bipolar tube is set up from a standard –200 kV tube. The original probe head is changed to the bipolar head which has a built-in anode with an additional high voltage supply of up to +120 kV. (In practical operation the second high voltage is fixed to +120 kV while the variation in energy is done with the standard voltage supply, resulting in a range of 130 kV to 320 kV.) The distance between X-ray spot on the internal target and the tube window is enlarged to

25 mm because the target position is no longer at ground voltage level. This means that a µCT system with this kind of tube provides a lower maximal magnification, which causes no problems as the system is designed for objects of large size.

The set up with 1,500 mm distance between source and detector, and a detector movement in width and height, allows objects with a diameter of up to 700 mm to be measured. The smallest possible volume of examination (voxel) has a side length of 10 µm. The spot size of the X-ray tube given for standard conditions at 90 kV is 10 µm, which is the same as a standard tube. With a two dimensional detector it is no longer possible to discriminate the scattered radiation released either by the object or the detector. The accumulated raw images therefore have to be carefully corrected to yield an undisturbed CT image after back-projection. /8, 9/ In all cases the back-projection is done by the well-known Feldkamp algorithm. /10/.

Image processing systems (like AVS 5.5 for Linux) can be used to examine the internal structure of the objects. Either two dimensional slices can be generated, representing the density of the object by grey values from black for zero to white for high density, or three dimensional isosurfaces, a representation of the surface of all voxels with the same value. In general different materials are discernible by their density and also small variations within each material can be detected. If the range is large, a different imaging for each density class is useful.

Technical data: The copper samples were measured with 320 kV, 100 µA and a pre-filtering of 1.0 mm Sn plus 0.5 mm Cu. 900 shadow graphs of 2.28 s each were taken, resulting in image slices. The size of each volume element of the image was $(0.025\ \text{mm})^3$. The detector was positioned at a distance of 62 mm from the X-ray source.

5.4 Reference measurements using ultrasonic testing

The detection of discontinuities by SKB using ultrasonic testing techniques has been quantitatively compared to reference measurements performed at BAM. Copper weld segments were examined to give reference values. The segments have similar geometric dimensions and weld types as the original lid. The quantitative detection probability is then evaluated by POD (probability of detection) calculations. The pulse echo method was used just to verify the presence of the defects.

The through transmission focussing UT-technique, with focus in the weld plane, was used to provide the quantitative reference for the area like discontinuities for EBW. Since no cross sectioning was performed for EBW the POD curves might suffer from an uncertainty in the "a"-value.

In preparation of the ultrasonic measurements on the copper ring segments reference measurements on small cylindrical copper samples have been performed to check the resolution and the measurement error of the inspection technique applied on small well defined reference reflectors.

The determination of the measurement error for the immersion technique in through transmission was executed at two flat bottom holes each 1.5 mm in diameter. In Figure 5-12 the copper sample with two flat bottom holes is represented . The lateral distance between the bore holes amounts 0.8 mm and the bore holes have depths of 20 mm. The copper sample was positioned between transmitter and receiver probe. The 10 MHz probes chosen had a focus length 75 mm in water. The distance between the two probes aligned to each other was arranged in such a way that the two flat bottoms of the bore holes were lying in the focus region.

In Figure 5-13 a measured C-scan is illustrated. It can be seen that the two bore holes are represented as one reflector indication. The greater extension can quantitatively be determined with an amount of 4.9 mm using the 6 dB increase, measured from the middle of the reflector indication in both vertical directions towards the borders of the indication. In comparison to the real extension of 3.8 mm (see Figure 5-12) the measurement error has an amount of 1.1 mm. In both horizontal directions using the 6 dB increase from the middle of the reflector indication towards the borders the represented extension in the C-scan has an amount of 3 mm. In comparison to the real extension of 1.5 mm (see Figure 5-12) the measurement error has an amount of 1.5 mm.

The two different definitions of measurement error can be explained by having in mind that until an reflector extension of 3 mm the cross section of the ultrasonic sound beam is measured by the reflector extension and not vice versa. Having a reflector greater than 3 mm the ultrasonic sound beam can be used to determine the reflector extension.

To check the resolution of the inspection technique a copper reference specimen was used with three flat bottom holes each 1.5 mm in diameter. The bore holes with a depth of 20 mm were positioned between 2.3 mm and 3.7 mm apart.

The 10 MHz probes chosen had a focus length of 75 mm in water. The distance between the two probes aligned to each other was arranged in such a way that the three flat bottoms of the boreholes were lying in the focus region.

In Figure 5-14 the geometrical positions of the reference reflectors and a measured C-scan are illustrated. Because of the influence of copper texture only the reflector lying at a distance of 3.7 mm to the adjacent could be resolved as a single hole. The other two reflectors lying at a distance of 2.3 mm to each other could not be individually resolved. It was assumed this might have no consequence for the POD since the UT transmission was used as reference for area like flaws only.

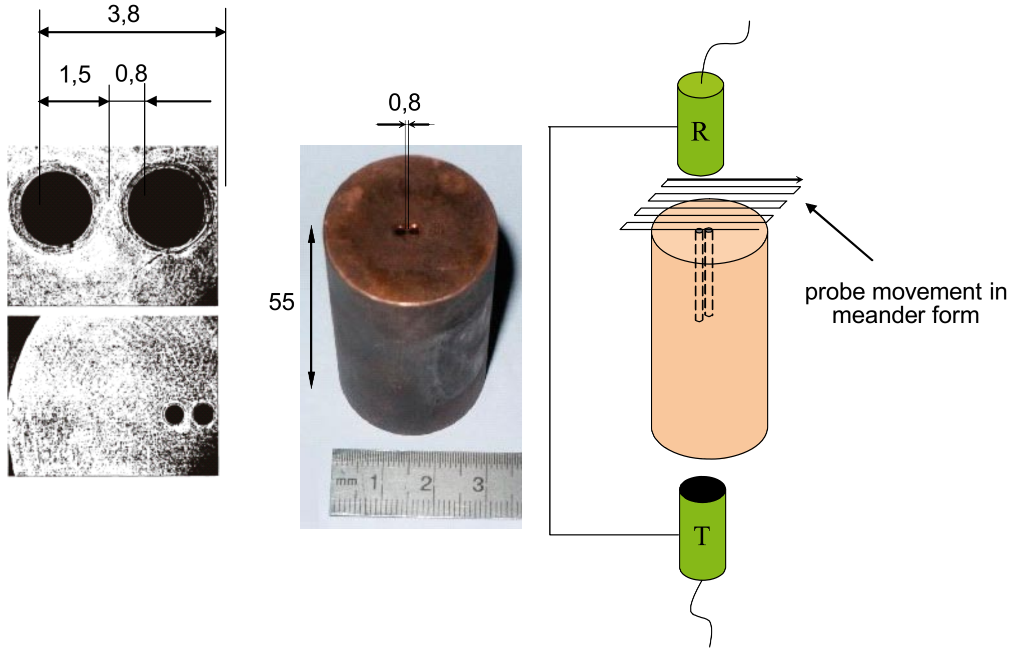

Figure 5-12. *Copper sample with two reference reflectors to determine measurement error when using immersion technique in through transmission method.*

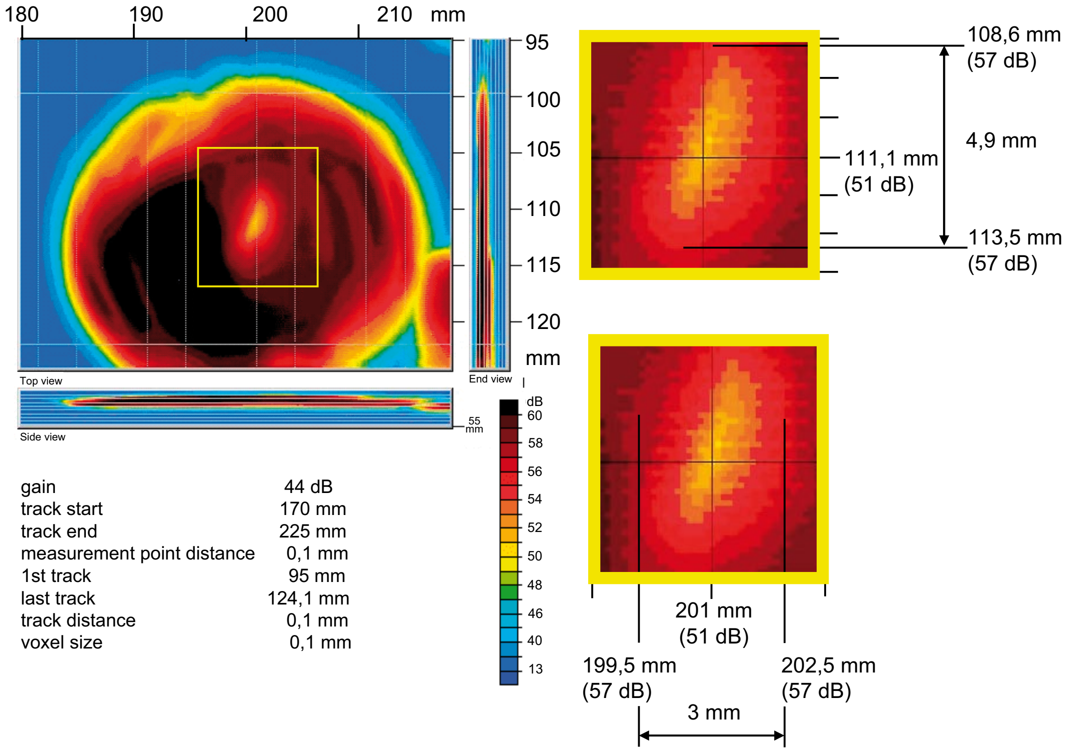

gain	44 dB
track start	170 mm
track end	225 mm
measurement point distance	0,1 mm
1st track	95 mm
last track	124,1 mm
track distance	0,1 mm
voxel size	0,1 mm

Figure 5-13. *C-scan with indication of reference reflectors, definition of measurement error: horizontal: 1.5 mm, vertical: 1.1 mm.*

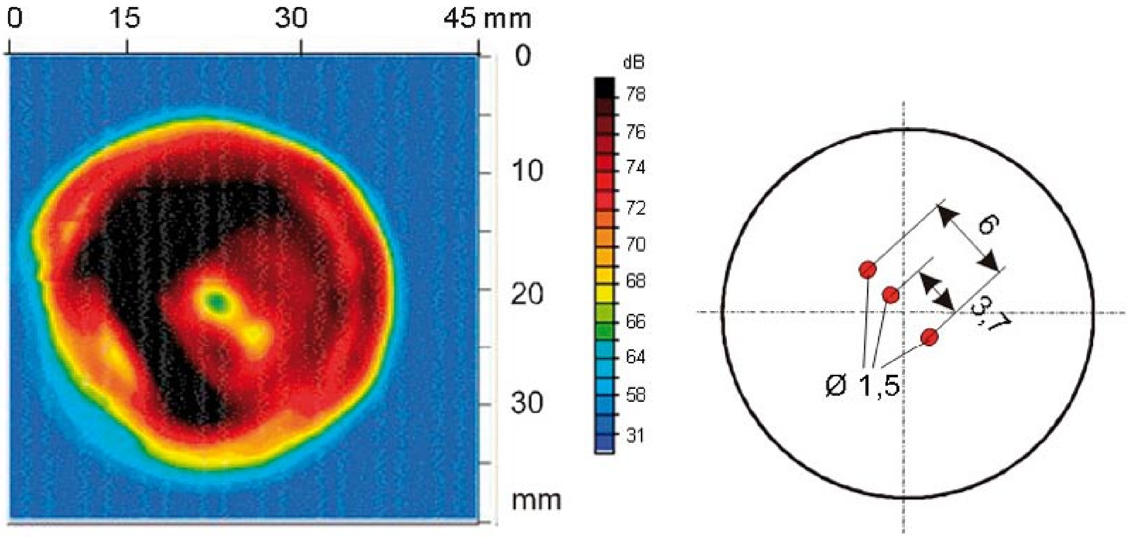

Figure 5-14. *C-scan with indications of reference reflectors using immersion technique in through transmission method.*

A further reference specimen was used to determine the resolution of the 10 MHz probes using the immersion technique and without having the texture influence of copper. This reference specimen had two flat bottom holes at a depth of 5 mm and at a distance of 3.5 mm apart. Borehole diameters were 1.5 mm. The measured C-scan is shown in Figure 5-15. Both indications of the reflectors may be clearly distinguished.

For the contact technique in pulse echo mode a copper reference specimen with one flat bottom hole was employed, with respective diameter and depth of 3 and 20 mm.

This reflector position is comparable to the copper ring segments with electron beam welds. The measurements were realised with a TR-probe showing a frequency of 4 MHz. The measured C-scan is shown in Figure 5-16.

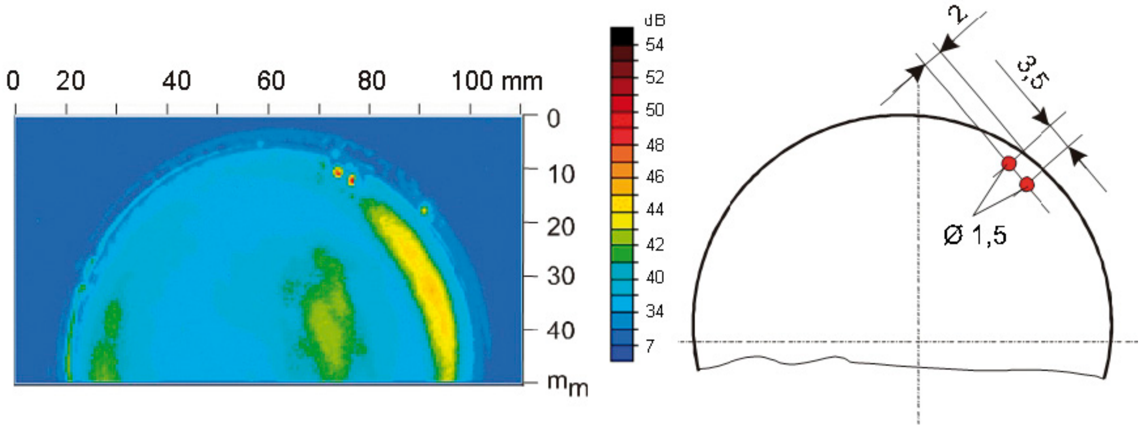

Figure 5-15. *C-scan with indications of both reference reflectors machined in a test specimen for resolution check of ultrasonic equipment in absence of influences induced by copper texture.*

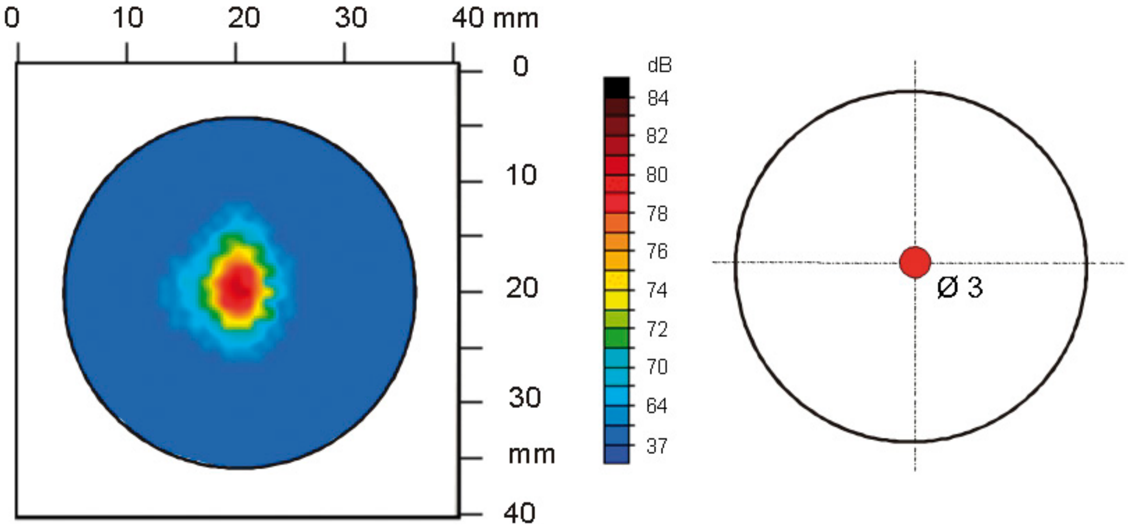

Figure 5-16. *C-scan with indication of reference reflector using contact technique in pulse echo method.*

5.4.1 UT Pulse-Echo-Technique examination of weld ring segments from L025 (EBW)

The electron beam welded copper ring segments were also investigated in pulse echo mode under conditions of contact. The measurement arrangement is shown in Figure 5-17. The Transmitter-Receiver (TR)-probe had a frequency of 4 MHz. For meandered scanning in case of measurement 0.5 mm was installed as distance between adjacent measurement points and tracks.

The C-scan in Figure 5-18 represents the electron beam welded ring segment with some typical weld discontinuities detected in contact technique.

The sensitivity calibration was completed using the reference specimen shown in Figure 5-16. The amplitude from the flat bottom hole was adjusted to a height of 78 dB (see Figure 5-16), hence a flat bottom hole of 1.5 mm diameter would have an echo height of 66 dB. Then the sensitivity was increased by 12 dB, so that the 1.5 mm flat bottom hole would be displayed with the same amplitude colour value as the 3 mm flat bottom hole before (see coloured amplitude scale in Figure 5-18). As a result of this high inspection sensitivity most of the echo indications are in saturation and the reflector size cannot be determined evaluating the 6 dB drop from their amplitude maximum. However, the aim of these measurements was to locate and size as much of the discontinuities inside the specimen as possible. In the immersion technique probes with higher frequency and focused sound beam were used so that the C-scan can give an image of the real reflector size.

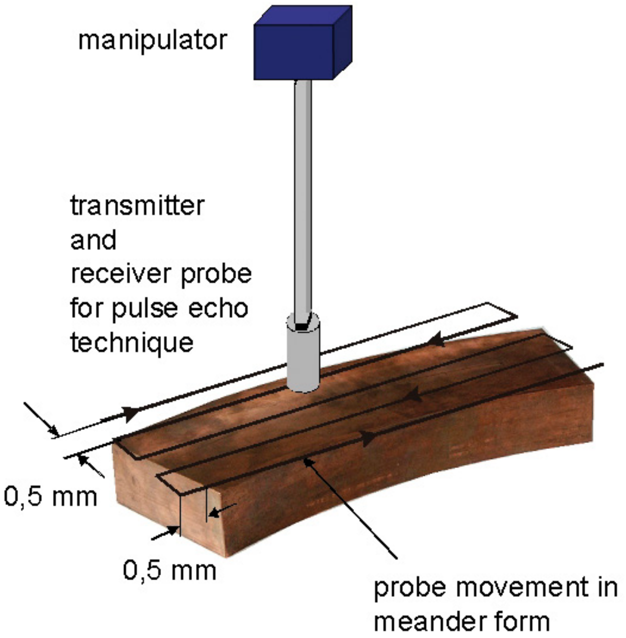

Figure 5-17. *Measurement arrangement for pulse echo method in contact technique.*

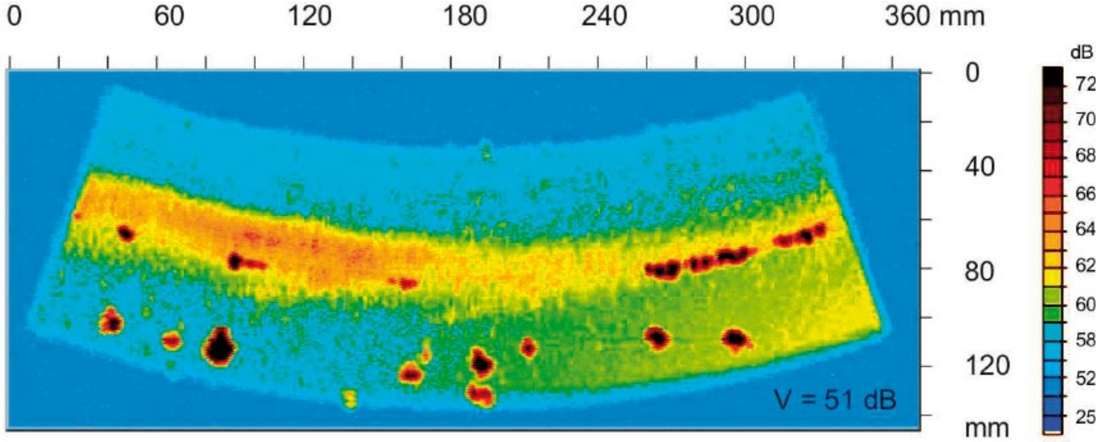

Figure 5-18. *C-scan of an electron beam welded ring segment (circumferential position: 32–72°) when using pulse echo method in contact technique.*

5.4.2 UT transmission examination of weld ring segments from weld L025 (EBW)

The examined copper ring segments with electron beam welds had a wall thickness of 40 mm and showed a number of discontinuities.

The copper ring segments welded using the electron beam technique, were examined using contact and immersion ultrasonic techniques for comparison purposes. For the immersion technique, through transmission mode with 10 MHz probes was used, as was the case for the friction stir welded specimen.

The C-scan in Figure 5-19 represents an electron beam welded ring segment with some typical weld discontinuities examined with the transmission technique. The ring segment had a radial extension of 100 mm and in the radial direction the weld is extended to a depth of almost 70 mm. At a distance of 50 mm in radial direction from the canister surface the gap between the lid and the tube is observed. The tube is located below the weld (see Figure 5-20). In the C-scan this gap is represented as a ring formed indication.

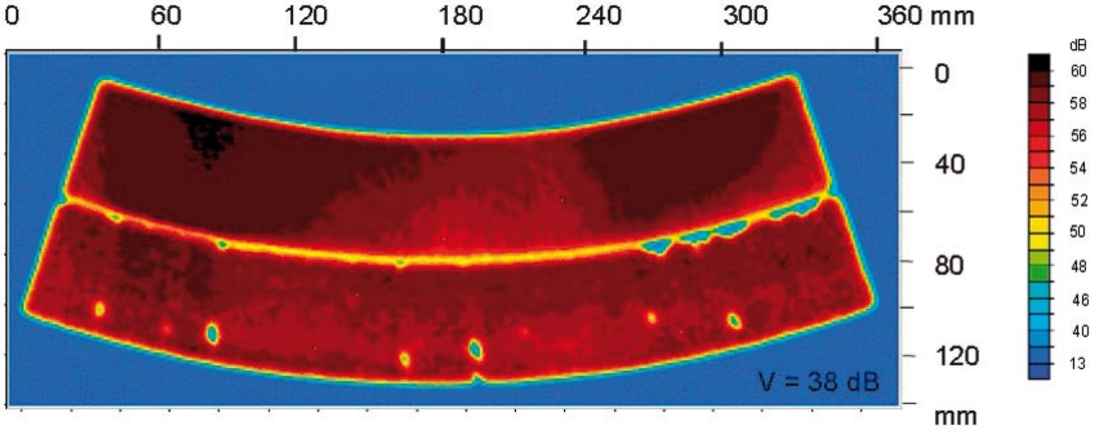

Figure 5-19. *C-scan of an electron beam welded ring segment (circumferential position: 32–72°) when using through transmission mode in immersion technique.*

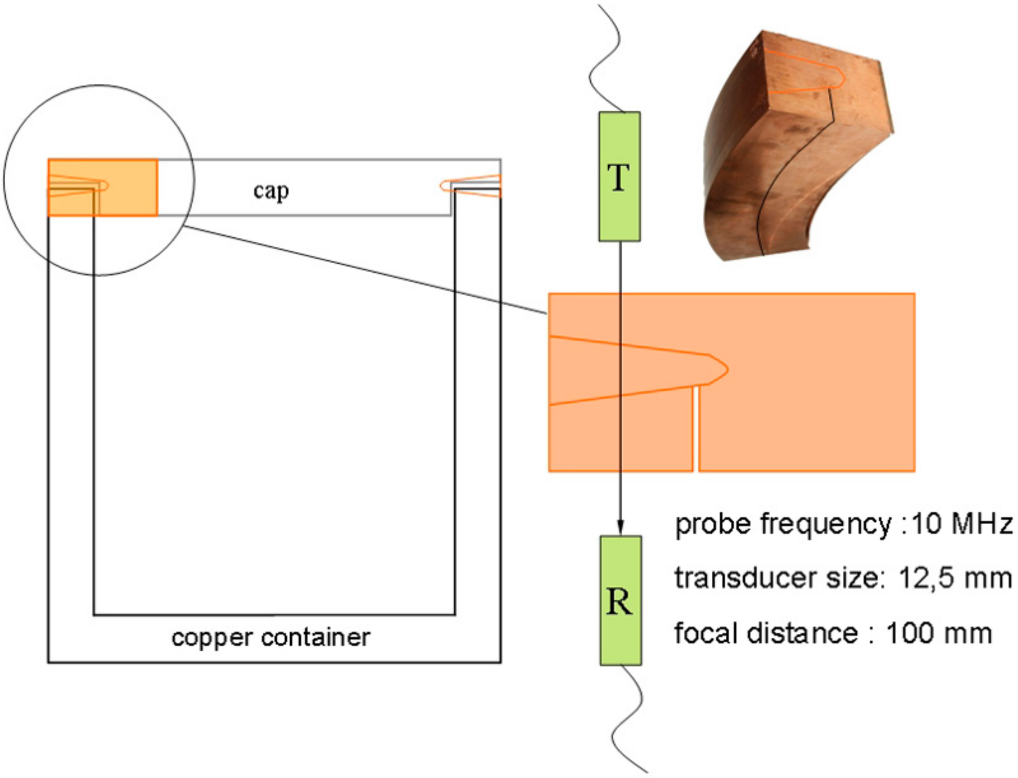

Figure 5-20. *Position of ring formed gap perpendicular to the weld.*

5.4.3 UT transmission examination of weld ring segments from weld FSW5

The examined copper specimens with friction stir welds were selected using the criteria that they contain a number of discontinuities, which could occur during the welding process.

The prepared copper specimen with friction stir welds had a wall thickness of 60 mm. For detection of discontinuities in the immersion technique, focused 10 MHz probes were used, as mentioned above in connection with resolution studies. The measurement arrangement is shown in Figure 5-21. The original position of a ring segment in the lid of the copper canister and the spatial orientation of the weld may be seen in Figure 5-22.

The copper ring segments were always scanned along meander like tracks (see Figure 5-21). The distances between adjacent measurement points and tracks were 0.5 mm.

A representative example of the 19 ring segments examined is shown in Figure 5-23. The C-scan of the segment covers the circumferential range 201–241°.

The ring segment had a radial extension of 100 mm and in the direction of the canister axis the weld had a depth of 50 mm (see Figure 5-22).

In the friction stir welded ring segment there are much less discontinuities compared to the electron beam welded ring segment (see Section 5.4.2). Discontinuities in the friction stir welded ring segment are located mainly in the outer surface and have a greater elongation in the circumferential direction than in the radial direction. A typical friction stir weld discontinuity arising in the root region is often caused by faulty process control during welding, referred to as joint line hooking. This particular discontinuity could not be detected in this ring segment.

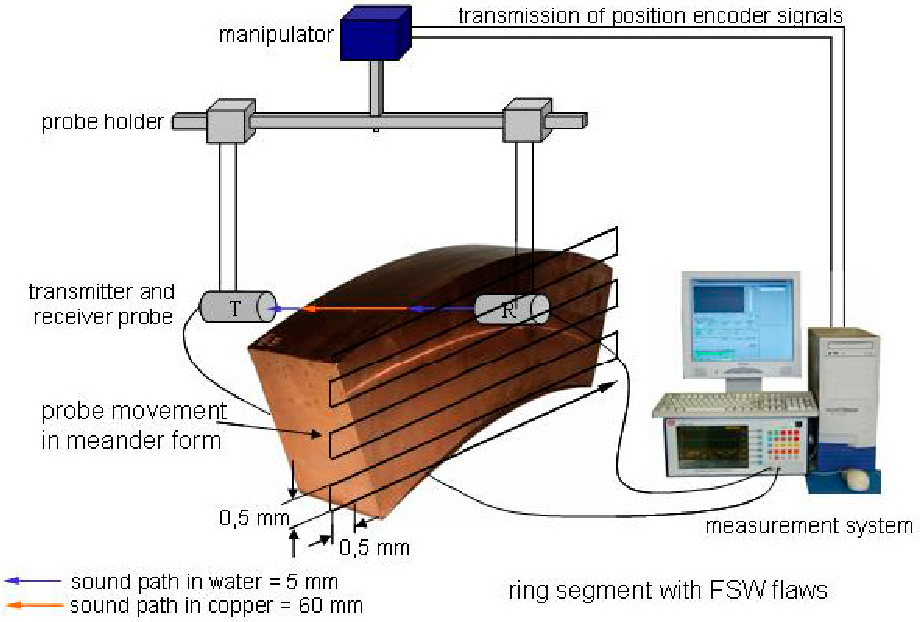

Figure 5-21. *Measurement arrangement for through transmission method in immersion technique.*

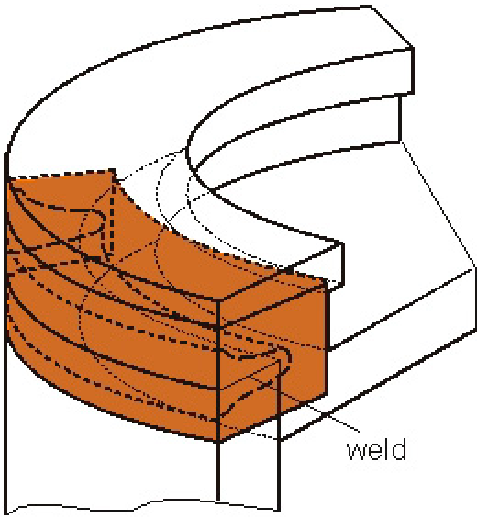

Figure 5-22. *Lid section of the copper canister and weld position.*

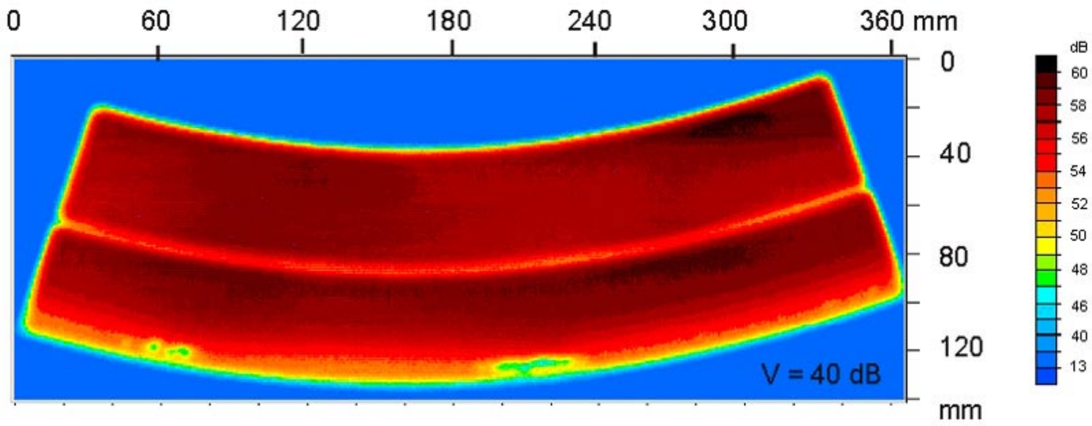

Figure 5-23. *C-scan of a friction stir welded ring segment (circumferential position: 201–241°).*

Summarizing the resulting uncertainty of the reference method UT transmission: All discontinuities smaller than 3 mm are measured as 3 mm because of the focus diameter and for all discontinuities greater than 3 mm the sizing error might be up to ± 1.5 mm. The estimation of the influence of this uncertainty onto the POD will be presented in Chapter 8.

6 Assistance by modelling

Apart from the modelling of the spectrum (6.1.1) the X-ray and Ultrasonic Modelling techniques are of quasi-deterministic nature. This means the rays and waves follow classical propagation rules which do not include quantum noise and any other random influencing factors like the surface roughness of flaws. To have this included to a certain extent the models add at the end of the calculation random noise to the intensity or amplitude the bandwidth of which was estimated according to physical reasoning.

6.1 X-ray modelling

6.1.1 Modelling of the spectrums

For the characterization of the X-ray source two methods are used: (*i*) Monte-Carlo simulation of the Bremsstrahlung production applying the Monte Carlo n-particle transport code MCNP /11/ and (*ii*) specially developed technique to estimate the photon spectrum from attenuation measurements.

Monte-Carlo calculations have been performed to describe the energy spectra of the linear accelerator. These spectra is used to describe the radiation source in the X-ray simulation program XRay /12/. For the calculations the Monte-Carlo code package MCNP from Los Alamos National Laboratory is used. The energy spectra of photons have been calculated resulting from 9 MeV electrons hitting a tungsten target. Target and filter thicknesses have been chosen according the BAM linear accelerator (28 mm tungsten, 15 mm water, 25 mm copper), because data for the Varian accelerator at SKB was not available. The Monte-Carlo code was also used to study the photon interaction processes for different materials in the considered energy range. Figure 6-1 shows the calculated photon spectrum after penetrating 15 cm of copper. The graphs of attenuated spectra show the total (black), primary (red), and scattered (blue) energy distribution of the photon intensity.

A second attempt was undertaken to gain information about the spectrum for high-energy X-ray sources if the spectrum is not directly accessible by measurements. To estimate the source spectrum in terms of an inverse problem, measurements of the total intensity or the dose are evaluated: If the measurement set-up is known, the Green function describing the response of a system to a delta pulse can be calculated. In case of a linear operator equation

$$f(E) = \boldsymbol{A} f_0(E) \tag{1}$$

for the transmitted spectrum $f(E)$ with the initial spectrum $f_0(E)$ and the linear projection operator $\boldsymbol{A}$, the Green function is given by

$$G(E,E') = \boldsymbol{A}\delta(E-E') \tag{2}$$

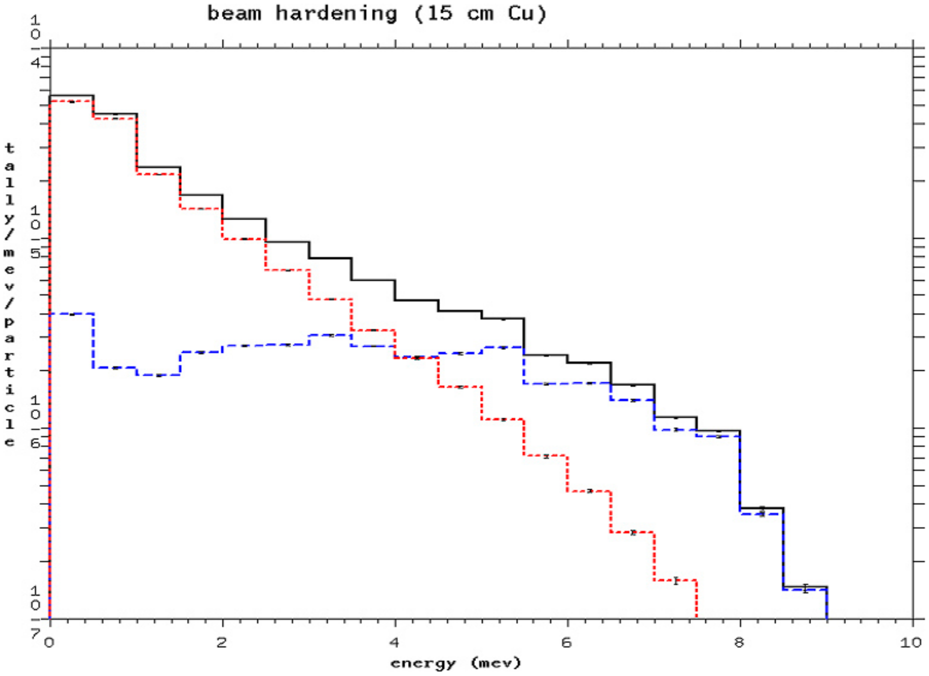

Figure 6-1. *Monte-Carlo results for spectrum evaluation (MCNP output): total (black), primary (red), and scattered (blue) photon spectrum.*

The transmitted spectrum follows with the Green function to

$$\begin{aligned} f(E) &= \boldsymbol{A} f_0(E) \\ &= \boldsymbol{A}\int \mathrm{d}E'\, f_0(E')\,\delta(E-E') \\ &= \int \mathrm{d}E'\, f_0(E')\,\boldsymbol{A}\delta(E-E') \\ &= \int \mathrm{d}E'\, f_0(E')\,G(E,E') \end{aligned} \tag{3}$$

If scattering is neglected, the attenuation law gives the linear operator ***A***. Otherwise the operator is given by the Boltzmann equation. The Green function can be calculated by Monte-Carlo simulation. Once knowing the Green function it can be used for reconstructing the initial spectrum f_0 (E) from measurements of the transmitted dose. For this purpose the following optimization criteria is applied

$$\hat{I}_0(E) = \min V\left[I(E)\right] \tag{4}$$

with

$$V\left[I(E)\right] = \left| \min_{E\in(0,E_{\max})} \left(\partial_E^2 f(E)\right) - \max_{E\in(0,E_{\max})} \left(\partial_E^2 f(E)\right) \right| \tag{5}$$

Here, the first term ensures minimum curvature the high-energy part of the spectrum, while the second term maximizes the curvature at the maximum of the spectrum. Combining dose measurements for aluminum, copper, and lead, the spectrum was reconstructed which is shown in Figure 6-2. The estimated average photon energy is about 3.5 MeV, which agrees with the experimentally determined integral attenuation coefficient.

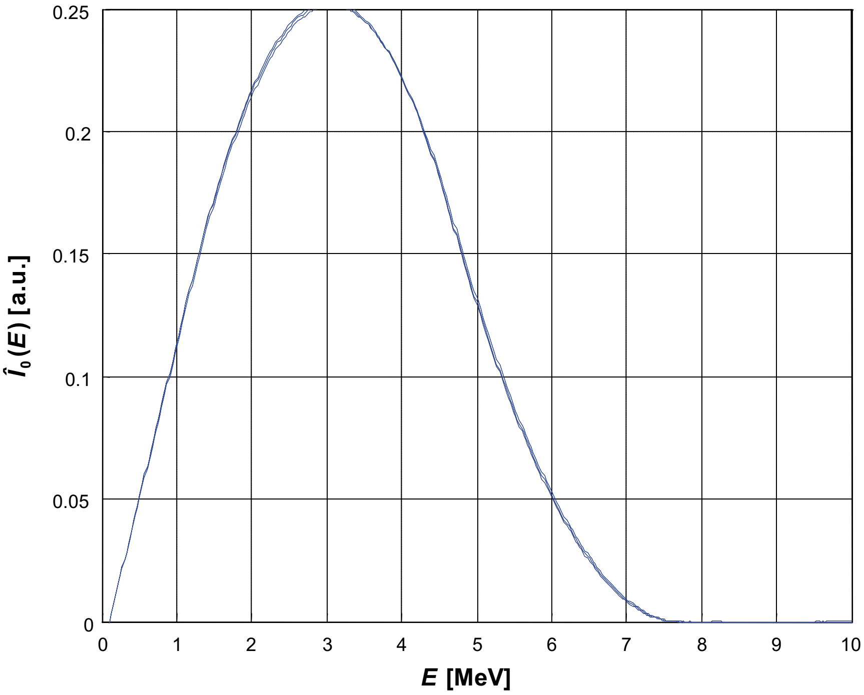

Figure 6-2. *Estimated spectrum from dose data.*

6.1.2 BAM X-ray model

For the detailed optimization of the radiographic technique the BAM XRay simulation tool XRay /12/ is applied to various parameter options thus saving lots of expensive experiments. The XRay simulation tool (see Figure 6-3) has been developed for several years and the applicability of the underlying radiographic model has been demonstrated for various practical cases /13/. With respect to the scope of the radiographic technique of SKB the simulation tool is expanded by additional features. This includes the specific detector characteristic and imaging procedure with pixel binning and white image correction. Furthermore, the image generation by line scanning while canister rotation is adopted.

X-Ray penetration model

The components of the radiographic inspection system are considered independently, i.e. the characteristics of the source, the geometry and the material properties of objects and discontinuities, and the imaging process itself. The model is based on a ray tracer technique describing the attenuation of the radiation. The scattering effect is included in terms of built-up factors. A CAD-interface provides the opportunity to arrange independent CAD objects, e.g. the component geometry or discontinuity shapes, defining a testing scheme.

The X-ray generation, the interaction between the radiation and the object, and the imaging process are treated as three independent parts of the X-ray projection. The initial X-ray beam model, describing the X-ray generation part, considers the extent of the beam and its energy spectrum because of the energy dependence of the interaction between the X-ray beam and the penetrated material. A raster of point sources defines the focal spot in its size. The source points are characterized by the initial intensity distribution of the assumed radiation source. By weighting the source points each other the radiation density distribution over the focal spot can be adjusted.

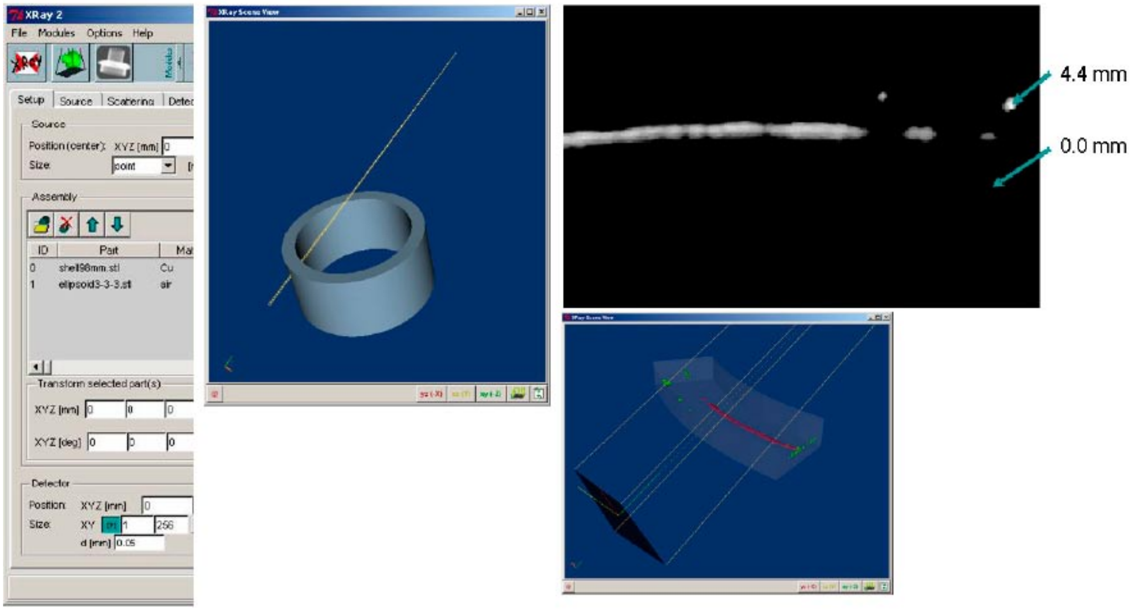

Source

Position (center): XYZ [mm] 0

Size: point

Assembly

ID	Part	Ma
0	shell98mm.stl	Cu
1	ellipsoid3-3-3.stl	air

Transform selected part(s)

XYZ [mm] 0 0 0

XYZ [deg] 0 0 0

Detector

Position: XYZ [mm] 0

Size: XY 1 256

d [mm] 0.05

Figure 6-3. *User interface of BAM-X-ray simulation tool.*

The radiation-material interaction with its stochastic processes of absorption, scattering, pair production, and production of characteristic radiation can be described by a transport equation of Boltzmann type. A detailed solution of this equation (e.g. using Monte-Carlo methods) for arbitrary object geometry is difficult and computing time intensive and not suitable for practical applications. The easiest approximation is to neglect additionally the sources of characteristic radiation as well as the scattering processes. For this case the transport equation becomes a homogeneous ordinary differential equation with the solution yielding the well-known exponential attenuation law. The material is characterized by the energy dependent linear attenuation coefficient. This approximation is valid when the photo absorption is dominant. The influence of scattered photons is considered by a build-up factor.

Rays from every of these source points are traced to all of the raster points in detector plane. The ray path length through an object under examination is registered and the attenuation of radiation calculated considering the objects material type. This ray casting procedure is simulating the imaging process. Transmission functions like the characteristic film curves for different types of film classes are used to describe the properties of different detectors. The inner unsharpness of the detection system is simulated by Gaussian filtering.

The geometrical computer model of the experimental setup has to support source, film, and the representation of the test sample geometry.

Within the simulation program the geometry and the material properties of the component are represented by an object-oriented code for a 3D volumetric model. For the simulation, a ray tracing algorithm is used which is optimized for the rectilinear propagation of primary photons based on the given boundary face model. Figure 6-4 shows a schematic view of the radiographic set-up of cupper canister lid weld inspection at SKB and its virtual implementation as 3D scene within the XRay program.

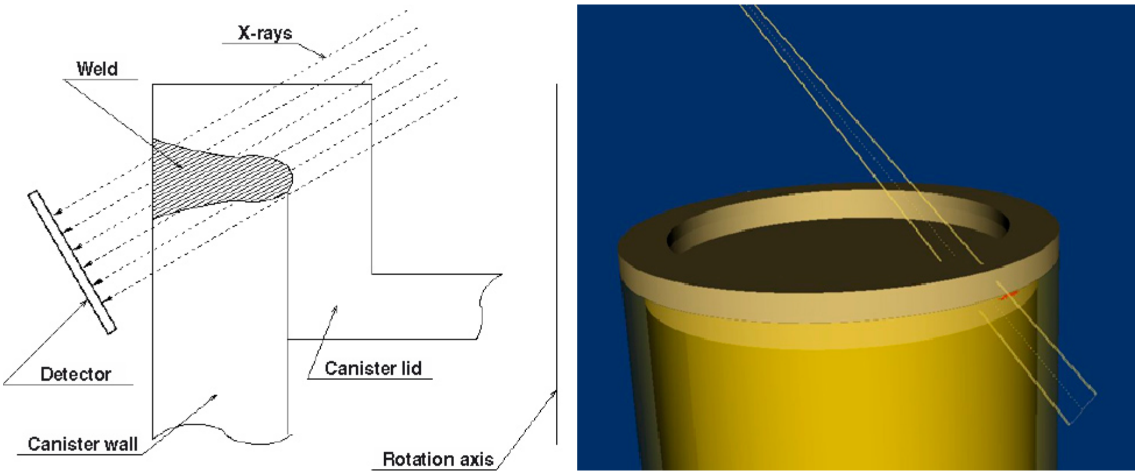

Figure 6-4. *Radiographic set-up: schematic view (left) and virtual scene (right).*

Comparison of modelling results with experiments

A test specimen with defined voids has been made to verify the measured radiographic and geometrical parameters of the SKB RT set-up and the simulation tool. Holes with diameters from 2 mm up to 32 mm were introduced to examine the radiographic projection. The arrangement of these boreholes is illustrated in Figure 6-5. The test specimen was placed on top of the 100 mm copper canister wall with support of an additional segment to have the holes at weld position. Figure 6-6 shows the virtual model within the simulation tool. The test specimen arrangement with fan beam at start position for line scanning is illustrated in Figure 6-6.

The comparison of the resulting synthetic image with the experimental radiograph gives an excellent visual correlation (compare Figure 6-7). The quantitative evaluation is focused on holes numbered 1 to 5. There are visual divergences in the images originated from disturbances of the radiographic process, which are not covered by simulation. This is amongst others the vertical striped background of grey value shifts from scan line to scan line. Also there is a dark horizontal stripe to be seen in the experimental image, which comes from a misalignment of test specimen and supporting segment. This misalignment is considered in the virtual model by a small opposite translational displacement of the two segments.

Table 6-1 shows measurements from the experimental radiograph and a corresponding simulation. First there are grey values for different penetrated lengths referenced by flaw number. The first line (without flaw number) gives values at full wall thickness for the sake of completeness. All other grey values are measured at maximal flaw depth, which is given by the hole diameter. Further, Table 6-1 lists the flaw depth or maximal reduction of penetrated length due to a flaw. Besides the real flaw depth as reference, there are values calculated from the radiographic contrast using the attenuation law. The comparison of depths for the different flaw numbers can be used to evaluate the simulation quality.

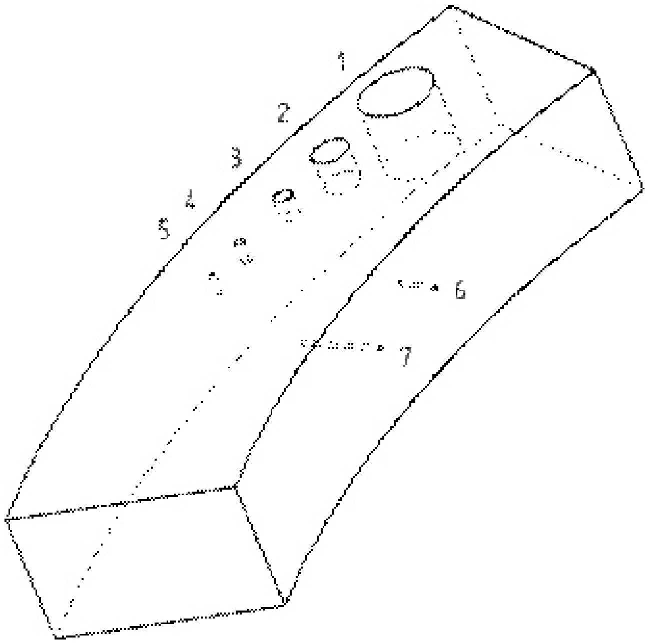

Figure 6-5. Test specimen with defined flat bottom holes.

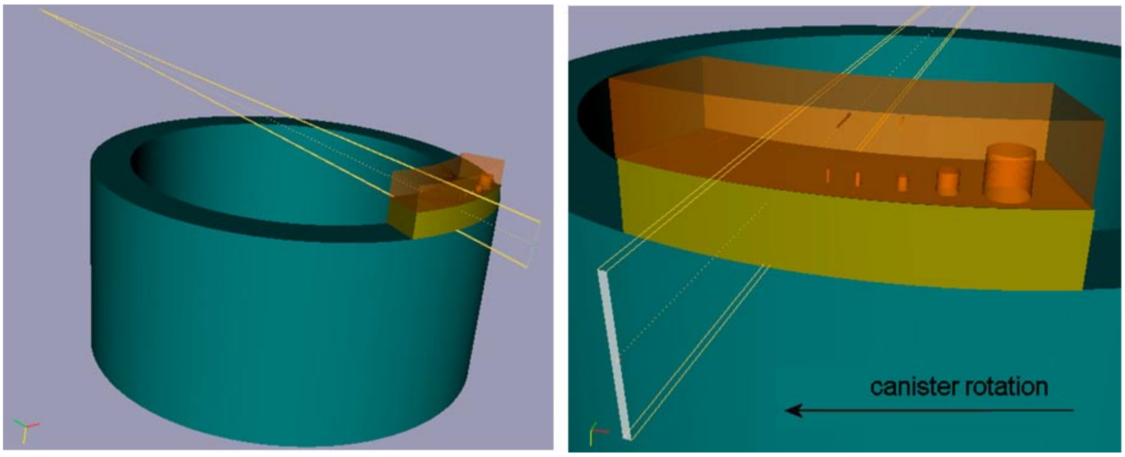

Figure 6-6. Virtual setup for test specimen examination (left) and arrangement of test specimen (in transparent view mode) and supporting segment on top of the canister for the exposure (right).

Table 6-1. Comparison of grey values and flaw depths of experimental and synthetic radiographs of test specimen.

Flaw no.	Gray value at flaw depth		Flaw depth (mm)		
	Experimental	Synthetic	Real	Experimental	Synthetic
–	10,000	10,000	0.0	0.0	0.0
1	26,649	26,898	33.0	32.6	33.0
2	15,750	15,968	15.6	15.1	15.6
3	12,544	12,692	8.0	7.6	8.0
4	11,258	11,296	4.2	4.0	4.1
5	10,566	10,586	2.0	1.8	1.9

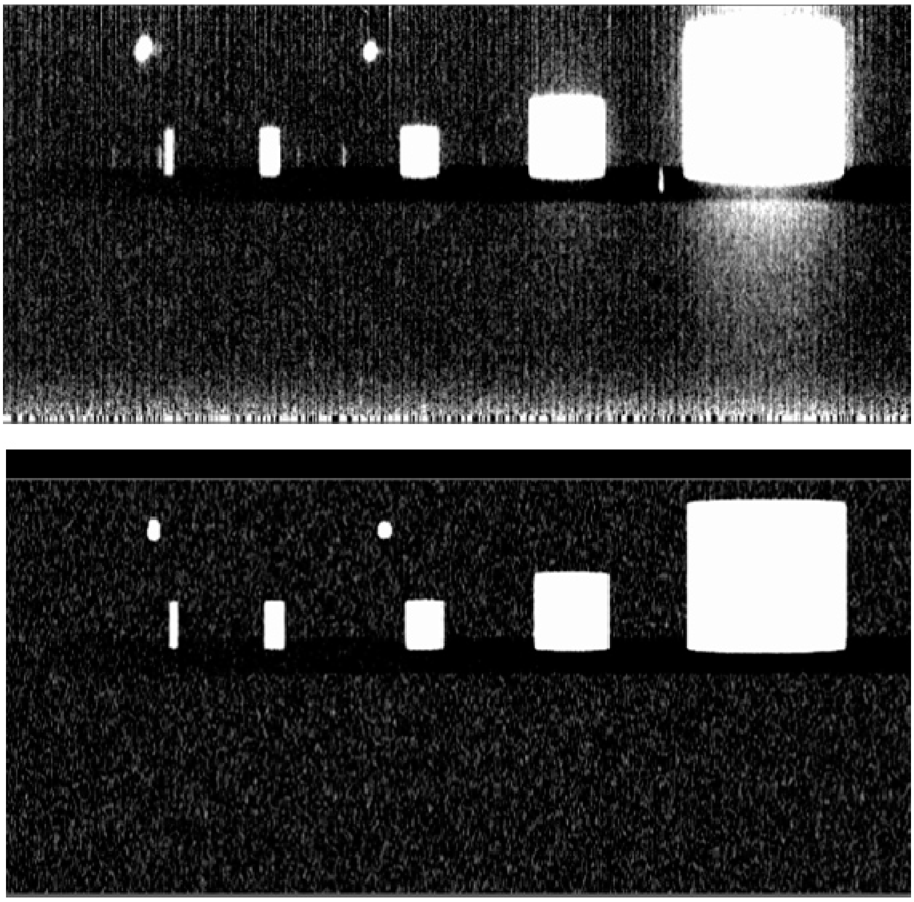

Figure 6-7. *Experimental (above) and synthetic (down) radiograph of test specimen.*

Figure 6-8 gives a graphical illustration of the values collected in Table 6-1. The comparison shows a good agreement between the real flaw depth and the flaw depth extracted from the experimental and the synthetic radiographs. In addition, Figure 6-9 presents the deviation in the synthetic radiograph compared to experiment concerning grey values and resulting flaw depths. The experimental grey values can be reproduced by simulation with an accuracy of about 1%. The corresponding extracted flaw depths are overestimated up to a maximum of 6%.

Finally, Figure 6-10 concludes the error of flaw depth extraction compared to the true values. Note that the flaw size decreases with the flaw number given in the image. For the large flaws a good agreement with the true flaw size (< 2%) is found. As the real flaw size decreases, the extracted flaw depth is increasingly underestimated. If the flaw size approaches the unsharpness of the system, the contrast of the indication is reduced due to this unsharpness, i.e. the contrast is not proportional to the flaw depth any more. Hence, the radiographic contrast does not reflect the attenuation law any more. Therefore the flaw depth is extracted too small.

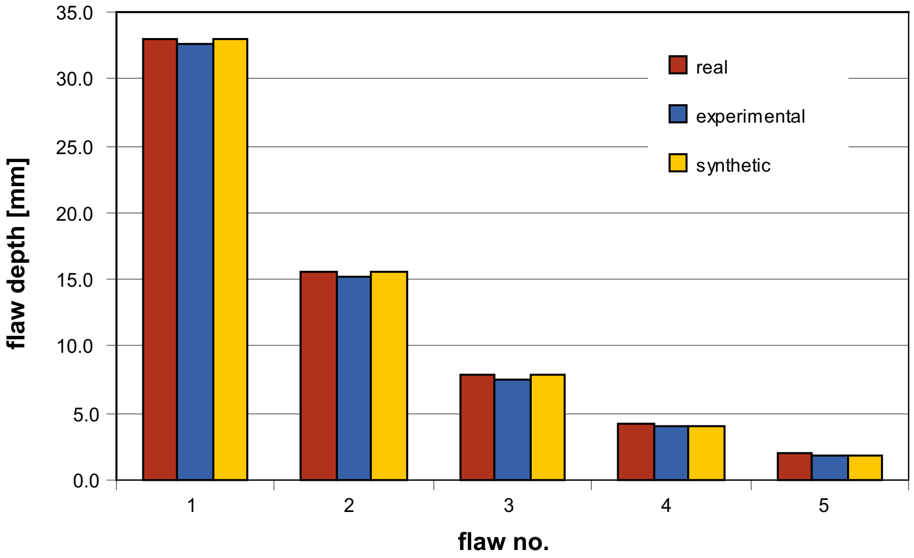

Figure 6-8. *Comparison of real flaw depth with the one extracted from flaw indications in experimental and synthetic radiographs of test specimen.*

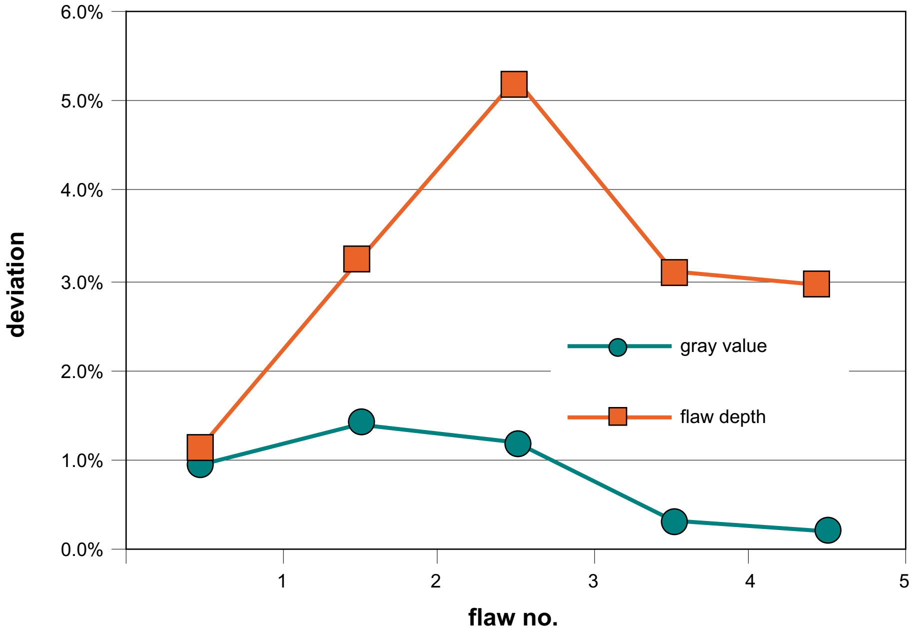

Figure 6-9. *Deviation in synthetic radiograph compared to experiment concerning grey values and resulting flaw depths.*

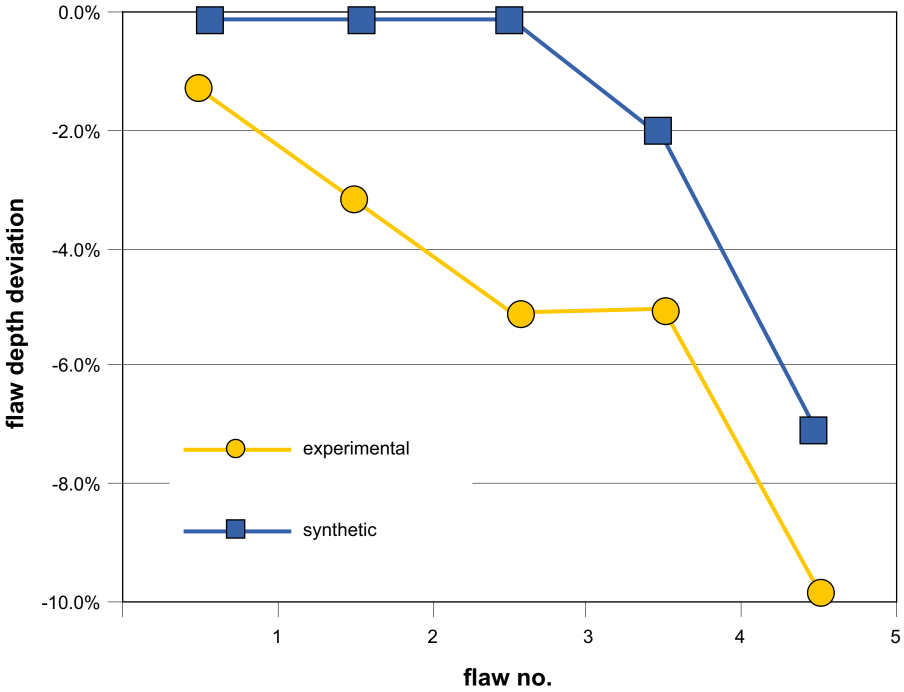

Figure 6-10. *Accuracy of flaw depths measured in experimental and synthetic radiograph of test specimen.*

6.2 Ultrasonic modelling

6.2.1 Description of applied ultrasonic models

The sub-department for acoustical and electrical methods of the Bundesanstalt für Materialforschung und -prüfung (BAM) have developed several beneficial computer models. The development of the models took place over a long period of time and they are employed for optimization of settings and validation results. The validation of these ultrasonic models was completed by comparing the theoretical results with measured data. For the comparison test specimens and real components containing artificial and real discontinuities were applied /14, 15, 16/. Components from in particular the power industry, especially nuclear power plants, and from the traffic sector were at the centre of interest.

During the investigations within this project two such computer models were used. The first one, named Array 2D 3D, was used for the sound field calculations. With the second one, named Echo 3D, the echo height of several reflector geometries was calculated in different geometrical setups. More information concerning the simulations will be given in the following /17, 18, 19/.

6.2.2 Soundfield calculations

The ultrasonic model Array 2D 3D was developed for sound-field calculation of ultrasonic matrix array transducers (2D arrays). The calculation is based on a point-source-synthesis-model implying Huygens's Principle of elementary waves. The model can be used for calculation of linear array transducers (1D array) by the use of a simpler geometry. Figure 6-11 shows the input dialog of the model with several input parameters, which have to be entered before the calculation. In Figure 6-11 the parameters for the sound-field calculation of the phased-array-probe used by SKB are shown for an incidence angle of 20° for the longitudi-

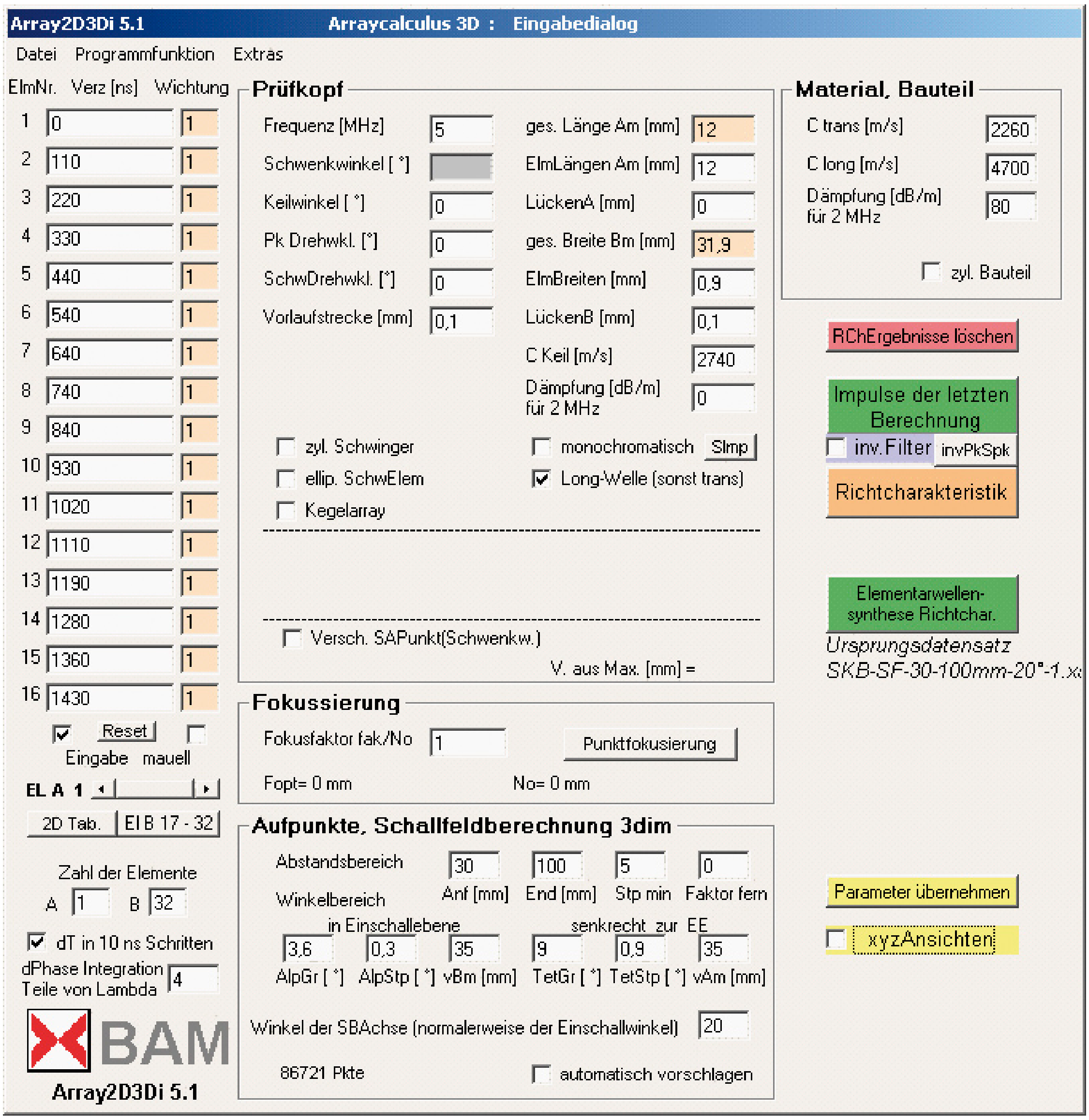

ElmNr.	Verz [ns]	Wichtung
1	0	1
2	110	1
3	220	1
4	330	1
5	440	1
6	540	1
7	640	1
8	740	1
9	840	1
10	930	1
11	1020	1
12	1110	1
13	1190	1
14	1280	1
15	1360	1
16	1430	1

☑ Reset ☐

EL A 1

Zahl der Elemente A 1 B 32

☑ dT in 10 ns Schritten

dPhase Integration Teile von Lambda 4

Prüfkopf

Frequenz [MHz] 5

Schwenkwinkel [°]

Keilwinkel [°] 0

Pk Drehwkl. [°] 0

SchwDrehwkl. [°] 0

Vorlaufstrecke [mm] 0,1

ges. Länge Am [mm] 12

ElmLängen Am [mm] 12

LückenA [mm] 0

ges. Breite Bm [mm] 31,9

ElmBreiten [mm] 0,9

LückenB [mm] 0,1

C Keil [m/s] 2740

Dämpfung [dB/m] für 2 MHz 0

☐ zyl. Schwinger

☐ ellip. SchwElem

☐ Kegelarray

☐ monochromatisch

☑ Long-Welle (sonst trans)

☐ Versch. SAPunkt(Schwenkw.)

V. aus Max. [mm] =

Material, Bauteil

C trans [m/s] 2260

C long [m/s] 4700

Dämpfung [dB/m] für 2 MHz 80

☐ zyl. Bauteil

☐ inv.Filter

Ursprungsdatensatz SKB-SF-30-100mm-20°-1.x

☐ xyzAnsichten

Fokussierung

Fokusfaktor fak/No 1

Fopt= 0 mm No= 0 mm

Aufpunkte, Schallfeldberechnung 3dim

	Anf [mm]	End [mm]	Stp min	Faktor fern
Abstandsbereich	30	100	5	0

Winkelbereich

in Einschallebene			senkrecht zur EE		
AlpGr [°]	AlpStp [°]	vBm [mm]	TetGr [°]	TetStp [°]	vAm [mm]
3,6	0,3	35	9	0,9	35

Winkel der SBAchse (normalerweise der Einschallwinkel) 20

86721 Pkte

☐ automatisch vorschlagen

Figure 6-11. *Input dialog for sound field calculation in ultrasonic model.*

nal wave. On the left side of the input dialog the delay times for each of the 32 transducer elements in nanoseconds are shown (in Figure 6-11 only the first 16 elements are visible). In the upper middle the probe parameters (category "Prüfkopf") are shown. Here the centre frequency of 5 MHz and the element length (transducer width) of 12 mm as well as the element width of 0.9 mm and the gap between the elements of 0.1 mm has to be defined. If the check box "monochromatisch" is marked the calculation will be carried out based on the centre frequency only. Otherwise a predefined impulse can be used, as in this case. The corresponding impulse with a bandwidth of about 37% and its frequency spectrum shows Figure 6-12. The input field for the incidence angle ("Schwenkwinkel") contains no value, because the sound field is point focused in a depth of 60 mm (see Figure 6-13) and the delay times represented are calculated for this condition.

The sound velocities for the longitudinal and the transverse wave plus the sound attenuation value inside the copper canister are defined within the category "Material, Bauteil". The attenuation value in the model is related to a frequency of 2 MHz, hence the attenuation value of 80 dB/m (0.8 dB/cm) was first assumed and displayed in the input dialog and corresponds to a sound attenuation of 5 dB/cm for a frequency of 5 MHz, assuming a quadratic law for the attenuation. For further calculations the chosen attenuation value of 0.64 dB/cm (or 4 dB/cm at 5 MHz), lies at the upper level within the range (from 3 up to 4 dB/cm), which was determined experimentally by attenuation measurements at SKB.

In this example for the sound field calculation a rectangular area of 35×35 mm^2 around the beam axis was calculated from 30 mm up to 100 mm distance from the transducer (category "Aufpunkte, Schallfeldberechnung 3 dim"). The calculation is done stepwise with small angle steps in the two directions perpendicular to the beam axis and with 5 mm steps in sound path direction. Thus the sound amplitudes and the phase shifts for 86,721 points within the area of interest were calculated. An interpolation technique, which takes into consideration surrounding amplitude and phase shift, was used to determine amplitude values for positions between these calculated points.

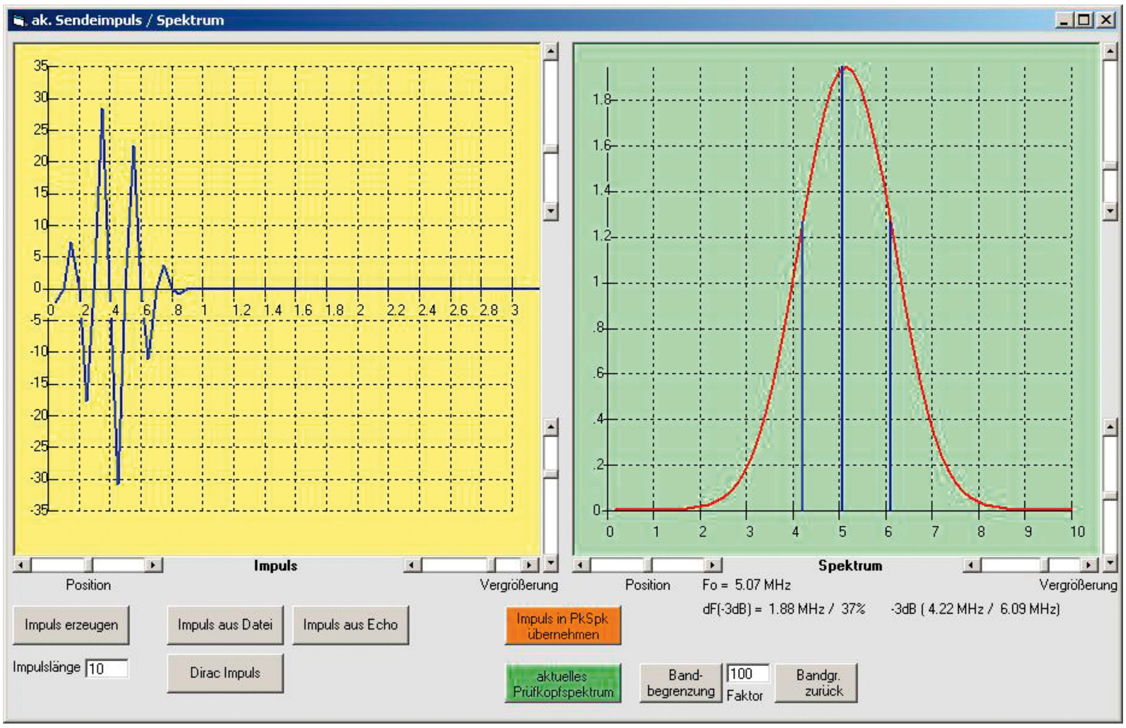

Fo = 5.07 MHz

dF(-3dB) = 1.88 MHz / 37%   -3dB (4.22 MHz / 6.09 MHz)

Impulslänge 10

100 Faktor

Figure 6-12. Impulse and spectrum for ultrasonic calculations.

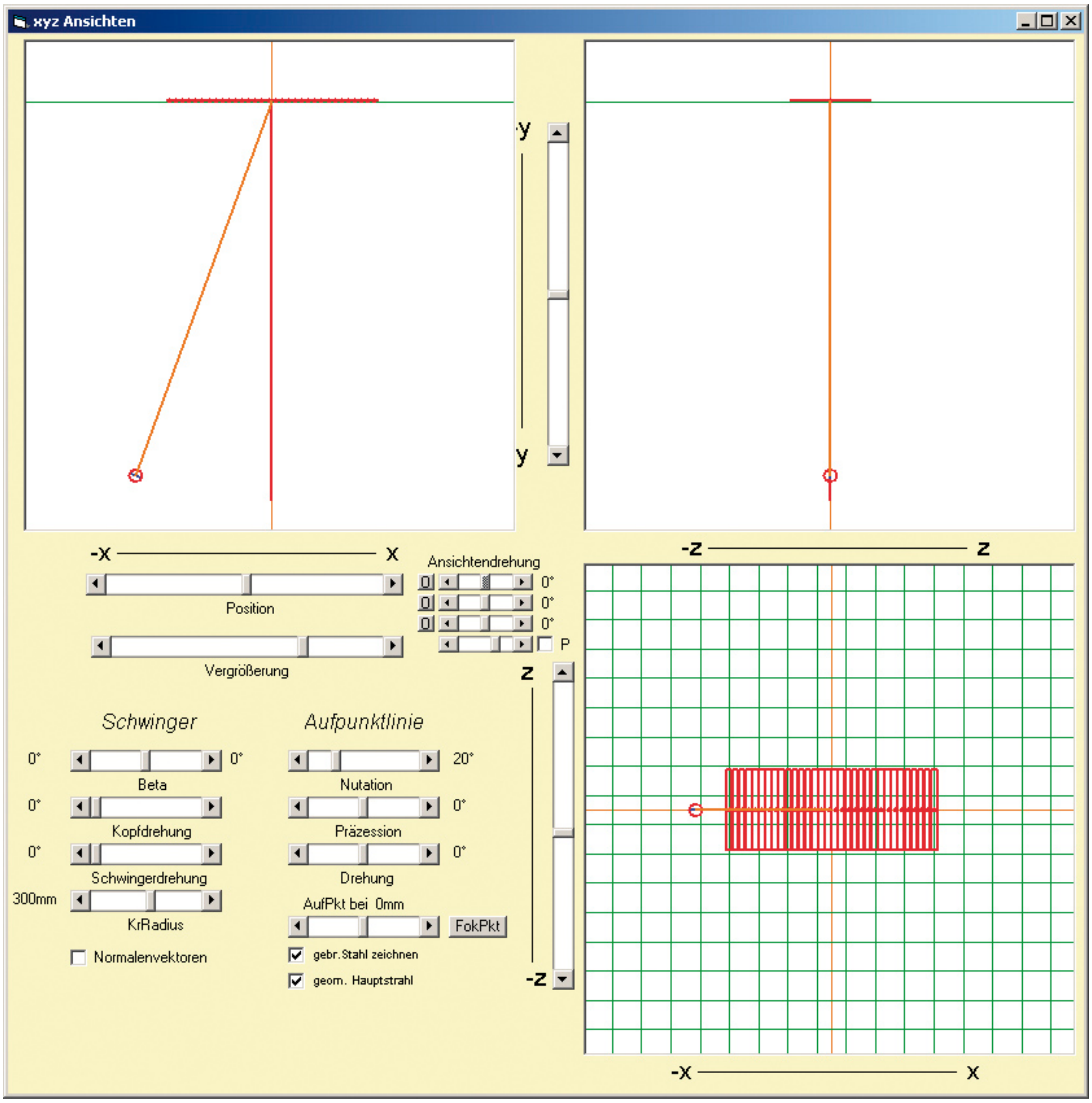

Ansichtendrehung 0°
0°
0°
☐ P

Schwinger
Beta 0° 0°
Kopfdrehung 0°
Schwingerdrehung 0°
KrRadius 300mm
☐ Normalenvektoren

Aufpunktlinie
Nutation 20°
Präzession 0°
Drehung 0°
AufPkt bei 0mm
☑ gebr. Stahl zeichnen
☑ geom. Hauptstrahl

Figure 6-13. *Point focusing for incidence angle of 20° in a depth of 60 mm.*

The Side View (X-Y-plane), Top View (X-Z-plane) and End View (Y-Z-plane) of the calculated area is displayed in Figure 6-14. For a better spatial representation Figure 6-15 shows the same arrangement rotated slightly at two spatial angles, so that the representation visualize a 3D effect.

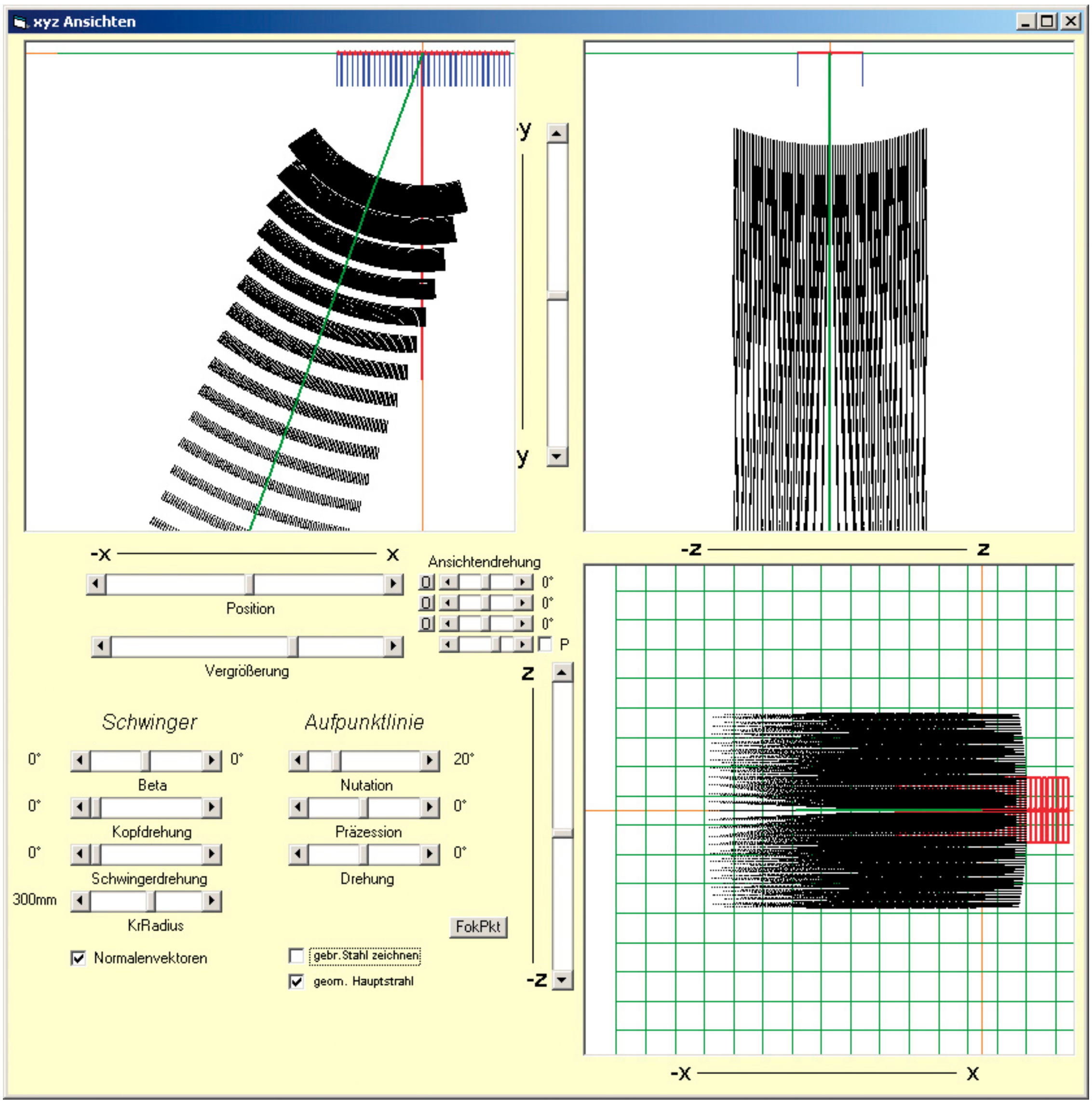

Ansichtendrehung
0 0°
0 0°
0 0°
☐ P

0° Beta 0°

0° Kopfdrehung

0° Schwingerdrehung

300mm KrRadius

☑ Normalenvektoren

Nutation 20°

Präzession 0°

Drehung 0°

☐ gebr. Stahl zeichnen

☑ geom. Hauptstrahl

Figure 6-14. *Side View (X-Y), Top View (X-Z) and End View (Y-Z) of calculation area.*

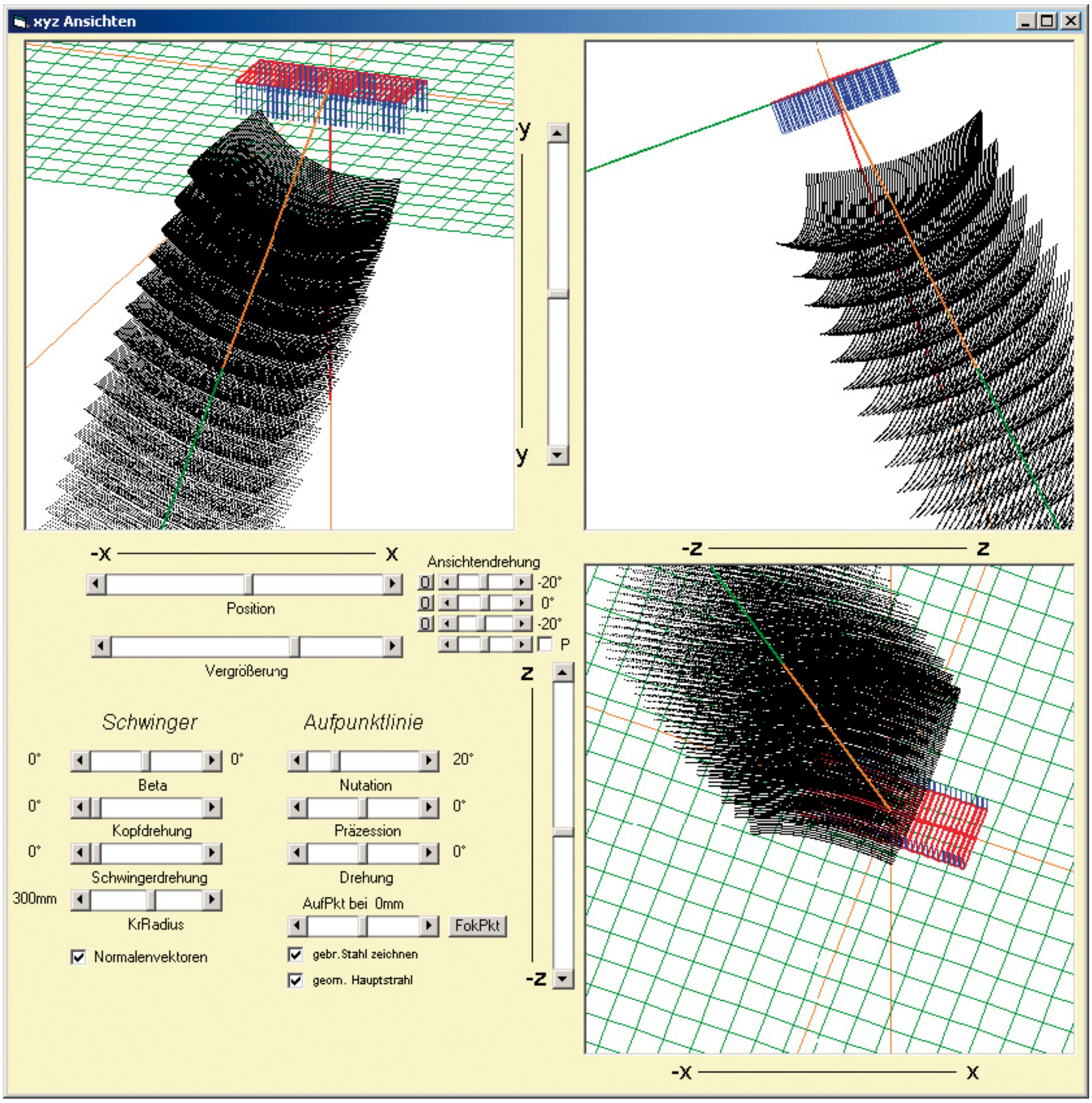

Ansichtendrehung: -20° / 0° / -20°

Beta 0° 0°

Kopfdrehung 0°

Schwingerdrehung 0°

KrRadius 300mm

☑ Normalenvektoren

Nutation 20°

Präzession 0°

Drehung 0°

AufPkt bei 0mm

☑ gebr. Stahl zeichnen

☑ geom. Hauptstrahl

Figure 6-15. *Side View (X-Y), Top View (X-Z) and End View (Y-Z) of calculation area rotated for better 3D-imagination.*

For the arrangement just described the sound field calculations were carried out at the incidence angles (0°, ± 10° and ± 20°), which is the configuration of the SKB inspection procedure. For the angular directions one of the two possibilities for each angle was calculated only, because the second one complies with a 180° rotation of the probe or the reflector respectively concerning the model. Hence all possible situations in reality (with the five angles mentioned above) can be simulated using only three calculated sound fields only. Some other sound field calculations have been performed in receiving mode when the reflector, which has to be located was positioned at alternative depths other than 60 mm. This was possible due to the dynamic possibilities (upon receiving the ultrasonic signals) of the SKB equipment, because SKB uses for the transmitting case always a focal depth of 60 mm and for receiving adapted to the real depth position. The model distinguishes between transmitting and receiving case in the same manner. Therefore all calculations with reflectors in 60 mm depth could be carried out using one sound field (the same for transmitting and receiving case), whereas two different sound fields had to be used for any other case.

The calculation of the different sound fields for the phased-array-probe used by SKB for each individual case was the basis of all further investigations. The calculated results could be used for the evaluation of the sound field itself and for the echo height calculations with the Echo 3D program as described in the next two chapters. In the next few figures the calculation results for the sound field with 0° incidence angle will be presented and is representative of all processed sound field calculations.

Figure 6-16 shows cross section pictures through the sound field with an incidence angle of 0° in and perpendicular to the plane of incidence. The picture size is about 80 mm considering the particular plane (plane of incidence/perpendicular plane of incidence) and about 75 mm in sound path direction.

Figure 6-17 shows an enlargement of the focus area in the sound field in two different manners. On the left side the presentation of the sound field itself is shown, whereas on the right side the echo height distribution considering a point reflector in the sound field is displayed. The last one can be used to determine the beam width or focus size (6 dB drop from maximum) in both represented planes taking effect in practise. Figure 6-17 shows that the beam width in the plane of incidence (focused plane) is 2 mm. In the plane perpendicular to it (unfocused plane) the beam width is 5 mm. The focus length in sound path direction can be determined to 21 mm.

The focus depth was defined in a depth of 60 mm based on optical focus laws. This point is called geometrical focus point (point of identical/equal phase). But because of the substantially bigger wavelengths in acoustics (with respect to optics) and the occurring interference effects the focus is not a single point but a focus area with the geometrical focus in the middle. Due to the influence of the distance law and the sound attenuation the amplitude values within this area decrease with increasing distance. For this reason the amplitude in a point closer to the transducer has a higher amplitude value than in the geometrical focus point. The location of this point depends on the relation between the distance law, the sound attenuation and the phase shift. This second point is called acoustical focus point and as one can see in Figure 6-17 it is located at a depth of 51 mm.

Nevertheless in the depth of 60 mm (geometrical focus depth) the sound amplitude reaches its local maximum and the sound amplitude in this depth cannot be increased using any other focus conditions.

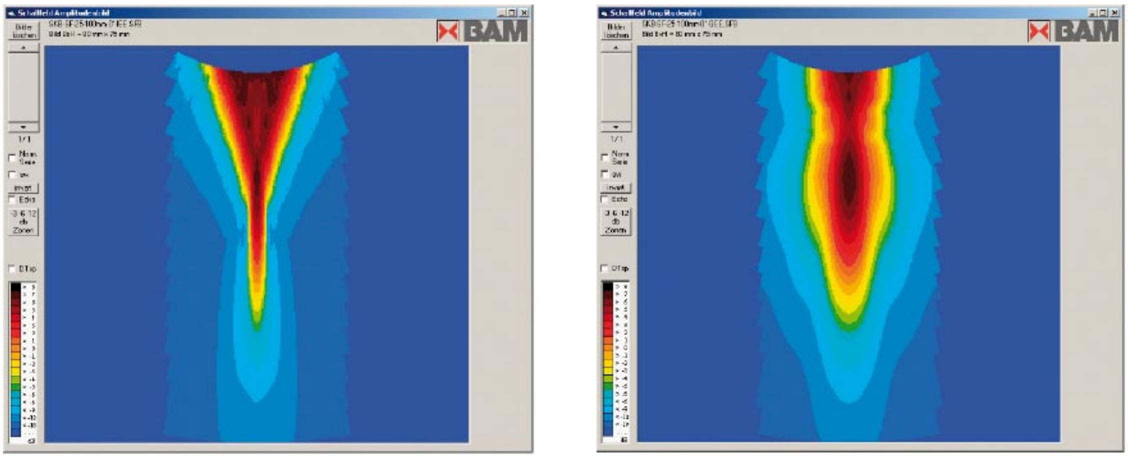

Sound field 0°, plane of incidence

Sound field 0°, perpendicular plane of incidence

Figure 6-16. *Cross sections through sound field with 0° incidence angle.*

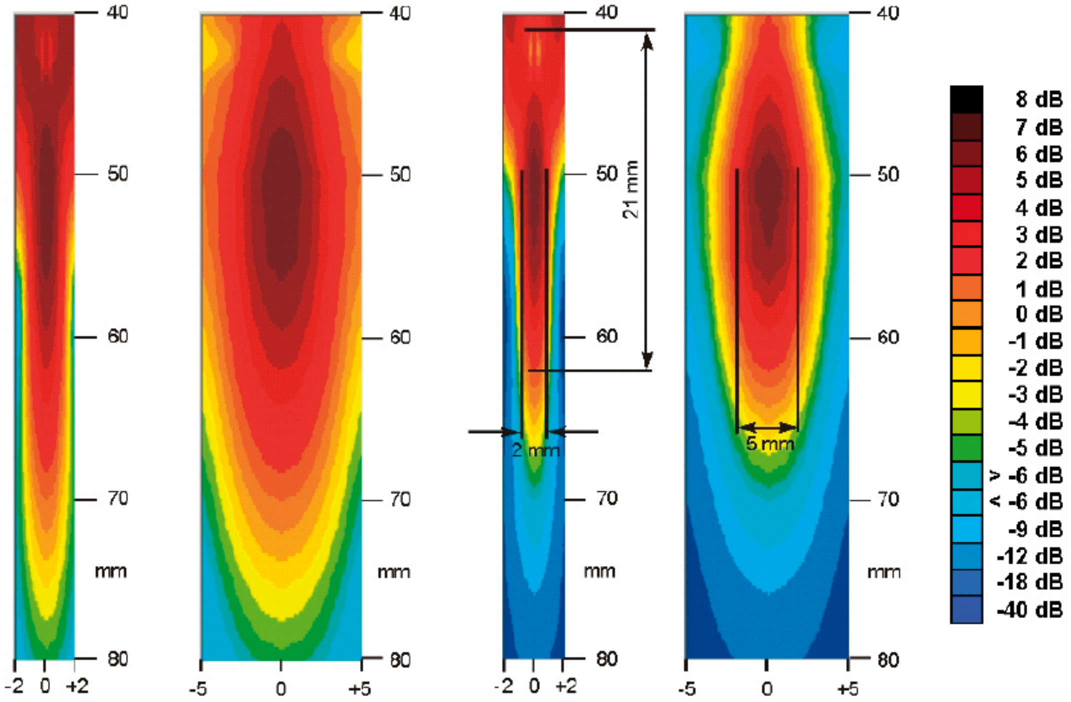

left: in plane of incidence
right: perpendicular to plane of incidence

Sound field presentation

left: in plane of incidence
right: perpendicular to plane of incidence

Echo height distribution

Figure 6-17. *Enlargement of focus area, sound-field presentation and echo height distribution.*

In Figure 6-18 the cross section-picture parallel to the transducer is shown in the acoustical focus depth in the same manner, on the left side for the sound field and concerning the echo height distribution on the right side.

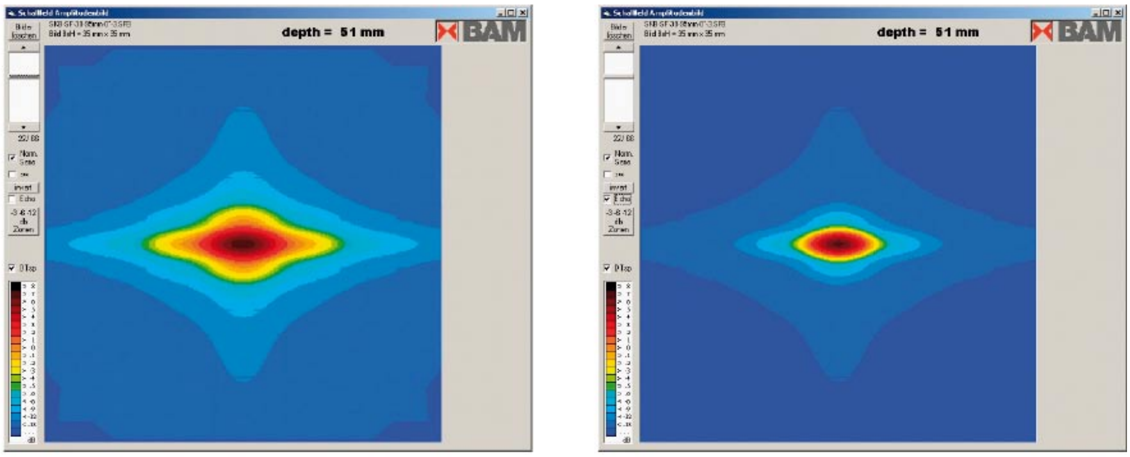

Sound field presentation

Echo height distribution

Figure 6-18. *Cross sections parallel to the transducer through 0° sound field in acoustical focus depth.*

Figure 6-19 illustrate cross section pictures through the 0° sound field parallel to the transducer in depths of 30, 40, 51 (acoustical focus), 60 (geometrical focus), 70 and 80 mm. Each picture represents an area of 35×35 mm^2. The amplitude values within all pictures are normalized with the maximum amplitude value reached in the acoustical focus point.

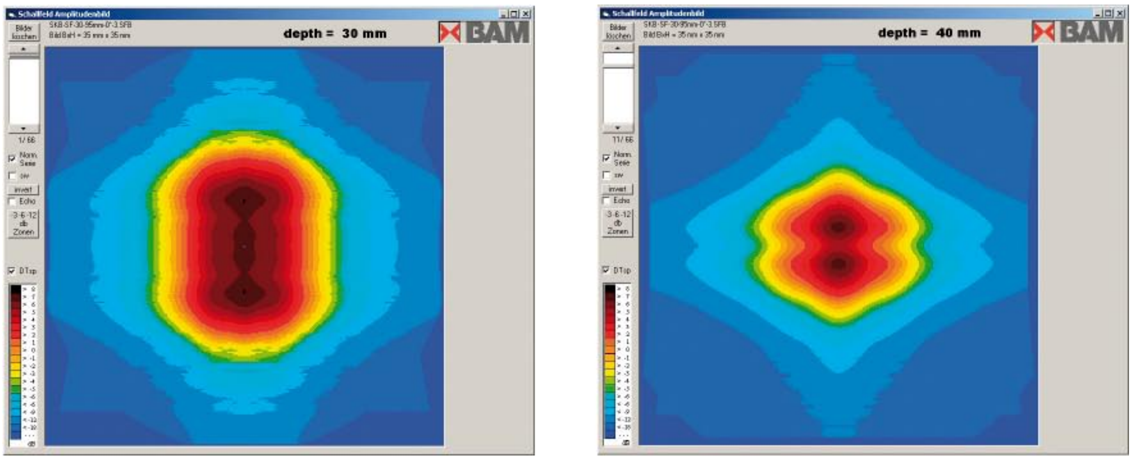

Depth: 30 mm

Depth: 40 mm

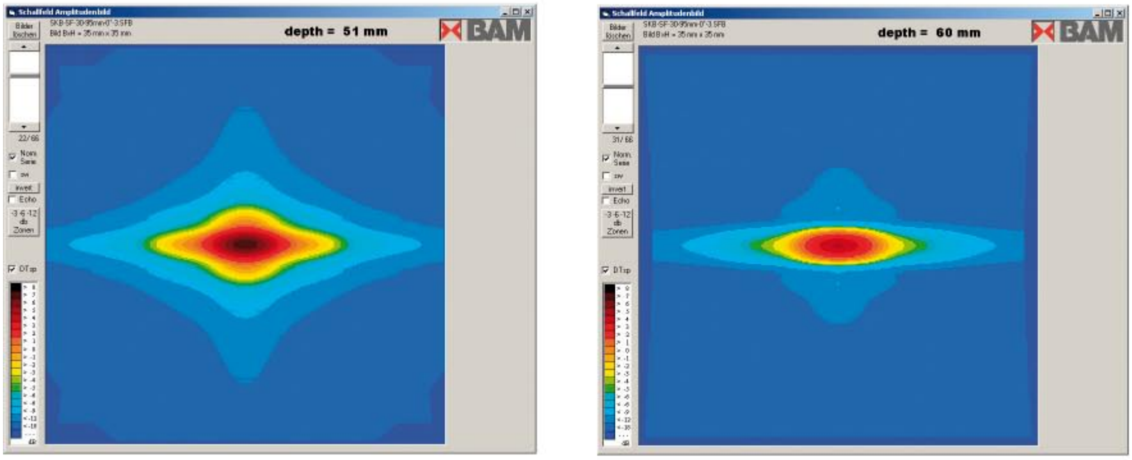

Depth: 51 mm (acoustical focus)

Depth: 60 mm (geometrical focus)

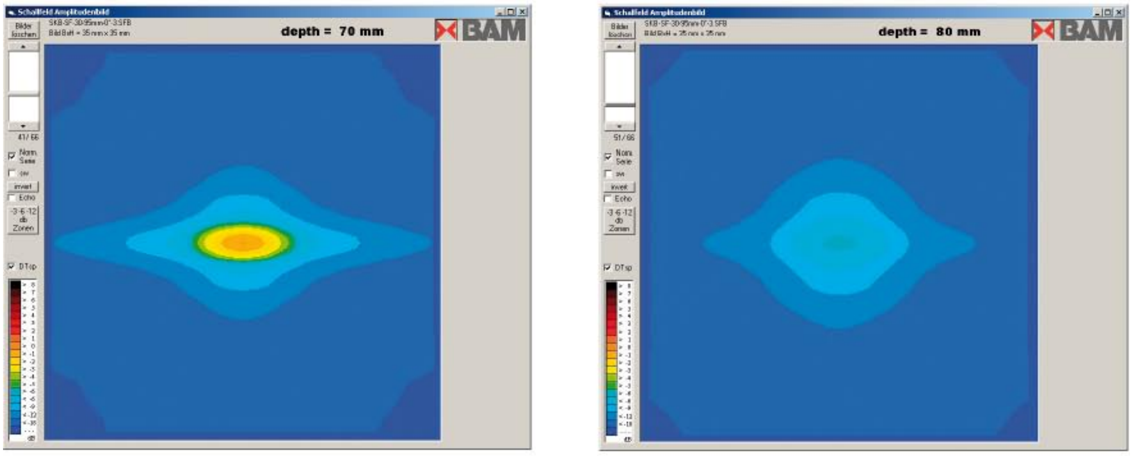

Depth: 70 mm

Depth: 80 mm

Figure 6-19. *Cross sections parallel to the transducer through sound field with 0° incidence angle.*

6.2.3 Modelling of several artificial flaw types

In assistance to the creation of POD curves concerning the measured data, especially for the joint-line-hooking-discontinuities, and the comparison between theoretical and measured echo heights computer simulations with different reflector geometries (reflector types) were carried out. The selection of reflectors was based on the knowledge of the possible occurring geometries ,see Figure 6-20, and were positioned at a depth of 60 mm, where echo indications from the joint-line-hooking-discontinuity had been found by SKB.

The individual reflector geometries will be presented in the following figures. The model has the capability to simulate various reflector geometries such as flat bottom holes, spherical and cylindrical reflectors as well as planar and curved rectangles.

As explained in the introducing paragraph to the modelling chapter the quasi-deterministic model yields for one flaw size one amplitude. In the reliability formula this would correspond to the very ideal left part of intrinsic capability only. To make it more realistic (including partially the AP factors) random noise was added. In a first attempt we added a scatter band of ± 3 dB which includes the repeatability from one scan to another, see e.g. Figure 6-31.

The calculations were processed for radial reflector sizes between 0.25 and 10 mm, so that the range of measured discontinuity sizes is generously included. For flat bottom holes, spherical reflectors and side-drilled holes the radial size is equal to their diameter. For all reflectors, except for the flat bottom hole and the spherical reflector, the width was assumed to be bigger than the sound field width in 60 mm depth. Under these conditions the amplitude will be independent from the reflector size in circumferential direction, because of the

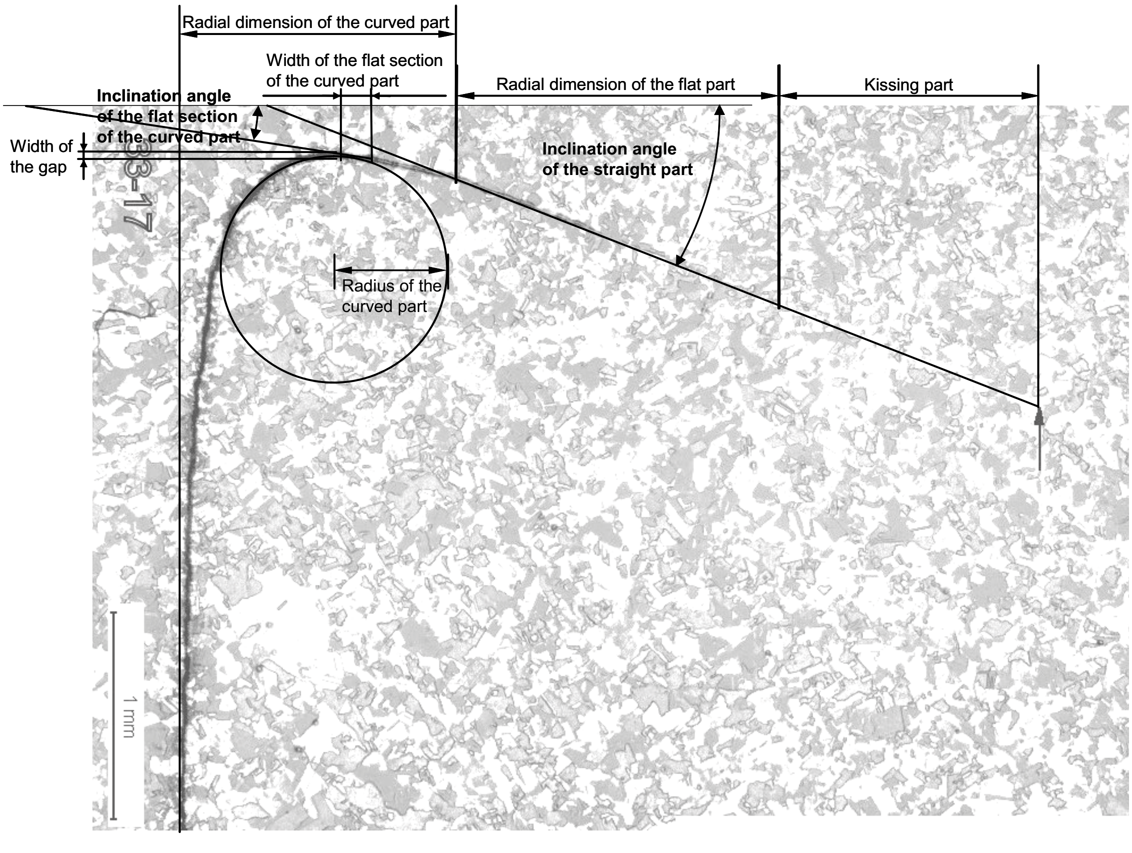

Figure 6-20. Cross section of a JLH with indications of the circular and straight par and its measurest.

occurring saturation effect. Some pre-calculations showed that a reflector width of 20 mm will safely fulfil the presupposition that the echo height does not rise if the reflector width is further increased. Under these conditions the echo height increase for specific reflector geometries is dependent on the radial reflector size only. The amplitude increase behaviour is certainly different if the various reflector geometries are compared.

In Figure 6-21 and Figure 6-22 the geometrical simulation of the flat bottom hole and the spherical reflector are presented. The transducer is on the top of the surface and the centre of the simulated reflectors lies in a depth of 60 mm under the centre of the transducer, thus the main beam is pointing to the reflectors centre also. Due to the specific reflector shapes the reflector sizes in the radial and circumferential directions are the same.

Figure 6-23 shows the geometrical simulation for a cylindrical reflector like a side drilled hole. The width of the cylinder was 20 mm and the radial sizes lay between 0.25 and 10 mm.

For the analysis of the occurring echo amplitudes at the beginning all incidence angles were used together, evaluating the maximum amplitude reached. A detailed investigation of the measured data and microsections concerning the joint-line-hooking-discontinuities yielded more information which has led to a new evaluation strategy for the joint-line-hooking-discontinuities. This strategy is based of the fact that the joint-line-hooking geometry, i.e. the curved part and the angle of the flat part, affects the echo height as well as the ultrasonic angle of incidence. Because of this fact the echo height evaluation has to be done individually for every incidence angle. Apart from this point of view the simulation of a reflector with a complex geometry like the joint-line-hooking is not necessary and the joint-line-hooking-discontinuity can be segmented into two parts (see Figure 6-24). One part can be described using a curved rectangle with a small radius (hooky part of joint-line-hooking); the second one can be described by a planar rectangle with an inclined orientation. The evaluation of all microsections had the result, that the radius of the first part lay approximately between 0.3 and 1.0 mm and that the inclination of the second part is about 70°.

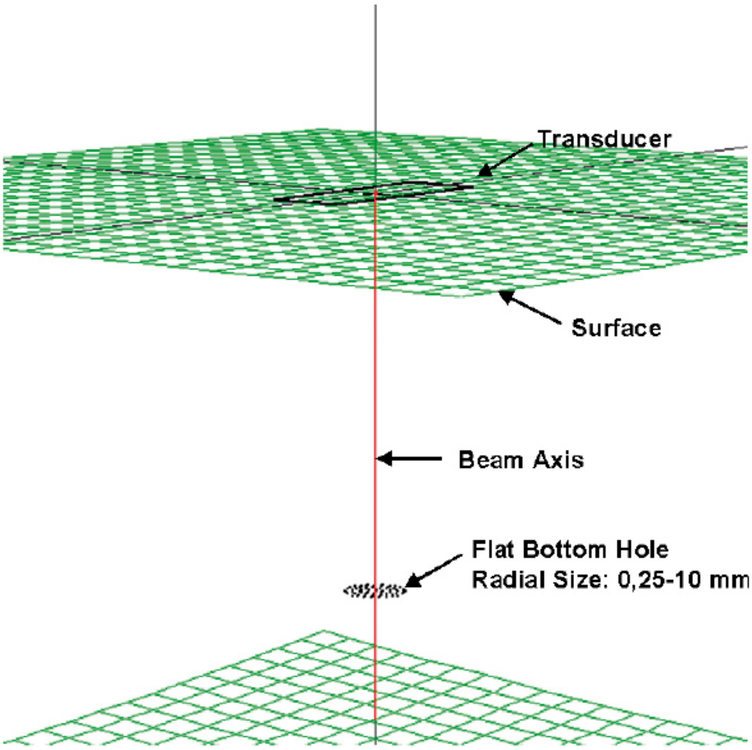

Figure 6-21. *Geometrical simulation of flat bottom holes.*

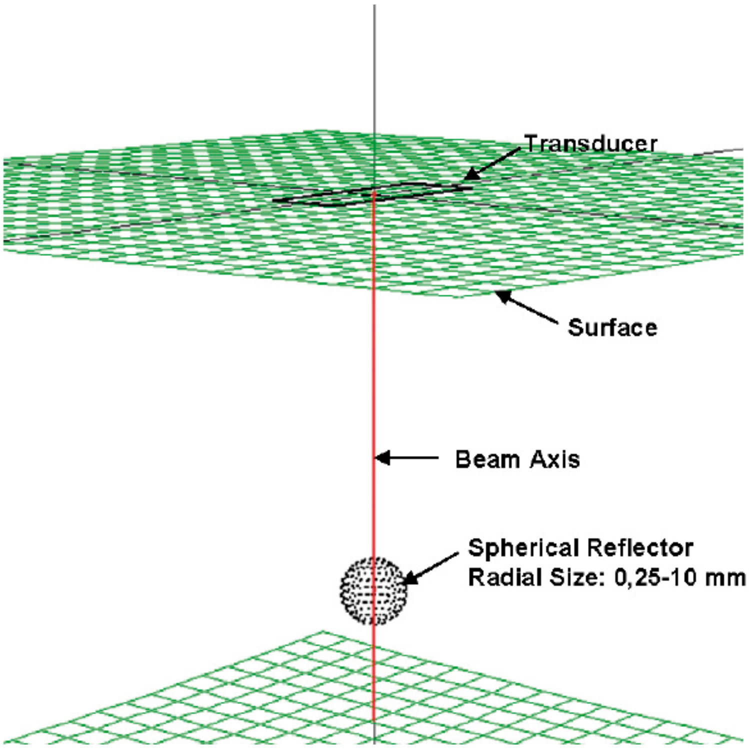

Figure 6-22. *Geometrical simulation of spherical reflectors.*

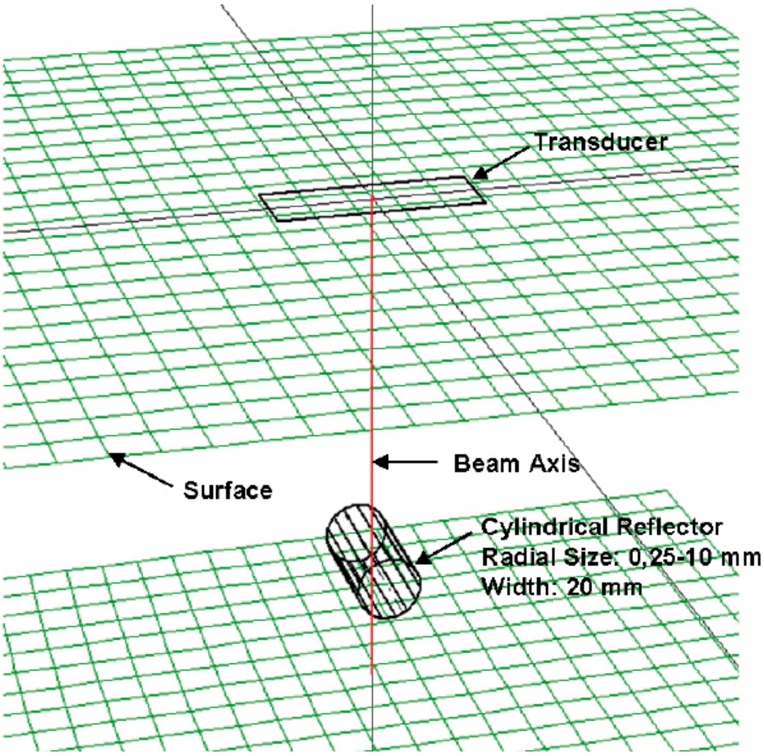

Figure 6-23. *Geometrical simulation of cylindrical reflectors.*

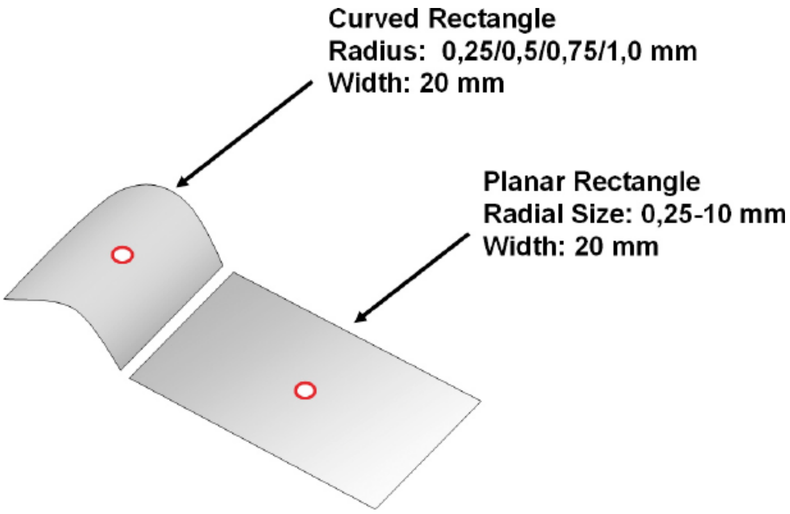

Figure 6-24. *Segmentation of joint-line-hooking-discontinuity in two parts.*

Curved rectangles as reference for the hooky part of the JLH

The curved rectangle sizes in the model are defined in circumferential direction along the rectangles surface. The minimal size for the calculation was 0.25 mm and was increased up to the point where the surface is spanning a circumferential size of 180° (see left side Figure 6-25). Because the radial size is the important value for the integrity of the canisters weld the circumferential sizes were converted into radial sizes after the calculation (see left side Figure 6-25). The curved rectangle geometry has been calculated for 0.25, 0.5, 0.75 and 1.0 mm radius, so that the spectrum of radii occurring in practise could be described.

In Figure 6-25 the geometrical simulation of a curved rectangle with a radius of 0.5 mm is presented. On the left side of Figure 6-25 the aforementioned circumferential sizes versus the radial sized are shown. The smallest circumferential size calculated was 0.25 mm, which corresponds to a radial size of 0.247 mm. The circumferential size then was increased up to 1.5 mm, which corresponds to a radial size of 0.997 mm. The reflector then spans a circumferential range of 180°. The situation for a curved rectangle with a radius of 1.0 mm is shown in Figure 6-26.

Figure 6-27 illustrates the calculated echo heights of the above mentioned reflector types up to radial sizes of 10 mm. All amplitude values are correlated with the echo height of a flat bottom hole with 2 mm diameter in 60 mm depth, which is used for the sensitivity adjustment in practice by SKB and is adjusted to 80% screen height.

An important conclusion from these calculations is that the curves of all reflector types are above the level of the curve for the flat bottom hole, except the curve for the spherical reflector, which is evident under this level. In other words these reflector types will give higher amplitude values when compared with a flat bottom hole of the same size. Furthermore one can see that the echo heights of all calculated reflectors are ≥ 80% screen height above a radial size of 0.4 mm. This shows the high sensitivity adjustment level for the inspection of the weld integrity, because such small reflectors are of no safety relevance. If ultrasonic behaviour of the real discontinuities is comparable with the theoretical simulated surfaces, one can conclude that the measurement sensitivity will be on a higher level.

Figure 6-27 shows that principally the amplitude values of all calculated rectangles are increasing with an increasing radial size. However, as theoretically expected this is not valid for arbitrarily large radial sizes. The amplitude values will increase until saturation is

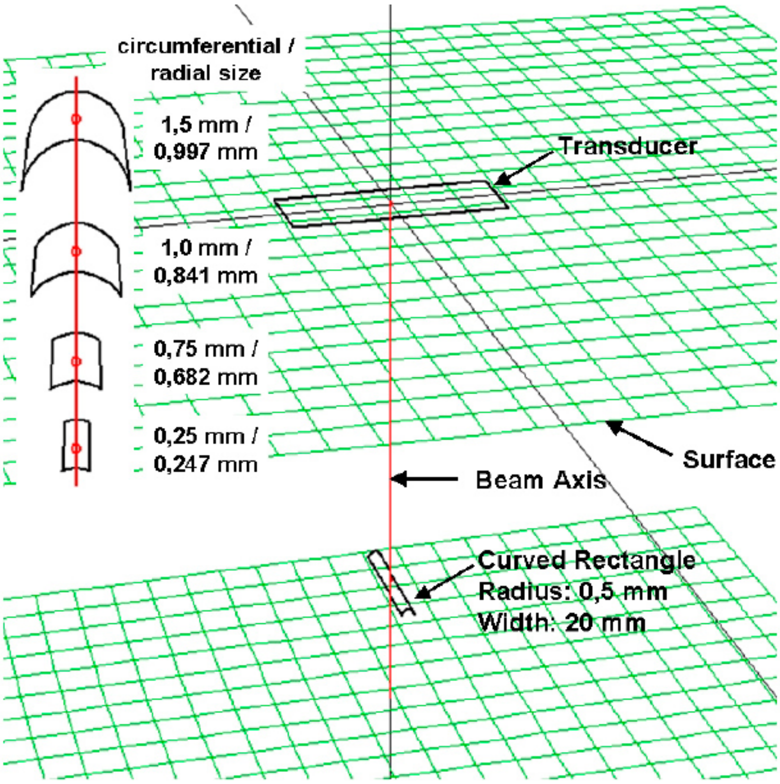

Figure 6-25. *Geometrical simulation of curved rectangles, radius 0.5 mm.*

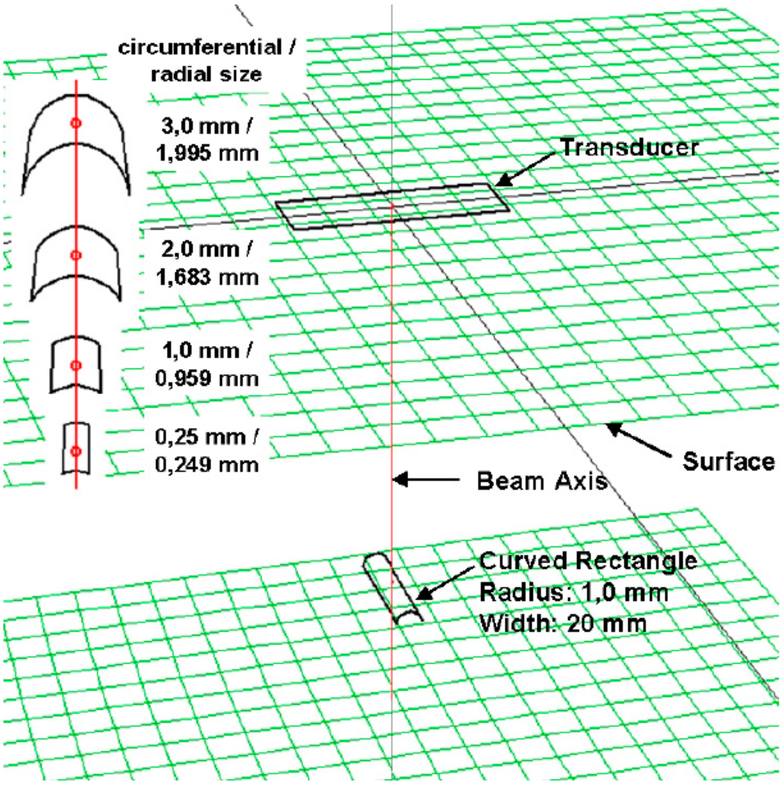

Figure 6-26. *Geometrical simulation of curved rectangles, radius 1.0 mm.*

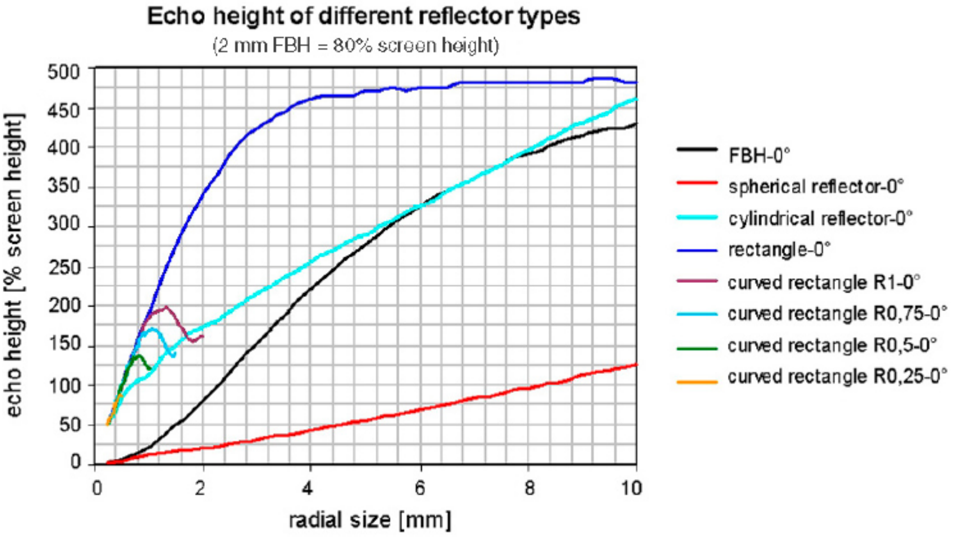

Figure 6-27. *Echo heights of different reflector types with radial sizes up to 10 mm.*

reached for each of the reflector geometries. An increase of the radial size will not result in higher amplitude values. The characteristic of the saturation effect depends on the geometrical conditions. Especially for the curved rectangles the saturation effect is already appearing for small radial sizes. Radial sizes above the maximum in the curve cannot be determined by evaluation of the amplitude value any more. A useful and reliable investigation of the radial size regarding only the amplitude value can just be performed in the region of the curves where an increase in echo height is expected.

Regarding the measured data points of the JLH the hooky part achieved the highest amplitude for angles of incidence of 0° and –10° in most of the cases. Therefore calculations for curved rectangles with these two angles of incidence were carried out. The curved rectangles had radii from 0.25 up to 1.0 mm as mentioned above. As examples the calculations for curved rectangles with radii of 0.5 and 1.0 mm are presented in the following figures. The Figure 6-28 to Figure 6-31 displays one calculated curve (black curve) and the ± 3 dB fluctuation margin (red curves).

The fluctuation value of about ± 3 dB has been determined out of the measured data points from two data files from SKB measured under the same conditions, with an amplification difference of 9 dB only. The echo height difference between the same data points in the two files shall be 9 dB, but in cause of mechanical drift, coupling loss etc. this difference will fluctuate around this value depending on the environment conditions. The evaluation of the available data points leads to the fluctuation mentioned above, which lies in the magnitude expected for an automatic measurement system. The complete calculation result will be used in Section 6.2.4 for the comparison with the measured data.

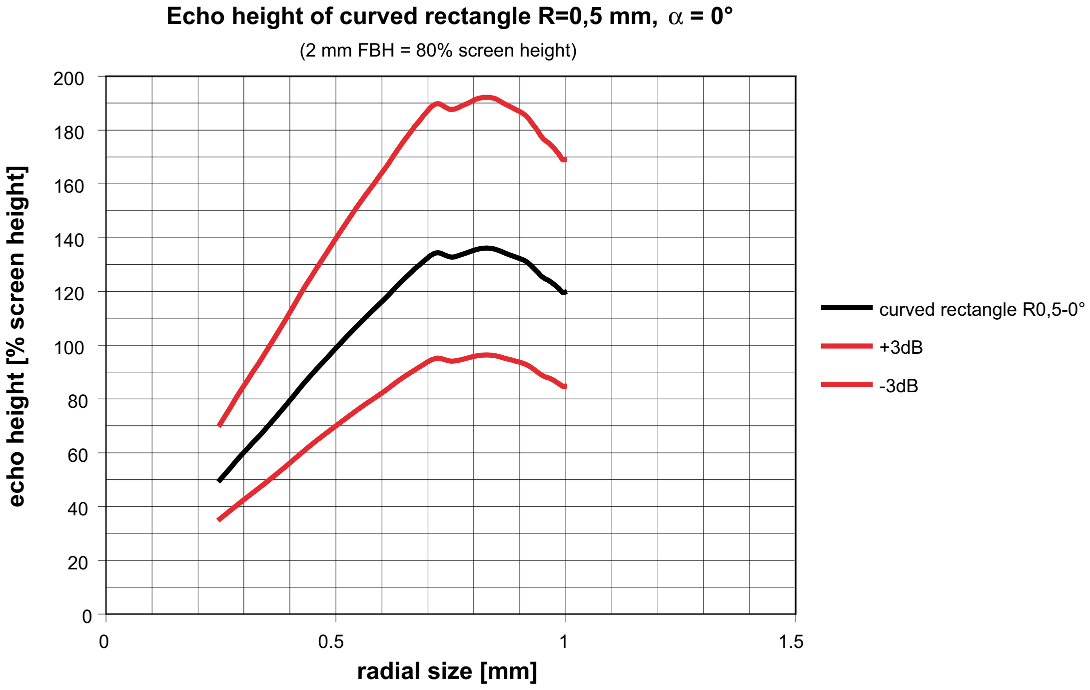

Figure 6-28. *Echo height of a curved rectangle with radius 0.5 mm,* α = *0°.*

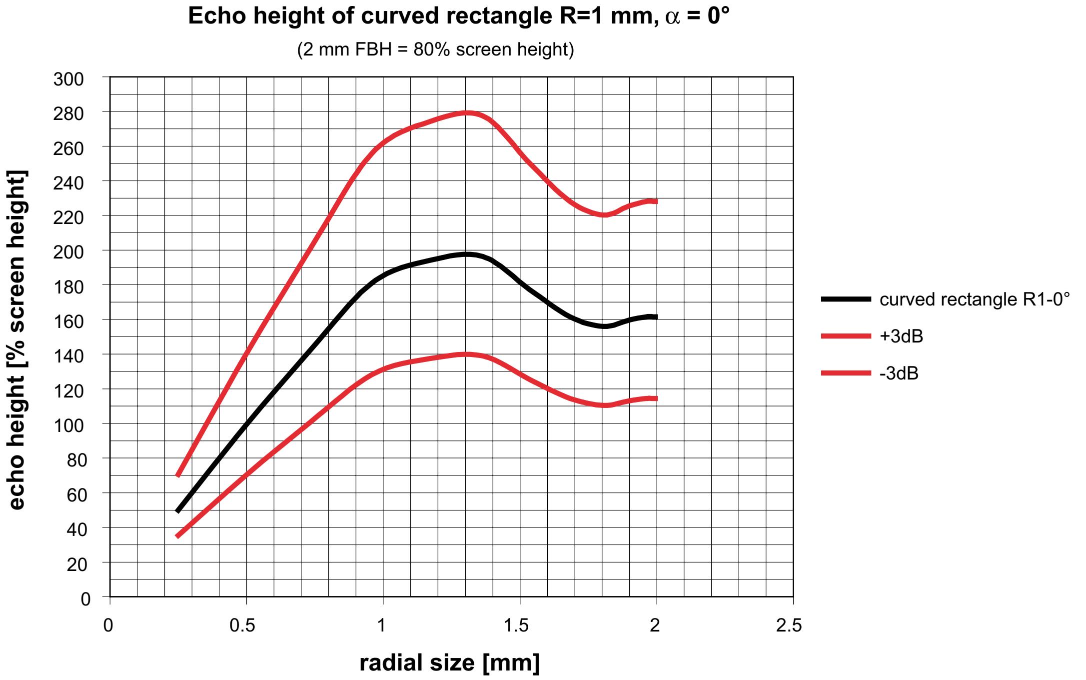

Figure 6-29. *Echo height of a curved rectangle with radius 1.0 mm,* α = *0°.*

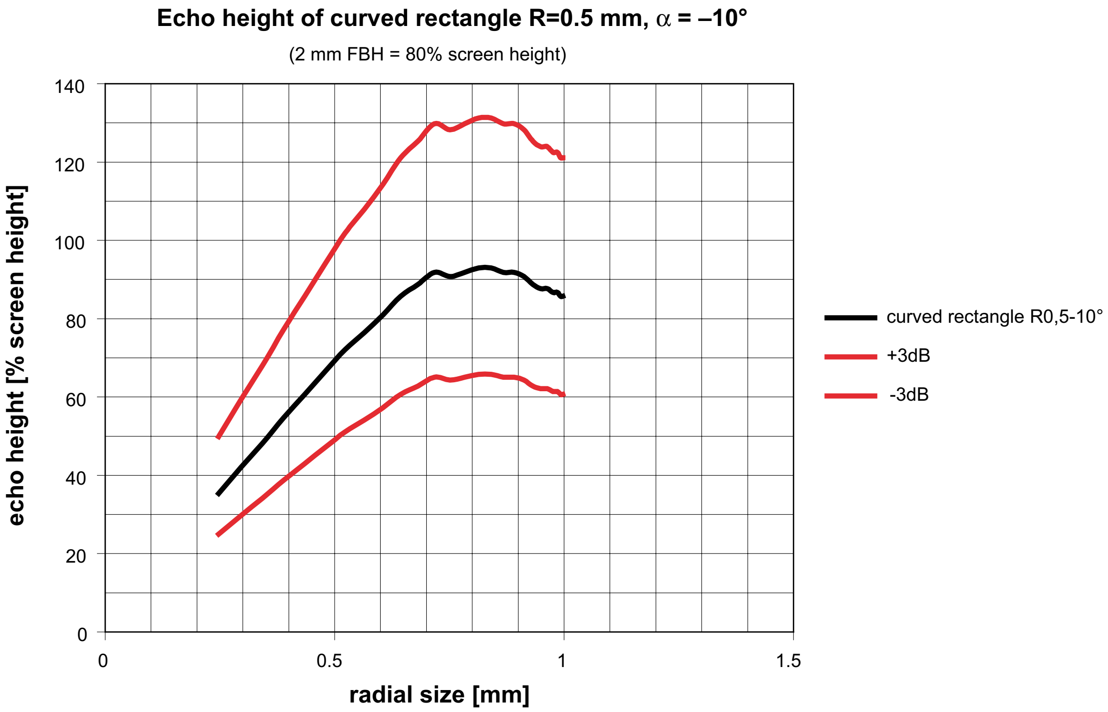

Figure 6-30. *Echo height of a curved rectangle with radius 0.5 mm,* α *= –10°.*

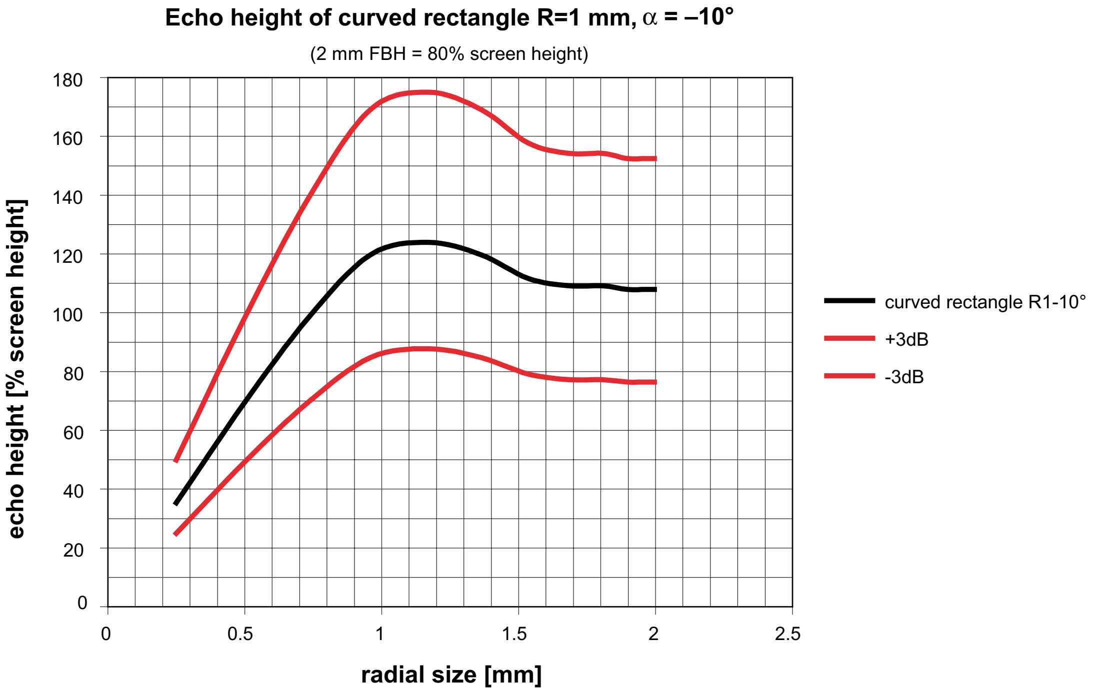

Figure 6-31. *Echo height of a curved rectangle with radius 1.0 mm,* α *= –10°.*

Planar rectangles as reference for the planar part of the JLH

The geometrical simulation of different inclined rectangles is shown in the next three figures. These planar rectangular reflectors were calculated as reference for the planar part of joint-line-hooking-discontinuities (see Figure 6-20 and Figure 6-24).

The modelling results for the planar rectangles are represented in Figure 6-35. A comparison of the curves for the inclined rectangles with the curve for the FBH in Figure 6-35 show that only the curves for the 90° and 80° orientated rectangles with incidence angles of 0° and 10° lie above the FBH curve for all radial sizes up to 10 mm. For the other curves this is true in a restricted area only. For the 70° orientated rectangle ($\alpha = 20°$) the crossing point of the two curves is located at a radial size of 5.25 mm. Concerning the two curves with about 10° difference (assumed mismatch) between the rectangle orientation and the incidence angle (80° orientated rectangle, $\alpha = 20°$ and 70° orientated rectangle, $\alpha = 10°$) the crossing points lie at radial sizes of 3.25 mm and 3 mm.

Because of the considered small reflector sizes the directivity pattern of the reflectors is broad and a small mismatch (e.g. of 10°) between the reflector orientation and the incidence angle will not cause a high loss of the echo height. A stronger effect on the echo height is the influence of the sound path length because of the high sound attenuation value in the copper. For example the curve for the 70° orientated rectangle with 10° mismatch concerning the incidence angle lies above the curve for the 70° orientated rectangle with 20° incidence angle up to a radial size of 1.6 mm. This is because of the stronger influence of the shorter sound path. Above radial sizes of 1.6 mm the directivity pattern will be narrower and becomes a more relevant influence on the echo height, than the sound attenuation value alone.

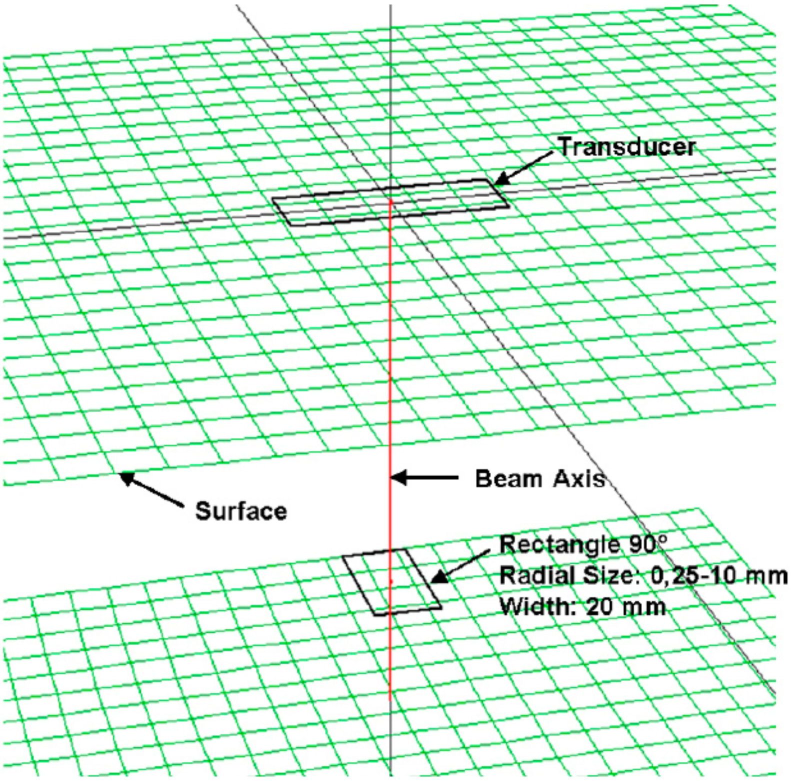

Figure 6-32. *Geometrical simulation of 90° orientated rectangles.*

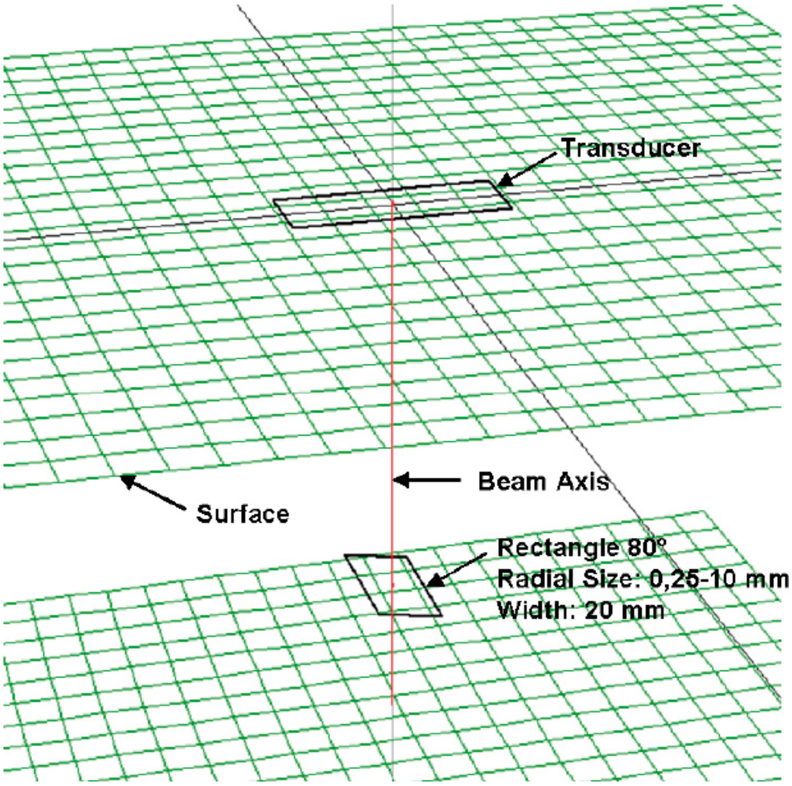

Figure 6-33. *Geometrical simulations of 80° orientated rectangles.*

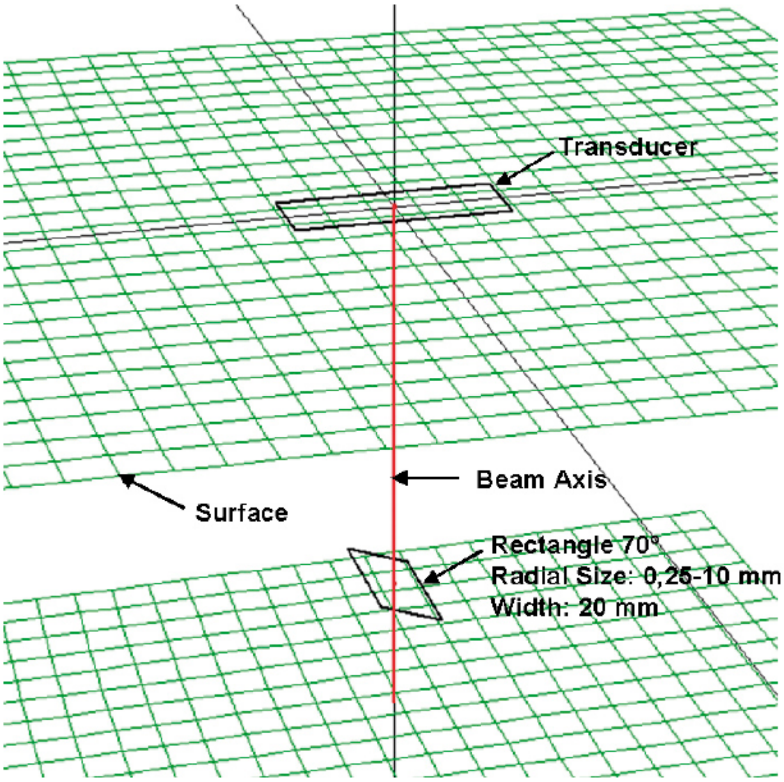

Figure 6-34. *Geometrical simulations of 70° orientated rectangles.*

Summing up one can say that for the area of interest (radial size for the planar part of the JLH up to 3 mm) the curves for the rectangles are generally higher than the curve for the FBH. Concerning the echo amplitude used for the sensitivity adjustment of the 2 mm flat bottom hole in 60 mm depth one can conclude the following. The echo heights of the calculated rectangles reaches ≥ 80% screen height at different radial sizes, depending on the rectangles orientation due to the main beam and the incidence angle of the probe. As can be seen in Figure 6-35 all calculated rectangles are ≥ 80% screen height for a radial size above 0.8 mm. Hence this leads to the same conclusion as for the other reflectors above, this reflector size is of no safety relevance and the high inspection sensitivity for these reflector geometries is implied in the inspection procedure. In the case where the saturation effect discussed is used as single criteria for the size estimation using the echo amplitude evaluation is only possible in a limited radial range. The curves for the three orientated rectangles (black, red and dark blue curve) perpendicular to the beam axis can be evaluated to at least a radial size of 3 mm, whereas the curve for the 80° orientated rectangle with 20° incidence angle and the 70° orientated rectangle with 10° incidence angle is already increased to the saturation value at about 1.6 mm radial size.

6.2.4 Comparison between the calculated and the measured data for the JLH

In this chapter the calculated data for the JLH is compared with the measured data points. The JLH discontinuity was segmented into two parts, as shown above (Figure 6-20 and Figure 6-24), because of the dependency of the amplitude values from the angle of incidence. First the comparison for the curved part of the JLH will be presented.

The investigation of the cross section pictures from the JLH discontinuities resulted in a bandwidth of 0.32 up to 1.00 mm radius for the curved part in the JLH. Hence curved rectangles with radii of 0.25, 0.5, 0.75 and 1.0 mm were calculated. As angles of incidence 0° and –10° were concerned, whereby the last angle of –10° would result in the same data for +10° for the model. In the next eight figures the results for these calculations are presented together with the corresponding measured data points.

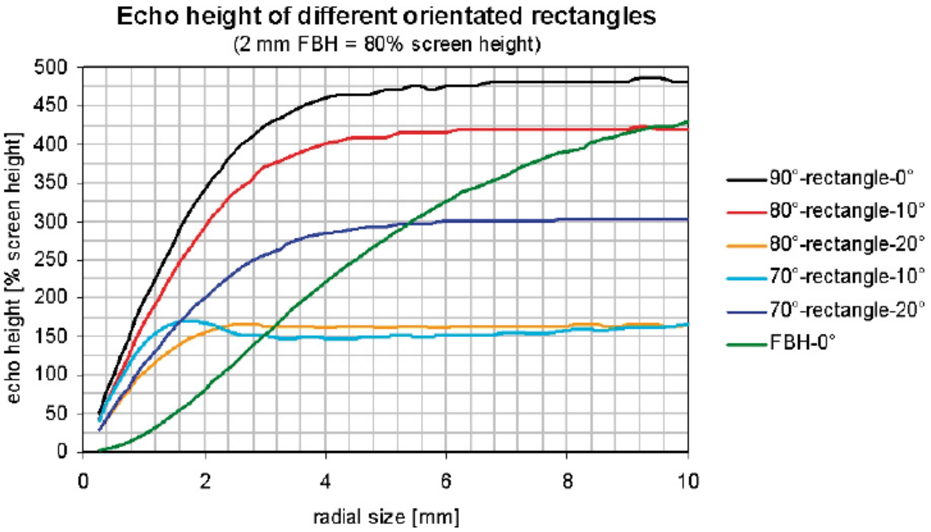

Figure 6-35. *Geometrical simulations of 70° orientated rectangles.*

All available data points were divided into four groups with a different bandwidth for the radii as shown in Table 6-2.

Some of the data points lie outside the calculated radial size spread for the considered theoretical reflector (see e.g. Figure 6-36 data point 36 –1.5 and 27 –5.5). For these cases the categorization has to be thought over. The amplitude values of many of the data points which fit the correlating radial sizes of the assumed reflector lie within the bandwidth expected by the calculation. Some data points lie outside this area with higher or lower amplitudes respectively. An investigation of the cross section pictures for the group with radii between 0.625 and 0.875 mm tries to give some explanations for these outlying data points (see Table 6-3). The main reasons for the stronger fluctuation of the amplitude values are the following:

Some reflectors have flat parts at the surface under different angles, so that the corresponding angle of incidence will reach higher amplitude values. Other effects like a bumpy or intercepted surface will decrease the amplitude for an affected angle of incidence.

The comparison between the calculated and the measured data shows that the description of the curved part of the JLH with a curved rectangle as been done in this case is valid in principle.

Table 6-2. Radius bandwidth groups.

Group	Radius bandwidth	Corresponding calculated radius
1	0.125 – 0.375 mm	0.25 mm
2	0.375 – 0.625 mm	0.50 mm
3	0.625 – 0.875 mm	0.75 mm
4	0.875 – 1.125 mm	1.00 mm

Table 6-3. Explanations for the amplitude deviations between modeling and measurement for the curved part of the JLH (Group 3; 0.625–0.875 mm).

Notation	Radius (mm)	Radial size (mm)	Echo height with 0°	Echo height with 10°	Echo height with –10°	Remarks
25-20.5	0.73	1.09	normal	normal	normal	Flat part at the top 0°
27-24	0.84	1.68	high	high	high	Flat part at the top 0°, radial size outside this radius group
27-31	0.66	1.08	low	low	low	Intercepted at the top, quick disappearing
28-19	0.68	1.24	high	high	high	Smooth surface, flat part at the top 0°
28-26	0.81	2.05	low	low	low	Bumpy surface, small slit, kissing effect
33-17	0.62	1.28	high	high	low	Wide slit, smooth surface, flat part at the top 10°
35-24	0.64	1.74	high	high	high	Smooth surface, flat part at the top 9°, radial size outside this radius group
36-17	0.62	1.04	normal	high	normal	Smooth surface, flat part at the top 10°
36-26.5	0.64	0.89	low	normal	normal	Bumpy surface at the top 0°, intercepted, flat part at the top 11°
41-21.5	0.68	1.01	normal	high	normal	Smooth surface, flat part at the top 10°

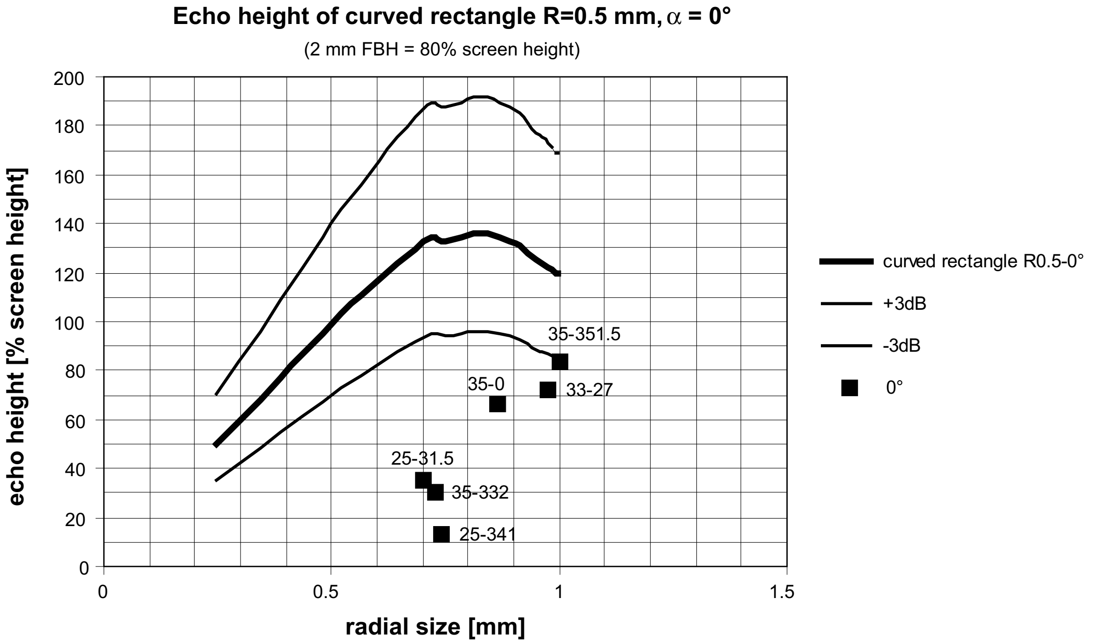

Figure 6-36. Comparison of curved rectangle R = 0.25 mm, α = 0° and corresponding measurement points.

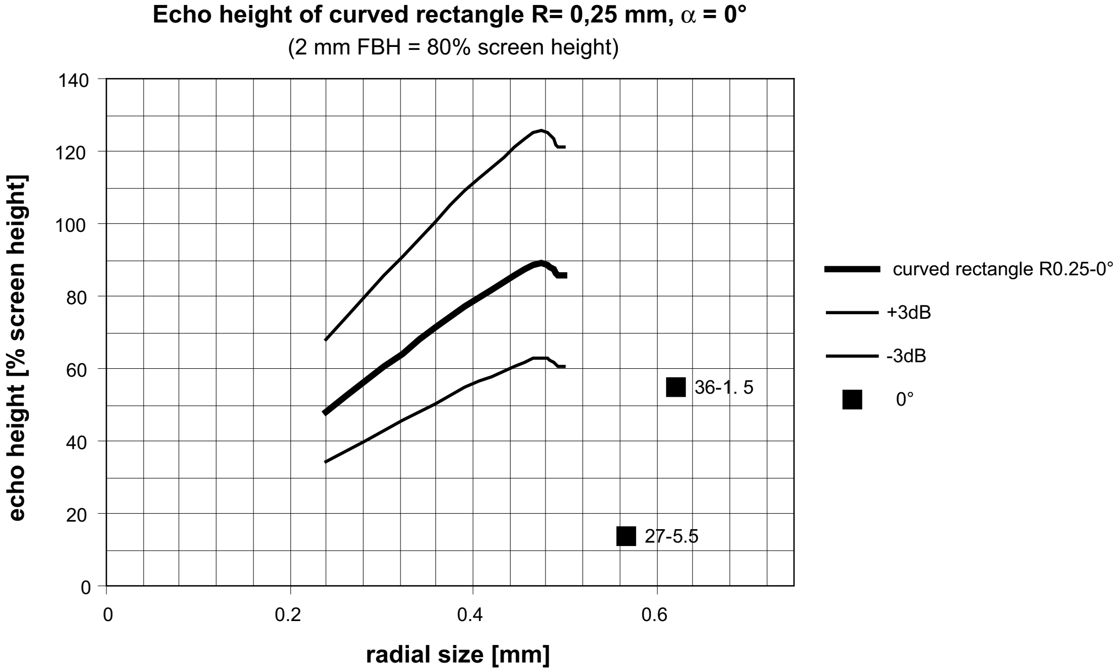

Figure 6-37. Comparison of curved rectangle R = 0.5 mm, α = 0° and corresponding measurement points.

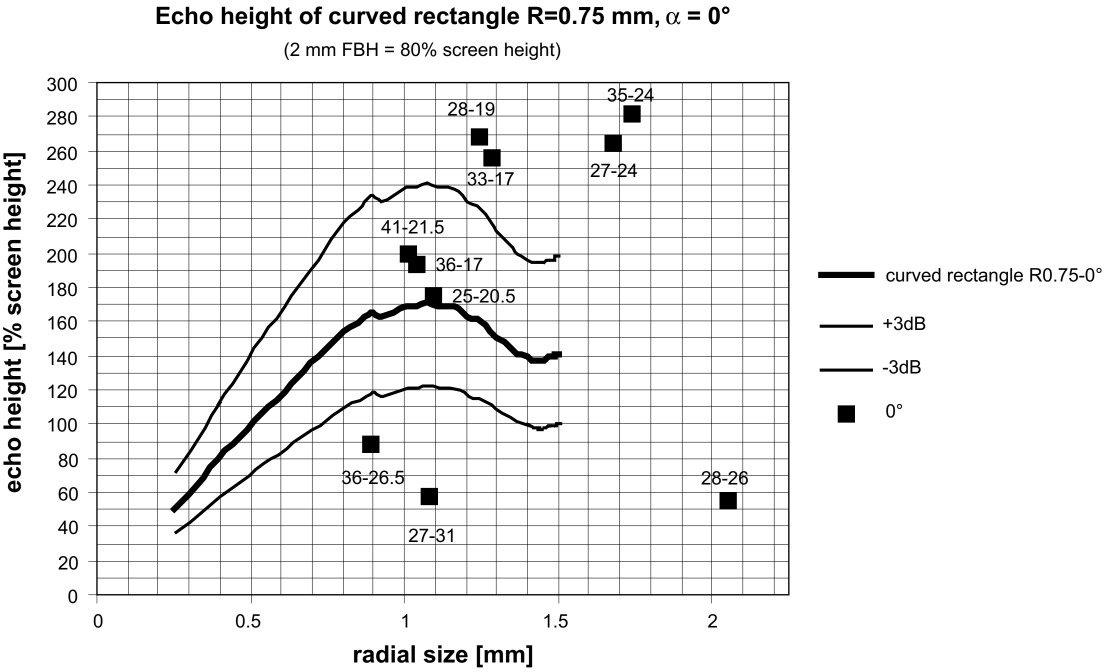

Figure 6-38. Comparison of curved rectangle R = 0.75 mm, α = 0° and corresponding measurement points.

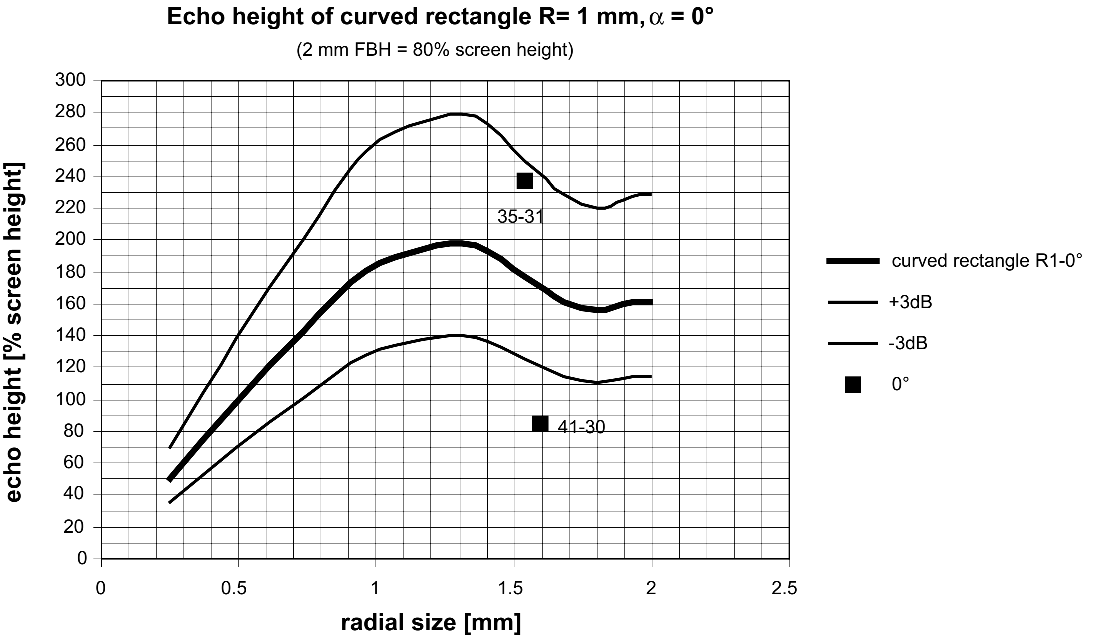

Figure 6-39. Comparison of curved rectangle R = 1.0 mm, α = 0° and corresponding measurement points.

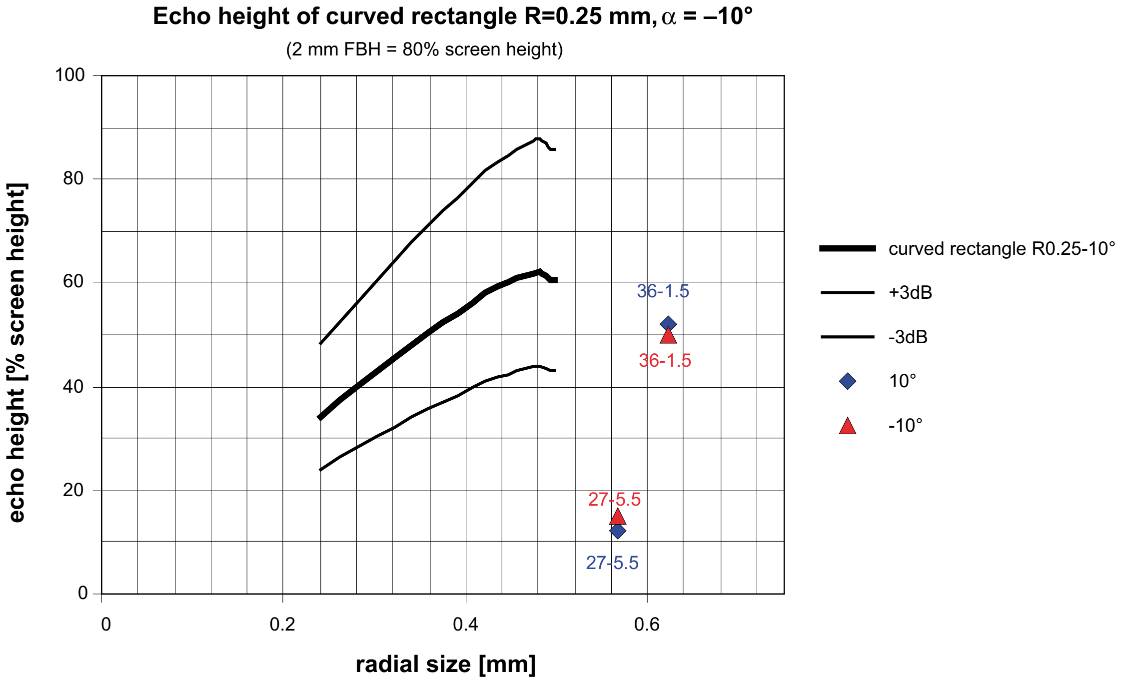

Figure 6-40. Comparison of curved rectangle R = 0.25 mm, α = –10° and corresponding measurement points.

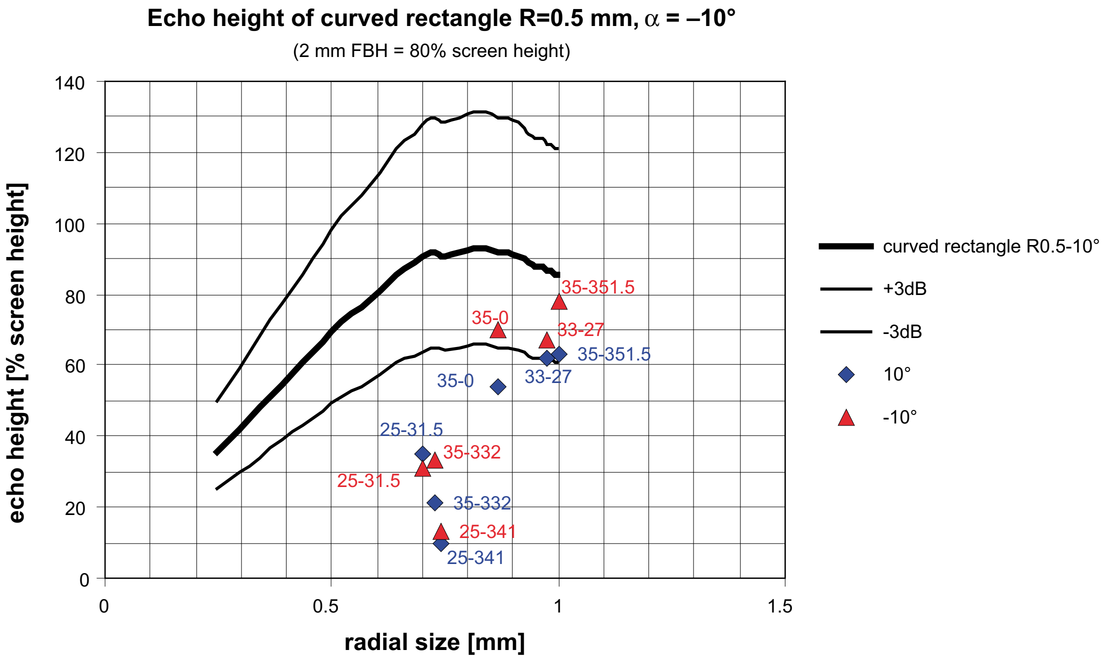

Figure 6-41. Comparison of curved rectangle R = 0.5 mm, α = –10° and corresponding measurement points.

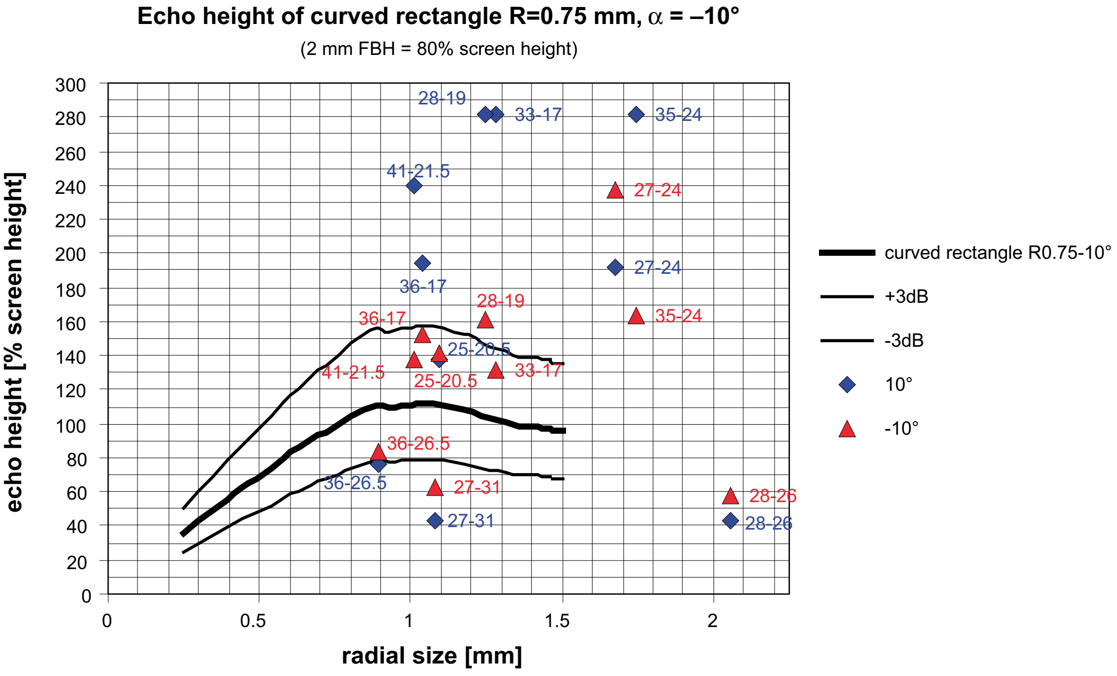

Figure 6-42. *Comparison of curved rectangle R = 0.75 mm, α = –10° and corresponding measurement points.*

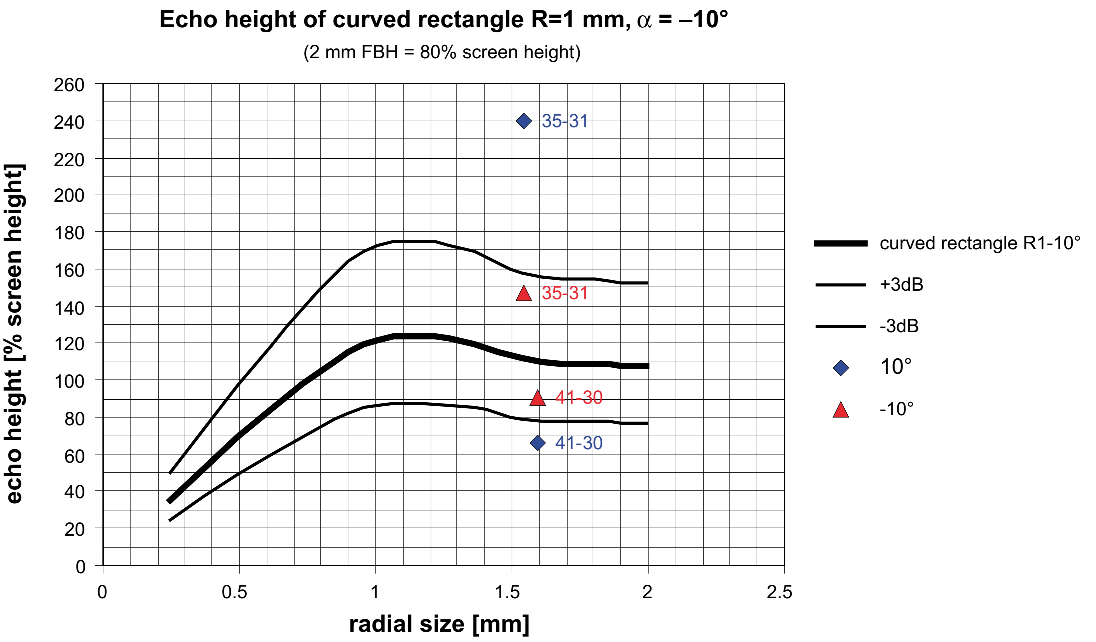

Figure 6-43. *Comparison of curved rectangle R = 1.0 mm, α = –10° and corresponding measurement points.*

Figure 6-44 shows the comparison between some measurement data points for angles of incidence of 10° and 20° with the modelled data for the 70° orientated rectangle under the same angles of incidence. One can see that there exist several measurement points, which are in good agreement to the modelled data. But nevertheless there is a tremendous part of measurement points with significant lower amplitude values compared to the model. The investigation of the corresponding data files shows that all these discontinuities have a circumferential extension above 20 mm, which was assumed for the model calculations. Hence the circumferential size is no criteria for the smaller amplitude values.

Bigger effects are to be expected from the geometrical differences and abnormalities of the various discontinuities. One influence can be expected from the kissing-bond-effect, because this would decrease the amplitude value. Therefore in Figure 6-45 the radial sizes of the flat part in the joint-line-hooking are reduced by the part of the kissing-bond-effect, which was estimated in the cross section pictures see Figure 6-47. Reducing the radial size moves the measurement points to the left and the deviation of some of them will decrease a little bit. Anyhow there still remain many data points under the calculated amplitude level.

An investigation of the cross section pictures of the JLH leads to the explanations for the amplitude deviations between the model and the measurement in Table 6-4. In Table 6-4 the echo height behaviour in the measurement is compared with the modelled data, concerning a fluctuation of ± 3 dB, for the angles of incidence of 10° and 20°. The comparison distinguishes between low, normal and high amplitudes. In the column for the remarks we made an effort to explain the differences. There could be found reasons for most of the measurement points. The greatest influences are caused by interceptions of the slit, small slit widths, flat parts at the top of the JLH with an angle around 10° and a quick disappearing interface with an angle about 20°. The simulated inclined rectangular reflector is shown in Figure 6-33 whereas the phenomenon "quick disappearing" can be observed in the two upper cross sections of Figure 6-46. In some cases the orientation of the flat part of the JLH, which differs between 17° and 25°, will be responsible. These parameters work together in a very complex way, so it is not possible to derive one or a few basic rules for a reliable description of the echo height behaviour of the JLH effect at the moment.

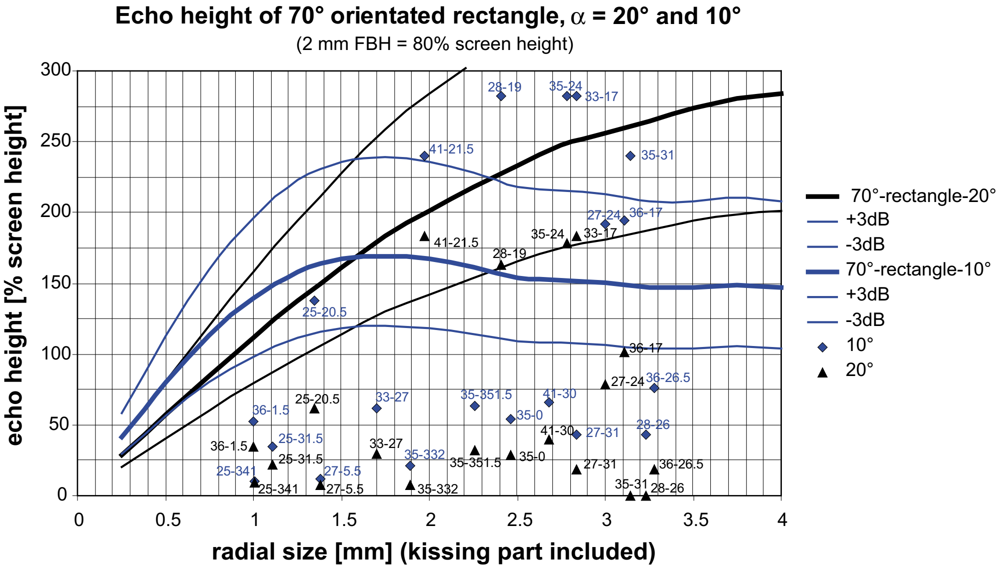

Figure 6-44. Comparison of 70° orientated rectangle, α = 10°/20° and corresponding measurement points.

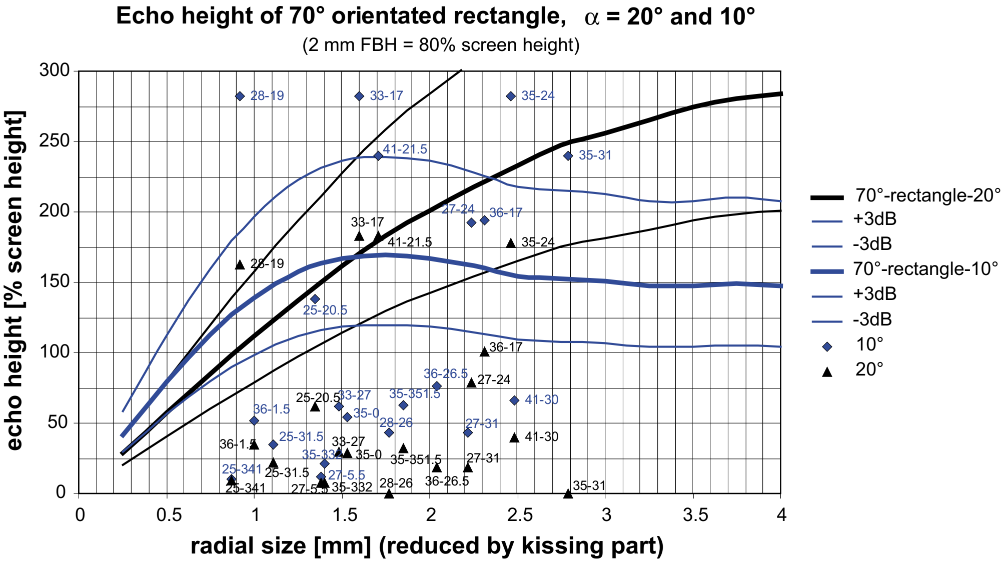

Figure 6-45. Comparison of 70° orientated rectangle, α = 10°/20° and corresponding measurement points, radial size reduced by kissing bond part.

Table 6-4. Explanations for the amplitude deviations between modeling and measurement for the flat part of the JLH.

Notation	Angle of flat part (°)	Reduced size (mm)	Slit width (mm)	Echo height with 10°	Echo height with 20°	Remarks
25-20.5	17	1.35	0.01	normal	low	Quick disappearing for 20°
25-31.5	21	1.11	0.03	low	low	Intercepted, quick disappearing
25-341	22	0.87	0.03	low	low	Intercepted, quick disappearing
27-5.5	25	1.38	0.03	low	low	Angle 25°, quick disappearing
27-24	18	2.24	0.03	normal	low	Not explicable at the moment
27-31	18	2.22	0.01	low	low	Quick disappearing
28-19	18	0.92	0.03	high	high	Smooth surface, flat part at the top
28-26	19	1.77	0.01	low	low	Smooth surface, small slit, kissing effect
33-17	22	1.60	0.04	high	normal	Wide slit, smooth surface, flat part at the top 10°
33-27	21	1.48	0.03	low	low	Quick disappearing
35-0	21	1.53	0.01	low	low	Quick disappearing, small slit, kissing effect
35-24	19	2.46	0.01	high	normal	Smooth surface, flat part at the top 9°
35-31	20	2.79	0.01	high	low	Small slit, flat part at the top 11°, kissing effect
35-332	20	1.40	0.03	low	low	Quick disappearing, kissing effect
35-351.5	20	1.85	0.03	low	low	Quick disappearing, kissing effect
36-1.5	23	1.00	0.03	low	low	Intercepted, quick disappearing
36-17	20	2.31	0.03	normal	low	Flat part at the top 10°, then quick disappearing
36-26.5	20.5	2.04	0.03	low	low	Intercepted, flat part at the top 11°, quick disappearing
41-21.5	18	1.71	0.03	normal	normal	Smooth surface, flat part at the top 10°
41-30	18	2.48	0.01	low	low	Small slit, 10° not explicable at the moment, quick disappearing for 20°

However the flat part of the JLH can be described with oblique orientated rectangles as shown above. The amplitude values of real JLH discontinuities are commonly smaller than the calculated echo heights, because of the abnormalities in their geometries.

The effects, which influence the amplitude values of the JLH discontinuities, are better understood at this point. Several effects are determined, but nevertheless there is complex conjunction and interaction cannot be described at this state of knowledge with a reliable rule. In addition some of the effects cannot be investigated “only” using non-destructive testing methods but an extended analysis e.g. of microstructure, micro roughness and anisotropy of the material would be necessary.

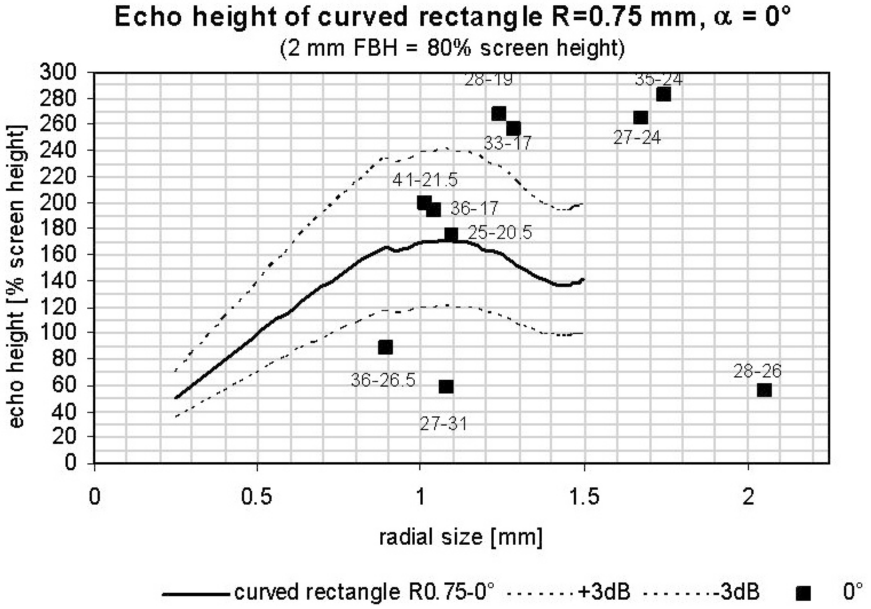

Figure 6-46. Echo height of curved rectangle R = 0.75 mm, α = 0°.

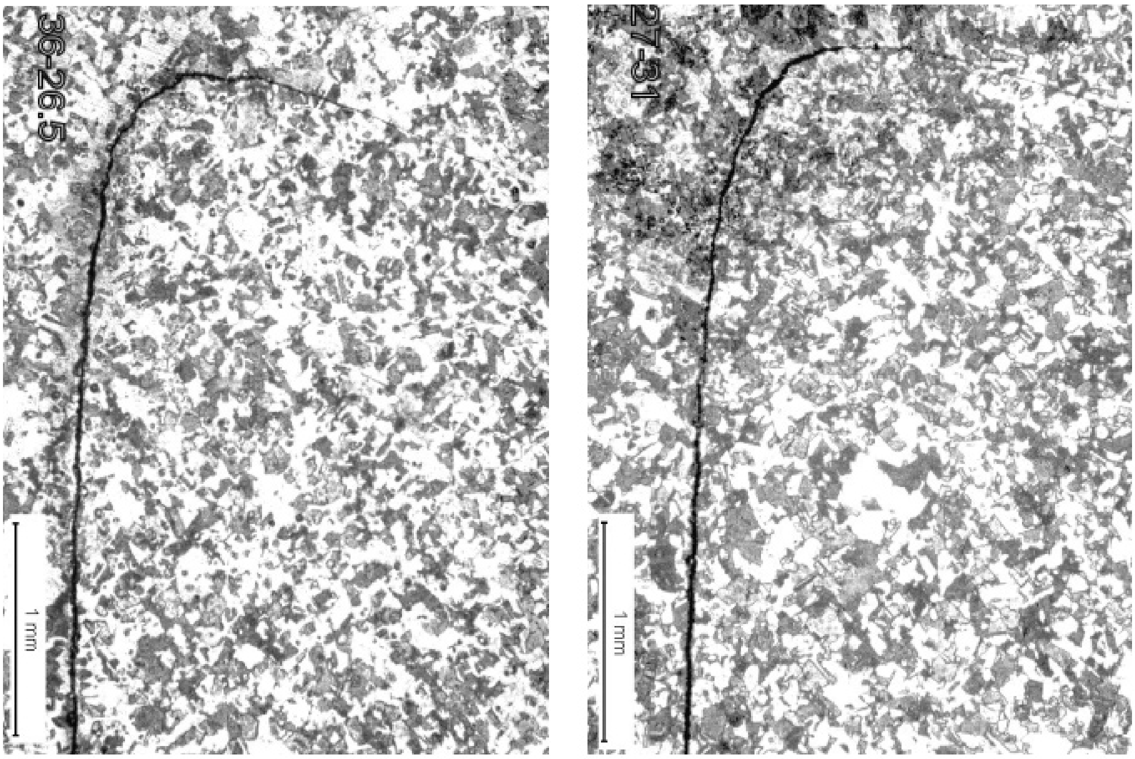

FSW 36-26.5 low amplitude

FSW 27-31 low amplitude

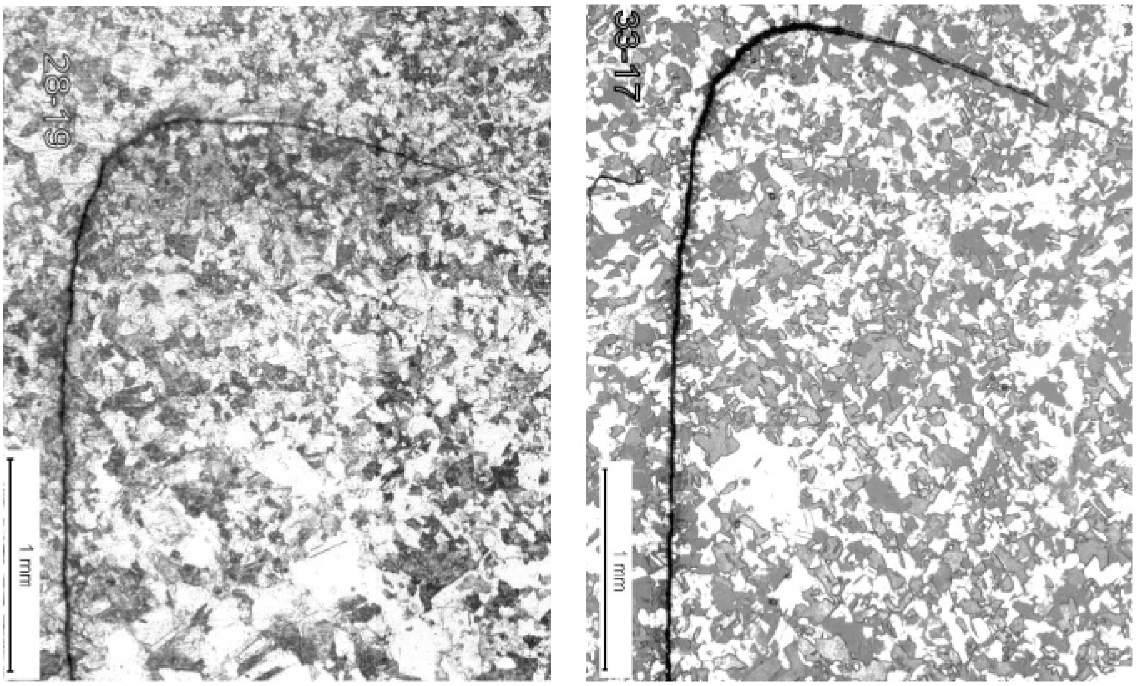

FSW 28-19 high amplitude

FSW 33-17 high amplitude

Figure 6-47. *Microsections of joint-line-hooking-discontinuities in FSW.*

7 Evaluation of the SKB system for digital radiography

7.1 Summary of BAM-Experiments at SKB Canister Laboratory

7.1.1 Measurement of linear attenuation coefficient

Experiments have been performed to determine the attenuation coefficient for Cu within the full application range. For this purpose the following experimental set-up was used:

(i) Plates of constant thickness are used to reduce geometrical influences to a minimum.

(ii) The plates were provided by SKB to guarantee that they are made from the canister material to exclude possible influences by material variations.

(iii) The material was placed directly in front of the line detector.

(iv) The experiments were repeated placing the material in front of the collimator of the radiation source. This arrangement reduces the scattered radiation from the object hitting the detector.

The set-up of the experiment is illustrated in Figure 7-1. Radiographs were measured in two detector modes: (*i*) original pixel size (50 µm) and (*ii*) 8 pixel binning (400 µm) corresponding to the written SKB procedure. The system was calibrated that a material thickness of 100 mm Cu corresponds to a grey value of 10,000. The full image was used to calculate the mean grey value and the corresponding standard deviation. The results of experiments for the specimen placed in front of the detector and 8 pixel binning are shown in Figure 7-5 together with the exponential fit giving the integral estimate of the linear attenuation coefficient. Note that the multiple R^2 value is close to 1 describing the correlation between the data and the regression. It can be concluded from this fact that the data fit well to the exponential attenuation law with a constant linear attenuation coefficient over the full application range between 50 mm and 165 mm thickness of Copper. The evaluation of all measurements is collected in Table 7-1.

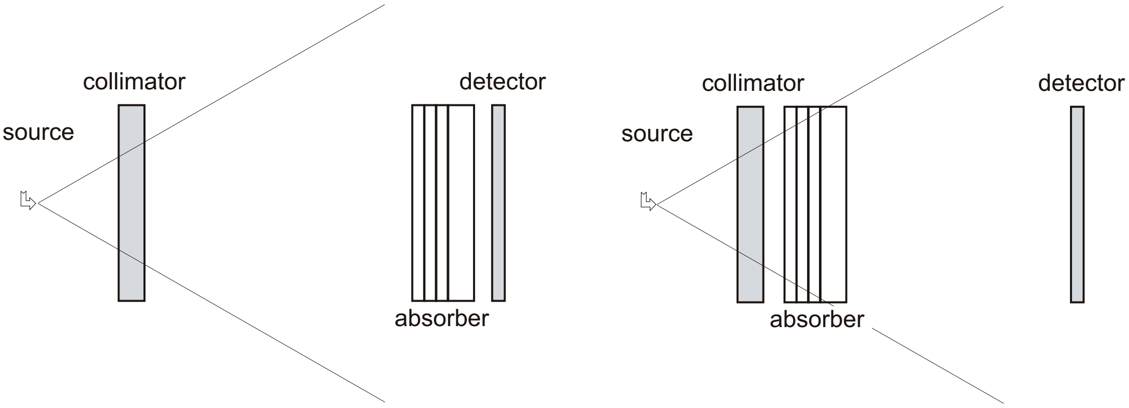

Figure 7-1. *Experimental set-up for the measurement of the attenuation coefficients: material placed in front of the detector (left) and in front of the source collimator (right).*

Table 7-1. Results of data evaluation.

Specimen position	No binning Attenuation coefficient (cm^{-1})	Multiple R-squared value	8 pixel binning Attenuation coefficient (cm^{-1})	Multiple R-squared value
Close to detector	0.301	0.9998	0.299	0.9998
Close to source	0.306	0.9999	0.305	0.9998

The corresponding average energy of the source spectrum was determined to 3.8 MeV using the mean value of 0.300 cm^{-1}. Comparing the estimated attenuation coefficients for the two investigated positions of the absorber a difference of about 2% has been found. If the distance between the detector and the specimen is increased the contribution of scattered radiation is reduced because of the divergence of scattered radiation.

In addition to the above data evaluation a second analysis was performed to investigate more detailed if the attenuation coefficient depends on the material thickness. For this purpose the differential linear attenuation coefficient was calculated from two neighbouring data points according to:

$$\mu = -\frac{1}{\Delta d} \ln\left(\frac{I(d+\Delta d)}{I(d)}\right) \tag{6}$$

with the thickness d and d+Δd of neighbouring data points. The error of the attenuation coefficients calculated by Equation (6) is given by the law of error propagation

$$(\Delta\mu)^2 = \left(\frac{1}{I(d)\cdot\Delta d}\right)^2 \left[\Delta I(d)\right]^2 + \left(\frac{1}{I(d+\Delta d)\cdot\Delta d}\right)^2 \left[\Delta I(d+\Delta d)\right]^2 + \left(\frac{\mu}{\Delta d}\right)^2 \left[\Delta(\Delta d)\right]^2 \tag{7}$$

with $\Delta I(d)$ and $\Delta I(d+\Delta d)$ given by the standard deviation of repeated measurements of the average grey value for a fixed material thickness. The standard deviation in the available images representing the pixel noise divided by the square root of the number of pixels considered for the calculation of the average grey value in the images was used as estimate of $\Delta I(d)$ and $\Delta I(d+\Delta d)$. The error of thickness measurement $\Delta(\Delta d)$ was estimated to 0.1 mm. The results of this analysis are presented in Figure 7-3 for the specimen positioned close to the detector (blue symbols) and close to the source (green symbols).

Figure 7-3 shows a tendency that the linear attenuation coefficient decreases with increasing material thickness. This behaviour can be understood by the hardening effect, i.e. with increasing material thickness the average energy of the transmitted spectrum increases. Taking into consideration the error of estimation this tendency of decreasing differential attenuation coefficient is statistically significant. Here a decrease of the differential attenuation coefficients of about 5% within a material thickness range of 50 mm to 165 mm can be found which corresponds to a hardening of the spectrum of about 1.4 MeV (average energy: 50 mm thickness: 3.0 MeV; 165 mm thickness: 4.4 MeV). Additionally it can be concluded from the figure that the estimated differential attenuation coefficients vary increasingly with the penetrated material thickness because fluctuation are amplified by differentiation.

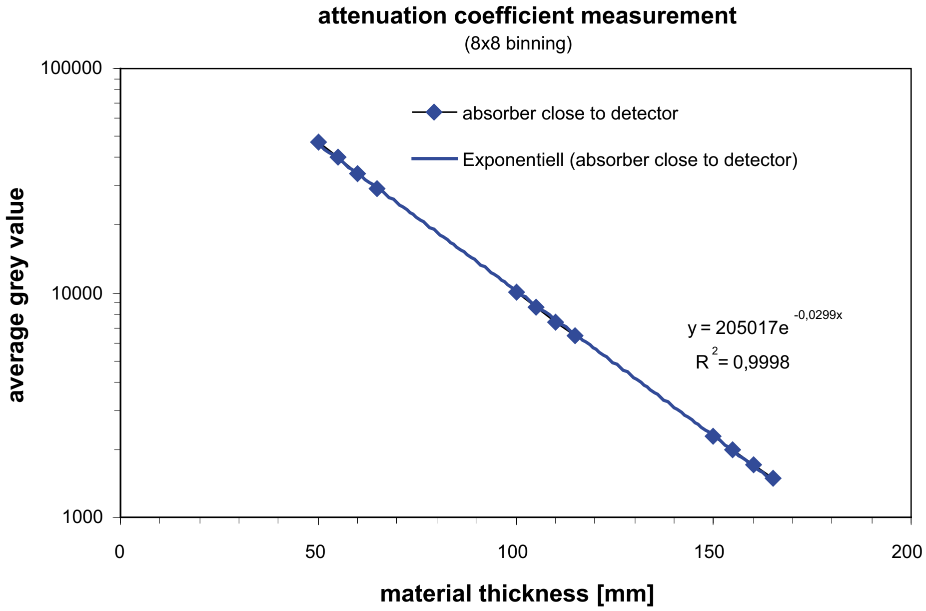

Figure 7-2. Result of exponential fit after 8×8 pixel binning (400 µm pixel size).

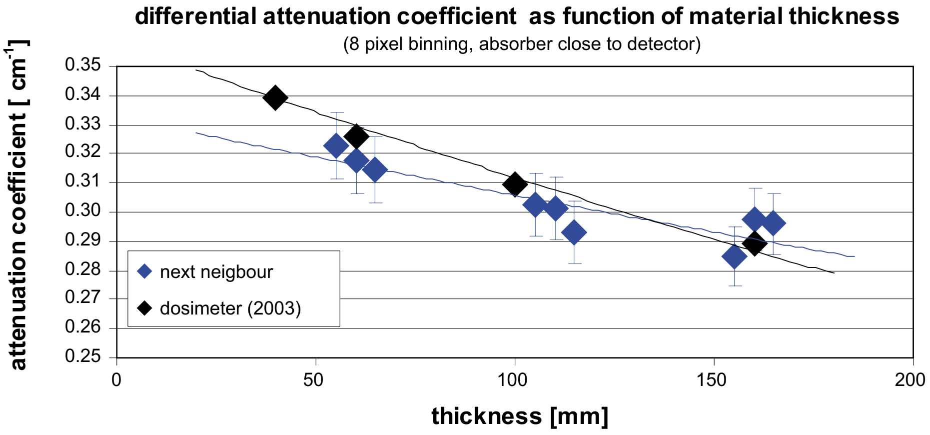

Figure 7-3. Differential attenuation coefficient as function of material thickness with absorber closed to detector (blue symbols) and close to source (green symbols) from images after 8×8 pixel binning (400 µm pixel size).

7.1.2 Hardware evaluation

In the white images of the previous measurements performed in 2003 peaks with large grey values were found. These peaks also appeared after the correction of the original image with the black- and white images in the corrected image (see Figure Figure 7-4).

We investigated the influence of the (*i*) switched on and switched off Linac and (*ii*) the external (local) and internal (remote) triggering of the Linac pulses with the readout cycle of the line camera. External triggering means the blocking of the Linac pulses during the readout cycle of the line camera. In the internal triggering mode the Linac pulses are not blocked. A Co-60 source with small activity was used for reference measurements. For shielding the Linac radiation a 220 mm copper block was positioned in the front of the Linac.

Figure 7-4 shows a white image for Linac power-on and local triggering. The distortions are visible as a line of white points from lower left to upper right in the image. In addition a regular pattern of these stripes can be seen.

Figure 7-5 shows a white image resulting from remote triggering. The distortions seen in Figure 7-4 are no more visible any more.

Figure 7-6 shows a white image under normal measurement conditions: (*i*) Linac –power-on, (*ii*) remote control, and (*iii*) fast motion (rotation) of the canister by external motor control (not connected to the ACTIS-system). The disturbances in the image, as described before, are missing.

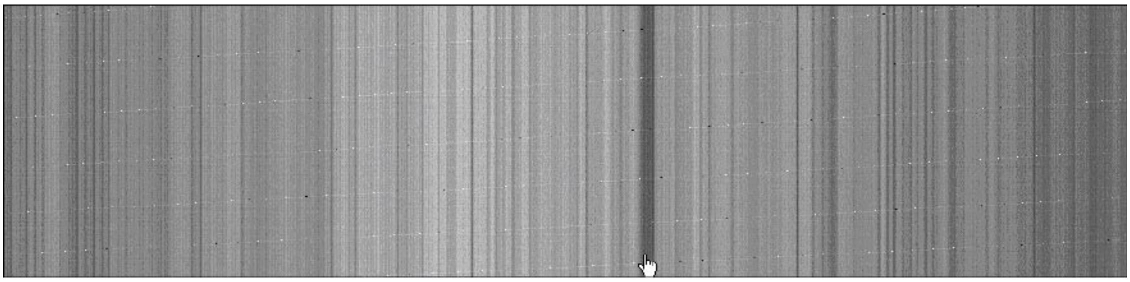

Figure 7-4. *White-image (# 634, uncorrected): Linac power-on, local triggering.*

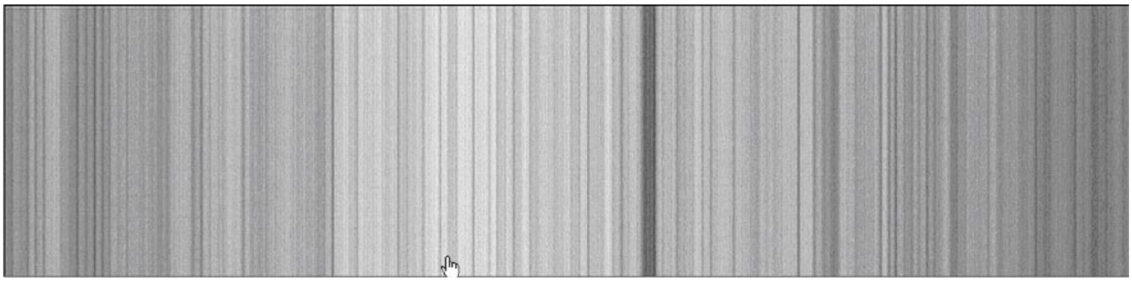

Figure 7-5. *White-image (# 635, uncorrected): Linac –Power On, remote triggering.*

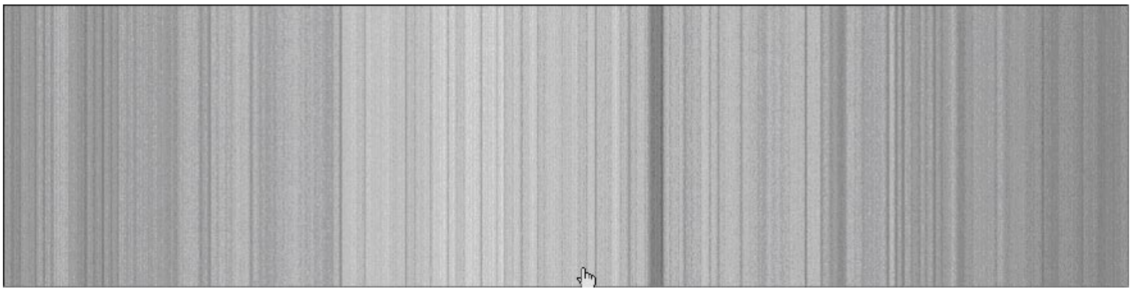

Figure 7-6. *White-image (# 637, uncorrected): measurement under normal conditions, canister motion (rotation) from an external motor.*

7.1.3 Contrast resolution

The measurements were performed on the original canister with ASTM penetrameters, which were positioned at the outer surface of the canister (*i*) above, (*ii*) centred on, and (*iii*) below the welding area (for details see Figure 7-7). Three positions were chosen in order to investigate the dependency of the contrast on the position of an indication at the radiograph parallel to the detector line. The standard set up was used for the projection measurements with an angle of incidence of 35°.

Table 7-2 gives an overview on the used ASTM penetrameters together with their normal (t(0°)) and penetrated (t(35°)) thickness.

The measurement procedure is schematically shown in Figure 7-8. The contrast was calculated as difference between the average grey value in the matrix material and (*i*) the average grey value or (*ii*) the minimum grey value measured at the bottom of the ASTM penetrameter. The first value results in the average contrast. The second one gives the maximum contrast as used for the POD evaluation (compare BAM Data Report delivered March 2005). For all measurements a window of 20×20 pixels was considered. The window positions are shown in Figure 7-8.

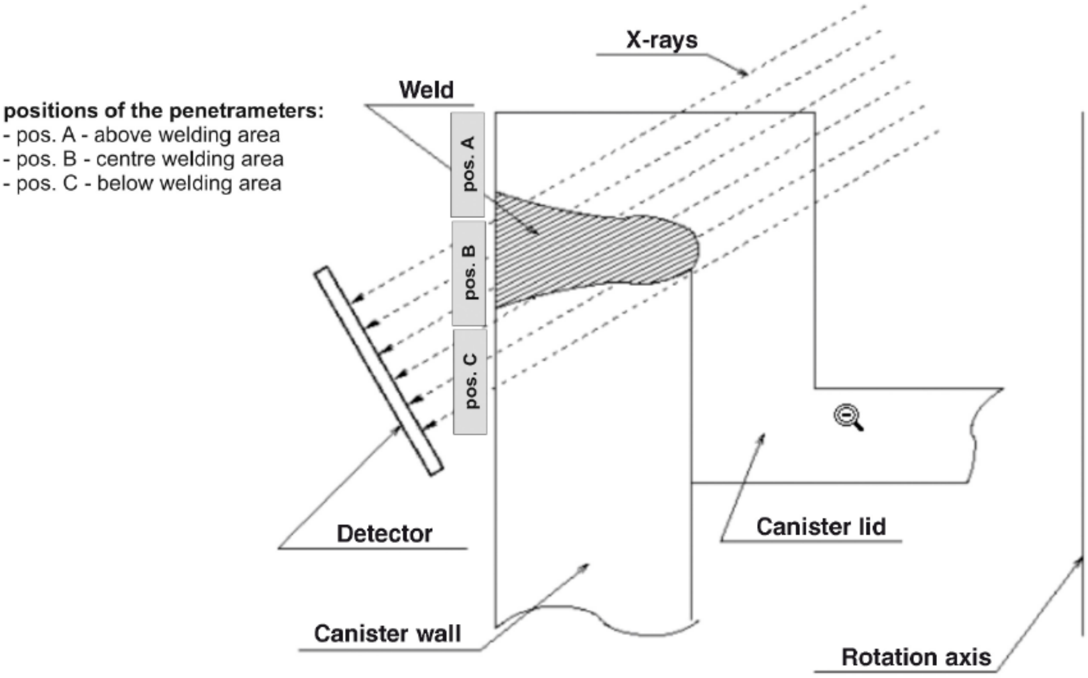

Figure 7-7. *Positions of the penetrameters at the outer canister surface relative to the welding area.*

Table 7-2. ASTM penetrameters.

ASTM	t(0°) (mm)	t(35°) (mm)
10	0.254	0.310
20	0.508	0.620
30	0.762	0.930
40	1.016	1.240
50	1.270	1.550

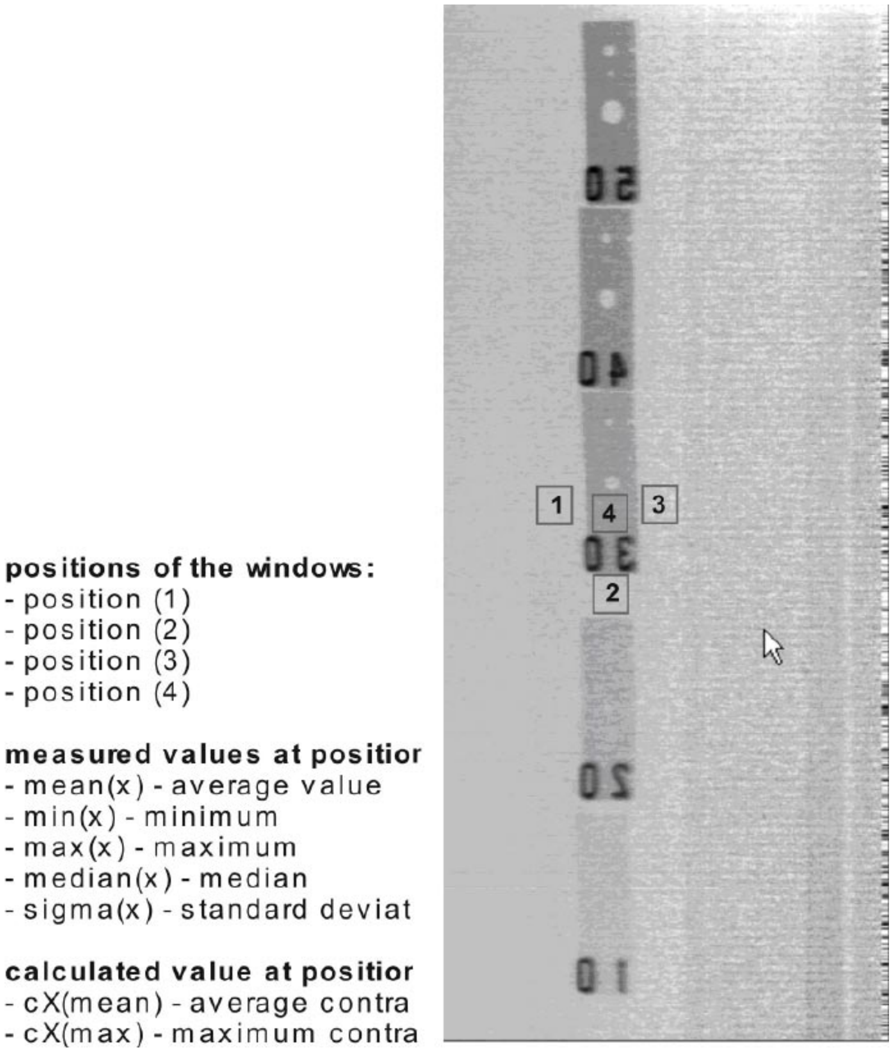

Figure 7-8. *Positions of the windows for the measurement procedure.*

The results of contrast evaluation are presented in Figure 7-9 and Figure 7-10. Figure 7-9 shows that the average contrast varies with the position of the penetrameter relative to the welding area. The largest contrast is observed for the penetrameter positioned above the welding area. A decrease of the contrast was found while the penetrameter was shifted below the welding area. This observation can explained as follows: The penetrated wall thickness in the matrix material increases from position (A) to position (C) (see Figure 7-7) because of the difference of the angle of incidence. Because the penetrated thickness of the penetrameters is small compared to the penetrated thickness of the matrix material ($t_{penetrameter} << t_{canister\ wall}$), the relative thickness variation $t_{penetrameter}/t_{canister\ wall}$ decreases for the three positions (A) to (C): $c_A > c_B > c_C$. As a result the average contrast decreases accordingly, which agrees with the experimental findings. The opposite behaviour was found for the maximum contrast (see Figure 7-10). In this case the measured contrast strongly depends on the standard variation of the grey values in the image, which increases with the penetrated length. Hence, the maximum contrast also increases with the penetrated length agreeing with the results shown in Figure 7-10: $c_A < c_B < c_C$.

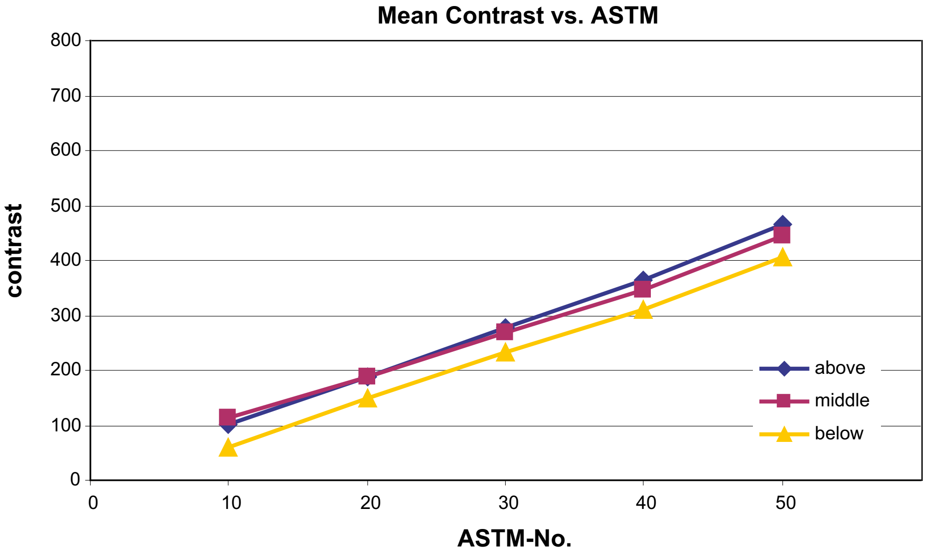

Figure 7-9. *Mean contrast for different penetrameter positions for window position (3).*

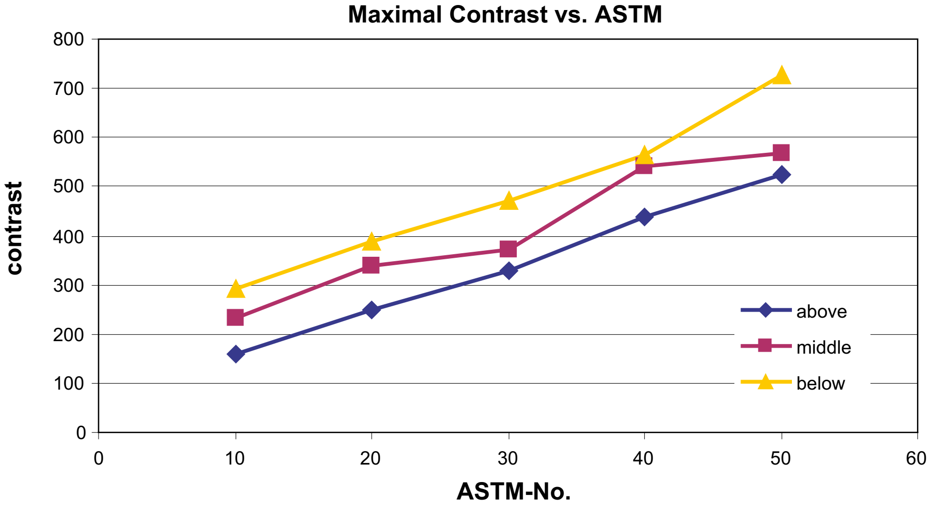

Figure 7-10. *Maximal contrast for different penetrameter positions for window position (3).*

7.2 BAM evaluation of the SKB equipment according to EU-standards

SKB Radiography device in Oskarshamn – Minimum requirements for radiographic testing in accordance with EN 1435 and evaluation of the digital radiography system –

Summary

The SKB radiography device was tested and its parameters were compared with the requirements of European standards. The new European standard EN 13068-3 (Radioscopy) does not cover material thicknesses > 85 mm. Therefore, the system test was related to the European standard EN 1435 for radiographic weld inspection only.

The SKB radiography device and its set up fulfil the requirements of EN 1435. The film specific parameters were transformed to the properties of the digital system. The SKB radiography provides the required image quality, measured with wires and step hole IQIs (see also EN 462). The total system unsharpness is significantly higher than the required one by EN 1435. The standard permits the compensation of parameters. The system provides significantly higher signal/noise ratio (SNR) than the specified film systems. The lost of contrast for small flaws is compensated by the better SNR in the order of the IQI dimensions (0.3–2 mm depending on wall thickness).

The image quality of the SKB-radiography depends on direction (line direction and scan direction of image). The unsharpness in direction of the detector line is higher (0.8 mm) than the unsharpness from line to line (0.64 mm, determined with method of EN 462-5). Therefore, all wire IQIs (douplex wires and single wires) have to be applied horizontally and vertically (line and scan direction). The wire and step hole IQIs corresponding to EN 462-1, -2 shall be positioned parallel to the detection plane of the camera, or the change in thickness due to the radiation angle of incidence of 35° has to be considered numerically (for vertical wire alignment).

The SKB radiography uses a shading correction mode, which allows the detection of different object wall thicknesses (50–142 mm) within one image with nearly same grey level (I~10,000). This simplifies the interpretation of the digital radiographs, but it also leads to a position dependent SNR and contrast sensitivity (CS). Finer flaws can be detected above the weld and near the outer surface and coarser flaws can be detected below the weld and near the root. The POD becomes position dependent in the direction of the detector line.

The selected angle of incidence of 35° allows the evaluation of the flaws in dependence on depth related to the object and weld surface. A smaller angle would increase the contrast sensitivity due to the reduction of wall thickness and would yield better radiation geometry in relation to planar horizontal flaws (joint line hooking for FSW and lack of fusion for EBW). The SKB radiography set up requires a flaw size or opening of planar flaws of more than 0.3 mm for sufficient detection (see POD curves). The unit could be modified for detection of smaller flaws. There exist basically three ways:

1. Extension of measurement time: The increase of measurement time per detected line increases the contrast/noise ratio. Four times longer measurement increases the CNR by the factor of two. This will shift the POD for volumetric flaws to the left and the 90/95 POD limit is expected to be about ½ of the flaw size which was determined in these trials. Due to unsharpness restriction the ½ value will not fully be achieved. Precondition for the CNR enhancement is the improvement of the calibration procedure for the camera and the reduction of internal electronic noise. The increase of the total measurement time is limited due to economic consideration on the maximum acceptable measurement time.
2. If the detector unsharpness limits the perception of fine flaws, the binning (currently 8 elements to 400 mm) has to be reduced to 200 µm. The collimator has to be adjusted to a width of about 200 µm opening. Since the effective detector area is reduced to ¼ the scan time has to be extended to four enabling the effective smaller detector elements to acquire the same number of photons as the larger detector elements to maintain the minimum required CNR. It is expected that the reduction of detector element size and increase of CNR has to be optimized. But consequently both actions result in an increase of measurement time.
3. Application of a digital detector array (DDA or flat panel or area detector) instead of a line camera: DDAs will detect a certain area of the object in the same time which the line camera needs for one line. A detector with e.g. 500 lines needs only two thousands of the measurement time. A suitable DDA could be e.g. a high energy Perkin Elmer detector

with 400 µm pixel size. The real expected time gain is lower than 500, and will be about 10, because the DDAs have less quantum efficiency in comparison to line cameras and provide reduced contrast due to their higher sensitivity against scattered radiation. Corresponding test trials are required for optimum use. Nevertheless a reduction of measurement time down from one hour to 6 minutes with the same CNR would be a considerable economic advantage. Allowing the same measurement time as required with the line camera, the system would provide 3 times higher CNR.

Minimum requirements for radiographic testing in accordance with EN 1435

EN 1435 is the European standard for radiographic weld inspection. All radiographic tests, performed in the copper container project, can be considered as state of the art radiography if the requirements of EN 1435 are fulfilled.

Radiation geometry

Clause 6.1.5 recommends Figure 8 for inspection of pipe like structures.

Due to the selected radiation direction a wall thickness has to be considered from 50 to 142 mm. This yields different requirements for contrast sensitivity (IQI perception) and minimum source object distances.

The application of X-ray radiation between 4 and 12 MeV may be selected for wall thicknesses ≥ 80 mm for class B testing and ≥ 50 mm for class A testing. The range below 80 mm wall thickness can be accepted if the contrast sensitivity is increased. This is the case due to the high measured SNR of 475 at 50 mm wall thickness and the correct IQI-perception for class B.

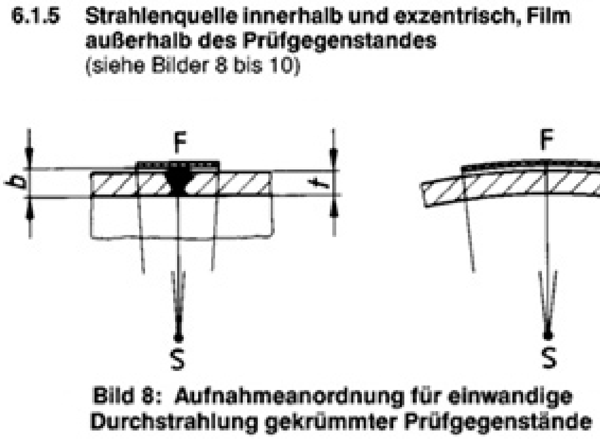

6.1.5 Strahlenquelle innerhalb und exzentrisch, Film außerhalb des Prüfgegenstandes
(siehe Bilder 8 bis 10)

Bild 8: Aufnahmeanordnung für einwandige Durchstrahlung gekrümmter Prüfgegenstände

The SKB-radiography unit is adjusted similar to Figure 8. Fig. 2 shows the two possible radiation geometries. The geometry of Fig. 2a is similar to Figure 8 but the source has an additional angle of incidence of 35° to avoid the less sensitive double wall inspection. This angle has to be considered for the orientation of the IQIs and the calculation of the wall thickness and radiation conditions

Figure 7-11. Figure 8 of EN 1435 for definition of radiation geometry.

Unsharpness

Measurement of the focal spot size of the LINAC

To characterize the geometrical unsharpness of the radiographic set-up used for canister inspection, the focal spot size and the intensity distribution of the LINAC have to be known. For these measurements no special standards are available, so the available standards for X-ray tubes (EN 12543) have been adopted to the LINAC energy range. In Figure 7-12 the set-up of the imaging of a W-edge is shown.

From the edge unsharpness the size of the X-ray source can be determined perpendicular to this edge.

The pin-hole method (see EN 12543-2 for details) allows the direct imaging of the intensity distribution of the focal spot (see Figure 7-13). The critical part is the pin-hole, which has to be sufficient small and with a high stopping power to provide sharp images for measurements. The pin-hole used for these LINAC measurements was a 1 mm hole in a 5 cm W-cylinder (see Figure 7-14). Additional lead bricks were used as pre-collimators.

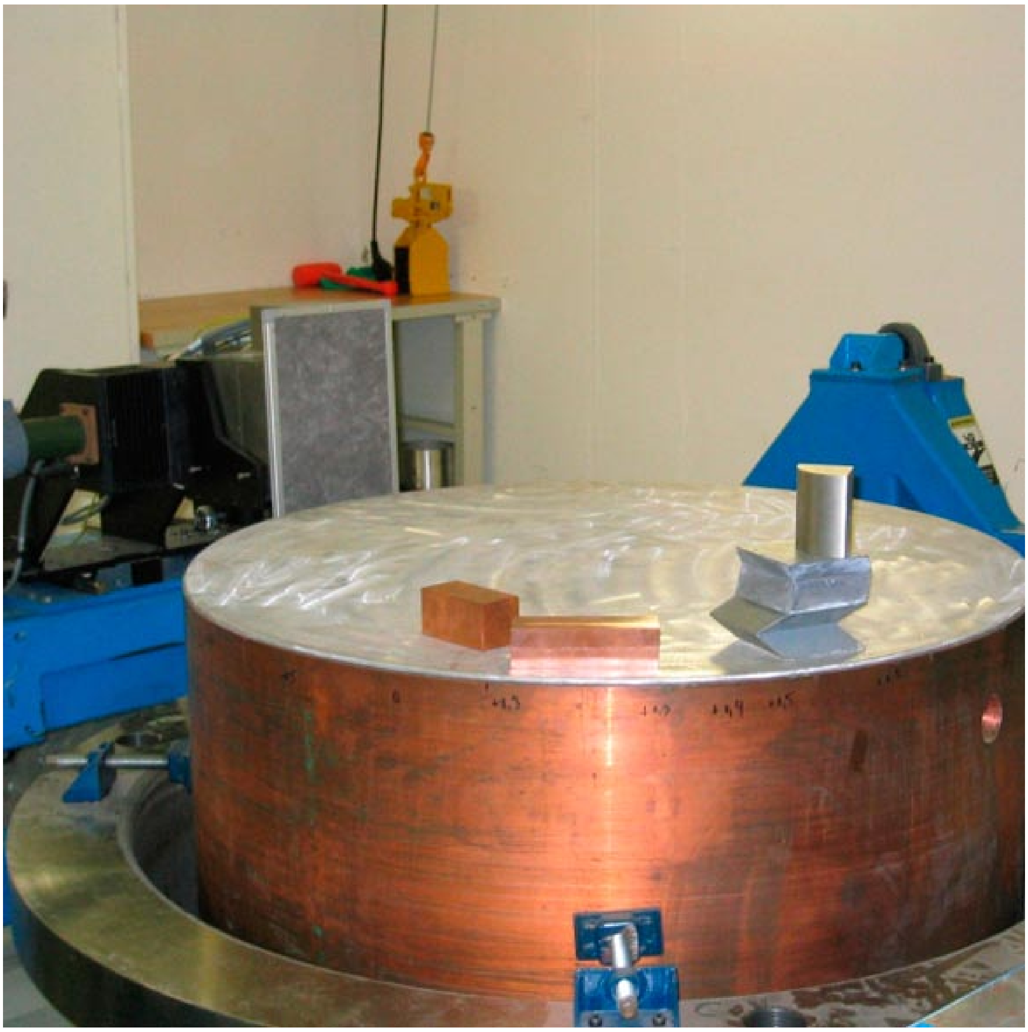

Figure 7-12. *Set-up of the Edge-method with CR according to EN 12543-3.*

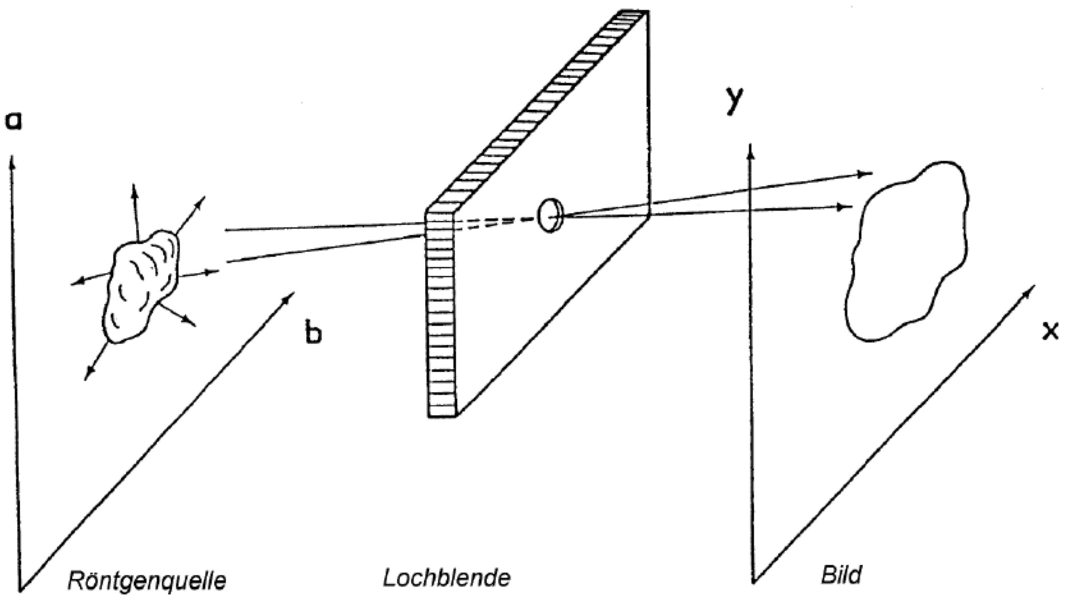

Figure 7-13. *Principle of the pin-hole camera method analogue to EN 12543-2.*

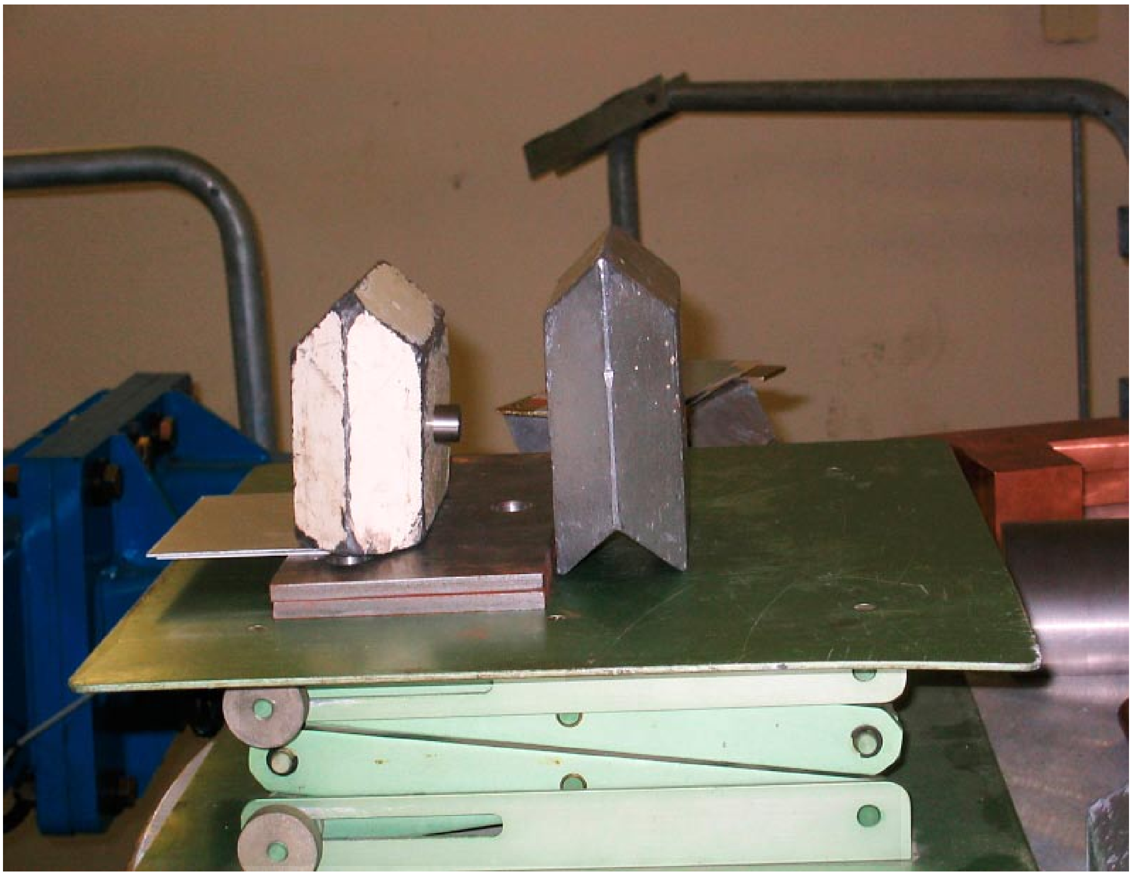

Figure 7-14. *Set-up used for pin-hole imaging (pin-hole of W in 40 mm thick Pb bricks as shielding and pre-collimator).*

The measured intensity distribution of the LINAC is shown in Figure 7-15. The focal spot size is defined as the maximum extension of the 10% intensity iso-dose line.

From Figure 7-15 a focal spot size of 2.6 mm was determined.

The minimum object focus distance for class B of EN 1435 shall be: 1,794 mm for 142 mm wall thickness and a detector distance of further 170 mm. The distance of detector collimator (lower edge) to object was assumed with 40 mm (worst case). The source detector distance (SDD) should be 2,106 mm. The real SDD distance is 2,250 mm and fulfils the class B condition.

a) Double wall inspection with low contrast.

b) Single wall inspection with high contrast but geometrical distortions and wall thickness change over the inspected area.

The required maximum geometric unsharpness (u_g for class B) is 348 µm for 142 mm wall thickness and 246 µm for 50 mm wall thickness. The values double for class A testing.

The measurements of the inherent detector unsharpness u_i with the duplex wire IQI provides the following values: Unsharpnes along the line: 0.8 mm; unsharpness in scan direction: 0.64 mm. The determined geometric unsharpness amounts to 420 µm.

The total unsharpness can be approximated by (see also ASTM E1000):

$$u_t = \sqrt{u_g^2 + u_i^2} \qquad (8)$$

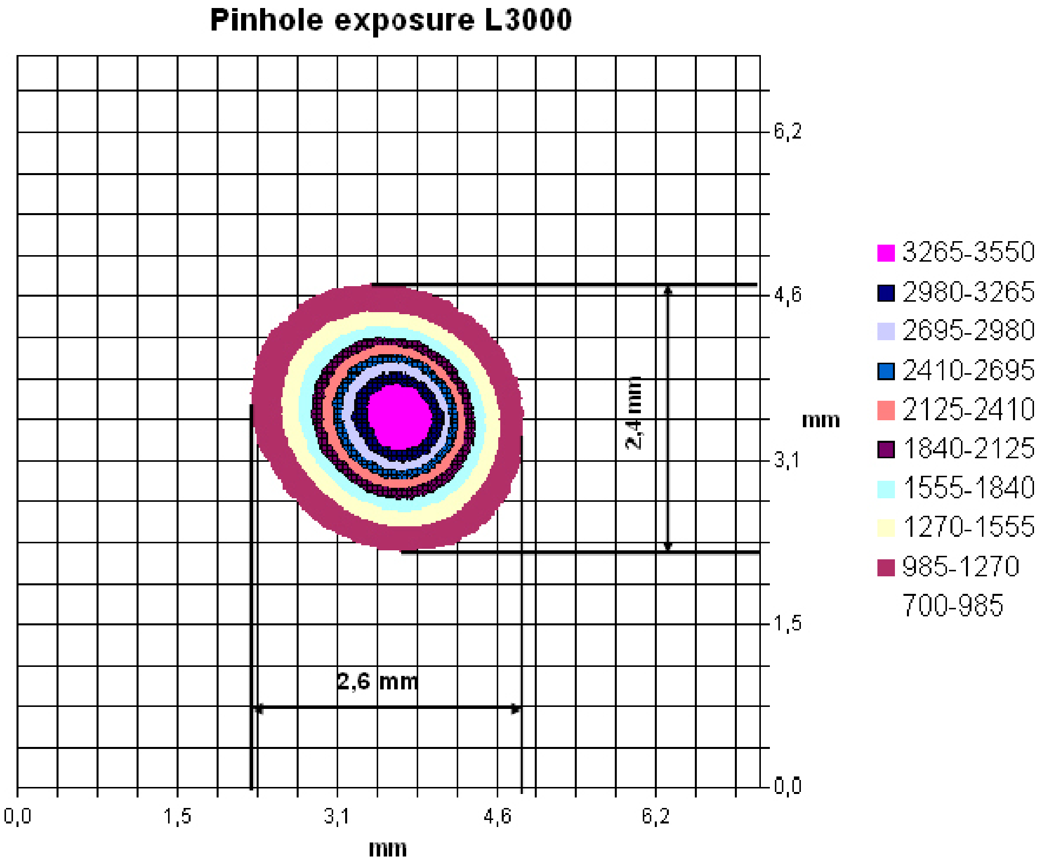

Figure 7-15. *Measurement results of the pin-hole image on a CR plate providing the focal spot size of the LINAC. The coloured rings are the 10% iso-dose lines.*

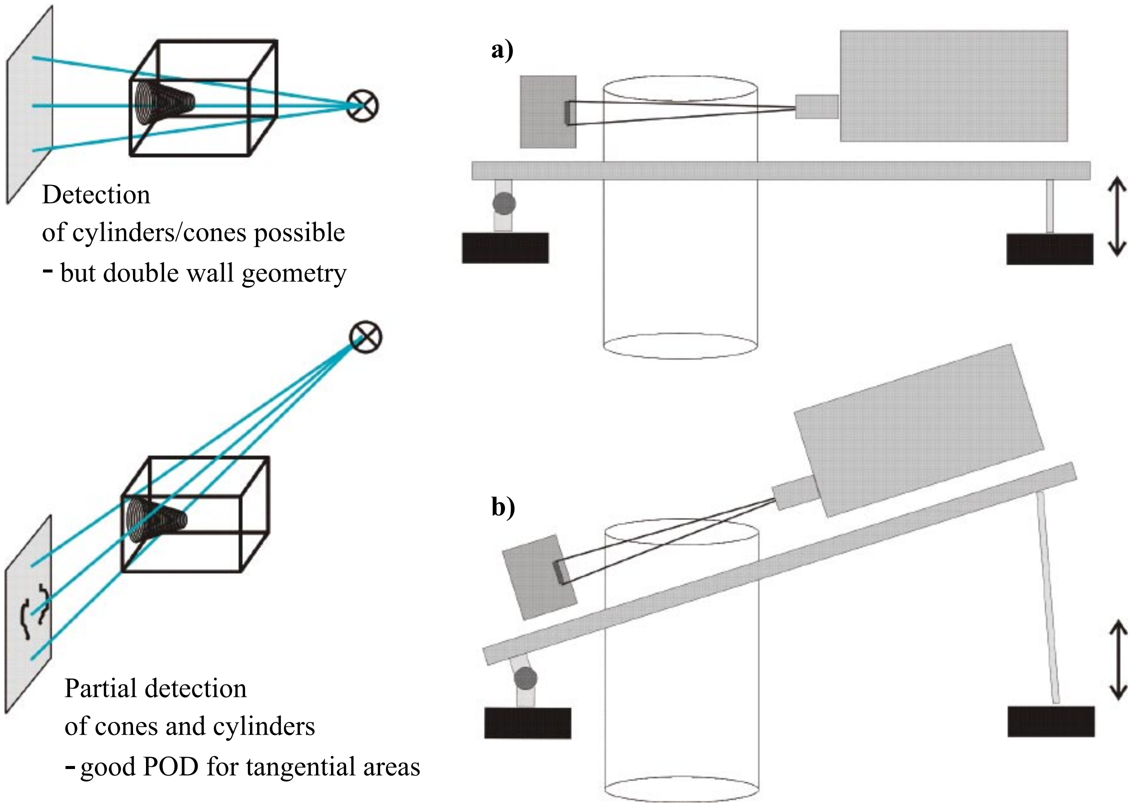

Figure 7-16. *Possible radiation geometries of SKB-Radiography.*

The total unsharpness u_t of the SKB-radiography (142 mm wall thickness) is:

- Direction of movement (scan direction) 765 µm.
- Direction along detector line 903 µm.

Contrast resolution

The contrast resolution is defined by the required IQI readings in Tables B.1–B.12 of EN 1435. These values define the just perceptible IQI. This can also be called the 50% POD value for the IQI.

Two types of IQIs are defined which provide different contrast sensitivities. The best IQI for measurement of contrast sensitivity of volumetric flaws as pores are the step hole penetrameters with a 1T hole (EN 462-2). The hole diameter corresponds to the step thickness (T).

The best IQI for measurement of contrast sensitivity of elongated flaws with sharp edges are the wires (EN 462-1). They are comparable with the cross hole drillings in UT-tests plates. Wire IQIs yield higher contrast sensitivity than step holes because the human eyes percept longer lines with higher sensitivity than pores in an image.

The following graph (Figure 7-17) presents the wall thickness dependent contrast sensitivity with approximated 50% POD.

The contrast resolution of the SKB radiography is always better or equal to the standard lines.

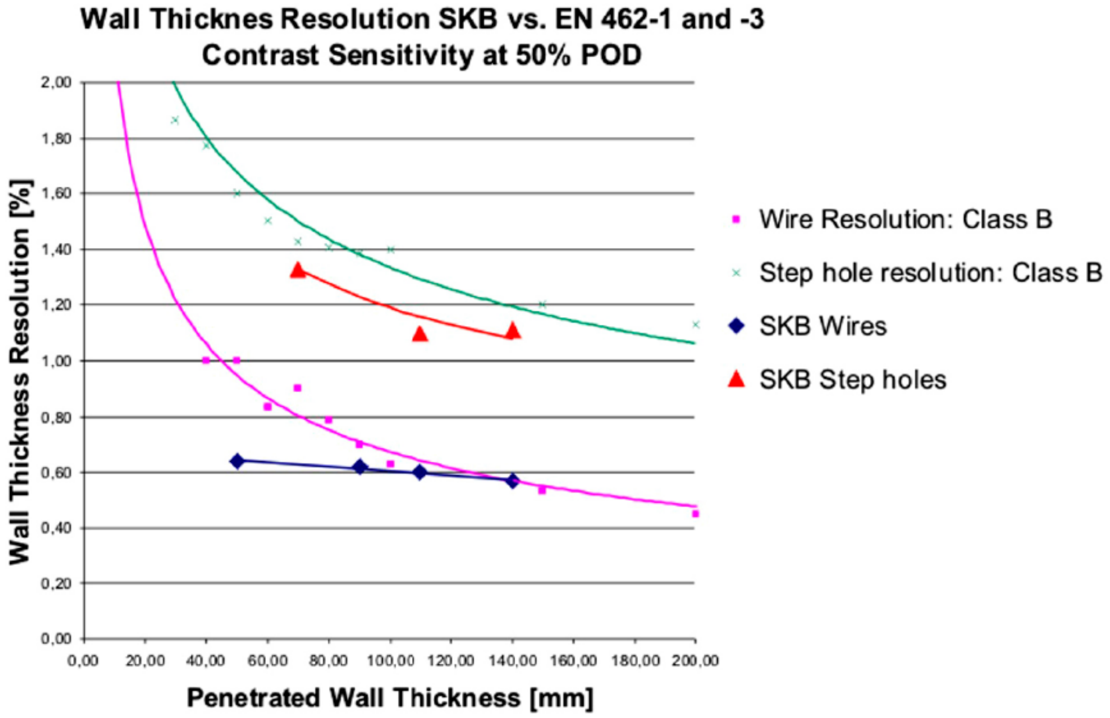

Figure 7-17. *Contrast sensitivity at 50% POD for 1T step holes (upper line green) and wires (lower line magenta) corresponding to EN 1435, Tables B3, B4.*

All measured values of the SKB radiography are better or equal to the required values by EN 1435. The diagram provides information about the expected contrast sensitivity (here: visual perception of an IQI with a given thickness in relation to the penetrated object thickness) in comparison to the applied equipment and wall thickness. This diagram is important for the understanding of the position dependent POD in the SKB radiographs.

If the wall thickness changes from 50 mm to 142 mm then the radiation intensity changes behind the object by a factor of 15.3 (attenuation law). The shading correction of the unit is used in a way that this intensity change is compensated in the final digital images. This results in a transformation of the noise. Finally the base material is characterised by a grey value of about 10,000. The image noise changes from the upper detector side to the lower detector side by a factor of 3.9 (square root law). The factor is higher in practice because an additional ripple noise is overlapped in the higher noise area.

Finally it is difficult to read the correct IQI value because the corresponding wall thickness has to be determined. Figure 7-8 is a typical digital radiograph of SKB unit with higher noise at the right side and shows an image of the BAM report of 06/2005. The increasing wall thickness leads to an increasing noise from left to right.

Possible increase of image quality

The spatial resolution can be increased by a factor of about 2 in both directions by change of binning. The lost in SNR must be compensated by 4 times higher measurement time to compensate the photon statistics. This applies only, if the ripple effect (Figure 7-8) can be neglected.

The better way is the increase of measurement time to increase the SNR and work in the subpixel resolution range. There exist two ways:

1 Increase of the integration time per line detection. The factor 4 in time yields the double SNR which reduces the percentage of the contrast sensitivity by two. Half size of flaw may be detected.

2 Use of new digital detector arrays (DDA; also known as flat panel detectors). The usage of array detectors instead of line detectors reduces the measurement time by a factor of up to ten and/or improves the contrast sensitivity.

Motivation for new digital detector array (DDA) technology

Experiments at BAM with the new digital detector array technique result in promising improvements of image quality. New calibration software enables an improvement of image quality by a factor of up to 10 in respect to the contrast sensitivity. The exposure time is comparable to the best films. Figure 7-18 gives an example for a comparison of image quality obtained by film radiography and the new DDA technique.

The DDA radiograph permits a significantly better evaluation of the finest details, which may be cracks or micro pores. This technology could be adapted to the SKB device and provide a radiographic testing quality, which is not available world wide yet.

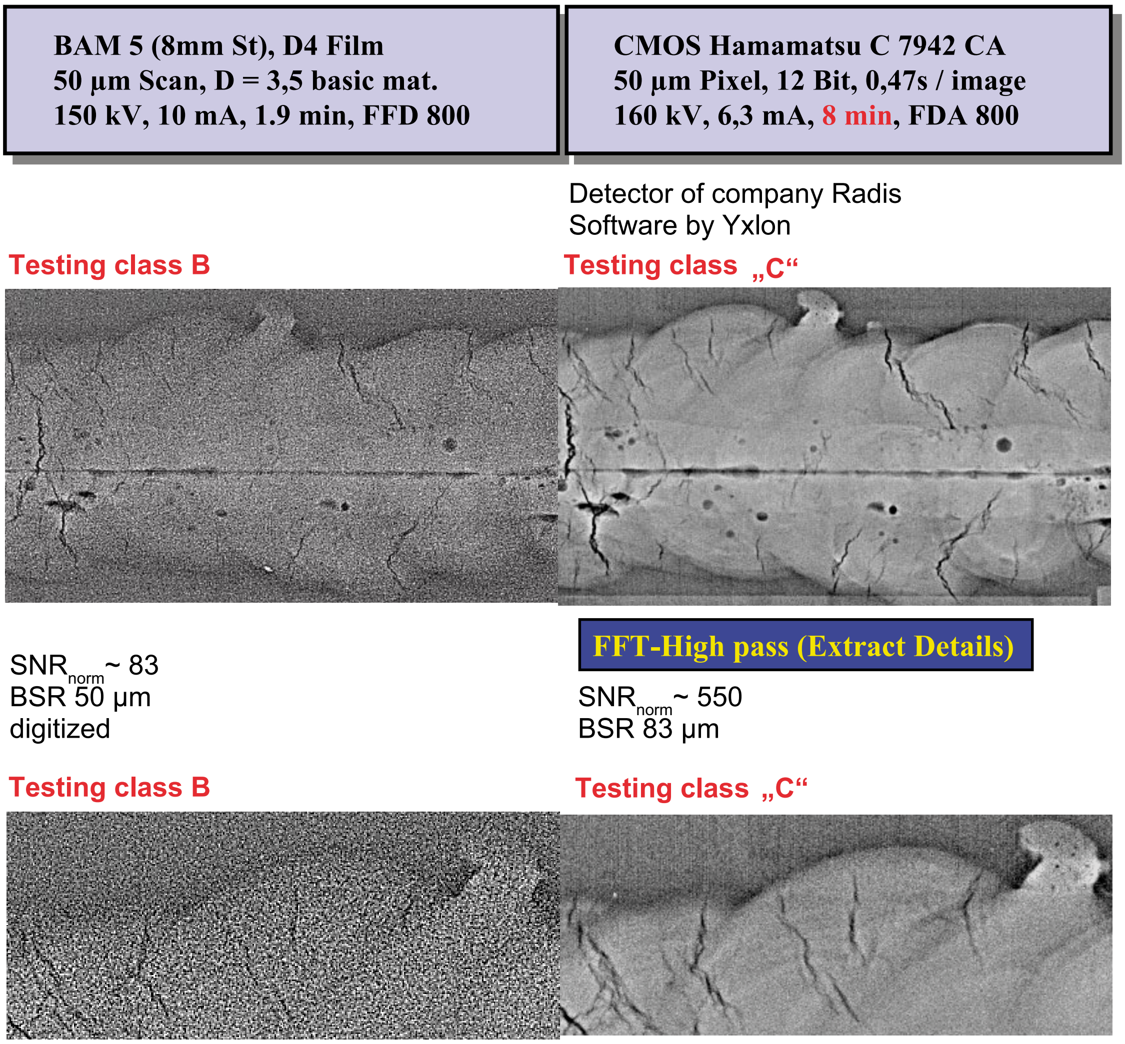

Figure 7-18. *Comparison of image quality of test weld BAM 5 with film left and Hamamatsu detector right. The lower image pair shows a magnified region.*

8 Reliability assessment using POD

8.1 Methodology for POD

The basic principle of the signal response analysis or "$\hat{a}$ versus a" evaluation is shown in Figure 8-1. A discontinuity of size a (crack depth in Figure 8-1) is causing a signal of height $\hat{a}$. The statistical distribution of the signals in dependence of the discontinuity size yields a certain POD curve, which is described in more exact terms in the following section.

8.1.1 â vs. a analysis

General description (2)

Consider a quantitative NDT system. As a result of the investigation of a discontinuity having size a, it generates a signal $\hat{a}$. If the signal exceeds a certain decision threshold $\hat{a}_{\text{dec}}$, the system registers a discontinuity detection. As the NDT system is influenced by uncontrolled factors, discontinuities of the same size can cause signals of different strength. For this reason the strength of the signal $\hat{a}$ to the discontinuity of size a is considered as a random value and associated with a probability density $g_a(\hat{a})$. The relation between a and $\hat{a}$ can be expressed as follows:

$$\hat{a} = \mu(a) + \delta \tag{9}$$

Here $\mu(a)$ equals the mean value of $g_a(\hat{a})$ and δ is the random error whose distribution determines the probability density $g_a(\hat{a})$.

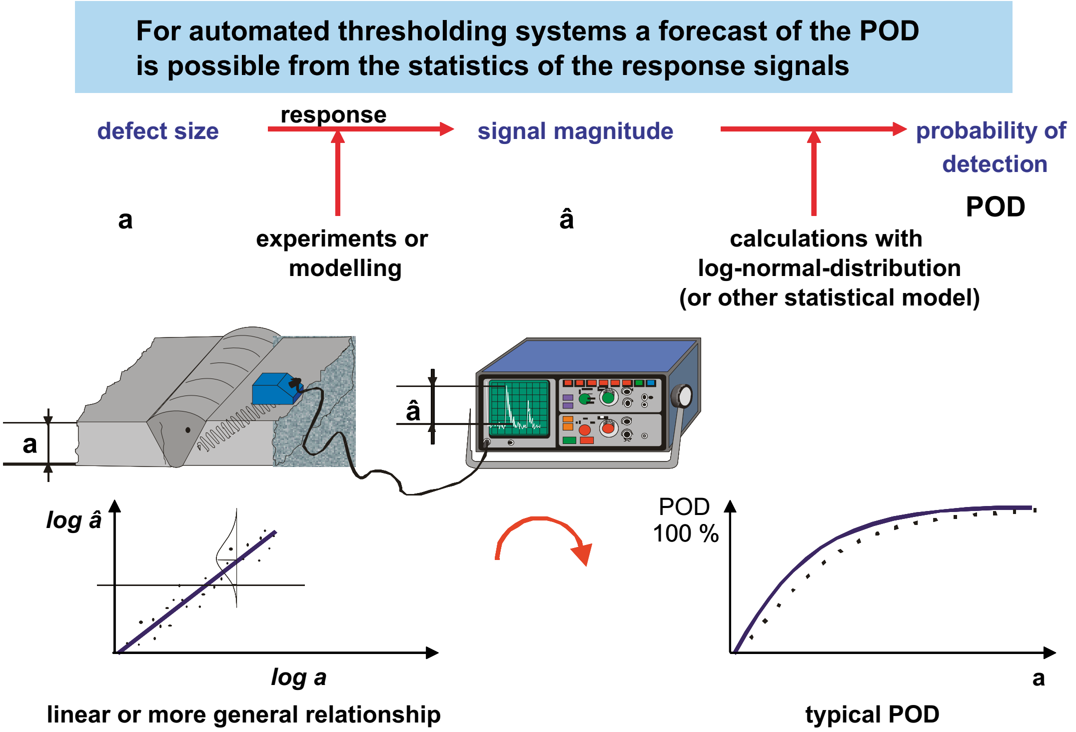

Figure 8-1. *Quantification of the risk: "â versus a".*

In practice, it is often assumed that δ is distributed normally with zero mean and constant (independent of a) variance. $g_a(\hat{a})$ is then the normal density function with mean $\mu(a) = 0$ and variance equal to that of δ.

The probability of detection (POD) as function of the size of the discontinuity is given by:

$$\mathrm{POD}(a) = P\{\hat{a}(a) > \hat{a}_{\mathrm{dec}}\} = \int_{\hat{a}_{\mathrm{dec}}}^{+\infty} g_a(\hat{a})d\hat{a} \tag{10}$$

Figure 8-2 illustrates this formula. The probability of detection is represented as hatched part of the area under the bell curve.

Calculation of the POD

Source data are a and $\hat{a}$ – arrays of length n that contain sizes of the discontinuities and response magnitudes, respectively, and the decision threshold $\hat{a}_{\mathrm{dec}}$. Note that the theory for dealing with censored data has been developed /20/ but is not used here, because the data sets available to us do no contain censored data. The censored data are the signals that cannot be registered by the system because they are either under the recording threshold or above the saturation threshold.

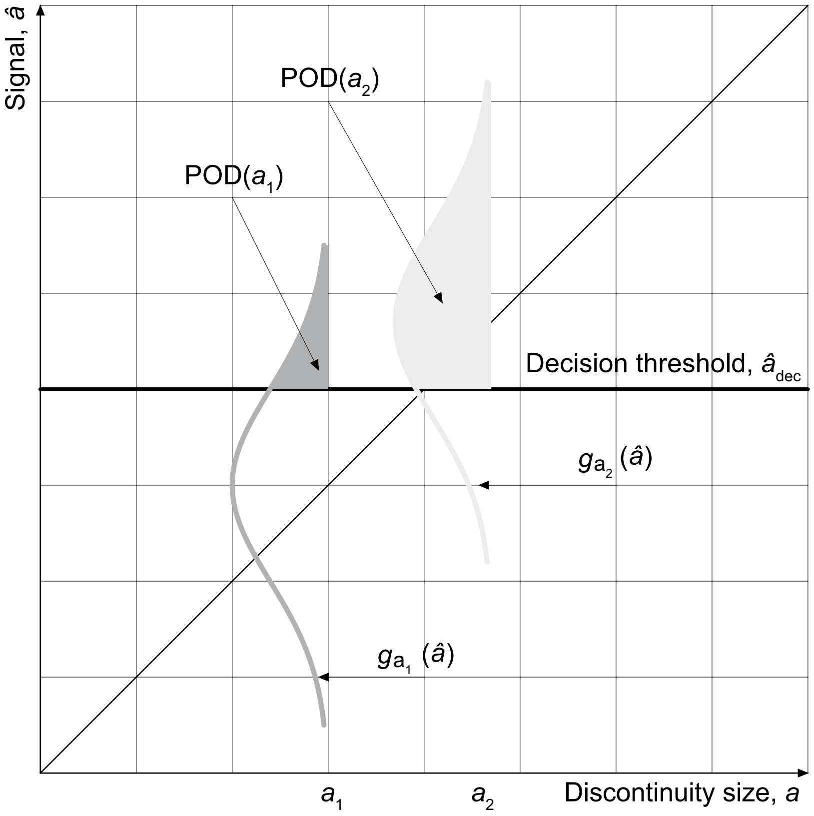

Figure 8-2. *Probability of detection.*

Calculation of the POD function parameters

The following formula is commonly used to model the relation between a and $\hat{a}$:

$$\ln \hat{a} = \beta_0 + \beta_1 \ln a + \delta \tag{11}$$

Here δ is normally distributed with zero mean and constant variance σ_δ^2.

Under the assumptions of the model, the POD function has the following form:

$$\mathrm{POD}(a) = P\{\hat{a} > \hat{a}_{\mathrm{dec}}\} = P\{\ln(\hat{a}) > \ln(\hat{a}_{\mathrm{dec}})\} = \Phi\left(\frac{\ln a - \mu}{\sigma}\right) \tag{12}$$

where Φ is the standard normal distribution function, and

$$\mu = \frac{\ln \hat{a}_{\mathrm{dec}} - \beta_0}{\beta_1} \tag{13}$$

$$\sigma = \frac{\sigma_\delta}{\beta_1} \tag{14}$$

The parameters β_0, β_1 and σ_δ describe the linear dependency of $\hat{a}$ on a and have the following meaning:

β_0	Intercept
β_1	Slope
σ_δ	Standard deviation of the residuals

Their values are estimated from the arrays a and $\hat{a}$ using the method of maximum likelihood.

The 95% lower confidence POD

The 95% lower confidence bound is given by the following formula:

$$\mathrm{POD}_{95}(a) = \Phi(\hat{z} - h) \tag{15}$$

where $\hat{z} = \frac{\ln a - \mu}{\sigma}$ and the variable h reflects the sample size and the scatter of the source data. The calculation of h is thoroughly described in /20/.

This general formalism has now to be applied to the discontinuity detection problem within the scope of welding optimization and risk assessment.

8.1.2 POD – the original task (full program)

The original task (together with the welding optimization) is to make sure that only one of 1,000 canisters might contain a critical discontinuity situation where in total more or equal 35 mm of the Cu-wall is missing.

From the naturally real existing POD as a function of all possible influencing parameters we have to extract the POD as function of the discontinuity radial dimension by a dedicated “Plan of Experiments” and reasonable mean value operations (see formula (16) below). The full program is only feasible with a number of additional expensive experiments. But in order to learn where we are with our current NDT technique and where to optimize, we need a POD assessment of the state of the art using a “Adapted POD Assessment”.

$$\mathrm{POD} = f(a_1, ..., a_n) \rightarrow \mathrm{POD} = g(a_{\mathrm{radial}}) \tag{16}$$

8.1.3 Adapted POD assessment

Volumetric discontinuities and area-like (non-volumetric) discontinuities will be treated separately – for EBW as well as for FSW

- Volumetric discontinuities RT
- Area like discontinuities UT

The physically reasonable “*â* versus *a*” POD including physically reasonable 2D extensions will be applied to the parameter configurations shown on Figure 8-3.

Explanation for the Assignement of a and â

Radiography RT

The physical reason for a signal (contrast) of a discontinuity in a radiographic image is the difference in penetrated length of material (Cu) along the X-ray beam caused by the dimension of the discontinuity in beam direction which we call “penetrated length” here. The contrast is the difference of the intensity behind the discontinuity with respect to the intensity I_b (b for background) behind the bulk material without the discontinuity. We apply the definition of the contrast derived from the absorption law according to ASTM E 1000, p. 438 /21/.

$$I = I_0 e^{-\mu\ \Delta w} \tag{17}$$

From this the exact expression for a wall thickness difference – in our case equivalent to penetrated discontinuity length – would be

$$\ln I_1 - \ln I_2 = \mu \Delta w \text{ and } \Delta w = w2 - w1 \tag{18}$$

where I_1 is the intensity behind the discontinuity and I_2 the intensity behind the bulk material in the surrounding.

For small Δw (with respect to the total penetrated wall length) we get

$$I = I \times \mu \times \Delta w \tag{19}$$

where we assume the I to be an almost constant “working point” I_b of the radiographic system.

The penetrated length is the intersection of the discontinuity with the beam with its 35° incident angle according to the set up of the RT system.

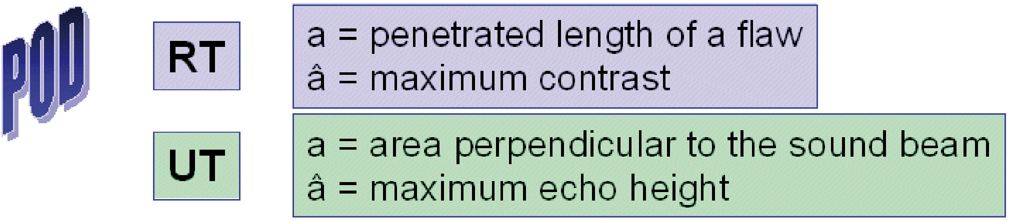

a = penetrated length of a flaw
â = maximum contrast

a = area perpendicular to the sound beam
â = maximum echo height

Figure 8-3. *Assignement of a and â for RT and UT.*

Ultrasound UT

According to the MIL 1823 handbook for reliability assessment /22/ appendix C the UT echo height behind the discontinuity is recommended as the signal response "*â*" and as the causing discontinuity dimension "*a*" the reflecting area of the discontinuity. The ASNT NDE handbook recommends /23/:

"The height of an echo depends on the size (reflecting area) of the discontinuity, its depth, shape, orientation and the nature of the test object surfaces (roughness, contour and acoustic impedance). When the discontinuity is smaller than the diameter of the sound beam, the size maybe deduced from the height of the echo, provided the following essential conditions are fulfilled:

(1) the plane of the discontinuity must be parallel with the sound entry surface,

(2) surface roughness less than 200 µm,

(3) the reflectivity is 100 percent and the discontinuity distance from the sound entry surface is in the far field and there is no edge interference."

For the application of the POD concept using "â versus a" the precondition is, that the echo height will in principle grow with defect size. There will be of course a scatter due to the uncomplete fulfilment of the points *(1)*, *(2)* and *(3)* especially point *(2)* for the discontinuities in FSW. These types of scatter are taken into account in the POD calculation. Important is that the scatter due to other influences is not completely overwriting the principal growing with size.

As will be seen in the following detection diagrams all discontinuities thicker than or equal to 1 mm (in Z direction of the experimental system) are well indicated by the RT system. Therefore we call these discontinuities "volumetric discontinuities". Discontinuities thinner than 1 mm and with a minimum area of about 4 mm^2 are well seen in the UT scans and we will call them "area like" or "non-volumetric" discontinuities. The discontinuities with thickness smaller 1 mm and area smaller than 4 mm^2 we are gong to call indifferent material discontinuities.

As the basic parameter for the discontinuity's detectability /20, 22/ we determine the $a_{90/95}$ magnitudes, i.e. the size *a* of the discontinuity for which the lower 95% confidence bound crosses the 90% POD level, i.e. it is guaranteed that discontinuities with a size of $a_{90/95}$ will be detected with 90% probability where only 5% might fall outside this confidence limit in case the experiment is repeated. We work with the assumption – given by the manufacturing experts – that only one of 100 canisters might have a critical discontinuity. Then the above argumentation yields: Only each of 1,000 canisters might have a leakage.

8.1.4 Integrity requirement

The discontinuity radial size has to be limited so that a remaining wall thickness of 15 mm is guaranteed against ground water corrosion. The maximum allowed discontinuity size in the radial direction is 35 mm. Together with the above POD an additional discontinuity geometry statistics has to provide for the group:

- FSW volumetric area-like
- EBW volumetric area-like

separately, no discontinuities of $a_r \geq 35$ mm will be present. No discontinuity of radial size $a_r \geq 35$ mm can be among the discontinuity assembly below $a_{90/95}$, that means no $a \leq a_{90/95}$ should have at the same time an $a_r \geq 35$ mm. This would yield a reasonable justification of the system to meet the above integrity requirement, as long as the existing discontinuity configurations are representative for the welds. Look for the "correlation" in scatter diagrams named "Critical Region …" below:

- penetrated discontinuity length by X-ray ←→ radial dimension,
- area perpendicular to UT beam ←→ radial dimension.

8.2 POD evaluation from experimental data

Steered by the plan of experiments for the welding procedure optimization and verification, the POD (Probability of Detection) for the discontinuities is determined using a systematic statistical methodology. The POD method, where the detection probability is determined as a function of discontinuity size, was originally developed for the US military aerospace sector /22/ for 1-dimensional signals. For the more complex 3-dimensional discontinuity situation in the canister welds and 2-dimensional data fields the method needs to be developed further. From the POD-curve and its lower confidence bound the discontinuity size is derived that will be detected with sufficient reliability and compared to the demand for integrity. This procedure includes a series of experiments with the SKB X-ray and ultrasonic methods foreseen for the production.

These results have to be compared to true discontinuity configurations in the welds. To determine these "true discontinuity configurations" the welds have to be tested destructively or tested with a more comprehensive non-destructive reference method. To get a complete 3D view to the discontinuities, the BAM selected a high-energy computed tomography (HECT, or CT) method as reference for volumetric discontinuities. The insight of CT results was at the end compared to exact destructive measurements. For the area like "JLH-discontinuities" only destructive testing could be applied as reference. Figure 8-4a shows an example of a cross section of a wormhole and Figure 8-4b shows several spatial vies on this discontinuity from the CT data.

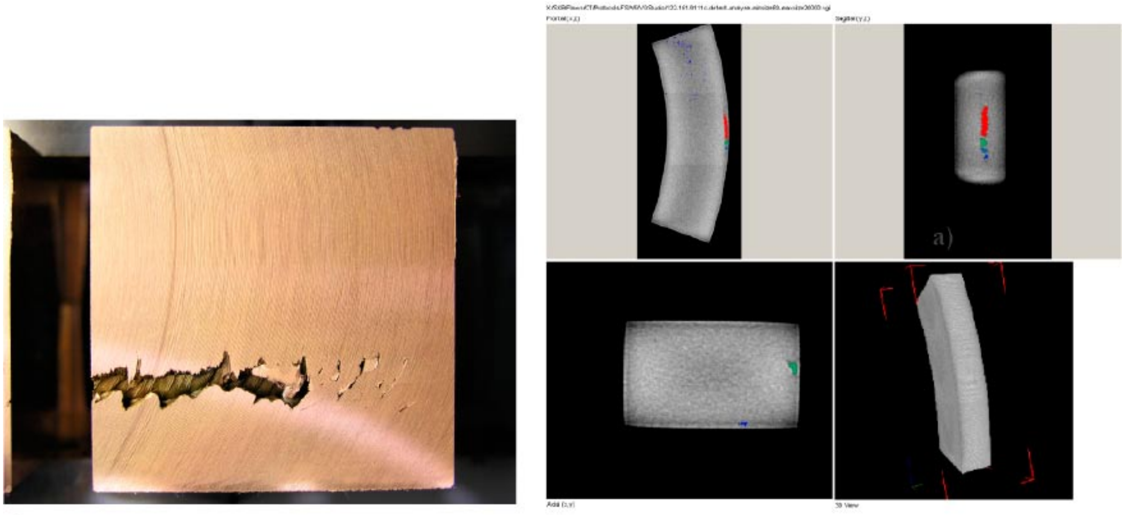

a) **b)**

Figure 8-4. *Cross section FSW5-136 (a) and CT wormholes (b).*

8.2.1 Results for electron beam welding (EBW)

Figure 8-5 shows the basic “*â* versus *a*” logarithmic diagram for the radiographic maximum contrast as a function the discontinuity size penetrated by the X-rays. The dependence is quite linear but shows a considerable scatter. The original values are shown in the diagram on the upper side side. The lower diagram shows the values without outliers. These version is more reasonable because the discontinuities behind the outliers were created with perturbations to the welding process far outside the normal parameter window.

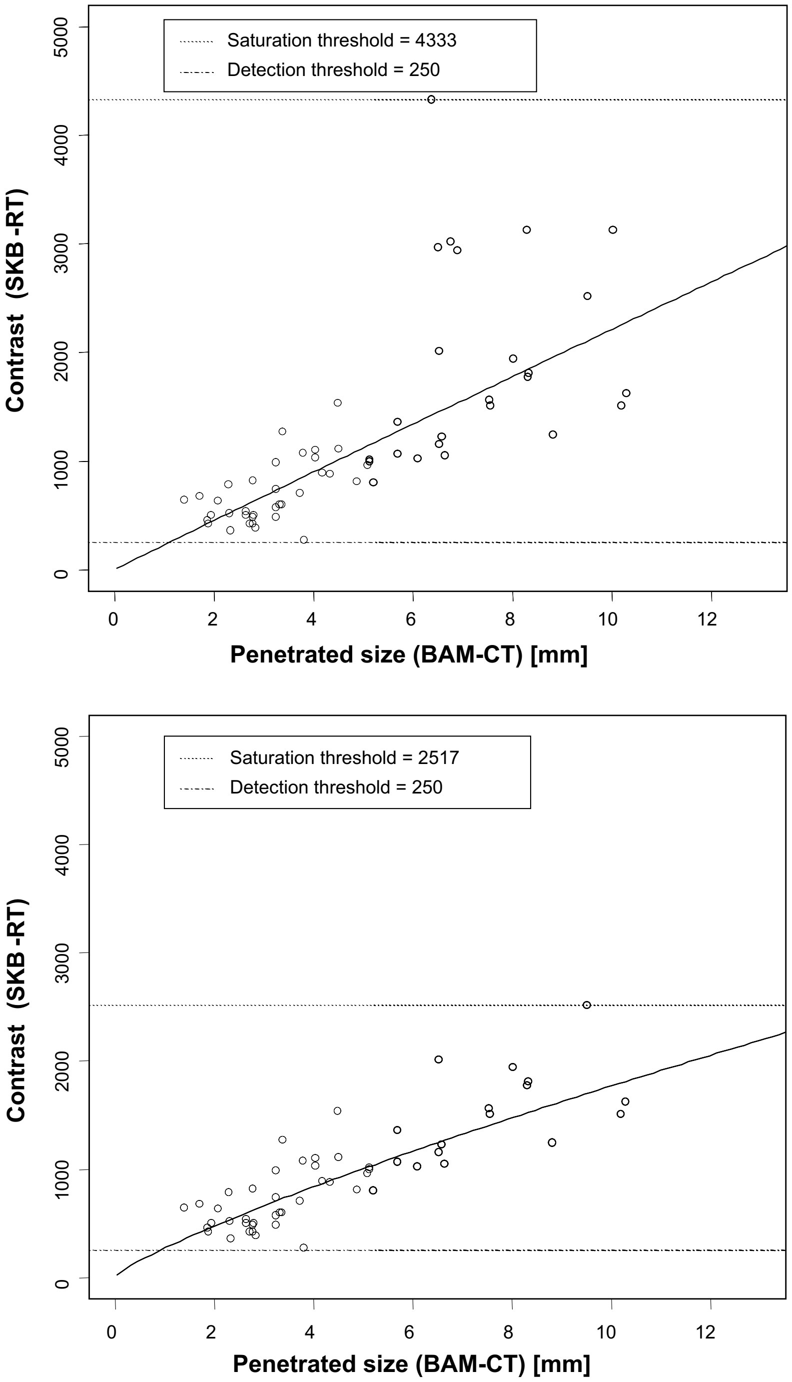

Figure 8-5. *L025 RT scatter diagram.*

The corresponding probability of detection and its lower confidence bound Figure 8-6 yield an $a_{90/95}$ value of about 2 mm for the penetrated size (2.3 with outliers and 1.9 without). Now we have to make sure the corresponding radial dimension will not exceed the critical size for all penetrated sizes below $a_{90/95}$.

Figure 8-7 shows the discontinuity size statistics, where the penetrated sizes are plotted against the radial dimensions for all observed volumetric discontinuities for the EBW. The critical region is the red hatched area, where discontinuities with critical radial dimensions above the critical size would occur belonging to sizes a below $a_{90/95}$. As seen in the Figure 8-7, the real discontinuity configurations are far away from this. The radial

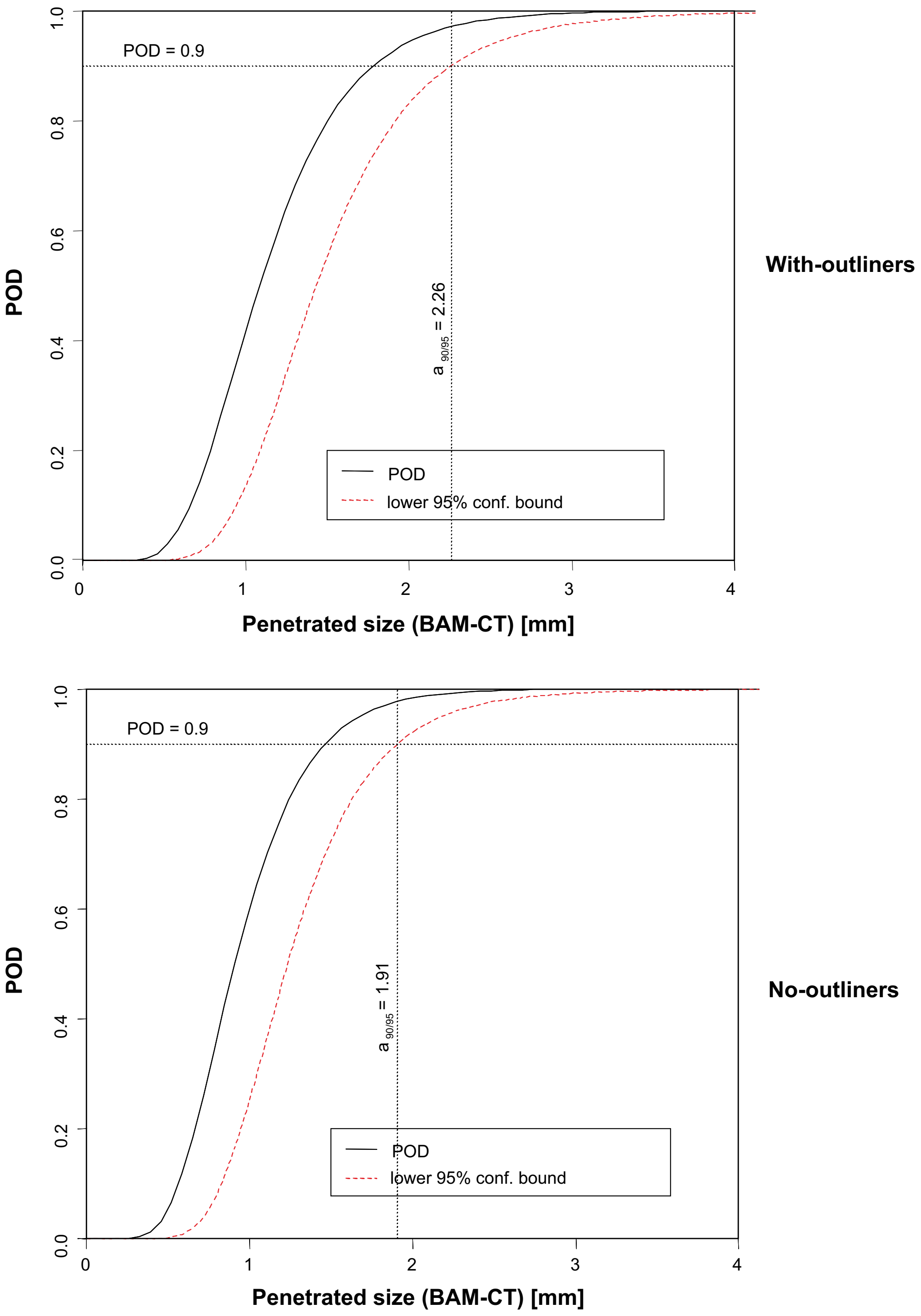

Figure 8-6. *L025 RT POD.*

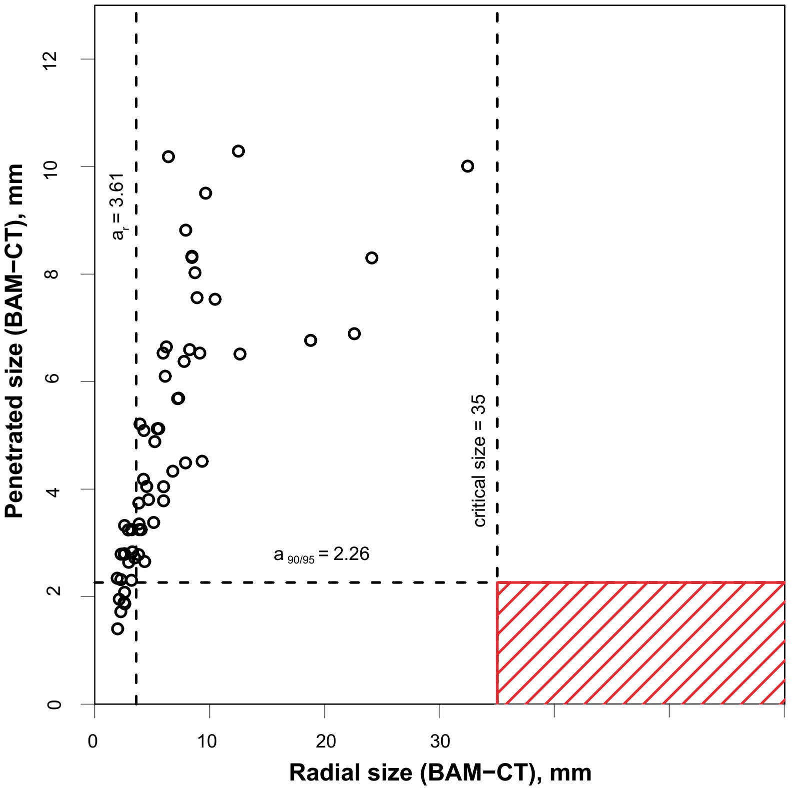

With-outliners

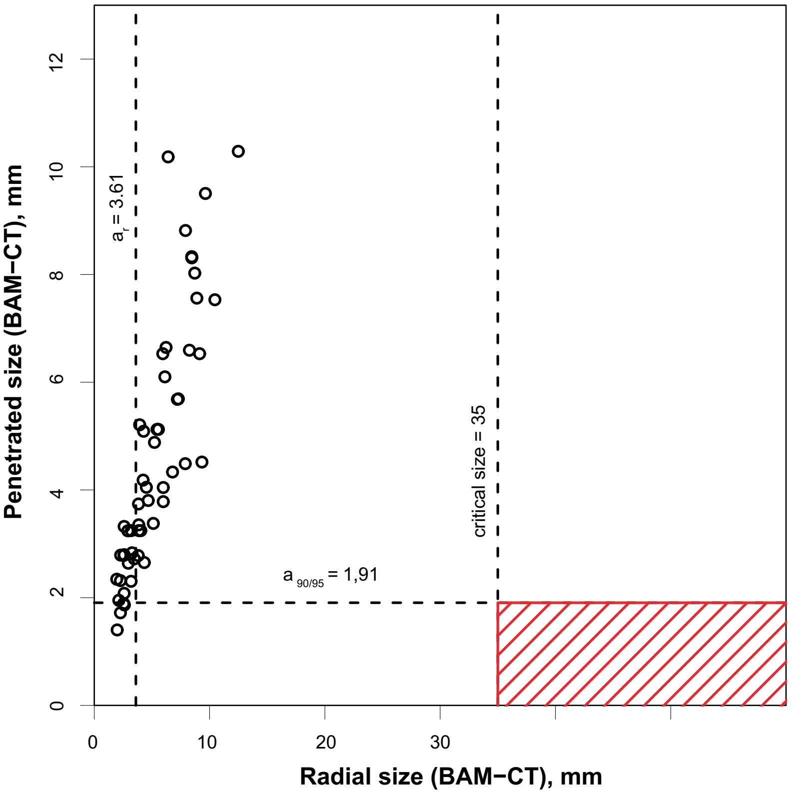

No-outliners

Figure 8-7. *L025 RT critical region.*

disconinuity a_r dimension belonging to $a_{90/95}$ is about 3.6 mm. For an exact determintation of the corresponding radial dimension a complete geometrical model for the discontinuities shape would be necessary. The data points were too few for this that is why we turned to an empirical assessment: The value a_r is taken as the maximum radial size between the discontinuities with the area/penetrated length less than $a_{90/95}$ plus 1 mm. The 1 mm is for the uncertainty in the radial dimension from destructive testing/reference methods.

The possible influence of an uncertainty in the reference HECT method is treated in Section 8.3.1 when the experimental results are compared to theoretical forecasts.

The Figure 8-8 to Figure 8-10 show the same types of diagrams (as presented in Figure 8-5 to Figure 8-7 for RT) for the UT-investigation of area like discontinuities for EBW. The $\hat{a}$ is the ultrasonic echo height and a is the reflecting area of the discontinuity. The scatter of signals is wider and the $a_{90/95}$ is larger. When the area is plotted in a logarithmic scale the "$\hat{a}$ *versus* a" looks quite linear even when the bigger flaws of the right hand side are taken into account which are not so typical for the EBW process. As seen in Figure 8-10: L025 UT critical region, again all observed discontinuities are far away from the critical region.

These results should be taken as a rough confirmation that the SKB NDT system is able to detect the volumetric discontinuities with X-ray technique and the area like discontinuities with UT phased array technique with high probability already far below all critical values. Since for EBW no destructive tests have been carried out the $a_{90/95}$ might change a couple of millimetres due to the uncertainty of the true a values determined via reference methods. The effort of destructive tests has not been made for EBW since the focus of attention switched to FSW in April 2005. For this reason an error estimation of the influence of the reference method's uncertainty on the POD was done. For the error in the reference value taken from UT-transmission (L025 area like flaws) the analysis is done below and for the uncertainty from HECT for the volumetric flaws it is done in Section 8.3.1.

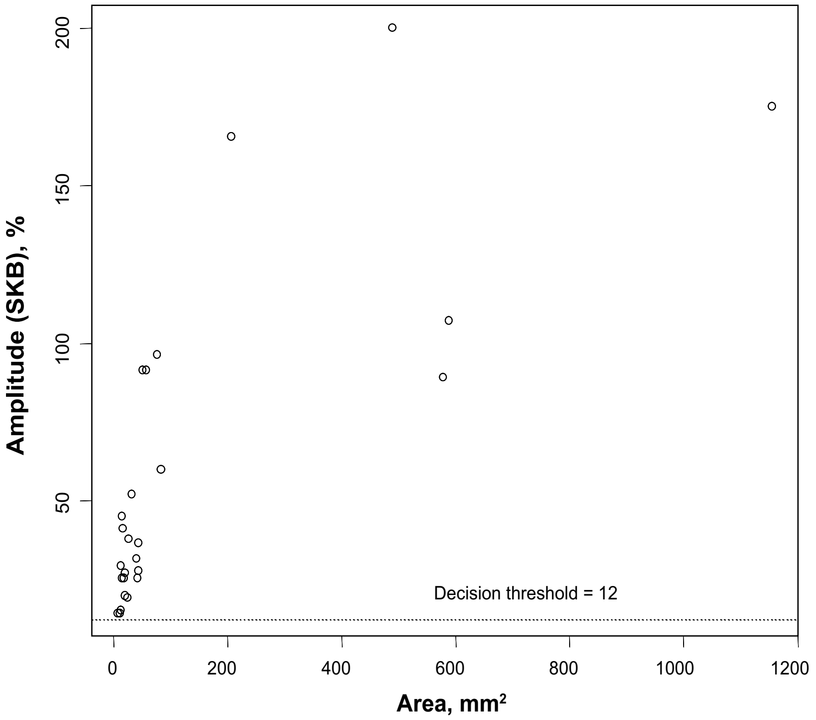

Figure 8-8. *L025 UT scatter diagram.*

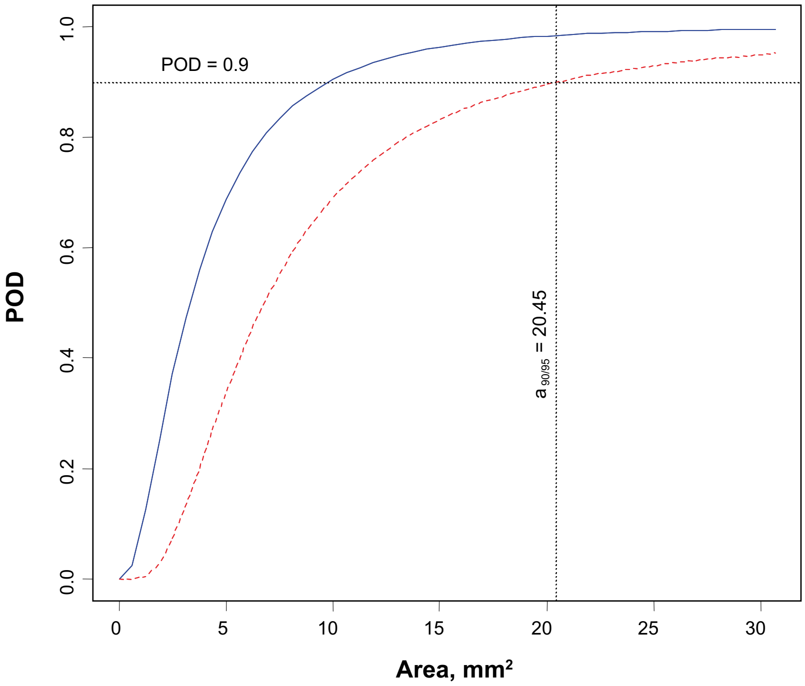

Figure 8-9. *L025 UT POD.*

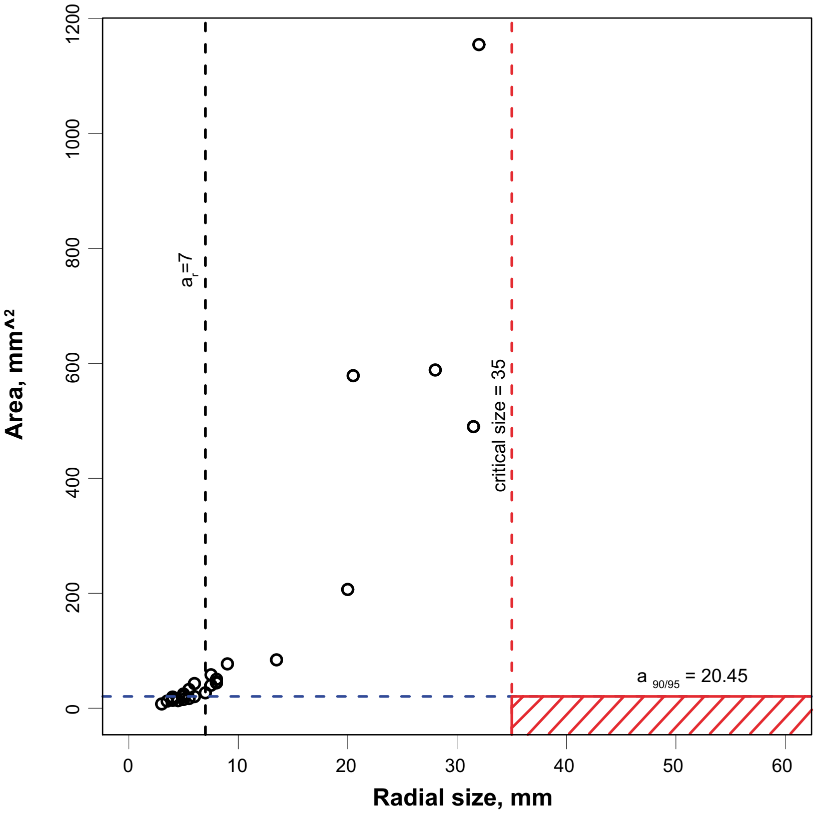

Figure 8-10. *L025 UT critical region.*

Influence of the limited resolution and uncertainty of the reference ultrasonic inspection on the POD

The problem

It is known that the measured values of the indication area used as independent variables in the investigation of the ultrasonic testing, are not known exactly, but contain measurement error that influences the POD curve and thus the $a_{90/95}$ value and should be taken into account. Moreover, it has been found that the reference ultrasonic inspection is only able to resolve discontinuities possessing the linear size larger than a certain value, while clusters of smaller discontinuities may be represented as single discontinuities by the inspection system. However, both the area and the number of detected discontinuities also influence the POD curve and thus the $a_{90/95}$ value. Therefore the influence of the measurement error and of the possible representation of multiple discontinuities as one discontinuity on $a_{90/95}$ computationally as described e.g. in /24/ were investigated. To estimate the influence of the measurement error recalculations of $\mathrm{a}_{90/95}$ were performed repeatedly, based on theorethically or practically justified perturbations, for the independent variable (the area in this case). To estimate the influence of the possible mis-representation of multiple discontinuities, large indications were randomly split into smaller ones and $a_{90/95}$ was recalculated. The concept used is described in more detail below.

Measurement error, circular model

The model of the measurement errors for flat bottom holes (FBH) reflectors as stated in the Section 5.4 is as follows: FBH having the diameter of less than 3 mm, provided they are detected, are measured as if they had the diameter of 3 mm, and the diameter of larger reflectors is known to be possibly over- or underestimated by up to 1.5 mm. Since the independent variable of interest is the area, and not a linear size of the reflectors, it is necessary to assume a model relating the linear size to the area. A circular model of the indications was considered, i.e. every indication is considered to be a circle and thus can be described by its diameter. Now the change in the diameter can be easily propagated to the area. Namely, let S denote the area of an indication. The diameter d is proportional to the square root of the area:

$$d = 2\sqrt{\frac{S}{\pi}}$$

Now let Δd be the difference between the true diameter and the measured value. The area of the indication having the diameter $d+\Delta d$ is expressed as the function of the original area S and of Δd:

$$S' = S + \frac{\pi}{4}\left(2\sqrt{\frac{4S}{\pi}}\Delta d + (\Delta d)^2\right)$$

The obtained expression can now be used to calculate the area S' of the perturbed indication.

Influence of the reference measurement uncertainty

In order to investigate the influence of the measurement error in the area on the $a_{90/95}$ value the computation is repeated 1,000 times. For the perturbation of the diameter, Δd, a uniformly distributed random numbers in the range (–1.5; 1.5) mm was used. The perturbed area is computed as described in the previous paragraph.

Table 8-1 shows the distribution of the $a_{90/95}$ values across the repetitions. Figure 8-11 presents the same data in form of a box plot (see Section 8.4 for an introduction to box plots).

Although the perturbations introduced to the diameter are symmetric, the box plot is not. This asymmetry is explained by the fact that the increase of the circle area caused by the growth of the diameter by an amount Δd is larger than the decrease of the area caused by the diminution of the diameter by the same amount.

Influence of the limited resolution, artifical splitting of large discontinuities

The goal is to model the possible representation of multiple small discontinuities as a larger one by randomly splitting larger discontinuities. In the Section 5.4 it is stated that single discontinuities can be resolved provided their linear size is greater than 3 mm. Again assuming the circular discontinuity shape, a list of candidates for splitting from discontinuities having the area larger than $\frac{\pi 3^2}{4}$, or about 7.1 mm^2 were constructed (it should be noted that almost all of the discontinuities fall into this cathegory). Further, with the probability of 50% every candidate were split into two parts having the equal area, while retaining the same amplitude value for both parts. This process provides new input data for the $a_{90/95}$ calculation. By repeating the described process multiple times, the distribution of $a_{90/95}$ was obtained. Table 8-2 shows the distribution of $a_{90/95}$ after 1,000 repetitions, and Figure 8-12 presents the same in form of the box plot.

The obtained $a_{90/95}$ values are smaller than that based on the unmodified reference data. This is reasonable, since the larger number of indications leads to the higher confidence bound. Moreover, splitting of the discontinuities while retaining the same amplitude value results in faster growth of the regression line describing the dependence of the signal from a discontinuity on its size.

Table 8-1. Descriptive statistics of the $a_{90/95}$ showing its sensitivity to the perturbations of the area (perturbation of 0 down to 1.5 mm, 1,000 repetitions).

	mean	std. dev.	min	1st quantile	3rd quantile	max
$a_{90/95}$, mm^2	22.32	3.03	14.76	20.15	24.32	33.45

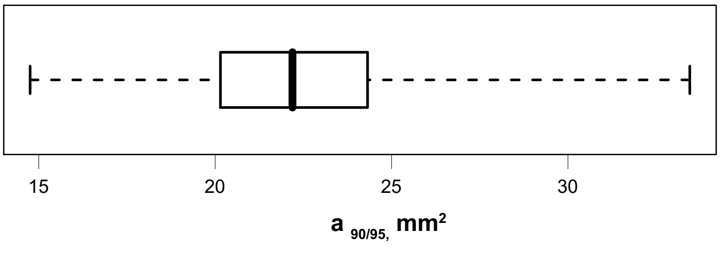

Figure 8-11. Box plot of the $a_{90/95}$ after 1,000 computations based on the perturbed values of the area.

Table 8-2. Descriptive statistics of the $a_{90/95}$ showing its sensitivity to the possible mis-representation of the clusters of smaller discontinuities (resolution 3 mm, probability of mis-representation 50%, 1,000 repetitions).

	mean	std. dev.	min	1st quantile	3rd quantile	max
$a_{90/95}$, mm^2	11.90	1.38	9.41	11.05	12.96	15.61

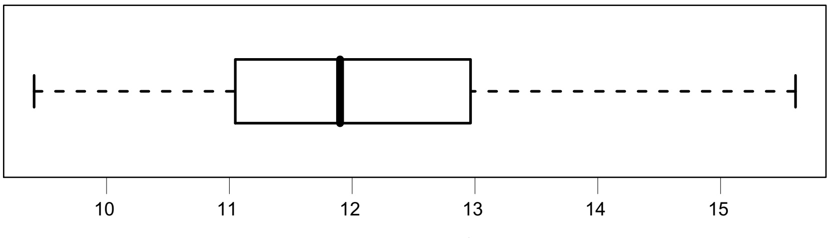

Figure 8-12. *Box plot of the $a_{90/95}$ after 1,000 repetitions based on modeled possible misrepresentations of the clusters of smaller discontinuities.*

Uncertainty in terms of the radial size

Results obtained in the previous subsections describe the uncertainty of $a_{90/95}$, whereas the value of interest is the radial size a_r. As no physical model relating $a_{90/95}$ and a_r has been established so far, the obtained $a_{90/95}$ values to a_r were transferred according to the following principle:

$$a_r = \max_{z \in Z}\{a_r^{(z)}\} + 1, \text{ where } Z = \{z : a^{(z)} \le a_{90/95}\}$$

In other words, as a_r is the radial size of the largest discontinuity having the area not larger than $a_{90/95}$ used, with additional 1 mm distance.

To compute the lower and upper values of a_r have the 1st and 3rd quartiles of the $a_{90/95}$ distribution been used. Figure 8-13 shows the influence of the reference measurement uncertainty in terms of the radial size and is based on the values given in the Table 8-1 and illustrated as the edges of the boxed part on the Figure 8-11. Figure 8-14 shows the influence of the limited resolution of the reference system and is based on the values given in and Table 8-1 the and shown in the Figure 8-12, respectively.

8.2.2 Results for friction stir welding (FSW)

Below the “Adapted POD Results” for the wormholes for RT- and UT-inspection are presented with the following pattern: First we present the “$\hat{a}$ versus a” scatter diagrams where the $\hat{a}$’s in terms of maximum radiographic contrast and the maximum echo height, respectively are plotted in dependence of the “a” in terms of penetrated length and area perpendicular to the sound beam. For these signal sizes the actual thresholds are applied yielding the mean POD curves and the 95% confidence bound and the $a_{90/95}$ as key parameter. As discussed above the additional scatter diagram showing the statistics of the “a” dimension in dependence of the radial dimension reveals for all cases that the “critical” region with critical radial dimensions belonging to “a”-values below $a_{90/95}$ are far away from the actually occurring configurations.

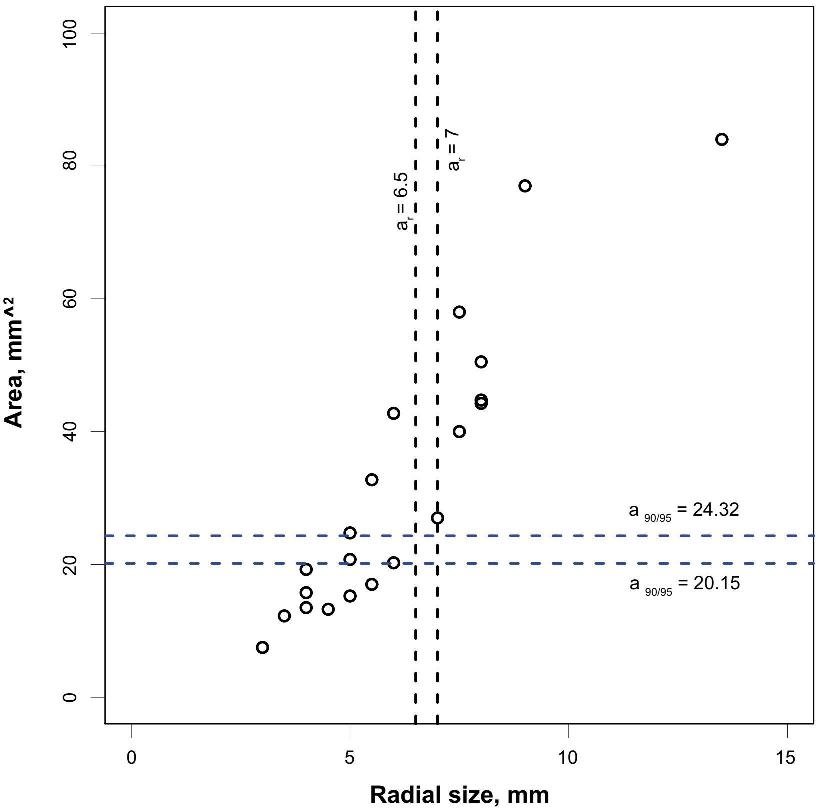

Figure 8-13. *Influence of the $a_{90/95}$ distribution on the a_r due to the measurement uncertainty of the reference system.*

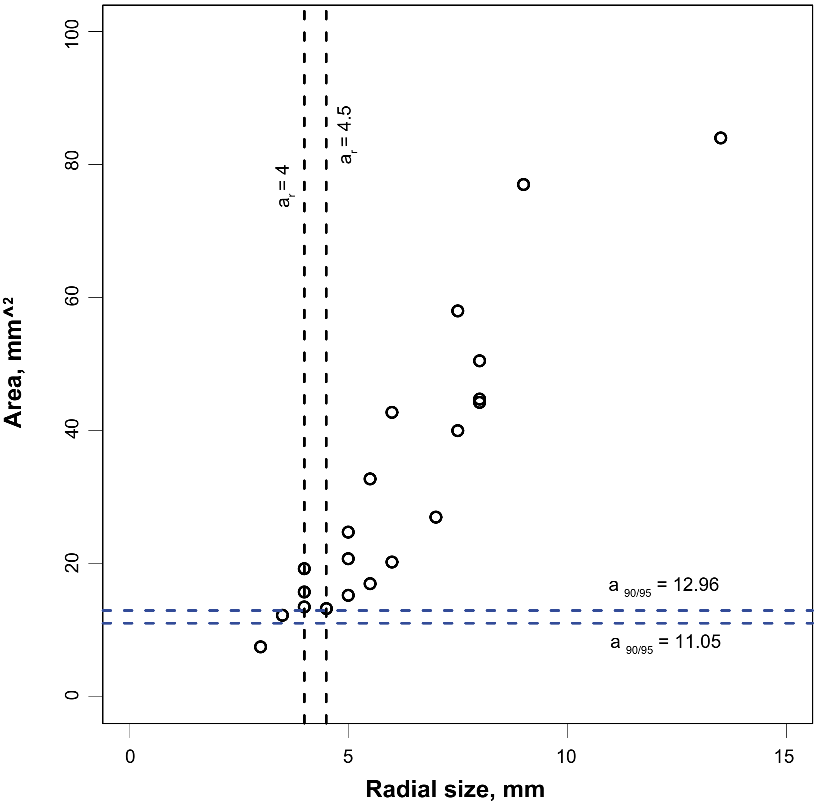

Figure 8-14. *Influence of the $a_{90/95}$ distribution on the a_r due to the limited resolution of the reference system.*

In April 2005 an additional measurement campaign of BAM took place at the canister laboratory in Oskarshamn (see revised report March 2006), One of the practical results for the radiographic testing was that the variation in signal to noise ratio according to the growing penetrated wall thickness requires also different decision thresholds for discontinuity detection to be considered in the POD curves. The smallest value (grey values) applies for the discontinuities above the centre of the weld (80), medium in the centre (160) and the biggest below (240). All the levels are below the 250 from the former investigation which equals the level set in the SKB procedures, which represents in this way a very conservative estimation.

RT wormhole

Figure 8-16 shows the "â versus a" scatter diagram in terms of maximum radiographic contrast versus the by the X-rays penetrated length. A linear behaviour can be seen but with considerable scatter which might be due to the zig-zag shape (see Figure 8-15) causing uncertainties in the determination of the penetrated length. Further the data should be separated in future according to the position above, centre and below as discussed above.

The resulting POD curve and the 95% confidence bound in Figure 8-17 indicate an $a_{90/95}$ of 2.6 mm for the penetrated length. The corresponding radial dimension of the discontinuities "to detected for sure" is 4 mm as indicated in Figure 8-18. This is a very conservative assessment and can be improved by applying the three lower thresholds determined detailed for centre, below and above on the basis of perceptibility of ASTM step-hole penetrameters as described in Section 7.2.

The three different decision thresholds yield new POD curves with the corresponding $a_{90/95}$ values of 0.9, 1.6 and 2.3 mm for above, center and below. In Figure 8-20 these $a_{90/95}$ values are indicated for the estimation of the corresponding detectable radial dimension which is improved in the case of $a_{90/95}$ = 1.6 to 2.3 mm. For the lowest value the data point density becomes too low in this region we turned to the safest statement: the detectable radial dimension is about 2 mm.

The influence of the uncertainty in the reference values is investigated in Section 8.3.1.

Figure 8-15. *Volumetric discontinuity.*

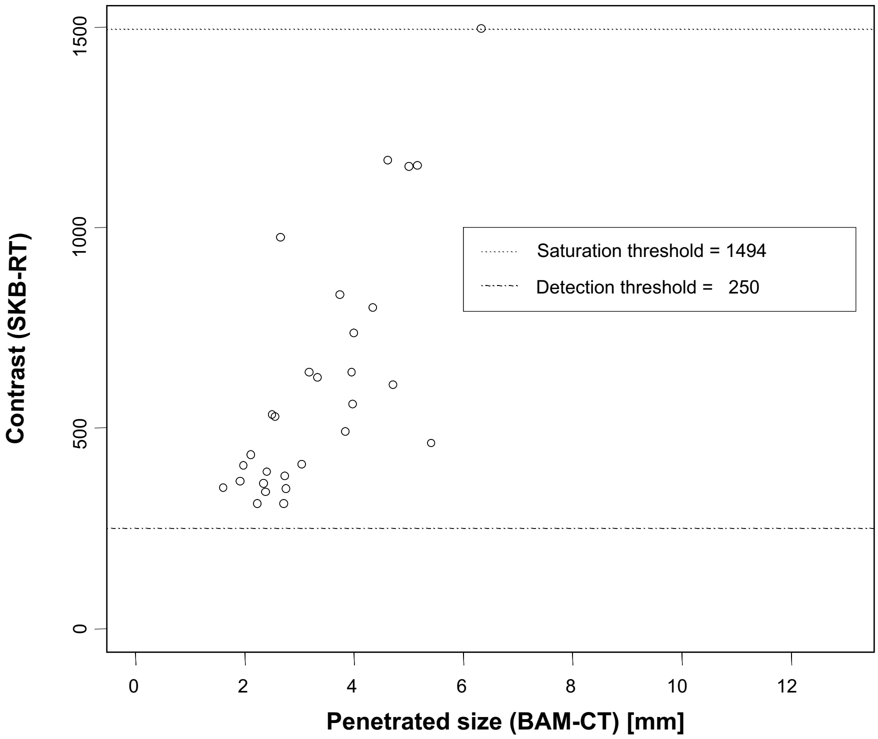

***Figure 8-16.** FSW5 RT scatter diagram.*

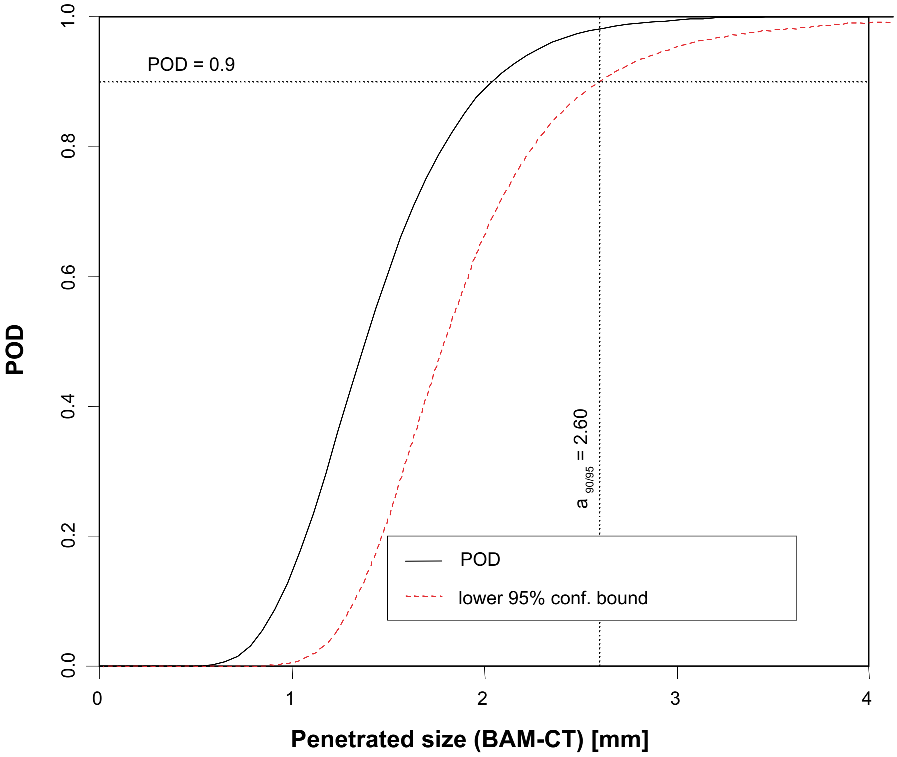

***Figure 8-17.** FSW5 RT POD.*

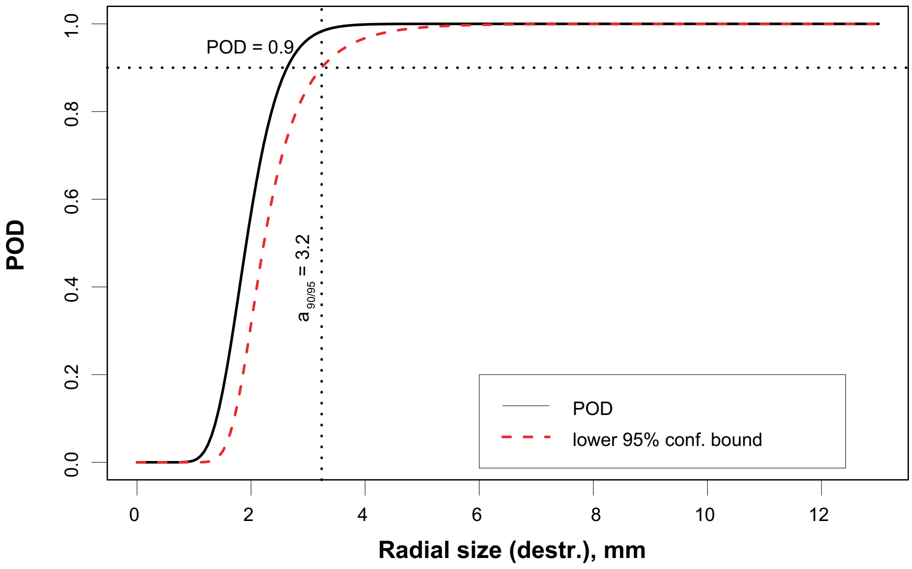

Figure 8-18. *Critical region based on radiographic inspection of volumetric discontinuities with the threshold 250 levels.*

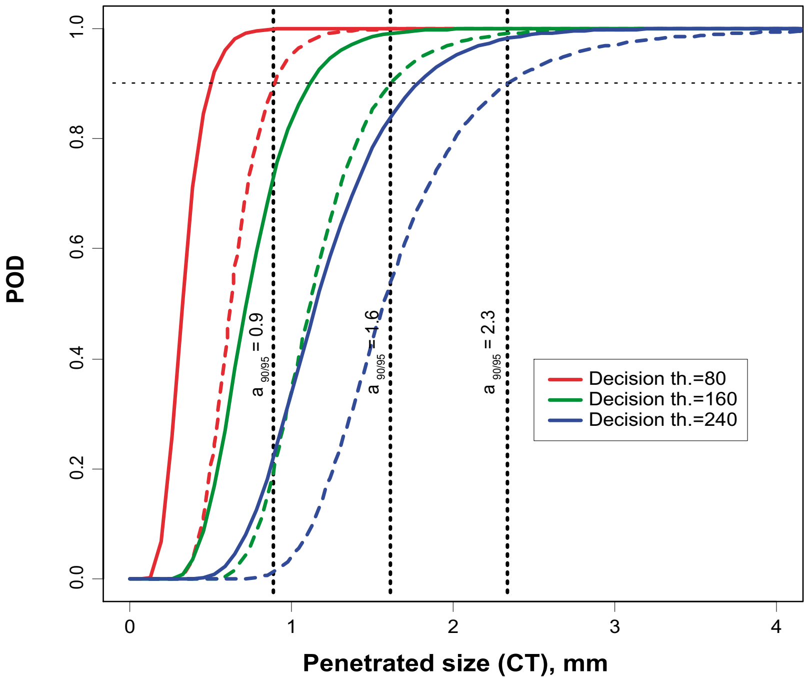

Figure 8-19. *POD curves based on radiographic inspection of volumetric discontinuities with different threshold values (80, 160, 240 levels).*

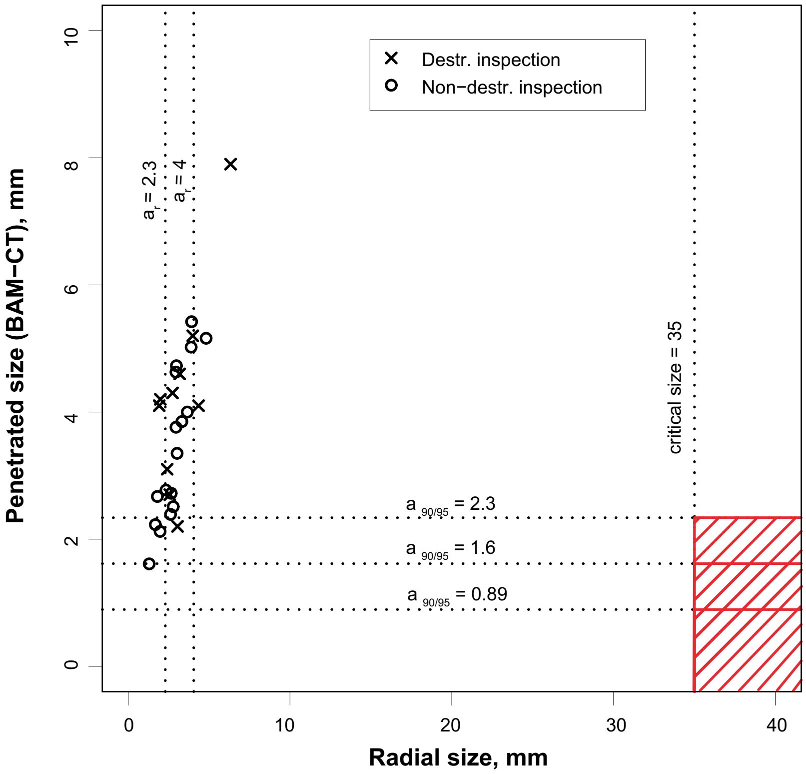

Figure 8-20. *Critical region based on radiographic inspection of volumetric discontinuities with different threshold values (80, 160, 240 levels).*

UT wormhole

The same set of wormhole discontinuities as investigated above were inspected by ultrasound with "*a*" as area perpendicular to the sound beam and $\hat{a}$ as maximum echo amplitude. The reference value for the area was taken from results from destructive tests (cubes). The scatter diagram in Figure 8-21 indicates the already known fact that these discontinuities are not ideal reflectors of ultrasound and that the echo amplitude is affected by a number of other factors than the discontinuity size as listed in /23/ for UT. The corresponding POD curve in Figure 8-22 and the "critical region"-Figure 8-23 reveals for $a_{90/95}$ 12.5 mm² and a corresponding detectable radial dimension of 6.3 mm. The crosses in diagram 8.2–20 represent results from destructive testing.

Both methods are capable to detect the wormholes far below the required critical size but show even a potential to detect smaller discontinuities in studying the detection processes in more detail.

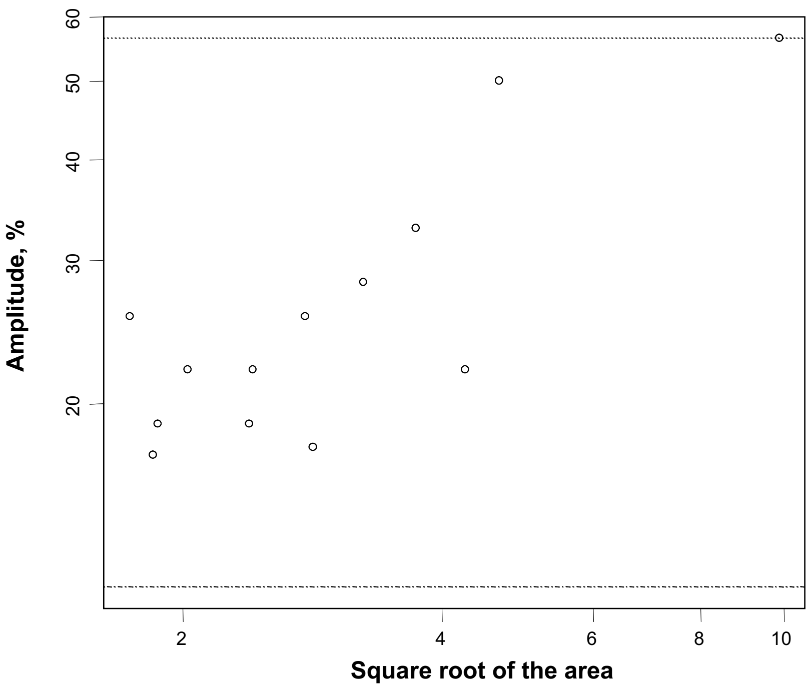

Figure 8-21. FSW5 UT scatter diagram.

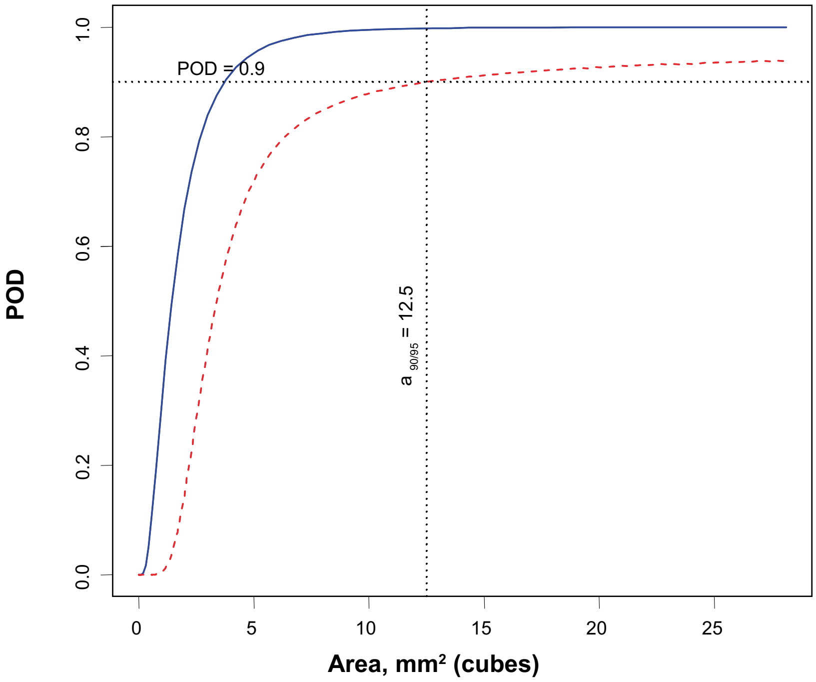

Figure 8-22. POD curve based on ultrasonic inspection of volumetric discontinuities (threshold 15%).

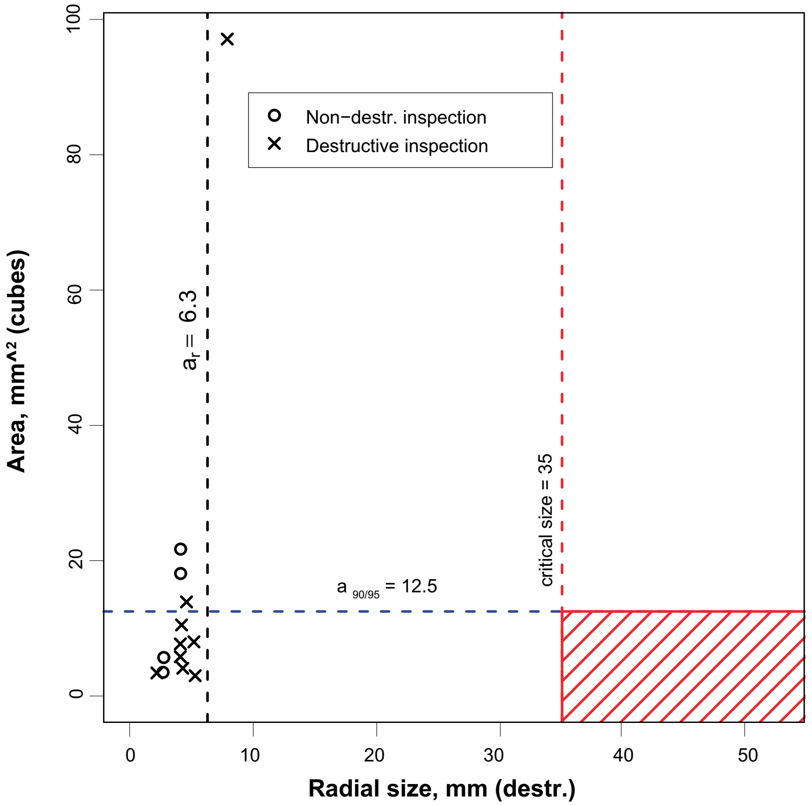

Figure 8-23. *Critical region based on ultrasonic inspection of volumetric discontinuities (threshold 15%).*

JLH

Figure 8-24 shows a typical cross section of a JLH (joint line hooking) discontinuity. It is clear that this shape not easily matching the empirical POD approach. The investigation was refined step by step: The first approach in investigating the JLH discontinuities was to apply the POD method in an empirical way. For this approach, the maximum echo amplitude was used as $\hat{a}$ as before. First, a totally empirical "$\hat{a}$ versus a" scatter (Figure 8-25) diagram and POD (Figure 8-26) were created. These included all the values of the SKB experiments which yields the $a_{90/95}$ equal to the detectable radial dimension of 4.0. In the next step, outliers (too small and too big values compared to a "normal" amplitude versus size behaviour – compare also the argumentation in 6.2.4), were excluded. This resulted in detectable radial dimension is 3.2 mm due to the decreased scatter.

A deeper analysis of the JLH geometry and echo heights showed that the "hook" part is in almost all cases indicated by the 0° or –10° sound beam and the straight part, the inclined plane or rectangle by the 10° and 20° sound beam. Consequently the forming of the POD separately for hook and rectangle with the corresponding angle of the sound beam should be considered. Because the number of data points becomes too small after separation hasn't this analysis been done yet. It might be considered as a future investigation to look deeper to the forming of the POD for the two parts of the JLH and the different angles separately in combining experimental and modelling insight after all the influencing factors has been listed carefully. It will depend on the importance of the JLH in the future welding process.

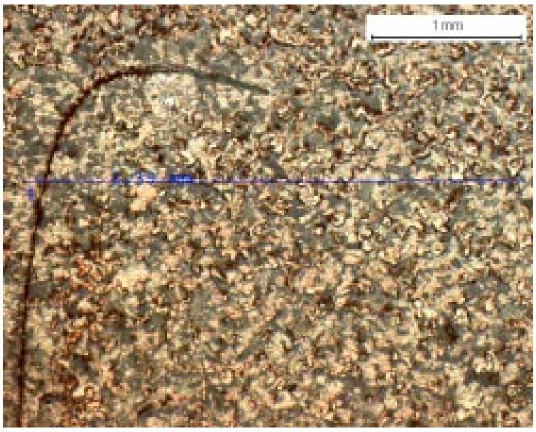

Figure 8-24. *Cross section of a JLH (joint line hooking).*

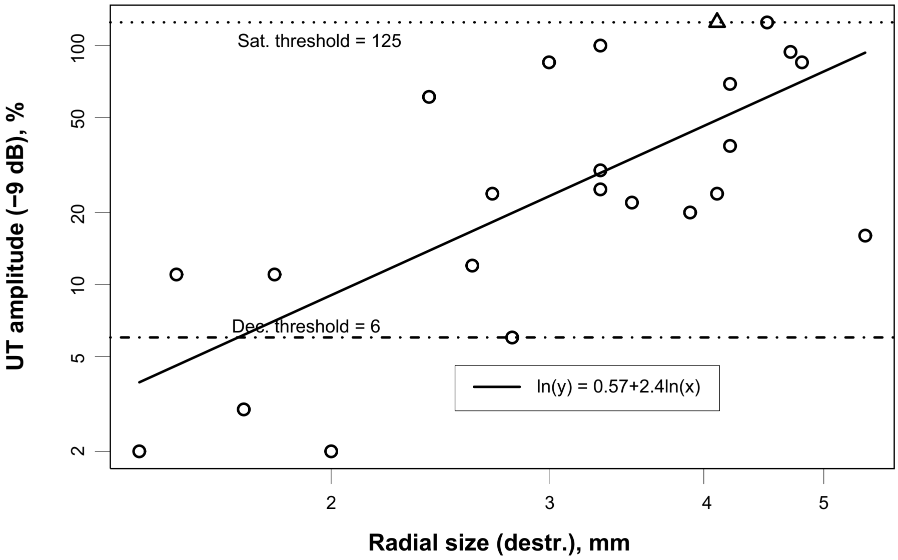

Figure 8-25. *Scatter diagram of the amplitude vs. radial size for the JLH-type discontinuities (log. axes).*

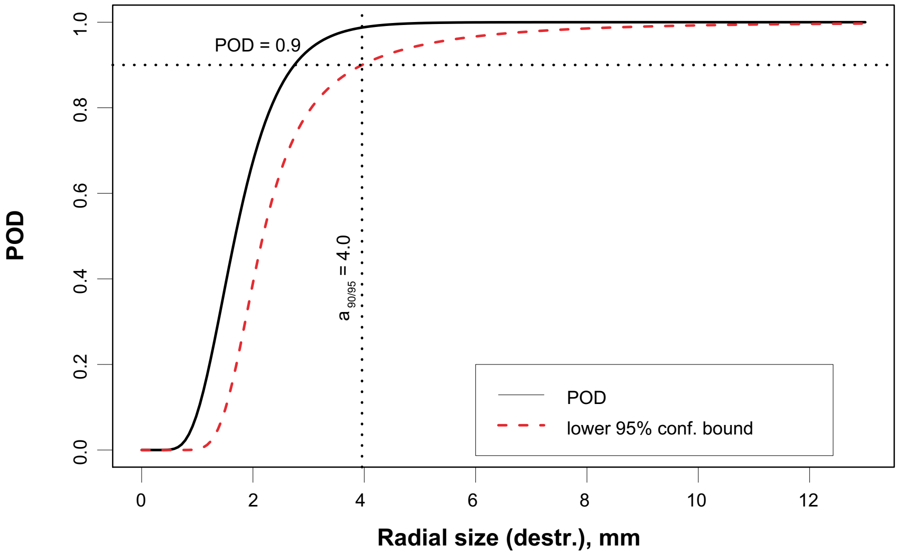

Figure 8-26. *POD curve for the JLH-type discontinuities (with outliers).*

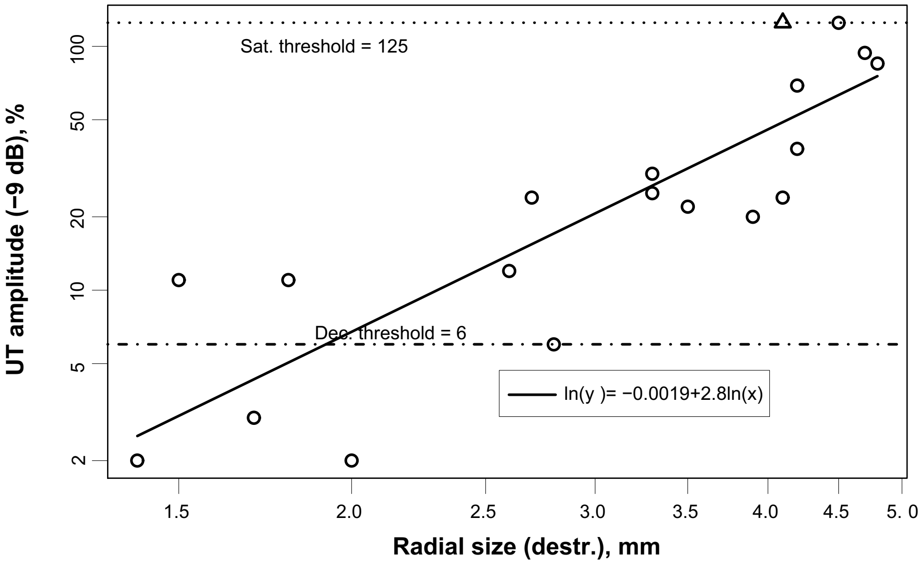

Figure 8-27. *Scatter diagram of the amplitude vs. radial size for the JLH-type discontinuities (log. axes, without outliers).*

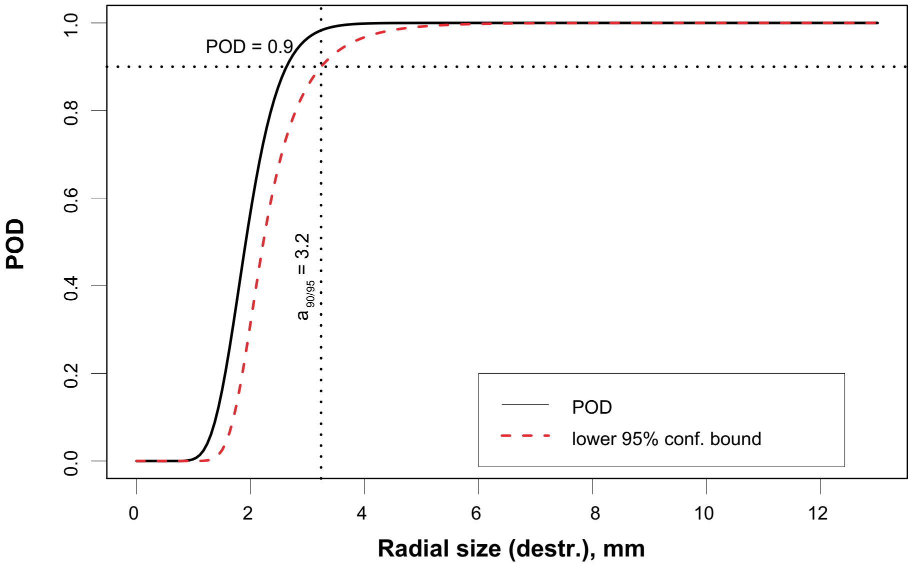

Figure 8-28. *POD curve for the JLH-type discontinuities (outliers excluded).*

8.3 POD from modelled data

8.3.1 Radiography

POD from simulated radiography data

Because almost all discontinuities are of sizes above the $a_{90/95}$ it is important to make sure that the "foot region" of the POD is described correctly. A way to find out this is by using the results of the X-ray simulation tool. For the theoretical POD assessment to evaluate the reliability of radiographic testing according to /20/ the following assumptions are made: (*i*) the contrast of an indication can be directly correlated with the size of the discontinuity, particularly with the wall thickness difference in beam direction, (*ii*) the contrast of an indication contains all information necessary to interpret the image, (*iii*) the noise in the radiographic image is normally distributed with zero mean. The contrast is measured as the difference between the maximum gray value at the discontinuity indication and the average gray value at the same position without a discontinuity present.

The $\hat{a}$ (maximum contrast) over a (pore diameter) data are shown in Figure 8-29. For pore sizes above 1 mm a linear correlation between pore size and contrast is found. For smaller pore sizes this correlation becomes nonlinear. This behaviour can be understood easily from the attenuation law. If the pore size, i.e. the wall thickness difference, is small compared to the total penetrated wall thickness, the resulting contrast ΔI is proportional to the difference in penetrated length Δd.

$$\begin{aligned} \Delta I &= I_2 - I_1 \\ &= I_0 \left(e^{-\mu(d-\Delta d)} - e^{-\mu d} \right) = I_0 e^{-\mu d} \left(e^{\mu \Delta d} - 1 \right) \\ &\approx I \mu \Delta d \end{aligned} \tag{20}$$

The simulation was carried out for fictive pores from 0.1 to 3 mm diameter. The diameter works for pores as penetrated length and the contrast as $\hat{a}$. The behaviour of the mean contrast as well as for the maximum contrast was checked because the final POD estimation is planned to use a reasonable combination of both.

As expected, the best detectability is registered for exact pores simulated for maximum contrast detection. The contrast of the indications for pore sizes comparable to the system unsharpness or smaller is reduced due to the effect of unsharpness. The corresponding POD is given in Figure 8-30 for different decision thresholds $\hat{a}_{dec}$ reflecting a SNR of 2.7 for different noise contribution in the image. Additionally the $a_{90/95}$ values together with the 90% POD value are listed in Table 8-3. The calculated a_{90} and $a_{90/95}$ values increase with the amount of noise in the image. Anyway, indications from volumetric discontinuities larger

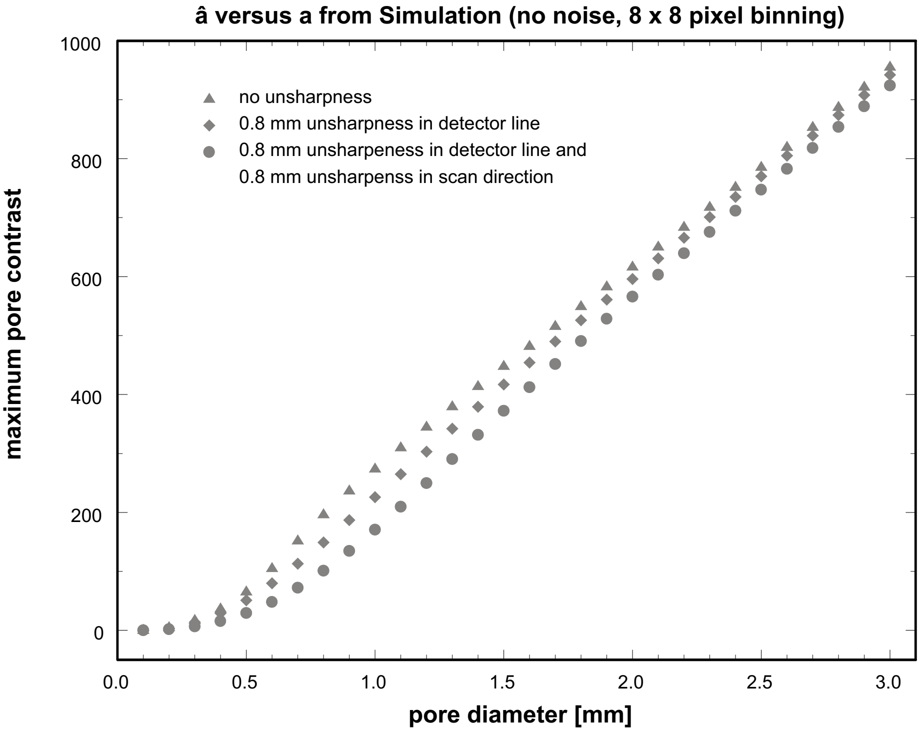

Figure 8-29. *Theoretical investigation: maximum contrast vs. pore diameter (no noise).*

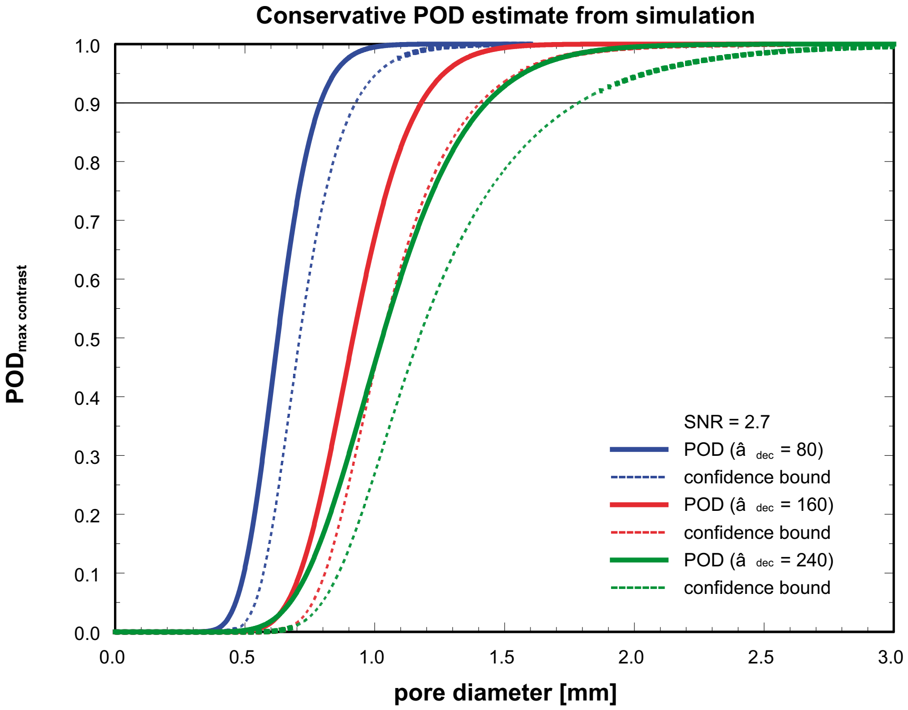

Figure 8-30. *Theoretical POD investigation.*

Table 8-3. Results of $a_{90/95}$ estimate from simulation.

contrast threshold	$a_{90/95}$	
	average pore contrast	max pore contrast
60 (SNR = 1)	0.75	0.48
120 (SNR = 2)	1.35	0.79
250 (experiment)	2.71	1.36

than 2 mm, which corresponds to a wall thickness change of about 1%, are detected with high reliability in any case. This result agrees with radiographic practice. As pointed out before, the presented POD evaluation gives a conservative estimate of the system reliability.

Critical discussion of experimental values of radiographic penetrated length using destructive results

Figure 8-31 shows the scatter diagram of the maximum radiographic contrast vs. penetrated length for the volumetric discontinuities in the friction stir weld FSW5 together with the fitted regression line and the "ideal" line corresponding to the attenuation coefficient measured experimentally (see the report on "BAM experiments at SKB 2005" summarized in Section 7.1). In the present section we will refer to the experimentally measured value of the attenuation coefficient and the corresponding line (green line in Figure 8-31) as "reference" value, since it serves as reference for the values determined by non-destructive testing.

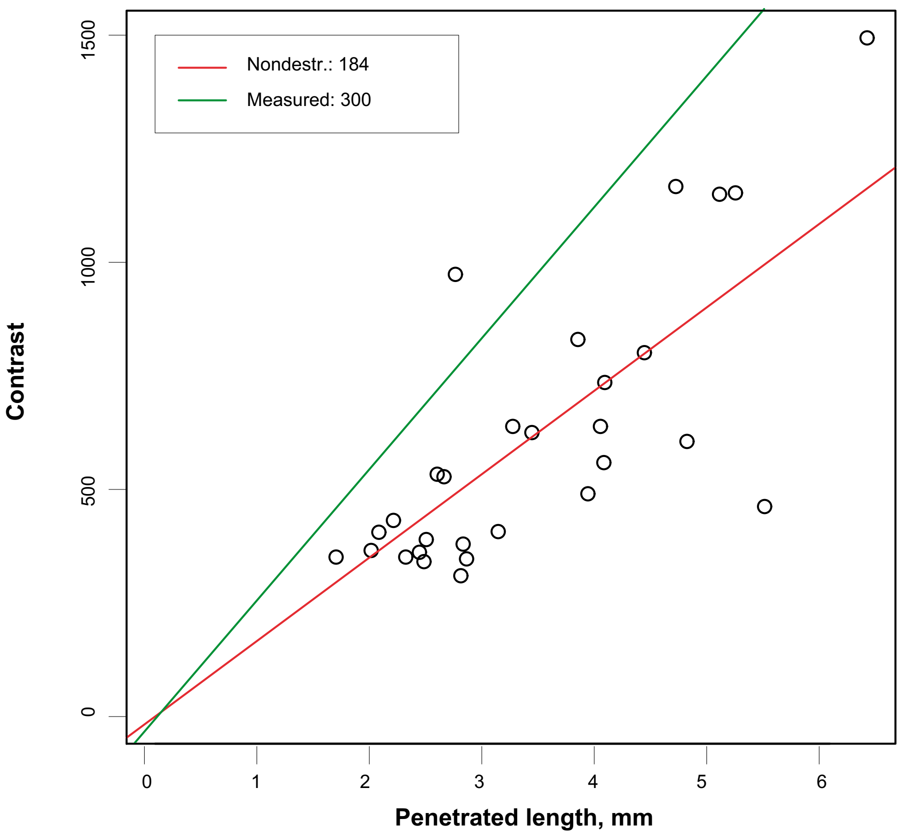

Figure 8-31. *Scatter diagram of the maximum radiographic contrast vs. penetrated length for volumetric discontinuities in the friction stir weld FSW5 and the reference line according to the attenuation law.*

It can be seen that the attenuation coefficient is lower (184×10^{-3} cm^{-1}) than the reference value according to the attenuation law (300×10^{-3} cm^{-1}). The purpose of the present section is the critical discussion of the possible reason for the mentioned discrepancy of 117×10^{-3} cm^{-1} (39%) between the slopes of the “ideal” and experimental lines.

Two hypotheses explaining the discrepancy have been established:

- the contrast has been measured too low,
- conversely, the penetrated length has been over-estimated.

To check whether the contrast has been under-estimated, the images of the image quality indicators (IQI) having the known thickness and present on the experimental radiographic image, have been investigated. The values are shown in the Table 8-4.

Although the values of the attenuation coefficient are scattered, the absolute deviation from the reference value does not exceed 45×10^{-3} cm^{-1} (15%). It follows that the magnitude of the difference between the contrast values for the IQI’s and the reference value cannot sufficiently explain the observed discrepancy for volumetric discontinuities.

To test for the over-estimation of the penetrated length, possibly due to the high noise level in the experimental data set and corresponding difficulties of the segmentation, results of the destructive testing have been used.

Table 8-4. Contrast values and corresponding attenuation coefficients for ASTM IQI's with known thickness.

ASTM No.	Thickness, mm	Maximum absolute contrast	Attenuation coefficient, $cm^{-1} \times 10^3$
40 (left)	1.016	345	339.566929
40 (right)	1.016	260	255.905512
80	2.032	539	265.255906

The results of the destructive testing were available as sets of high-resolution digital photos. In order to compute the penetrated length of discontinuities the following steps were necessary:

- registration of single images, i.e. the transformation of the images as to match fiducial points on the images (Figure 8-32),
- segmentation of discontinuities, i.e. the separation of the points belonging to the discontinuities from those belonging to the bulk material (Figure 8-33),
- ray tracing in order to calculate the number of voxels that belong to the discontinuities and have been traversed by the X-rays (Figure 8-34).

This process resulted in corrected values of penetrated length for certain discontinuities. Results are presented on Figure 8-35.

Based on the new results, the regression line has been recalculated and exhibited the slope of 313×10^{-3} cm^{-1}. This corresponds to the absolute deviation of 12×10^{-3} cm^{-1}, or 4%.

Furthermore, a POD curve has been plotted for updated results (Figure 8-36). The $a_{90/95}$ value decreased to 0.97 mm.

Finally, an updated diagram showing the radial size of volumetric discontinuities vs. the penetrated length is presented on Figure 8-37. The corresponding a_r value is 2.4 mm.

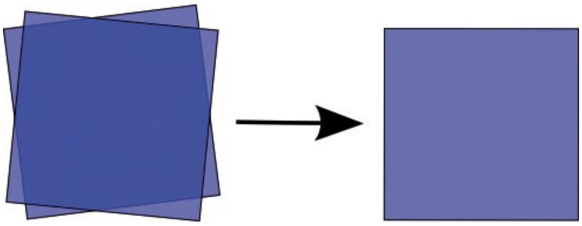

__Figure 8-32.__ Image registration.

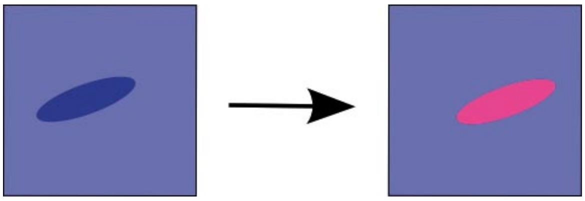

__Figure 8-33.__ Image segmentation.

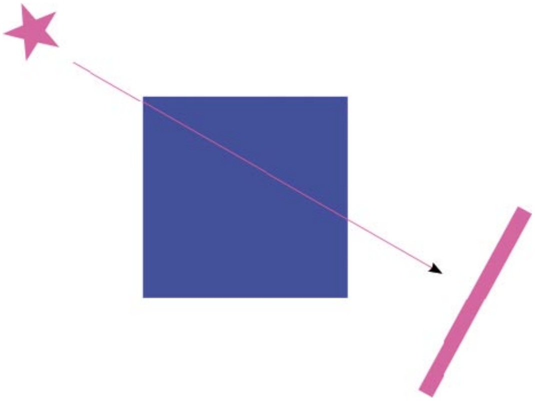

Figure 8-34. *Simulation of the radiography.*

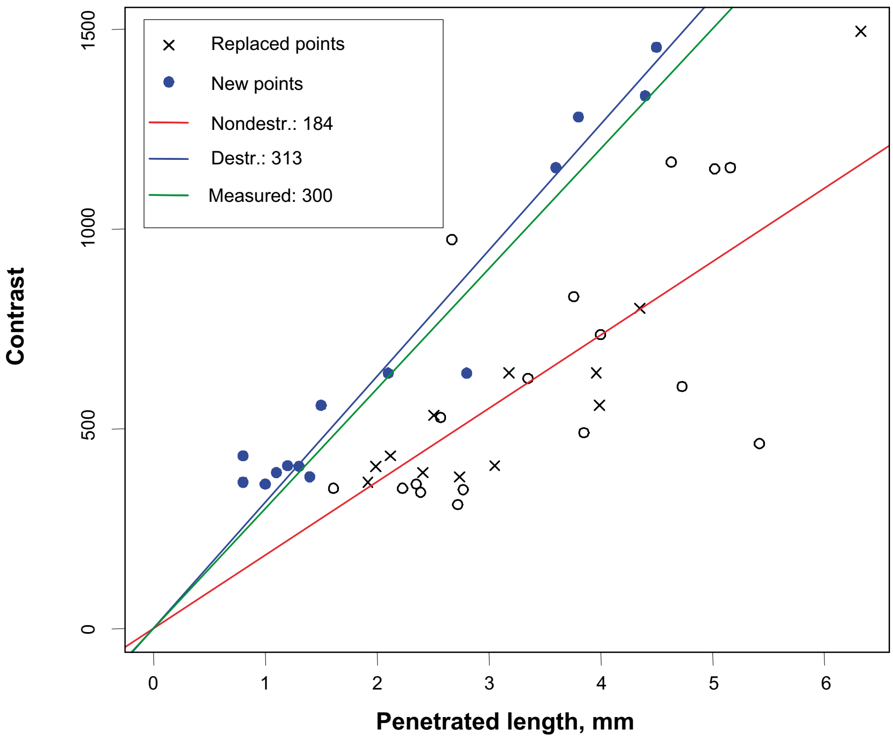

Figure 8-35. *Scatter diagram of the maximum radiographic contrast vs. penetrated length with destructive data.*

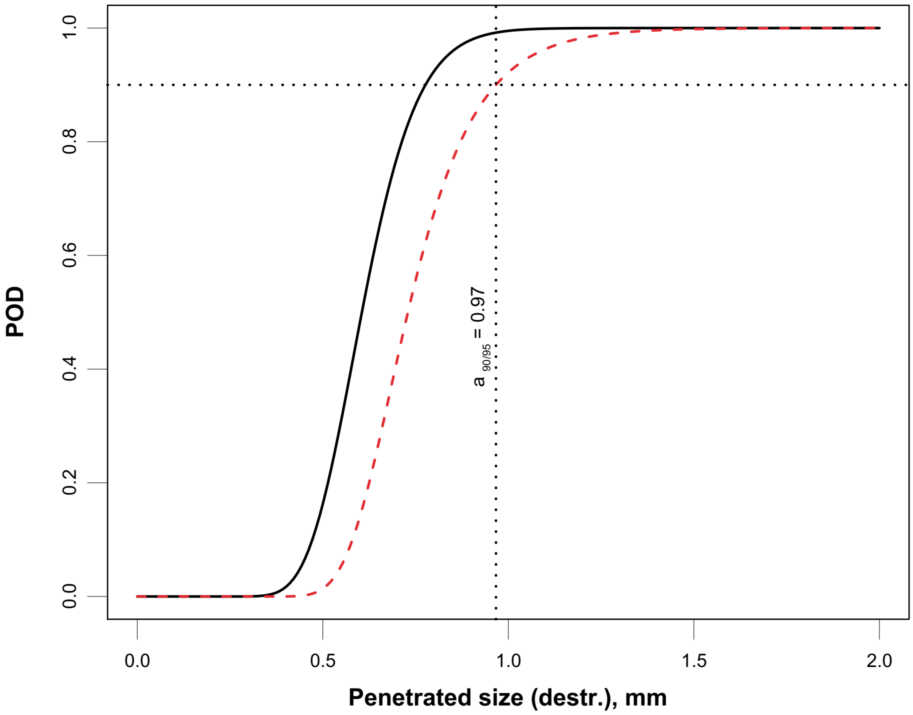

Figure 8-36. *POD curve and the 95% lower confidence bound based on the data obtained by destructive testing (threshold value: 250 counts).*

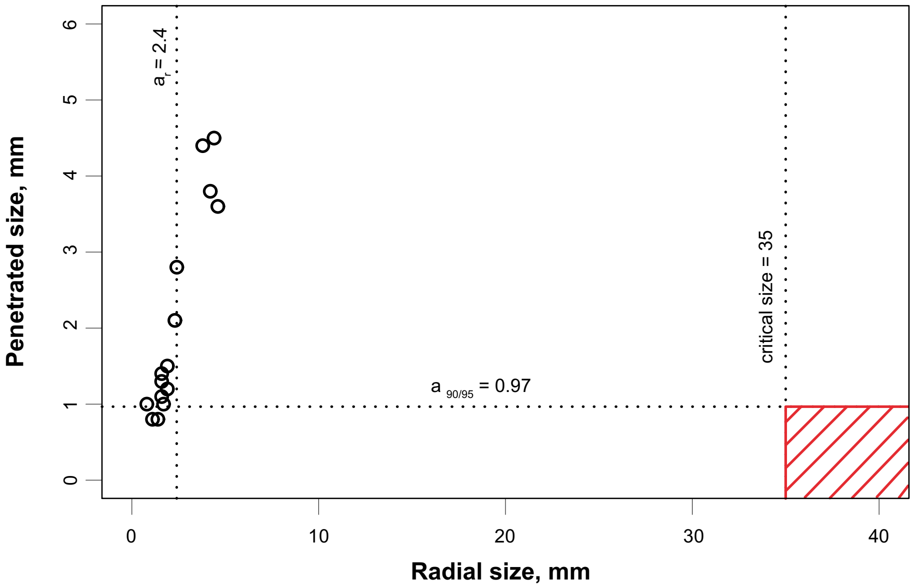

Figure 8-37. *Scatter diagram and the critical region of the radial and penetrated sizes of volumetric discontinuities.*

Conclusion

The correction of the sizes of discontinuities using the information from destruction testing displaces the experimental "$\hat{a}$ vs. a" line in good agreement with the ideal line of contrast vs. penetrated length. The corresponding $a_{90/95}$ value and the radial dimension a_r both move in direction of higher safety, i.e. a void with the diameter of 1 mm is detected with a high probability in radial direction also in good correspondence with the simulated POD for pores as discussed above in this section.

Correction of the penetrated sizes for the electron beam weld L025

In the previous paragraph penetrated sizes of volumetric discontinuities occurring in the friction stir weld FSW5 are investigated. It is shown that the penetrated sizes obtained by non-destructive testing (CT) are overestimated with respect to those obtained by destructive testing due to sub-optimal segmentation of the CT volumes. In the present section we transfer the results to the electron beam weld L025 by calculating and applying the correction factor for the penetrated size. The underlying assumption is that the sizes of volumetric discontinuities from CT data sets in the weld L025 have been determined using the same extraction procedures under the same conditions as FSW5.

Let $x_N^{(i)}$ be the penetrated size of the i^{th} discontinuity obtained by non-destructive testing (CT), and $x_D^{(i)}$ be the penetrated size of the same discontinuity obtained by destructive testing.

Consider the mean relative difference between $x_N^{(i)}$ and $x_D^{(i)}$:

$$q = \frac{1}{K}\sum_{k=1}^{K}\frac{x_N^{(i)} - x_D^{(i)}}{x_N^{(i)}} \tag{21}$$

where K is the number of discontinuities in the weld FSW5, for which both $x_N^{(i)}$ and $x_D^{(i)}$ are known.

Applying the equation (21) to the weld FSW5 yields $q = 0.42$, or 42%.

Penetrated sizes of volumetric discontinuities in the weld L025 corrected by subtracting 42% are shown in the Figure 8-38. The slope corresponding to the corrected values (350×10^{-3} cm^{-1}) is in better agreement with the measured value (300×10^{-3} cm^{-1}) than the uncorrected one (177×10^{-3} cm^{-1}). Using corrected penetrated sizes, newer calculation of $a_{90/95}$ was done and a value of 1.10 mm was obtained. The corresponding POD curve is shown on the Figure 8-39.

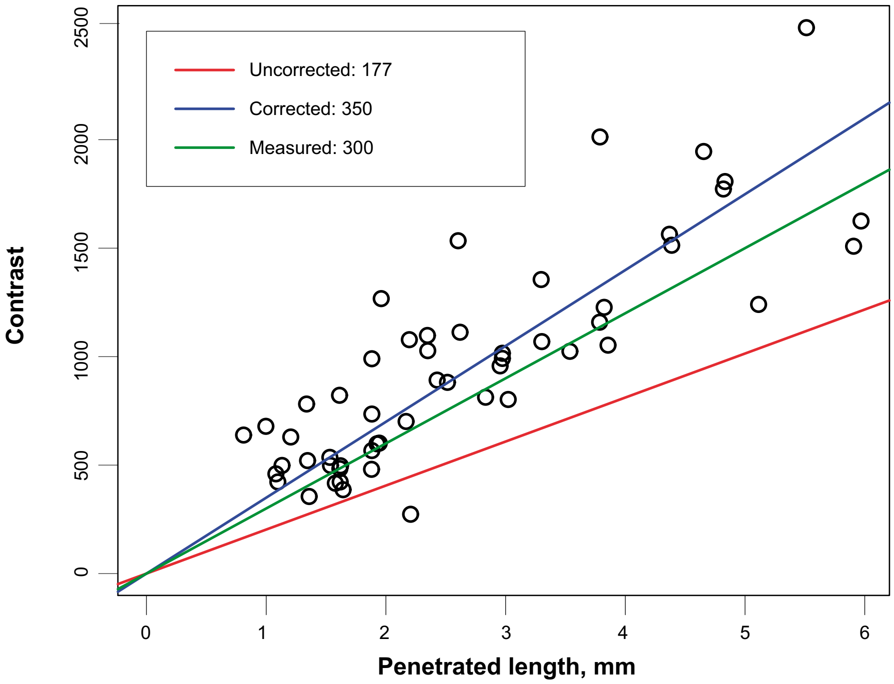

Figure 8-38. *Scatter diagram of the contrast and corrected penetrated sizes of volumetric discontinuities with reference lines.*

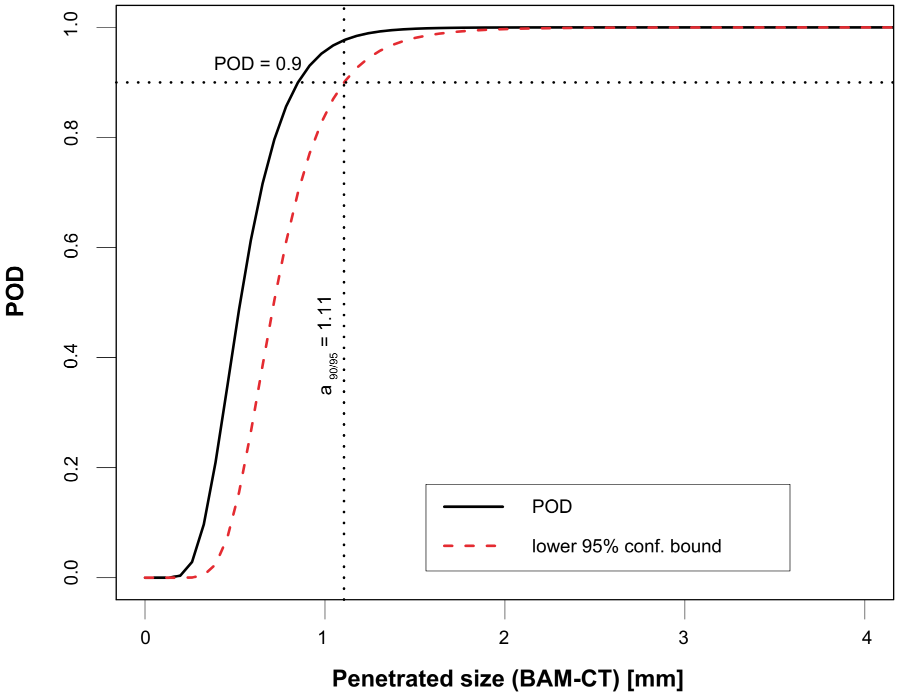

Figure 8-39. *POD curve based on the corrected penetrated sizes of the volumetric discontinuities in the weld L025.*

8.4 Determination of the sizing capabilities

In order to estimate the sizing capabilities of non-destructive testing, radial sizes of volumetric and JLH-type discontinuities determined by means of radiographic and ultrasonic inspection have been compared with the corresponding values determined by destructive inspection. Results have been summarized using box plots and a descriptive statistics that can be called “mean relative error”. Introductions of the box plot and give the formula for the mean relative error is presented below.

Box plots provide a five-number summary for a set of observations. The summary consists of:

- smallest observation,
- 1st quartile, i.e. the observation that is larger than one quarter and smaller than three quarters of all observations,
- median, i.e. the observation that is larger than one half and smaller than the other half of all observations,
- 3rd quartile, i.e. the observation that is larger than three quarters and smaller than one quarter of all observations,
- largest observation.

Box plots provide an insight about the location and variation of the set of observations. We have used box plots to present the set of differences between measured and true (known from CT or destructive testing for the weld L025 or FSW5, respectively) values of radial sizes. The results are given in the Section 9.2.

Further, the differences for each non-destructive method were summarized using the “mean relative error” that has been calculated according to the formula (22).

$$r = \frac{1}{K}\sum_{i=1}^{K}\left(\frac{s_E - s_T}{s_T}\right)\times 100\% \qquad (22)$$

The designations are as follows:

S_T true radial size known from the destructive testing

S_E experimental (measured) radial size

K number of observations

8.4.1 Results for FSW

Figure 8-40 shows the box plot of the differences between the radial sizes of volumentric discontinuities measured by radiographic inspection (35°) and by destructive segmentation. It can be seen that:

- all of the observed differences lie between –2.4 and 6.2 mm,
- half of the observed differences lie between –1.2 mm (1st quartile) and 0.9 mm (3rd quartile),
- although the radial sizes of some discontinuities have been overestimated by as much as 6 mm, the median difference value is negative (–0.2 mm), i.e. the trend is to underestimate the radial size.

Figure 8-41 shows the box plot of the differences between the radial sizes of volumentric discontinuities measured by ultrasonic inspection and by destructive segmentation. As shown in the figure,

- all of the observed differences lie between –2.1 and 1.2 mm,
- half of the observed differences lie between –1.6 mm (1st quartile) and –0.2 mm (3rd quartile),
- The ultrasonic testing tends to under-estimate radial sizes of discontinuities in the data set under investigation (median difference value: –0.7 mm).

Figure 8-42 displays the box plot of the differences between the radial sizes of the JLH-type discontinuities measured by ultrasonic inspection and by destructive inspection. Apparently,

- All of the observed differences lie between –1.4 and 2.5 mm.
- Half of the observed differences lie between –0.1 mm (1st quartile) and 1.1 mm (3rd quartile).
- The ultrasonic inspection tends to over-estimate the radial sizes of JLH-type flaws in the present data set (median value 0.5 mm). Nevertheless, there are some flaws that have been underestimated by as much as 1.4 mm presumably due to the fact that in the certain region of the flaw the surfaces get so tight that the flaw ceases to reflect ultrasound (kissing bonds).

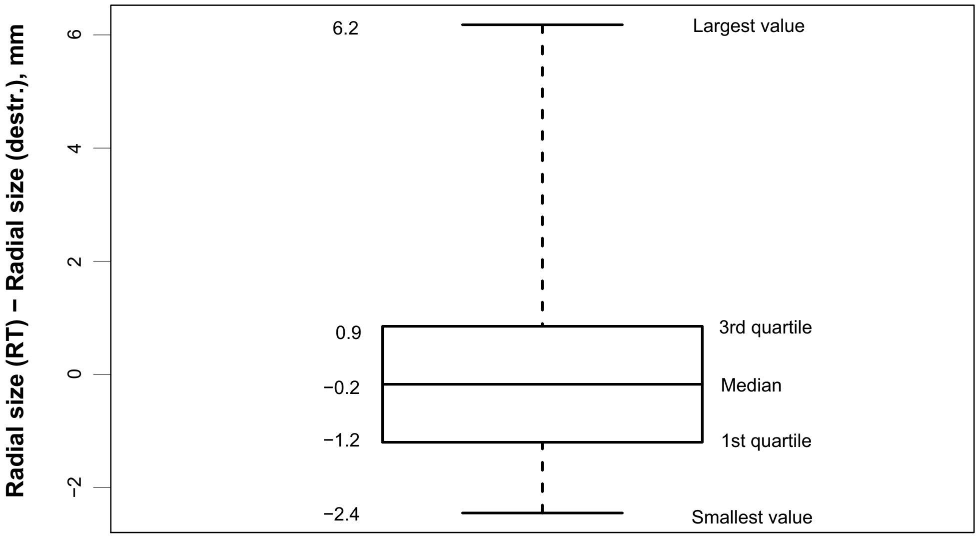

***Figure 8-40.** Box plot of the differences between the sizes of volumetric discontinuities measured by radiographic inspection (35°) and destructive inspection in radial direction (friction stir weld FSW5).*

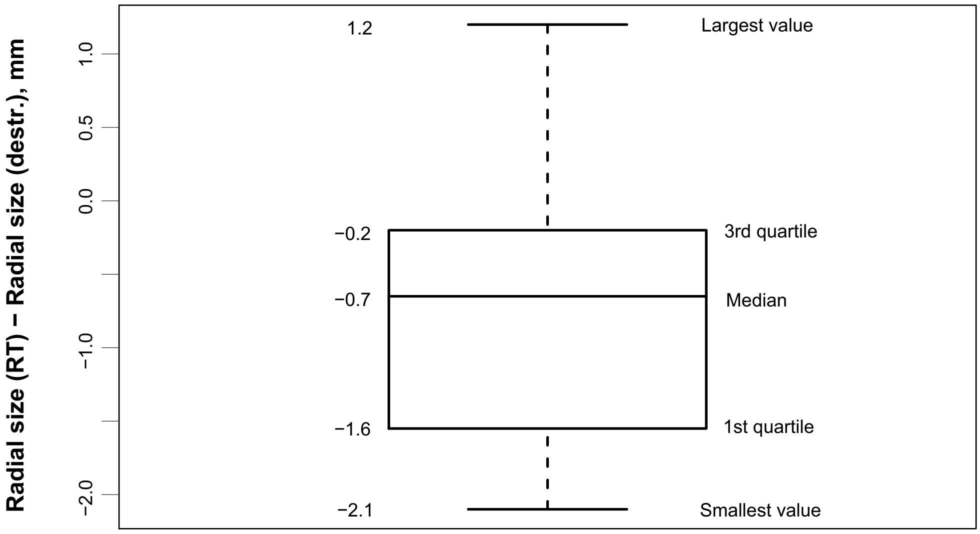

Figure 8-41. *Box plot of the differences between the radial sizes of volumetric discontinuities measured by ultrasonic inspection and destructive inspection (friction stir weld FSW5).*

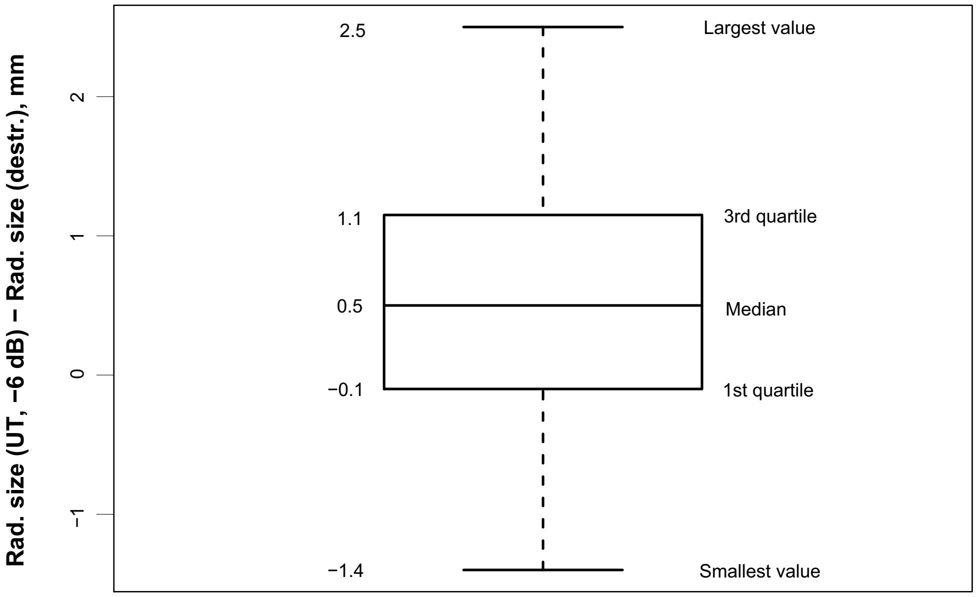

Figure 8-42. *Box plot of the differences between the radial sizes of the JLH-type dicontinuities measured by ultrasonic inspection and by destructive inspection (friction stir weld FSW5).*

8.4.2 Results for EBW

Figure 8-43 shows the box plot of the differences between the radial sizes of volumetric discontinuities measured by radiographic inspection (35°) and by segmentation of the computed tomography data. It can be seen that:

- all of the observed differences lie between –1.6 and 8.9 mm,
- half of the observed differences lie between 0.3 mm (1st quartile) and 2.4 mm (3rd quartile),
- the median difference value is positive (1.1 mm), i.e. the trend is to overestimate the radial size.

Figure 8-44 shows the box plot of the differences between the radial sizes of the area-like discontinuities measured by ultrasonic inspection and by transmission ultrasonic inspection. Apparently,

- all of the observed differences lie between –12.5 and 0.8 mm,
- half of the observed differences lie between –3.5 mm (1st quartile) and –0.5 mm (3rd quartile),
- the median difference value is negative (–2.3 mm), i.e. the transmission inspection tends to give larger size estimates.

It should be noted that no no destructive tests have been made to verify the values obtained by HECT- and UT-reference for EBW. Thus the results are subject to change provided destructive data.

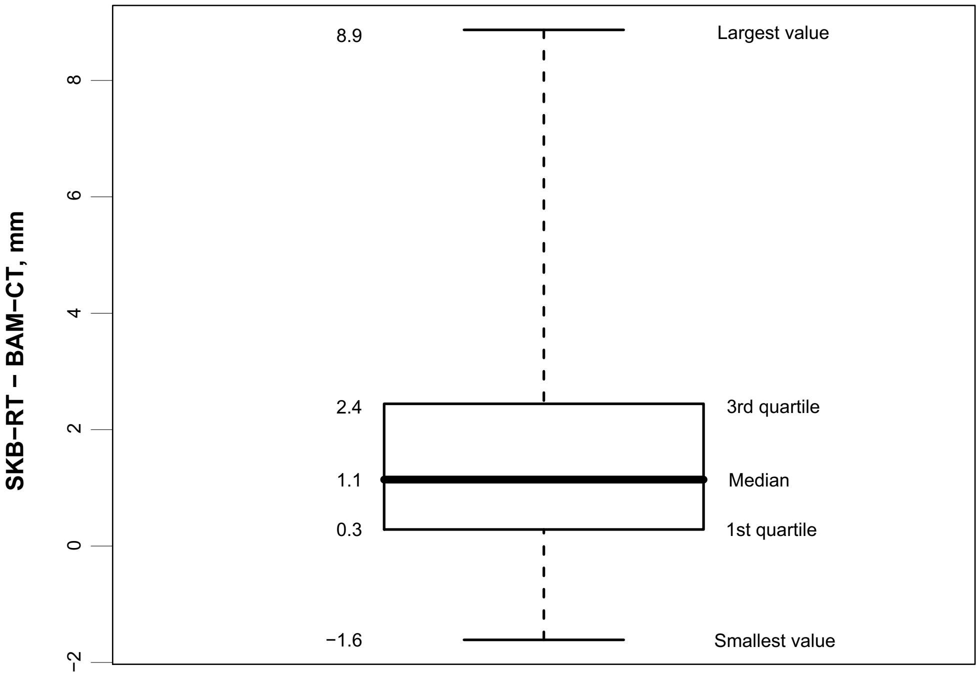

Figure 8-43. *Box plot of the differences between the radial sizes of volumetric discontinuities measured by radiographic inspection (35°) and by computed tomography (electron beam weld L025).*

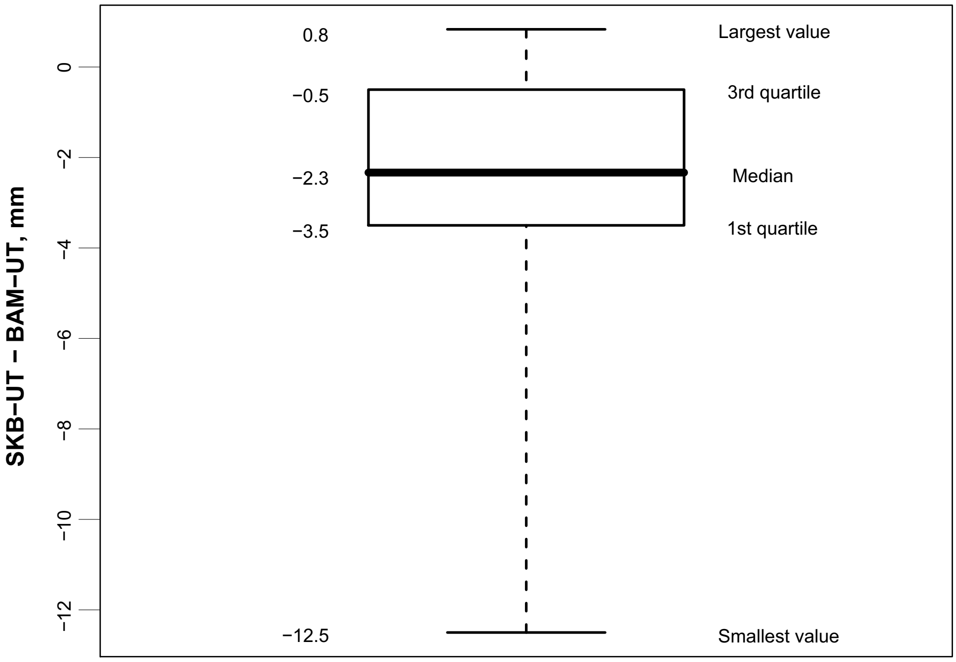

Figure 8-44. *Box plot of the differences between the radial sizes of area-like discontinuities measured by pulse-echo ultrasonic inspection at the SKB and by transmission ultrasonic inspection at the BAM (electron beam weld L025).*

9 Results

9.1 Probability of detection

9.1.1 EBW

At the current state of the art all observed $a_{90/95}$ values – as listened in Table 9-1 – are for radiographs not larger than 3 mm and for UT not larger than 20 mm^2. The corresponding radial dimension are at maximum also 4 mm for RT and 7 mm for UT in case the flaw configurations investigated here represent the full possible scale which might occur in the welds under production conditions. The tendency is towards smaller values when taking into account the correction of HECT reference. The simulations for small flaws show they would be detected for sure from a discontinuity size of 1.36 mm on when they would actually occur.

9.1.2 FSW

Subject of consideration in this section is the detectability of volumetric wormholes and area-like "joint line hooking" in friction stir welds with the SKB radiographic and ultrasonic methods. At the current state of the art all observed $a_{90/95}$ values – as listed in Table 9-2 – are for the wormholes for RT not larger than 3 mm and for UT not larger than 13 mm^2. The corresponding radial dimensions are at maximum also 4 mm for RT and 6 mm for UT in case the flaw configurations investigated here represent the full possible scale that might occur in the welds under production conditions. The simulations for small flaws show they would be detected for sure from a discontinuity size of 1.36 mm on when they would actually occur. The investigation revealed a potential for improvement in considering the actual possible physical signal to noise ratio for a reasonable decision threshold which shifts the $a_{90/95}$ to lower values. The empirical detectable radial dimension with UT for the "joint line hooking" is also 3..4 mm here. The modeling supported calculation for the curved and straight part separately yields a better understanding of the angle dependence of the UT echo.

Table 9-1. Table of the $a_{90/95}$ values for different datasets and modes of processing.

Dataset/process	$a_{90/95}$	a_r
EBW, radiography (without outliers)	1.91 mm	3.61 mm
EBW, radiography (with outliers)♣	2.26 mm	3.61 mm
Simulated pores (max. contrast)	1.36 mm	1.36 mm
EBW, ultrasound	20 mm²	7 mm

Table 9-2. Summary of POD curves and corresponding $a_{90/95}$ and a_r values for the friction stir weld FSW5.

Identification	Description	a (independent variable)	a-hat (dependent variable)	Decision threshold	$a_{90/95}$	a_r
Wormholes RT with standard threshold	Based on measured contrast resulting from volumetric flaws	Penetrated size	Contrast	250 counts	2.60 mm	4 mm
Wormholes RT with standard threshold (corrected)	Based on meas. contrast resulting from volum. flaws and penetr. sizes measured destructively	Penetrated size (destr. testing)	Contrast	250 counts	0.97 mm	2.4 mm
Wormholes RT with 3 thresholds	Based on measured contrast resulting from volumetric flaws	Penetrated size	Contrast	80 counts	0.89 mm	2.3 mm
				160 counts	1.61 mm	2.3 mm
				240 counts	2.34 mm	4 mm
Wormholes RT with 3 thresholds (corrected)	Based on meas. contrast resulting from volum. flaws and penetr. sizes measured destructively	Penetrated size (destr. testing)	Contrast	80 counts	0.28 mm	2.4 mm
				160 counts	0.59 mm	2.4 mm
				240 counts	0.92 mm	2.4 mm
Wormholes UT	Based on measured reflection from volumetric flaws	Area	Echo height, %	15%	12.5 mm^2	6.3 mm
JLH with “outliers”	Based on measured reflection from JLH-type flaws	Radial size	Echo height, %	6%	4.0 mm	4.0 mm
JLH without “outliers”	Based on measured reflection from JLH-type flaws	Radial size	Echo height, %	6%	3.2 mm	3.2 mm
Pores RT simulation (max. contrast)	Based on simulation of the radiographic inspection of pores	Penetrated size	Contrast	250 counts	1.36 mm	1.36 mm

9.2 Sizing capabilities

9.2.1 EBW

Results of the comparison of radial sizes are presented in the Section 8.4.2.

Radial sizes of volumetric flaws determined by radiography are larger compared to the results of computed tomography. The radial sizes determined by UT of area like flaws seem to be smaller than the reference measurements. However, it should be noted that the results are based on the reference data not verified by destructive testing and thus are subject to change provided destructive data is available.

9.2.2 FSW

Overall results of the comparison are recapitulated in the Section 8.4.1.

RT of wormholes underestimates the size in radial direction. The underestimation might be due to the fact that the flaws become smaller towards the ends (as confirmed by the cross sections) decreasing the contrast. Basically the difference of radiation direction of 35° and the radial measurement of the flaw dimension makes the method dependent on the typical geometric distribution of the flaws. The wormholes belong more to the type of volumetric flaws and have in addition often a zig-zag shaped surface so that the sound is reflected in all possible directions which makes an exact sizing by the 6 dB drop rule hard. The JLH's are overestimated due to the fact that they are in absolute value very small and might tend to the behaviour of a point reflector rather than a reflecting curved or flat plane.

Table 9-3. Summary of sizing capability in the radial direction.

Flaw type	Inspection method	Smallest deviation of the measured value from the reference value, mm	1st quartile, mm	Median deviation of the measured value from the reference value, mm	Mean relative deviation, %	3rd quartile, mm	Largest deviation of the measured value from the reference value, mm
Volumetric	Radiography	–1.6	0.3	1.1	26.7%	2.4	8.9
Area-like	Ultrasound	–12.5	–3.5	–2.3	–22.6%	–0.5	0.8

Table 9-4. Summary of sizing capability in the radial direction.

Flaw type	Inspection method	Smallest deviation of the measured value from the reference value, mm	1st quartile, mm	Median deviation of the measured value from the reference value, mm	Mean relative deviation, %	3rd quartile, mm	Largest deviation of the measured value from the reference value, mm
Volumetric	Radiography	–2.4	–1.2	–0.2	3.7	0.9	6.2
Volumetric	Ultrasound	–2.1	–1.6	–0.7	–16.2	–0.2	1.2
JLH	Ultrasound	–1.4	–0.1	0.5	26.1	1.1	2.5

9.3 High resolution computed tomography on FSW samples

9.3.1 Introduction

Due to some technical problems with the 320 kV Micro-CT equipment only the measurements 0650a.bm and 0651a.bm (unique identification of CT measurements at BAM) could be performed with standard conditions. The measurements before the final repair of the 320 kV X-ray tube (0627a.bm up to 0647a.bm) are done with a not very well defined focal spot size of the 320 kV X-ray tube. Table 9-5 lists all investigated samples.

9.3.2 Experimental set-up

The most important measurement parameters are listed in Table 9-6.

Due to the voxel size of 40 µm all samples could be measured with one or two overlapping volumes at one respectively two positions, which means the interesting volume with a height of 55 mm is completely measured. Figure 9-1 shows the sample arrangement. All measurements are performed with the identity mark on top.

Table 9-5. List of samples, investigated with high-resolution computed tomography.

Sample size: 20×20×20 mm^3			
FSW5-46.7	0627a.bm		
FSW5-49	0628a.bm		
FSW5-28	0629a.bm		
FSW25-26	0630a.bm		
Sample size:20×20×50 mm^3			
FSW28-202	0631a.bm		
FSW33-39	0633a.bm		
FSW31-280	0635a.bm		
FSW25-79	0637a.bm		
FSW37-33	0639a.bm		
Sample size: 20×20×80 mm^3			
FSW22-201	0641a.bm	0650a.bm	0651a.bm
FSW23-143	0643a.bm		
FSW24-264	0645a.bm		
FSW26-225	0647a.bm		

Table 9-6. Parameters of measurement.

X-ray	310 kV (120+190kV), tube current 100µA
Prefilter	1.5 mm Sn and 0.5 mm Cu
Projections	900/360°
Integration time	10 sec
Voxel size	40×40×40 µm^3

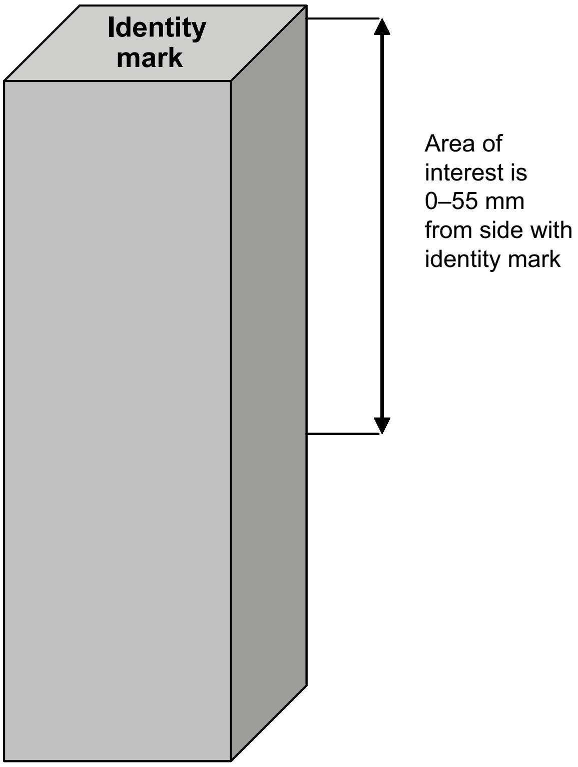

Figure 9-1. Scheme of the measurement. All the samples are measured with the identity mark on top, which means the first cross sections show the identity mark.

9.3.3 Results: Volumetric discontinuity

Samples (20×20×20 mm^3)

Two typical examples of samples with dimension (20×20×20 mm^3) are shown in Figure 9-2 and Figure 9-3, showing some volumetric flaws (wormholes) in the samples. The iso-surface images are view rotated 90° compared to the cross sections for better readability of the identity mark.

FSW5-46.7

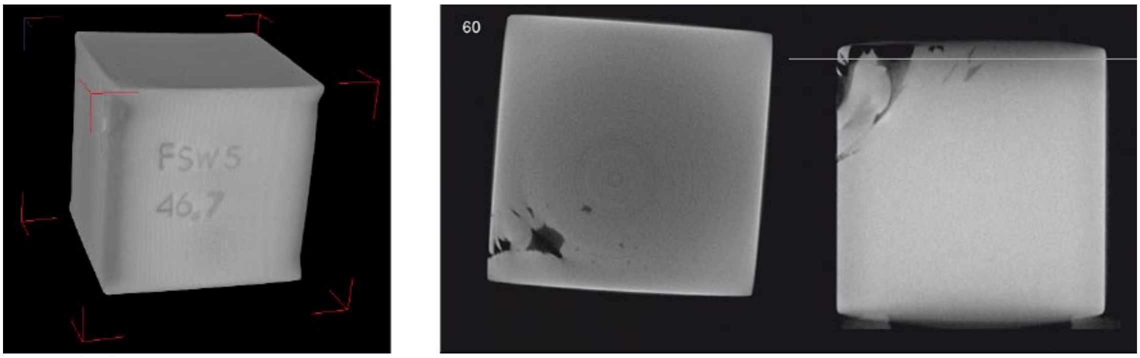

Figure 9-2. Iso-surface representation (left image), showing the identity mark. The image at right shows the horizontal slice # 60 together with a vertical slice, where the location of the horizontal slice is drawn as white line.

FSW5-49

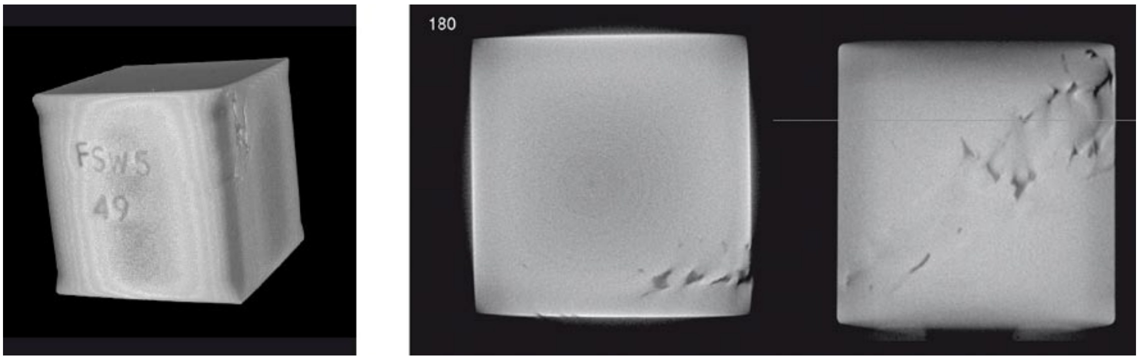

Figure 9-3. *Iso-surface representation (left image). The image at right shows the horizontal slice # 180 together with a vertical slice, where the location of the horizontal slice is drawn as white line.*

9.3.4 Results: Planar discontinuity

Samples (20×20×50 mm^3) and samples (20×20×80 mm^3)

The regions, where the larger samples are cut out are shown in Figure 9-4. The volume of interest extends to a depth of about 55 mm, which can be covered by two CT-measurements.

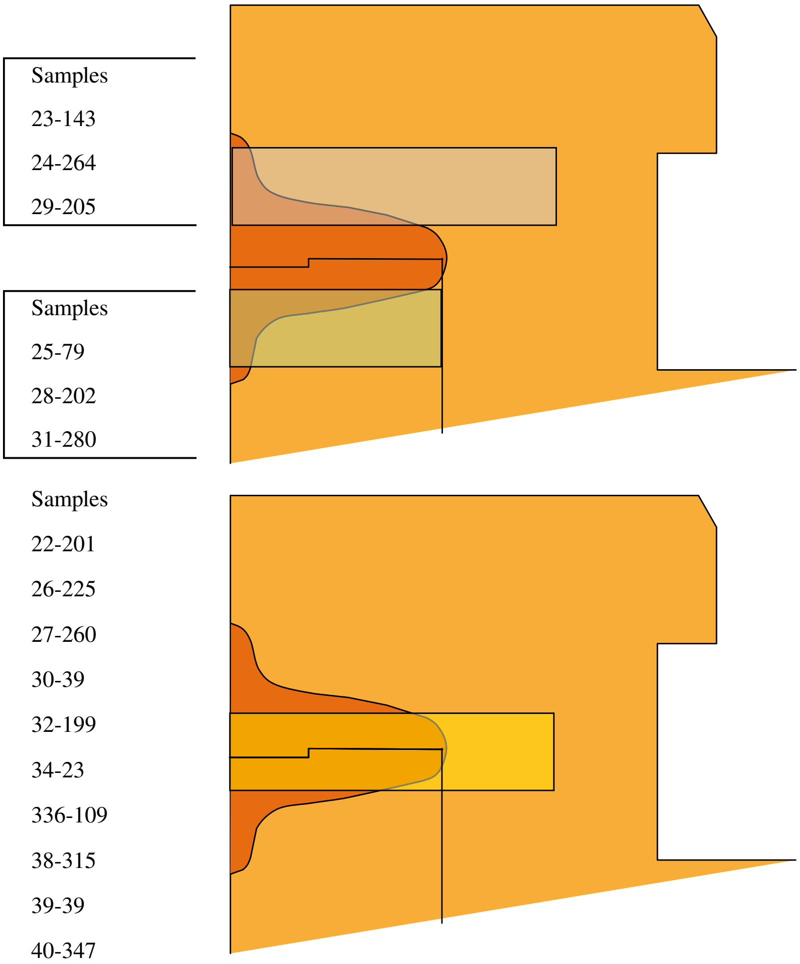

Figure 9-4. *Scheme of the regions, where the larger samples are cut out.*

FSW31-280

The CT images of this sample show no discontinuity.

9.3.5 Limit of detection

To get some information about the capability of CT to detect planar discontinuities the joint line between lid and the tube was measured, depending on the position of the sample in respect to the central slice (red arrow) of a CT measurement. Sample FSW22-201 was measured at two positions. If the vertical joint is near the location of the central slice (Figure 9-6) the vertical joint is detectable with a good contrast. The upper image shows the end of the vertical joint (vertical slice # 531), the image at bottom the slice # 562, which is 1.24 mm more close to the surface of the sample. The enhanced contrast of the vertical joint means that the joint is more open. Even at the surface itself the opening width appears with a width of lower than about two voxels e.g. lower than 80 μm. This corresponds to the result of microsections (Figure 6-32), from which the opening of the joint line can be estimated to be lower than 80 μm.

If the sample was measured in another position (Figure 9-7) , that means the joint line is 10.9 mm out of the central slice, the joint line appears with reduced contrast due to the inclined X-ray beam but is still clear detectable.

Figure 9-8 shows a vertical slice perpendicular to the orientation in Figure 9-6, where the extend of the joint into the sample can be measured. On this sample no evidence for a JLH is visible with CT.

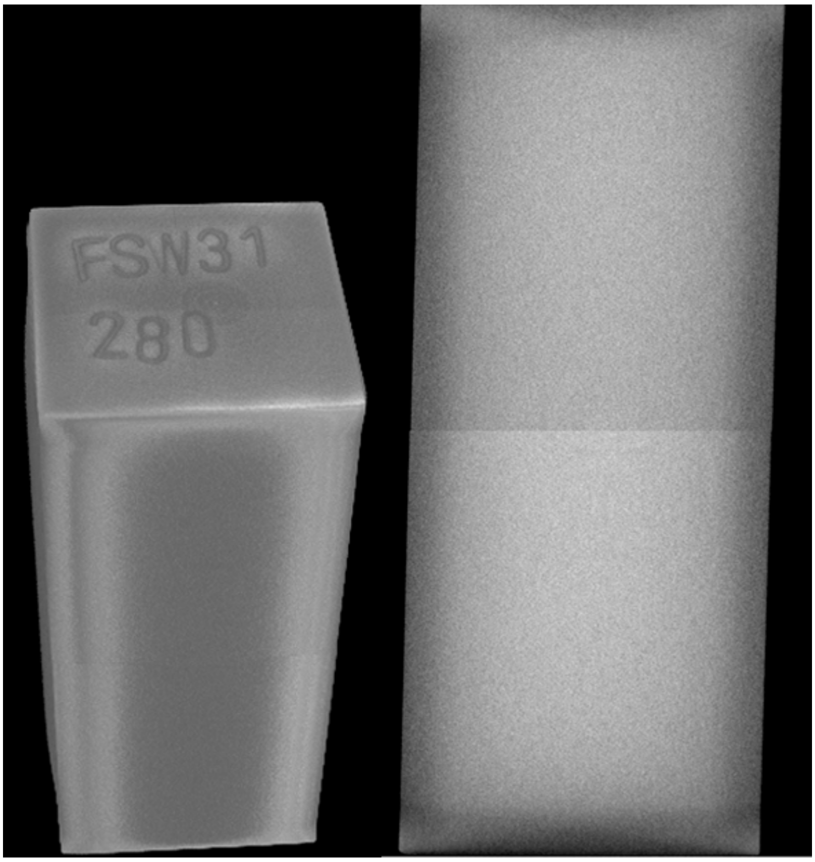

Figure 9-5. *Iso-surface representation (left image). The image at right shows a vertical slice trough the sample. The two parts of the measurement are visible.*

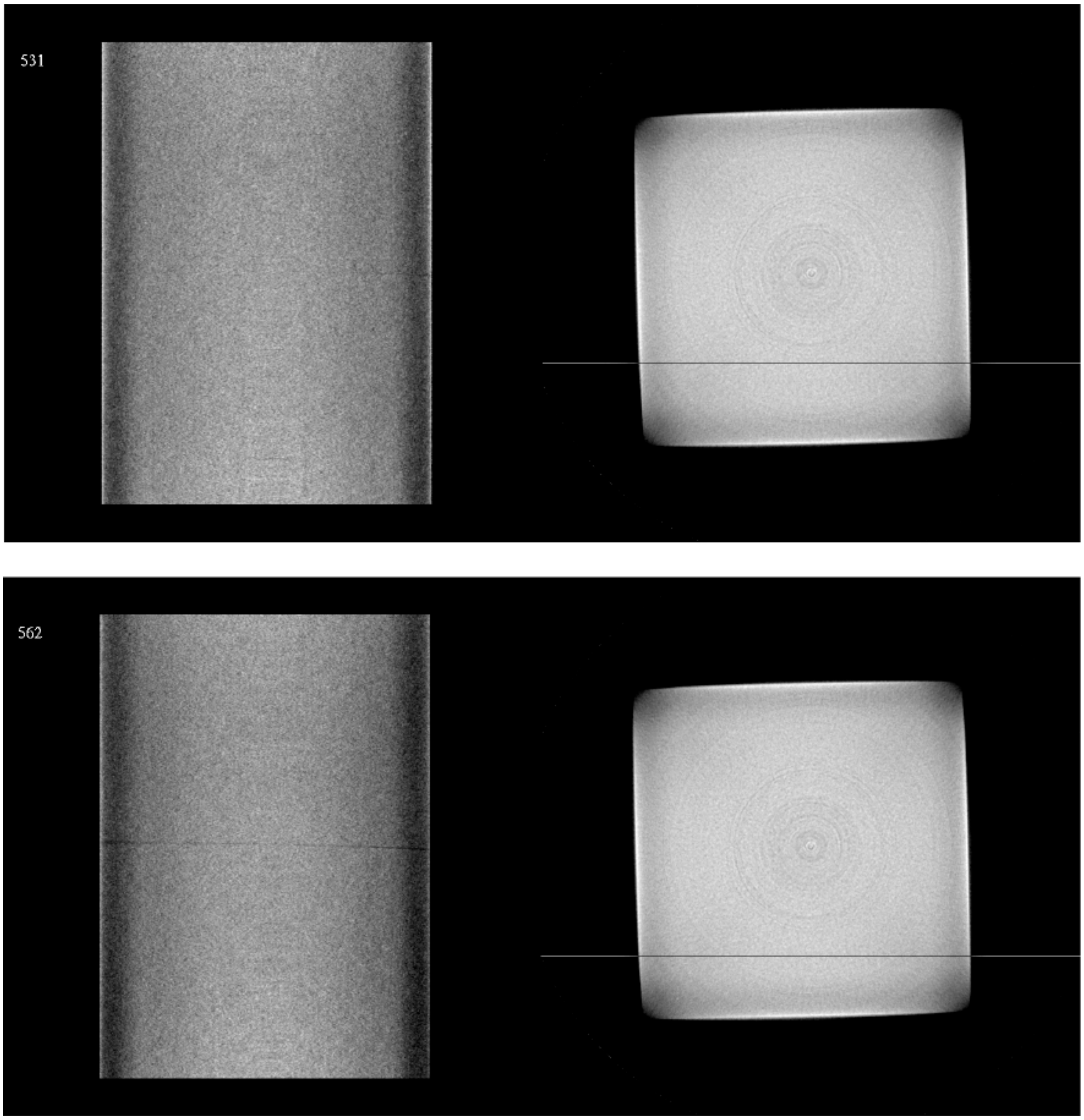

Figure 9-6. *Two vertical slices (left images) together with their location in the sample, indicated through the grey line in the horizontal slice of the sample (right images).*

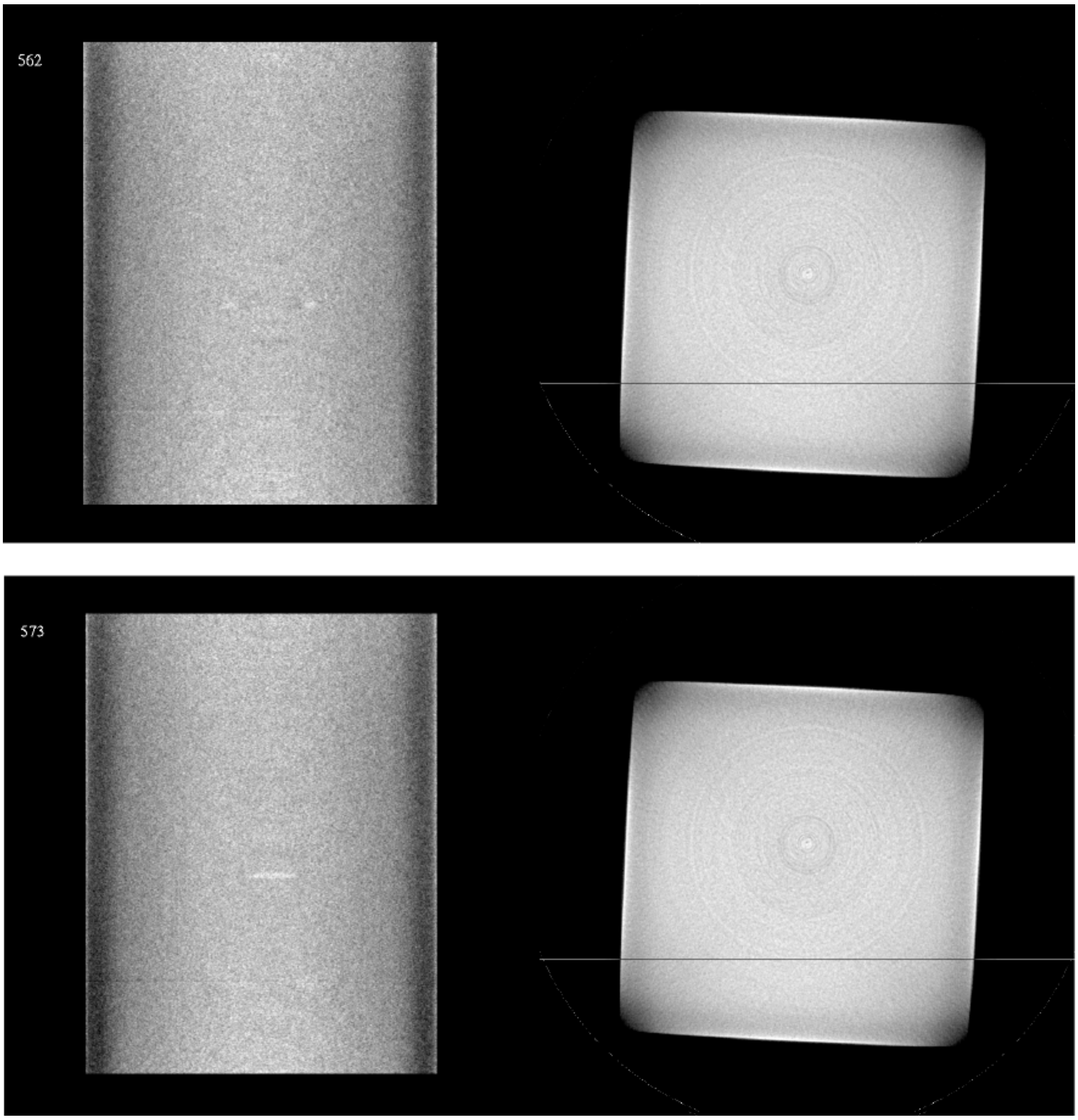

Figure 9-7. *Vertical slice at a different position (sample was moved 10.9 mm in height). The joint line is now out of the central slice of the X-ray beam.*

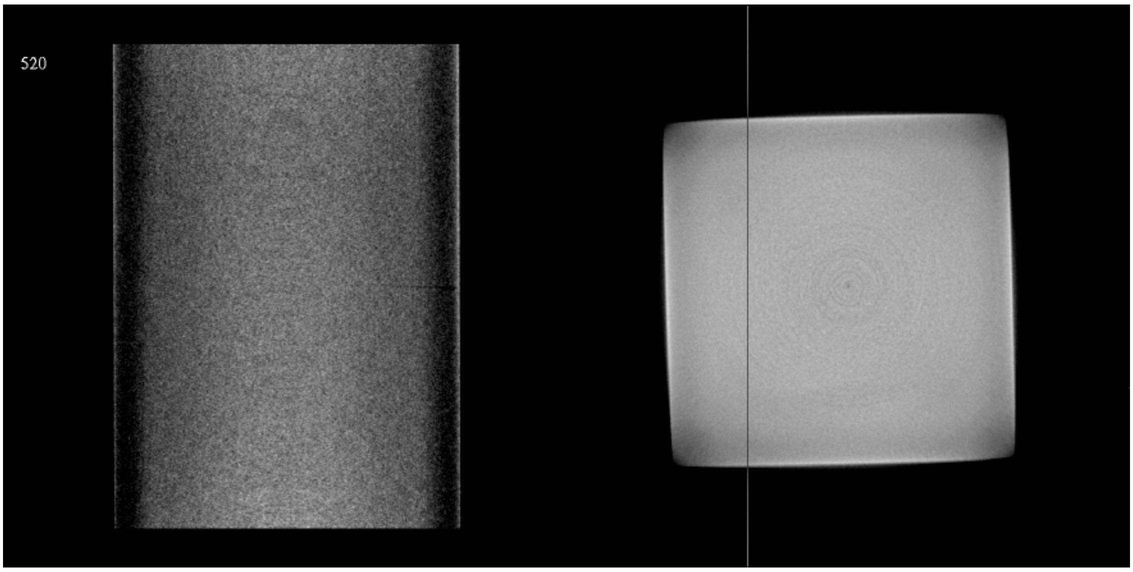

Figure 9-8. *Vertical slice (perpendicular to the orientation in Figure 9-6), showing the extend of the joint into the sample .*

9.3.6 Additional measurements

As an extension of the tomographic measurements two samples are investigated with the 225 kV tomographic equipment. The available energy is too low to perform tomographic measurements of the Cu samples under economical conditions, but the equipment can be used for digital radiography. The detector is a flat panel detector with a CsI scintillator with 2,048×2,048 pixels à (200 µm)^2. The X-ray conditions are 200 kV and 150 µA and a 1 mm Sn pre-filter. With an integration time of 2 sec per projection a signal-to-noise ratio of 56 was reached, averaging over 400 projections. Figure 9-9 shows the result of the three samples FSW 41/154 – FSW 38/315 – FSW 34/233 together with a wire penetrameter. The magnification is about 5×. The smallest wire penetrameter with a diameter of 0.25 mm can be clearly detected behind the 20 mm Cu samples resulting in a contrast ratio of 1.25%.

The samples FSW 38/315 and FSW 22/201 were measured again to get information about a possible JLH indication. Figure 9-10 shows a section of this projection which can be suggestively read as a JLH, but this effect can also be caused by an inclined position of the sample. Therefore the number of projections was extended to 1,200 resulting in a signal-to-noise ratio of about 180. Figure 9-11 shows the result of the sample FSW 38/315 alone, where the maximum magnification of about 20 is used. On this image no indication of JLH can be detected, but the presence of this effect can not be excluded within the limit of the spatial resolution of about 10 µm.

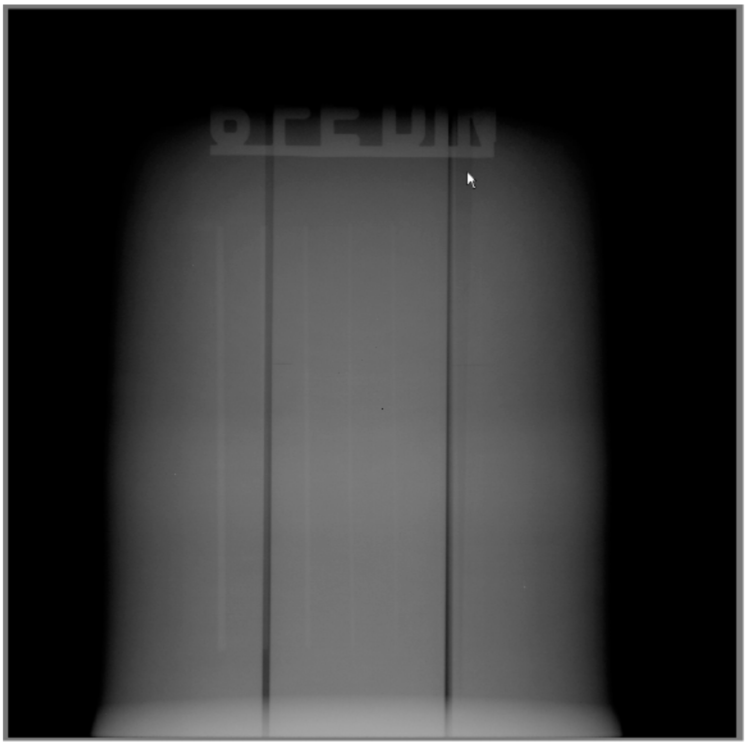

Figure 9-9. *Projection image, averaged over 400 single projections of the three samples (from left to right) of FSW 41/154 – FSW 38/315 –FSW 34/233.The joint lines are clearly detected together with the smallest wire penetrameter of 0.25 mm.*

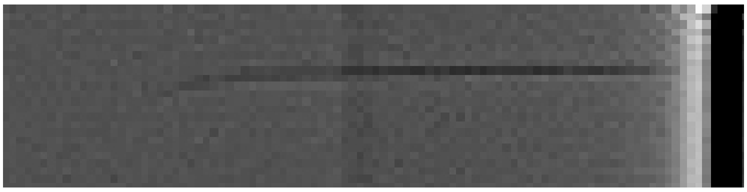

Figure 9-10. *Projection image, averaged over 400 single projections, of the two samples FSW 38/315 and FSW 22/201.*

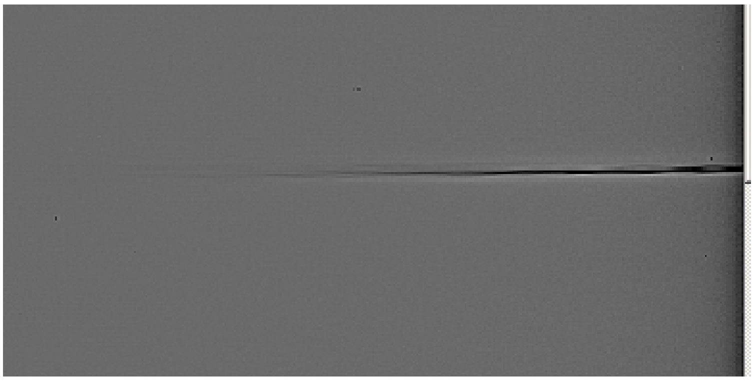

Figure 9-11. *Projection image, averaged over 1,200 single projections, of the sample FSW 38/315. No JLH can be detected.*

9.3.7 Conclusions

The measurements show that volumetric and planar discontinuities can be clearly detected with micro computed tomography. The detection limit is in the order of about two pixels, that means for samples with a cross section of 20×20 mm^2 and a resulting voxel size of (40 µm)^3 pores, inclusions and planar flaws where the dimensions are at least larger than about 80 µm can be clearly detected. Discontinuities can be distinguished from the ring artefacts due to the symmetric structure of these artefacts.

To detect smaller discontinuities, the cross section of the samples has to be reduced at minimum about a factor of two (10×10 mm^2). In this case discontinuities down to 15 µm (with an detector matrix of 1,024^2 pixel) or 7.5 µm (detector matrix of 2,048^2 pixel) should be detectable.

9.4 Evaluation of FSW test samples by radiography

SKB delivered 28 extra test samples to be examined by micro-CT in addition to the specimen investigated for the POD analysis. To complete the results of the micro-CT BAM performed additionally standard radiographs from two directions with a Seiffert tube (320 kV) used at 270 kV for optimum contrast (set up see Figure 9-12).

8 of the test samples (20×20×20) were already a subject of NDT indications and were investigated to get more detailed insight in flaw sizes and shapes and hints for indications below the recording level.

X-Ray parameters		Legend
Voltage	270 kV Seiffert 320 kV	
Current	5 mA	JLH? – suspicion of Joint Line Hooking
Focus size	1.5 mm	
Film-focus-distance	1,000 mm	
Film	Agfa D2	
Screens	Pb 0.02×0.02 mm	
Exposure time	6 min.	
Optical density (inside object)	2.6	

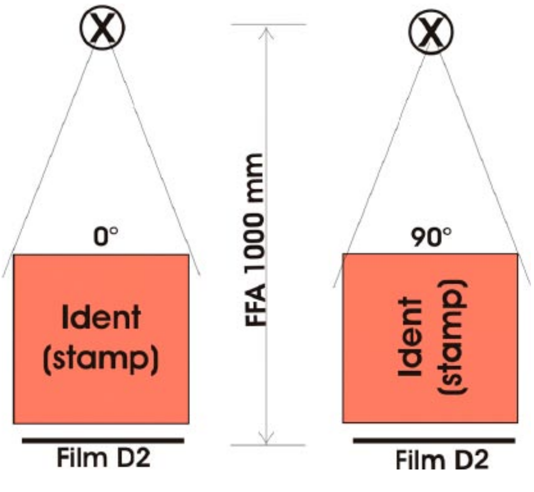

Figure 9-12. *Radiographic set up for the Cu-blocks.*

9.4.1 Results

The focus of interest here is on the randomly taken 20 test samples from all the FSW's created during the welding experiments for the safety analysis. Here we can observe one type of flaw: This type is "tails" from the JLH type of flaws, which are described in former chapters (see JLH-indications in the table). The maximum observed size including the open joint between the tube and the lid amounts to 4.5 mm (see Figure 9-14).

Table 9-7. Evaluation results of radiographs of the FSW-test samples.

SKB: FSW-samples (Cu) for Micro-CT (sizes in mm)		Film/Image Indentification		Evaluation results
		0°	90°	
FSW5/46.7	20×20×20	1	+X	shrinkage (circle)
FSW5/49	20×20×20	2	+X	shrinkage (line by line)
FSW5/78	20×20×20	3	+X	
FSW25/26	20×20×20	4	+X	
FSW25/359.5	20×20×20	5	+X	
FSW27/355.5	20×20×20	6	+X	
FSW36/64	20×20×20	7	+X	
FSW36/46	20×20×20	8	+X	
FSW28/202	20×20×49	9	+X	
FSW31/280	20×20×49	10	+X	
FSW33/39	20×20×49	11	+X	
FSW37/33	20×20×49	12	+X	
FSW22/201	20×20×80	13	+X	linear indication (gap), suspicion of JLH?
FSW23/143	20×20×80	14	+X	
FSW24/264	20×20×80	15	+X	
FSW25/79	20×20×50	16	+X	
FSW26/225	20×20×80	17	+X	linear indication (gap)
FSW27/260	20×20×80	18	+X	linear indication (gap)
FSW29/205	20×20×80	19	+X	
FSW30/39	20×20×80	20	+X	linear indication (gap)
FSW32/199	20×20×80	21	+X	linear indication (gap)
FSW34/233	20×20×80	22	+X	linear indication (gap)
FSW35/100	20×20×80	23	+X	
FSW36/109	20×20×80	24	+X	linear indication (gap)
FSW38/315	20×20×80	25	+X	linear indication (gap), suspicion of JLH?
FSW39/39	20×20×80	26	+X	linear indication (gap)
FSW40/347	20×20×80	27	+X	linear indication (gap)
FSW41/154	20×20×80	28	+X	

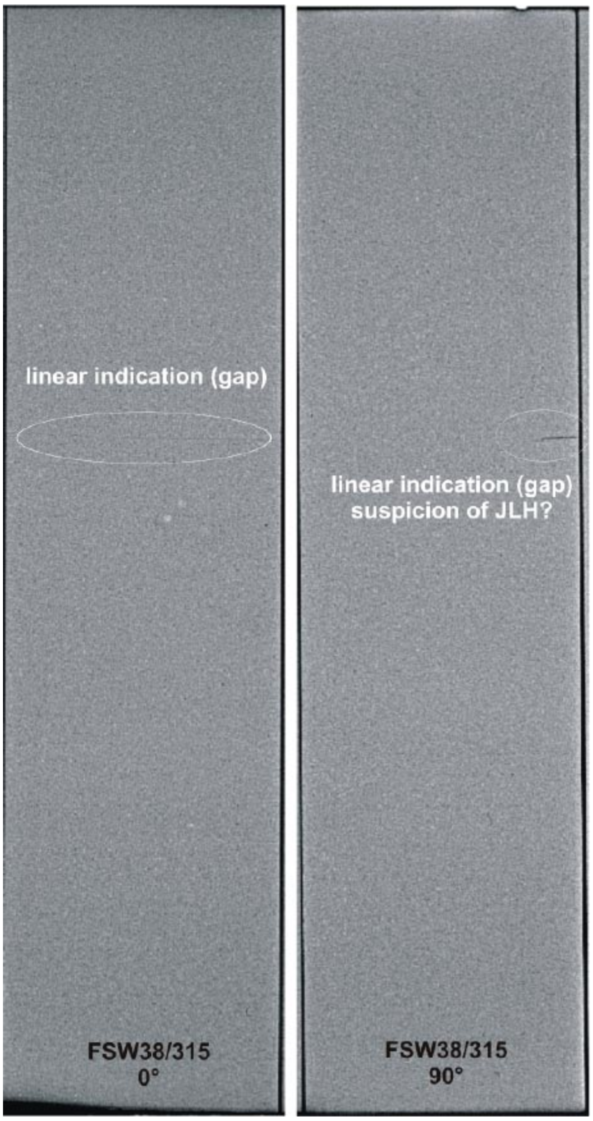

Figure 9-13. *Examples of indications in radiograph after image processing.*

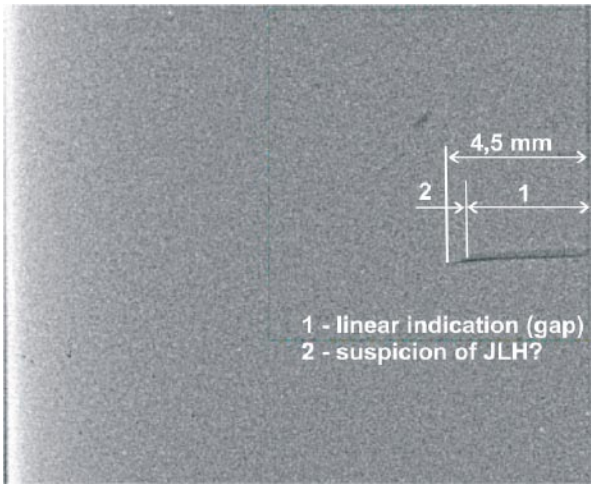

Figure 9-14. *Detail of FSW22/201.*

9.4.2 Comparison film radiography vs. micro-CT

The comparison of the results between the film radiography and the computer-tomography can be summarised as follow:

1. Volumetric indications (e.g. pores, tungsten inclusions) were not found.
2. The open joint between the lid and the canister of the samples FSW22/201, FSW34/233, FSW26/225, FSW36/109, FSW27/260, FSW38/315, FSW30/39, FSW39/39, FSW32/199 and FSW40/347 could be recognised with both test methods.
3. From the results of the filmradiography and digital radiography (made by flat panel detector) of the samples FSW38/315 and FSW22/201 can be assumed any indications of the JLH-flaw. Due to the limits of the spatial resolution a quantitative evaluation can not be performed.

10 Conclusions

The BAM expertise for SKB had two parts: (i) validation of the physical parameters of the X-ray system against the current European standards and (ii) determination of the reliability of the applied NDT methods. Both tasks were assisted by modelling calculations for deeper understanding and avoiding too much experiments and reference experiments.

The SKB radiography device and its set up fulfil the requirements of EN 1435. The film specific parameters were transformed to the properties of the digital system. The SKB radiography provides the required image quality, measured with wires and step hole IQIs (see also EN 462). The total system unsharpness is significantly higher than the required one by EN 1435. The standard permits the compensation of parameters. The system provides significantly higher signal/noise ratio (SNR) than the specified film systems. The lost of contrast for small flaws is compensated by the better SNR in the order of the IQI dimensions (0.3–2 mm depending on wall thickness). These parameter settings verified in the following probability of detection evaluations that the system is able to fulfil the requirements. Further they gave hints for possible steps of improvement.

A Probability of Detection evaluation for the SKB-NDT processes has been successfully established to make sure the applied NDT techniques are able to reveal the occurring discontinuities and to quantify the discontinuity sizes, which might be overseen by NDT as an input for the final risk assessment. A generalization of the existing prescription for the signal response POD from the MIL 1823 standard was necessary because the EBW and FSW welds of 50 mm thick Cu-canister-welds are more complex than thin aerospace structures.

The physical reasonable $a_{90/95}$ values as discontinuity sizes, which are detected for sure need to be set in correspondence to the corresponding radial dimensions of discontinuities to provide the expected wall thickness reduction, which is of importance for the integrity requirement. For EBW these values are below 4 mm for volumetric flaws detected by radiography and are not larger than 7 mm for area like flaws detected by UT.

Subject of consideration for FSW was the detectability of volumetric like wormholes and area like "joint line hooking" with the SKB radiographic and ultrasonic methods. At the current state of the art all observed $a_{90/95}$ values are for the wormholes for radiographs not larger than 3 mm and for UT not larger than 13 mm^2. The corresponding radial dimension are at maximum 4 mm for RT and 6 mm for UT in case the flaw configurations investigated here represent the full possible scale which might occur in the welds under production conditions. The empirical detectable radial dimension with UT for the "joint line hooking" is 4 mm.

The simulations for small flaws show they would be detected for sure from a discontinuity size of 1.36 mm when they would actually occur. The investigation revealed a potential for improvement in considering the actual possible physical signal to noise ratio for a reasonable decision threshold which shifts the $a_{90/95}$ to lower values.

The sizing errors for both types of welds are for area like flaws of only a couple of mm using UT technique. Even for volumetric flaws, where UT is not so well suited, in FSW the absolute deviations are a couple of millimeters underestimation only. The joint line hooking discontinuities are overestimated even when there is a kissing part. All flaws are detected and sized with sufficient accuracy with respect to the intended purpose to avoid a critical flaw size of 35 mm.

11 Abbreviations

BAM	Bundesanstalt für Materialforschung und -prüfung (Federal Institute for Materials Research and Testing)
BIR	Bio-Imagine Research Inc.
CS	Contrast sensitivity
CT	Computed Tomography
EBW	Electron Beam Welding
FBH	Flat Bottom Hole
FSW	Friction Stir Welding
HECT	High energy computerized tomography
in_w	Inclusion of higher absorption
JLH	Joint Line Hooking
lin	Straight linear indication
lin_t	Tilted linear indication (length)
NDT	Nondestructive Testing
POD	Probability of Detection
SDD	Source detector distance
SKB	Svensk Kärnbränslehantering AB
sp	Singular porosity
TR	Transmitter-Receiver
TWI	The Welding Institute

12 References

/1/ **Non-Destructive Evaluation System Reliability Assessment.** MIL-STD-1823 (U.S. Department of Defense).

/2/ **Goebbels J et al. 2003.** BAM CT test report Pr_0003a.be for SKB. BAM.

/3/ **The International Institute of Welding, 1987.** Guidance and recommendations on evaluation of ultrasonic signals in manual weld examination and on defect acceptance/rejection criteria.

/4/ **Haase O, Goebbels J, Illerhaus B, Bailey M, Sené M, 1999.** High Energy Tomography and Crack Dection, Proceedings of the Int. Symp. on Computerized Tomography for Indiustrial Applications and Image Processing in Radiology, March 15–17, 1999, Berlin, DGZfP Proceedings BB67 CD, 233–239.

/5/ **VG Studio Max 1.2** – User's Manual; Volume Graphics, 2004.

/6/ **Illerhaus B, Goebbels J, Riesemeier H, 1997.** 3D Computerized Tomography – Synergism Between Technique and Art in Optical Technologies in the Humanities, Vol. IV of the International Series on Optics Within Life Sciences (OWLS), Springer Verlag Heidelberg, ISDN 3-540-63280-8.

/7/ **Illerhaus B, Jasiuniene E, Kottar A, Goebbels J, 2002.** 3D Microtomography (µCT) of Cellular Metals using an up to 320 kV X ray tube, Proc. and Prop. of Lightweight Cellular Metals and Structures, Ed. A. Gosh et al., TMS 271–280.

/8/ **Illerhaus B, Goebbels J, Riesemeier H, Staiger H, 1997.** Correction techniques for detector systems in 3D CT . Proceedings of SPIE Vol. 3152.

/9/ **Illerhaus B, Onel Y, Goebbels J, 2004.** Correction techniques for 2D detectors to be used with high energy X ray sources for CT, part II, Prcoceedings of SPIE 5535/Denver USA/1. 8.8.2004.

/10/ **Feldkamp L A, Davis L C, Kress J W, 1984.** J. Opt. Soc. Amer. A1, (1984), pp. 612–619.

/11/ **Briesmeister J F (ed.), 2000.** MCNP–A General Monte Carlo N–Particle Transport Code, LANL Report LA–13709–M, Los Alamos.

/12/ **Bellon C, 2001.** Computersimulation radiographischer Prüfverfahren. PhD thesis, Dresden University of Technology, Logos-Verlag, Berlin.

/13/ **Tillack G-R, Bellon C, 1999.** Simulation von Durchstrahlungsprüfungen – Möglichkeiten und Grenzen. Materialprüfung, Carl Hanser Verlag, 41:90–97.

/14/ **Boehm* R, Wüstenberg* H, Hauser* T, Hintze** H, Fischer*** E, 2001.** Neue Ansätze zur Ultraschallprüfung von Eisenbahnachsen mit Array-Prüfköpfen. Conference contribution, DGZfP Jahrestagung, 21–23 May 2001, Berlin, Berichtsband 75-CD, Berlin, Germany, *BAM, **Deutsche Bahn, ***intelligeNDT Systems & Services.

/15/ **Boehm* R, Erhard* A, Rehfeldt** T, 2003.** Einfluss fokussierter Schallfelder auf das Reflexionsverhalten von Testfehlern. Conference contribution, DGZfP Jahrestagung, 26–28 May 2003, Berichtsband 83-CD, ISBN 3-931381-39-0, Weimar, Germany, *BAM, **intelligeNDT Systems & Services.

/16/ **Boehm* R, Erhard* A, Rehfeldt** T, 2004.** Reflexionsverhalten in fokussierten Schallfeldern. In: Materialprüfung 46 (2004) 1–2, Carl Hanser Verlag, München, S.46–52, *BAM, **intelligeNDT Systems & Services.

/17/ **Boehm* R, Erhard* A, Wüstenberg* H, Rehfeldt** T, 2002.** Dreidimensionale Berechnung von Schallfeldern unter dem Einfluss zylindrischer Bauteilkrümmungen für fokussierende Prüfköpfe und Gruppenstrahler. Conference contribution, DGZfP Jahrestagung, 6–8 May 2002, Berichtsband 80-CD, ISBN 3-931381-39-0, Weimar, Germany, *BAM, **intelligeNDT Systems & Services.

/18/ **Rauschenbach* H, Friedrich* J, Heinrich* W, Boehm** R, 2002.** Nachqualifizierung von Gasturbinen-Radscheiben mittels portablem, mechanisierten Prüfsystem – ein Baustein zum Lebensdauerkonzept bei Gasturbinen. Conference contribution, DGZfP Jahrestagung, 6–8 May 2002, Berichtsband 80-CD, ISBN 3-931381-47-1, Mainz, Germany, *Siemens Power Generation, **BAM.

/19/ **Rehfeldt* T Boehm** R, Matthies** K, Wüstenberg** H, 2004.** Kompensation von Krümmungseinflüssen bei fokussierenden Systemen mit Linsen und Gruppenstrahlern. Conference contribution, DGZfP Jahrestagung 17–19 May 2004, Berichtsband 89-CD, ISBN 3-931381-55-2, Salzburg, Austria, *intelligeNDT Systems & Services, **BAM.

/20/ **Berens A P, 1989.** NDE reliability data analysis. In Metals Handbook, volume 17. ASM International, 9 edition.

/21/ **ASTM, E1000.** Chapter 11: Image Quality Considerations, p. 438.

/22/ **US Department of defense.** Nondestructive evaluation system. Reliability assessment, 1999. Handbook.

/23/ **ASNT Nondestructive Testing Handbook.** Second Edition, Volume 7: Ultrasonic Testing pp. 445 (Factors Determining Amplitude of Discontinuity Echo Signal).

/24/ **Altman M, Gill J, McDonald M P, 2003.** Numerical Issues in Statistical Computing for the Social Scientist. John Wiley and Sons, New York. (Software version: R Package, Accuracy, version 1.11) ISBN 0-471-23633-0.